

CONTENS

ADDRESS OF PUBLISHER & EDITOR'S OFFICE:

**GDAŃSK UNIVERSITY
OF TECHNOLOGY**

**Faculty of Ocean Engineering
& Ship Technology
G. Narutowicza 11/12
80-233 Gdańsk, POLAND**

tel.: +48 58 347 13 66
fax: +48 58 341 13 66

EDITORIAL STAFF:

Jacek Rudnicki
| Editor in Chief
Rafał Szłapczyński
| Associate Editor
Jerzy Świryczuk
| Associate Editor
Przemysław Wierzchowski
| Associate Editor
Maciej Galik
| Associate Editor
Aleksander Kniat
| Editor for international
relations

Price:
single issue: 25 PLN

Prices for abroad
single issue:
- in Europe EURO 15
- overseas USD 20

WEB:

pg.edu.pl/pmr
degruyter.com/view/j/pomr

ISSN 1233-2585

3	Piotr Szymak <i>COMPARISON OF FUZZY SYSTEM WITH NEURAL AGGREGATION FSNA WITH CLASSICAL TSK FUZZY SYSTEM IN ANTI-COLLISION PROBLEM OF USV</i>
15	Andrzej Chybicki <i>MAPPING SOUTH BALTIC NEAR-SHORE BATHYMETRY USING SENTINEL-2 OBSERVATIONS</i>
26	Krzysztof Czarnecki, Wojciech Leśniak <i>BEARING ESTIMATION USING DOUBLE FREQUENCY REASSIGNMENT FOR A LINEAR PASSIVE ARRAY</i>
36	Cezary Specht, Emilian Świtalski, Mariusz Specht <i>APPLICATION OF AN AUTONOMOUS/UNMANNED SURVEY VESSEL (ASV/USV) IN BATHYMETRIC MEASUREMENTS</i>
45	Ryszard Jasiński <i>PROBLEMS OF THE STARTING AND OPERATING OF HYDRAULIC COMPONENTS AND SYSTEMS IN LOW AMBIENT TEMPERATURE (PART IV)</i>
58	Paweł Śliwiński <i>INFLUENCE OF WATER AND MINERAL OIL ON THE LEAKS IN SATELLITE MOTOR COMMUTATION UNIT CLEARANCES</i>
68	Kamil Urbanowicz <i>MODERN MODELING OF WATER HAMMER</i>
78	Jerzy Sawicki <i>MAGNETOHYDRODYNAMIC FLOW OF VISCOUS FLUID IN A SLOT BETWEEN FIXED SURFACES OF REVOLUTION</i>
86	Guven Gonca <i>AN OPTIMIZATION STUDY ON AN ECO-FRIENDLY ENGINE CYCLE NAMED AS DUAL-MILLER CYCLE (DMC) FOR MARINE VEHICLES</i>
99	Ireneusz Pielecha, Jacek Pielecha, Maciej Skowron, Aleksander Mazanek <i>THE INFLUENCE OF DIESEL OIL IMPROVERS ON INDICES OF ATOMISATION AND COMBUSTION IN HIGH-EFFICIENCY ENGINES</i>
106	Mikołaj Miśkiewicz, Oskar Mitrosz, Tadeusz Brzozowski <i>PRELIMINARY FIELD TESTS AND LONG-TERM MONITORING AS A METHOD OF DESIGN RISK MITIGATION: A CASE STUDY OF GDAŃSK DEEPWATER CONTAINER TERMINAL</i>
115	Ali Cemal Toz <i>MODELLING OIL SPILL AROUND BAY OF SAMSUN, TURKEY, WITH THE USE OF OILMAP AND ADIOS SOFTWARE SYSTEMS</i>

Editorial

POLISH MARITIME RESEARCH is a scientific journal of worldwide circulation. The journal appears as a quarterly four times a year. The first issue of it was published in September 1994. Its main aim is to present original, innovative scientific ideas and Research & Development achievements in the field of :

Engineering, Computing & Technology, Mechanical Engineering,

which could find applications in the broad domain of maritime economy. Hence there are published papers which concern methods of the designing, manufacturing and operating processes of such technical objects and devices as : ships, port equipment, ocean engineering units, underwater vehicles and equipment as well as harbour facilities, with accounting for marine environment protection.

The Editors of POLISH MARITIME RESEARCH make also efforts to present problems dealing with education of engineers and scientific and teaching personnel. As a rule, the basic papers are supplemented by information on conferences , important scientific events as well as cooperation in carrying out international scientific research projects.

Scientific Board

Chairman : Prof. JERZY GIRTLER - Gdańsk University of Technology, Poland

Vice-chairman : Prof. MIROŚLAW L. WYSZYŃSKI - University of Birmingham, United Kingdom

Dr POUL ANDERSEN Technical University of Denmark Denmark	Prof. STANISŁAW GUCMA Maritime University of Szczecin Poland	Prof. EUGEN NEGRUS University of Bucharest Romania
Dr MEHMET ATLAR University of Newcastle United Kingdom	Prof. ANTONI ISKRA Poznań University of Technology Poland	Prof. YASUHIKO OHTA Nagoya Institute of Technology Japan
Prof. GÖRAN BARK Chalmers University of Technology Sweden	Prof. JAN KICIŃSKI Institute of Fluid-Flow Machinery of PASci Poland	Dr YOSHIO SATO National Traffic Safety and Environment Laboratory Japan
Prof. SERGEY BARSUKOV Army Institute of Odessa Ukraine	Prof. ZBIGNIEW KORCZEWSKI Gdańsk University of Technology Poland	Prof. KLAUS SCHIER University of Applied Sciences Germany
Prof. MUSTAFA BAYHAN Süleyman Demirel University Turkey	Prof. JANUSZ KOZAK Gdańsk University of Technology Poland	Prof. FREDERICK STERN University of Iowa, IA, USA
Prof. VINCENZO CRUPI University of Messina, Italy	Prof. JAN KULCZYK Wrocław University of Technology Poland	Prof. ILCEV DIMOV STOJCE Durban University of Technology South Africa
Prof. MAREK DZIDA Gdańsk University of Technology Poland	Prof. NICOS LADOMMATOS University College London United Kingdom	Prof. JÓZEF SZALA Bydgoszcz University of Technology and Agriculture Poland
Prof. ODD M. FALTINSEN Norwegian University of Science and Technology Norway	Prof. JÓZEF LISOWSKI Gdynia Maritime University Poland	Prof. WITALIJ SZCZAGIN State Technical University of Kaliningrad, Russia
Prof. PATRICK V. FARRELL University of Wisconsin Madison, WI USA	Prof. JERZY MATUSIAK Helsinki University of Technology Finland	Prof. BORIS TIKHOMIROV State Marine University of St. Petersburg, Russia
Prof. HASSAN GHASSEMI Amirkabir University of Technology Iran	Prof. JERZY MERKISZ Poznań University of Technology Poland	Prof. DRACOS VASSALOS University of Glasgow and Strathclyde United Kingdom

COMPARISON OF FUZZY SYSTEM WITH NEURAL AGGREGATION FSNA WITH CLASSICAL TSK FUZZY SYSTEM IN ANTI-COLLISION PROBLEM OF USV

Piotr Szymak

Polish Naval Academy, Poland

ABSTRACT

The paper presents the research whose the main goal was to compare a new Fuzzy System with Neural Aggregation of fuzzy rules FSNA with a classical Takagi-Sugeno-Kanga TSK fuzzy system in an anti-collision problem of Unmanned Surface Vehicle USV. Both systems the FSNA and the TSK were learned by means of Cooperative Co-evolutionary Genetic Algorithm with Indirect Neural Encoding CCGA-INE.

The paper includes an introduction to the subject, a description of the new FSNA and the tuning method CCGA-INE, and at the end, numerical research results with a summary. The research includes comparison of the FSNA with the classical TSK system in the anti-collision problem of the USV.

Keywords: neuro-fuzzy system, neural aggregation of fuzzy rules, cooperative co-evolution, anti-collision of USV

INTRODUCTION

Unmanned Surface Vehicles (USVs) are vessels which can perform many different missions both civilian and military. Civilian usage of USVs is mainly connected with different inspections of underwater environment, especially for oceanography and marine biology purposes. Military applications of USVs are focused on mine countermeasure, anti-submarine warfare and Intelligence, Surveillance and Reconnaissance (ISR) tasks.

USVs can be operated remotely and/or autonomously. USVs moving in a marine environment are exposed to collisions with stationary obstacles as well as moving obstacles, mainly other vessels occurring in USV's operation area. Therefore, a significant problem appearing in the USV motion is counteracting possible collisions [5,7,20]. Software responsible for the anti-collision usually cooperates with navigation

devices such as: a radar system, an AIS receiver, GPS, a speed log, a gyrocompass, etc., and actuators such as: a propeller, a rudder, and additionally cooperates with software for route planning [14] and an electronic navigation map [9].

In the paper, the anti-collision problem is considered as a problem of selecting proper trajectory (i.e. desired waypoints achieved in desired time) for the USV operating in an area with other vessels which can be located on a collision course with the USV's course. Taking into account control task for the USV, proper changes of a course and a velocity have to be generated for avoiding the collision during motion of USV from starting to target position.

To resolve the USV anti-collision problem, an innovative Fuzzy System with Neural Aggregation of fuzzy rules (FSNA) was proposed. The FSNA was compared with the classical TSK fuzzy system. To tune the structure and parameters of both systems, Cooperative Co-evolutionary Genetic Algorithm

with Indirect Neural Encoding (CCGA-INE) was applied. To simulate the USV and other vessels motion, Control-Oriented Model of motion of Unmanned Marine Vehicle (COMUV) was used. A detailed description of the COMUV was included in [13]. The model parameters were applied for USV Edredon (Fig. 1) [6,16].



Fig. 1. Unmanned Surface Vehicle Edredon [6]

The Edredon was built by a consortium, whose leader was the Polish Naval Academy [6]. The vehicle can be controlled remotely from a Mobile Command Centre (MCC) (Fig. 2), or can be controlled locally from on board of the vehicle. As can be seen in Fig. 2, the MCC simulates an operator console located aboard USV with a classical steering wheel and a set of shifters and switches. To visualize the space around the USV, a set of three monitors that receive signals from daylight and thermal cameras, installed aboard USV is used.



Fig 2. Mobile Control Centre of USV Edredon [6]

During previous research devoted to the anti-collision system of the USV Edredon [15], the classical TSK system tuned by the new CCGA-INE method was used. The anti-collision problem was defined by 30 scenarios including trajectories of ten other vessels, which can be on collision course with the USV. The achieved TSK system successfully (without collision) controlled the USV in all the 30 collision scenarios [15]. Then, the 30 more complicated scenarios were created for testing the TSK anti-collision system. Unfortunately, the tests with 30 additional more complicated scenarios did not end successfully. Therefore, in this paper, an improved FSNA system was used to solve the anti-collision problem defined by the 60 scenarios (initial simpler 30 scenarios and additional more complicated 30 scenarios). Moreover, this paper included comparison of working TSK and FSNA anti-collision systems. Both systems were verified by means of 30 validating scenarios. It is worth underlying that the anti-collision problem defined by 60 scenarios is more difficult than the same problem defined by 30 scenarios. The first 30 scenarios are simpler and the next 30 scenarios are more complicated. The complexity is connected with trajectories of the other ships. The trajectory selection influences a greater number of possible collision situations.

The proposed FSNA is based on the classical TSK fuzzy system with two improvements. The first one is based on using an artificial neural network instead of classical operator for calculation of crisp value in the fuzzy system output (called in this paper fuzzy rules aggregation). Based on the literature [18], the FSNA can be classified as a concurrent neuro-fuzzy system. The second improvement depends on integration of the fuzzy rules and fuzzy sets. Both improvements allow to introduce more nonlinearity in the fuzzy system and consequently to achieve desired solution.

The CCGA-INE is based on Cooperative Coevolution Genetic Algorithm CCGA proposed by Potter and De Jong [11]. It was improved by adding indirect encoding of the fuzzy system by means of an artificial neural network. The CCGA depends on an evolution of cooperating subcomponents of an overall solution. The subcomponents evolve in different populations of species, which have to cooperate to achieve a desired solution.

The paper is as follows: Section 2 includes details of the Fuzzy System with Neural Aggregation (FSNA). Section 3 explains details of tuning method of FSNA called Cooperative Co-evolutionary Genetic Algorithm with Indirect Neural Encoding (CCGA-INE). Section 4 includes description of the anti-collision problem used as a testbed and section 5 presents the selected numerical research. The last 6th section includes a summary of the research. Detailed description of the classical TSK system for anti-collision problem is presented in [15,17], and control-oriented model of the motion used for the USV is the same, which was applied for an underwater vehicle (UV) [13]. The motion of UV is considered in 6 degrees of freedom, while the motion of USV usually in 3 degrees of freedom. Therefore, the UV model is useful to simulate motion of USV.

DESCRIPTION OF FSNA

ASSUMPTIONS

The new FSNA is based on the classical TSK fuzzy system proposed in [17]. The TSK system is well known and often used especially in control applications. Comparing to another a classical Mamdani type fuzzy system [8], the TSK system is computationally simpler but similarly efficient [4].

Comparing to the TSK system, following assumptions were made for the FSNA:

- 1) using a logical or an algebraic product for a rules' prerequisites aggregation (a conjunction of prerequisites),
- 2) input variables represented by gaussian membership functions (two parameters for each fuzzy set) and output variables represented by singletons (one parameter for each rule's consequent).

Modifications that led to the creation of the FSNA are as follows:

- 1) integration of the fuzzy sets and rules (the system is in the form of a matrix of integrated fuzzy sets and rules),
- 2) using an artificial neural network for the aggregation of the fuzzy rules instead of e.g. weighted sum [1].

The modifications are described in more details in the following subsections.

MATRIX OF INTEGRATED FUZZY SETS AND RULES

In the classical TSK system, each variable is defined by the specified number of fuzzy sets (represented by membership functions). The fuzzy sets are usually set by an expert. If the fuzzy sets are tuned automatically, usually, the expert specifies the number of fuzzy sets for each variable. In the TSK system, each rule's prerequisite can operate on one fuzzy set selected from all the fuzzy sets defined for the variable. In this case, a prerequisite is defined by a linguistic expression, e.g.:

$$X_i \text{ is HIGH}$$

(here: X_i is an input, HIGH determines one of the fuzzy sets of input X_i).

In the FSNA, fuzzy sets are integrated with the fuzzy rules. It means that instead of using linguistic expressions each prerequisite is defined by parameters of the fuzzy set (in the case of gaussian membership function, two parameters define this function: an expected value and a variance). In the FSNA, the same prerequisite (relating to the same input) in different rules can operate on different fuzzy sets. In an extreme FSNA case, each variable is defined by the number of fuzzy sets equal to the number of fuzzy rules. This approach is very useful in the situation, when the rules or all the fuzzy system parameters are tuned in an automatic way, e.g. by means of an evolution. In this case, division of an input-output space is only limited by the number of fuzzy rules, and the tuning

method decides on the number (and parameters) of fuzzy sets needed to represent a specified variable.

In the research presented in the following section, the following representation of the FSNA in the form of a matrix of integrated fuzzy sets and rules \mathbf{VB}_1 was applied:

$$\mathbf{VB}_1 = \begin{bmatrix} r_{11}^1 & r_{12}^1 & \dots & r_{1n_m}^1 & r_{21}^1 & r_{22}^1 & \dots & r_{n_k n_m}^1 \\ r_{11}^2 & r_{12}^2 & \dots & r_{1n_m}^2 & r_{21}^2 & r_{22}^2 & \dots & r_{n_k n_m}^2 \\ \dots & \dots \\ r_{11}^{n_n} & r_{12}^{n_n} & \dots & r_{1n_m}^{n_n} & r_{21}^{n_n} & r_{22}^{n_n} & \dots & r_{n_k n_m}^{n_n} \end{bmatrix} \quad (1)$$

where r_{km}^n is m -th parameter of fuzzy set or singleton of k -th input or the output variable in n -th fuzzy rule, n_k is the number of input and output variables, n_m is the maximal number of parameters describing a fuzzy set or a singleton, and n_n is the number of fuzzy rules.

In the matrix \mathbf{VB}_1 , some elements can be zero. In this case, appropriate prerequisites or conclusions will be removed, e.g. if the first and second elements in the first row are equal to zero, it means that prerequisite relating to the first input is removed in the first rule.

NEURAL AGGREGATION OF RULES

The next step of modification of the TSK fuzzy system is to apply an artificial neural network for the aggregation of implications of fuzzy rules. In the classical TSK system, the conclusion of i -th implication of a fuzzy rule is in the form of a functional dependence of the rule's predecessors. In this case, the aggregation of the implications is typically calculated using a weighted sum of individual rules [1].

Often (in engineering practice), due to the need of reduction the number of parameters necessary to tune and, consequently, to simplify the system, the functional dependence of the rule's predecessors is simplified into singletons. This leads to a reduction of a non-linearity of the system, which in turn may lead to the inability to match a problem. The possibility of using an artificial neural network to aggregate rule outputs, results mainly from the fact that they are successfully used to approximate non-linear functions [10]. Thus, it seems that the application of a neural network, in this case, is more flexible in obtaining a satisfactory solution fitted to the nonlinear control object.

It was assumed that an artificial neural network in the FSNA performs the duty of rule aggregation, i.e. inputs of the network are weights of rules w_j , and weights are determined using a logical or an algebraic product. Weights are calculated based on the membership function of the individual fragments of each rule's predecessor. In this case, the output of the whole TSK system is a crisp value of the neural network output y . The network architecture is always related to a number of rules (a number of neural network inputs) and generally a solved problem (internal network topology, weights and types of an activation function).

Fig. 3 shows the exemplary FSNA structure formed by a connection of a neural network with a TSK fuzzy system. In Fig. 3, the i -th neuron of the network is represented by N_i .

In the research presented in the following part of the paper, a feed-forward artificial neural network was applied for the aggregation of fuzzy rules [10]. The architecture of the network was determined by the evolutionary method CCGA-INE.

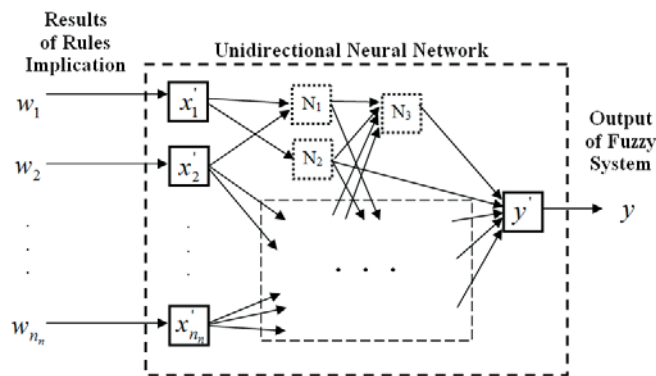


Fig. 3. The connection of neural network with TSK fuzzy system for the aggregation of fuzzy rules (N_i defines the i -th neuron)

The method of encoding an artificial neural network and its tuning by means of evolution is described in the next section.

DESCRIPTION OF CCGA-INE

CO-EVOLUTION

Co-evolution is a specific type of closely related species evolution. In the basic evolutionary algorithm, the process of evolution is seen as an attempt to adapt a population of individuals to a specific environment. Meanwhile, in the co-evolutionary approach, the process of co-evolution is seen as an attempt to adapt the population (or a subgroup of individuals from the population) to the specific environment that is affected by a population of another species (or another subgroup of individuals from the population). Usually, in the co-evolution, a complex solution is divided into sub-component solutions to evolve independently, i.e. there are many populations of individuals (multiple species), wherein each population encodes one sub-component solution.

A good example of co-evolution comes from the natural world in the form of relation between a predator and prey. The predator hunting the prey eliminates the weaker individuals from the population of prey. It causes those individuals which survive to have better features that can be transferred to their offspring. Similarly, the predators which achieve “worst results” in catching preys, have also less chance to transfer features to their offspring.

OVERVIEW OF CCGA

In general, a genetic algorithm (GA) is a heuristic search that mimics the process of natural selection. The GA is based on an iterative evolutionary procedure involving selection of genotypes for reproduction based on their fitness, and then introducing genetically changed (by means of mutation, crossover and other genetic operators) offspring into the next population. The procedure is finished after achieving satisfactory genotypes (a set of features of an individual) which correspond to phenotypes with high fitness function (the individual from a population) [3].

The CCGA is a specific Cooperative Coevolution Genetic Algorithm proposed by Potter and De Jong [11]. Generally, the CCGA solution is divided into sub-components that evolve in separate populations. There is no possibility of exchanging genetic information between populations of separate species, but individuals of different populations have to work together to achieve a satisfactory overall solution. Division into the sub-components is carried out by the following method. Initially, the solution is encoded in a single chromosome, which evolves in a single population. If the evolution of this population, after a specified number of iterations, does not lead to a satisfactory solution, then the next population is created, and next two populations evolve, etc. Sometimes, the CCGA algorithm may find that a particular species (population) does not make a significant contribution to the overall solution. In this case, the population is removed from the evolutionary algorithm. In the CCGA, to evaluate the overall solution a single individual of the first population must be connected with individual from each of the other populations [11].

When evaluating an individual from the given population, it is always combined with the fittest individual from each of the other populations, based on the evaluation (a fitness function) obtained in the previous iteration of an evolutionary algorithm (EA). During the first iteration of the EA, an individual is combined with the randomly selected individual from each of the other populations.

GENERAL IDEA OF CCGA-INE

Because the fuzzy system is described by a large number of parameters, the chromosomes coding these parameters should be very long. Evolution of long chromosomes is connected with complicated calculations, and in consequence, problems with achieving a final solution within assumed finite time. Due to potentially long chromosomes for the system defined by the large number of parameters, the indirect encoding of the fuzzy system is proposed. In the indirect encoding method, information from the chromosomes is used to generate other systems (neural network, nonlinear function, etc.), which in turn generates parameters of the FSNA. Such way of encoding is applied to create large fuzzy systems using relatively short chromosomes.

Generally, in the CCGA-INE a single chromosome encodes a neural network called coding network, defined by a Coding

Neural Network Definition Matrix **cNDM** [12], while the coding network or networks encode the FSNA (i.e. coding networks fills elements of matrices representing this system). In the case of a neural network for aggregation of fuzzy rules, coding networks generate elements of Aggregation Neural Network Definition Matrix **aNDM**, defining structure and parameters of the aggregation network. It should be noted that in the CCGA many populations can evolve, i.e. many chromosomes can generate many coding networks (Fig. 4). For many coding networks, each element of the matrices representing the FSNA is generated by one of the coding networks according to the algorithm described in the following subsection.

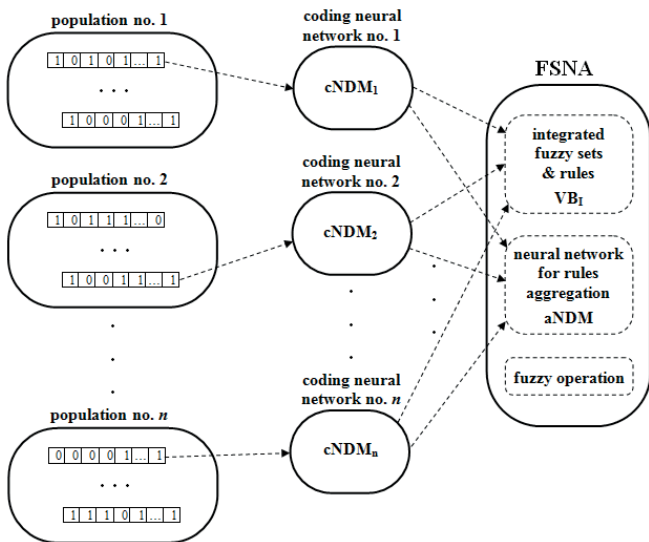


Figure 4. Generation of the FSNA using CCGA-INE

In conclusion, it should be noted that the task of CCGA-INE is to find the best structure and parameters of coding neural networks (one or several depending on the progress of co-evolution) which, in turn, encode integrated matrix of fuzzy sets and rules VB_1 and a matrix defining an artificial neural network for aggregation of fuzzy rules **aNDM**.

GENERATION OF CODING AND AGGREGATING NEURAL NETWORKS

Fig. 5 shows a method for generating a coding neural network (defined by **cNDM**) [12] using the information stored in the chromosome, consisting of four components. Each component is composed of 7 bits, i.e. the whole chromosome is built from 28 bits. During the research, co-evolution produced chromosomes consisting of four to more than thirty components, i.e. chromosomes consisting of more than two hundred bits. The number of components is depended on the complexity of the problem and the co-evolution. Division into components is a decomposition of the problem. Always the first component of each chromosome is considered as a string of bits, while the next components represent integer values

(scaled to real values), which are subsequent elements of the matrix. In the illustrated example (Fig. 5), the first component of the chromosome determines the topology of the neural network by indicating the elements of matrix **cNDM**, which should be reset (white boxes), and other which should adopt the values determined by the successive components of the chromosome c_1 , c_2 and c_3 (black boxes).

Consecutive bits included in component „topology” determine if the following elements of the matrix (beginning from the first column and row, and ending on the last row and column) are zero or non-zero (Fig. 5). Bit string „topology” is too short to determine all the elements of the matrix, therefore, the string is repeated, i.e. after the last bit is the first bit of the same string, then second bit, etc., until all the elements are calculated. The bit which has a zero value determines zero value of the relating element in the matrix. This element is illustrated by white boxes in the table in Fig. 5. Bit which has value “1” determines non-zero value of the relating element in the matrix. The non-zero element is marked by grey boxes in the table in Fig. 5. The precise values of non-zero elements are determined by other components of the chromosome „coefficient no. 1”, „coefficient no. 2” and „coefficient no. 3”. Assignment of values c_1 , c_2 and c_3 for successive elements of matrix **cNDM** is carried out according to the same principle as it is used for the bits of the component „topology”.

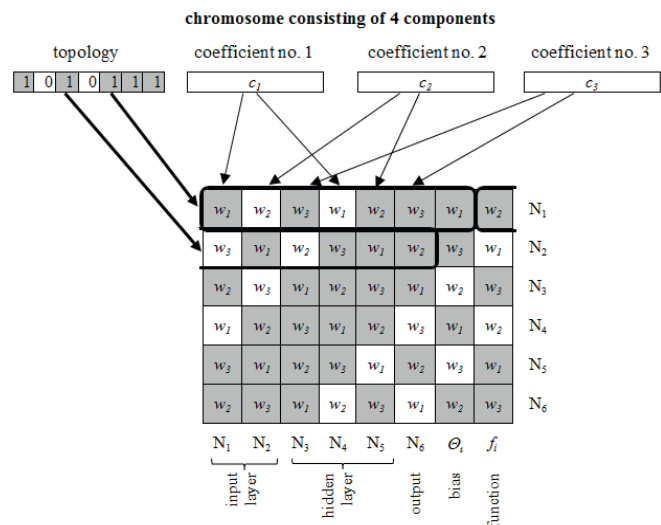


Figure 5. Generation of matrix **cNDM** by the chromosome consisting of four components

Matrix **cNDM** shown in Fig. 5 has n rows and $n + 2$ columns, where n is the number of neurons in the network layers, sequentially: input, hidden and output. Elements of matrix **cNDM** from the first element to the element of n -th row and n -th column determine the weights of connections between neurons. Column $n + 2$ determines type of the activation function, and the column $n + 1$ is a bias, i.e. a constant added to the total weight of input neurons.

Fig. 6 shows the architecture of an artificial neural network generated by means of information included in the chromosome and the relating matrix **cNDM**.

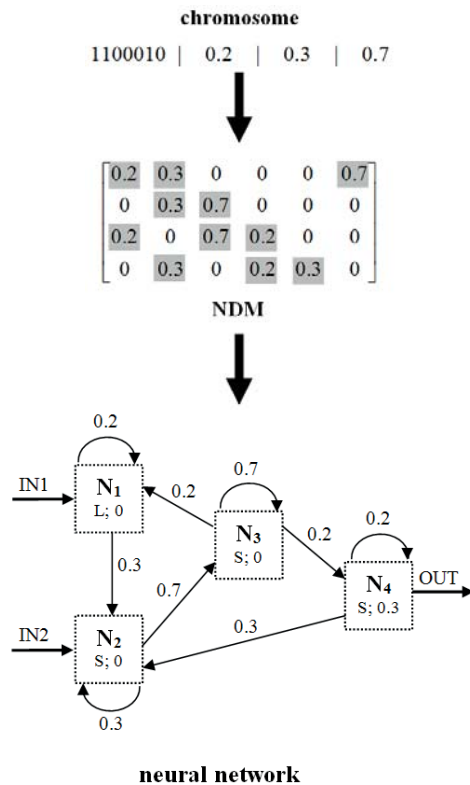


Fig. 6. Generation of the neural network based on NDM, formed on the basis of the chromosome

In Fig. 6, the chromosome components are presented in different forms: the first component in the form of a binary sequence, the other component in the form of real numbers (chromosomes include integers, which become real numbers after scaling). Individual neurons were visualized by succeeding numbers N_1, N_2, \dots, N_n and the type of the activation function: S - sigmoid, L - linear and additionally numerical value of the bias. The resulting neural network, presented in the Fig. 6 contains 4 neurons. The distribution of these neurons to the input and output layers, and possibly hidden, is determined by the designer of the system. In this case, it is assumed that two neurons are in the input layer, one is a hidden neuron and one is located in the output layer. As mentioned previously, the matrix **NDM** can define the coding neural network **cNDM** and also the neural network for the rules aggregation **aNDM** in the way as it was described for **cNDM**.

In the research, it was assumed that the coding neural network is composed of nine neurons: three in the input layer, three in the output layer, and three are the hidden neurons. Therefore, matrix **cNDM** is composed of 9 rows and 11 columns [12].

GENERATION OF FSNA MATRICES

Fig. 7 shows how to fill the matrices elements representing the FSNA. The values of elements are produced by the coding networks. The coding networks have three inputs and three

outputs. Network inputs determine parameters of the element, whose value is produced by the network on its output. The first and second inputs determine, respectively, the row and the column of the matrix, and the third input determine the ordinal number of the matrix.

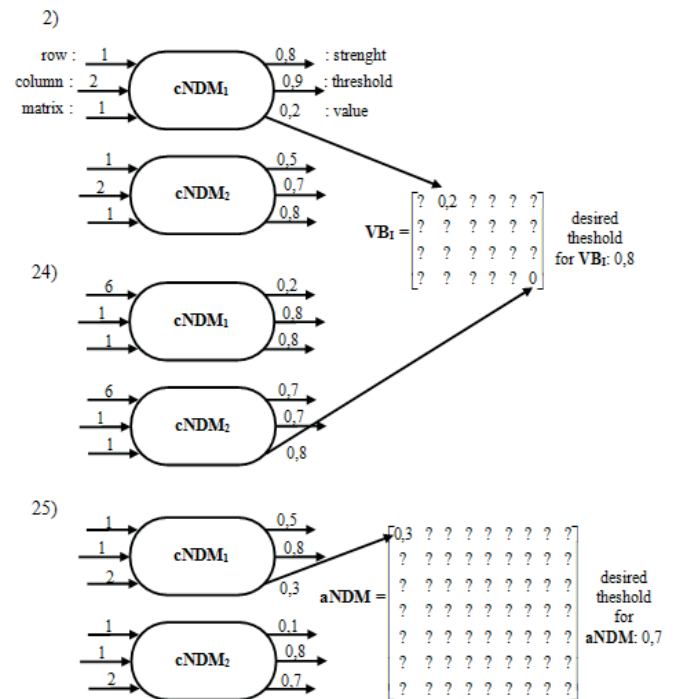


Fig. 7. Generation of the FSNA matrices by the coding neural networks in selected steps 2), 24), 25)

The coding network produces following outputs values:

- 1) strength: in a situation, where there is more than one network, this parameter determines which coding network should be used to „fill” the matrix in the current step (the coding network „wins”, which has the highest strength value),
- 2) threshold: this parameter determines whether the value should be written to a specific element of the matrix, or the item should be zero (the element is reset if the threshold value is less than the desired threshold for the matrix),
- 3) value: assigned to the specific matrix element, defined by the coding network inputs, if the network has the highest strength value, and the threshold output is greater than the desired threshold for this matrix.

Fig. 7 shows selected steps of „filling” the FSNA matrices by one of two coding networks, formed on the basis of information included in the chromosomes, evolving in two populations. Step 2 illustrates a situation in which the first coding neural network (defined by **cNDM₁**) has a higher strength value and its threshold output is greater than the desired threshold for **VB₁**. Therefore, the first coding network writes a value to a specified element of the matrix. Step 24 illustrates the case in which the second coding network is „stronger” (has higher strength value), but the network’s threshold value is less than the desired threshold for this matrix. In this case, the element specified by the coding network inputs obtains zero value.

Step 25 illustrates a situation similar to that which occurred in step 2, with the difference that in this case, the second element of the second matrix **aNDM** is filled. Generation of all the elements of the matrices requires iterations equal to the sum of elements in these matrices.

It can be seen that when using the CCGA-INE, the matrices consisting of even hundreds of parameters can be filled by means of information included in several chromosomes (depending on the number of populations).

In the next section, the anti-collision problem used to compare the TSK and the FSNA systems is described in details.

ANTI-COLLISION PROBLEM

ASSUMPTIONS

It was assumed that the information from an onboard navigation system, in particular about the detection of obstacles, was discretized in such a way that the USV anti-collision system received the distances from the obstacles located in the seven sectors around the USV. The four sectors with 45° view angle were located in the fore part and the three sectors with 60° view angle located in the aft part of the USV (Figure 8). Therefore, the anti-collision system obtained information about other vessels in the form of distances to the closest vessels in designated sectors from x_1 to x_7 (Figure 8). The sectors of detecting obstacles were limited in bearing and range of their view. The value of the view range was chosen experimentally. The anti-collision system provided desired course to the target ψ_s . Based on information about the obstacles and the target, the anti-collision system calculated the change of course $\Delta\psi$ and the change of advance velocity ΔV_a . The advance velocity is a velocity measured in a longitudinal axis of symmetry of the USV.

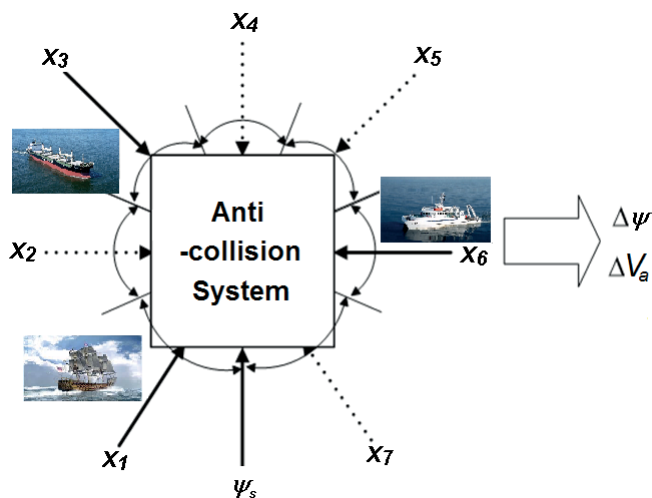


Fig. 8. Inputs and outputs of anti-collision system: x_1, x_2, \dots, x_7 – distances from obstacles in sectors, ψ_s – desired course to the target, $\Delta\psi$ – the change of course and ΔV_a – the change of velocity USV

SCENARIOS

In order to tune and then validate the TSK and the FSNA anti-collision systems, scenarios with increased difficulty level were designed. Each scenario contained information about starting and target positions of the USV and motion vectors of the ten other vessels, operating in the same area. The distance that had to be overcome by the USV was approximately 2 nautical miles. This distance is sufficient to deploy the collision obstacles. Due to USV dynamics [16], it was assumed that the anti-collision system took the decisions every 20 seconds.

Each of ten potential collision vessels moved with one fixed course and velocity. In the first part of the scenarios, the vessels moved along safe trajectories (not on collision course with the USV). At the beginning, the USV had to „learn” to reach the target. In the next part of the scenarios, the number of units moving on collision courses were gradually increased. Moreover, the number of vessels that moved near the starting position and the target were also increased. Such vessels are not on collision course at the beginning of the simulation, but may be on collision course in subsequent moments after various changes of the USV course.

In the following scenarios, the starting and the target positions were changed in such a way that potential trajectories ran in different directions: north, north east, south, etc.

In order to avoid too complex trajectories of the USV, including incorrect maneuvers, e.g. multiple passage on circular trajectory, an excessive descent from desired trajectory, etc., timeout for the each scenario was implemented. The timeout was equal to 150% of the time needed for movement along a straight route from the starting point to the target with an average velocity of 10 knots.

To tune and then validate the anti-collision systems, respectively, 60 learning scenarios (including 30 simpler and 30 additional scenarios), and 30 validating scenarios were designed. In the validating scenarios, an additional difficulty was implemented, i.e. the changes of course of the vessels were added.

EVALUATION FUNCTION

The scenarios are used for training and then validating sequentially, i.e. the first scenario was followed by a second, then the third, etc. Scenario finished at the moment of collision or after achieving the maximum time for the scenario (the maximal number of decisions).

The behavior of the n -th anti-collision system in 60 learning scenarios was evaluated using the fitness function $F(FL_n)$. The function $F(FL_n)$ was calculated as the sum of the rewards gained in all the scenarios. The following form of the reward function f in m -th scenario was applied [15]:

$$F_m(FL_n) = \begin{cases} 0, & \text{case a} \\ 0.5d_t - 0.5\frac{k}{I_{max}}, & \text{case b} \\ 0.5 + 0.5d_t - 0.5\frac{k}{I_{max}}, & \text{case c} \\ R_t + (I_{max} - I) / I_{max} - 50\frac{k}{I_{max}}, & \text{case d} \end{cases} \quad (2)$$

where k is a scenario number, FL_n is an estimated n -th FSNA, d_t is a distance to the target at the end of scenario, and k is a penalty for change of course greater than 90° , if the distance to the closest obstacle is larger than 0.15 nautical mile. Additionally, I_{max} is a maximal number of decision, which the USV can take moving to the target, I is a number of decisions taken by the anti-collision system, and R_t is a reward for the USV reaching target ($R_t = 100$).

The function (2) is calculated for the following cases:

- collision occurred,
- USV did not reach the target, but did not collide with other vessels; at the end of simulation, the USV was located at the distance larger than 1 nautical mile from the target,
- USV did not reach the target, but did not collide with other vessels; at the end of simulation, the USV was located at the distance less than or equal to 1 nautical mile from the target,
- USV reached the target.

The occurrence of collisions automatically stops the process of evaluating the TSK or the FSNA systems in the m -th scenario with the value of the function $F_m(FL_n)$ equal to zero. In the case where the USV did not collide with other vessels and did not reach the target, the evaluation is dependent on the distance to the target at the end of simulation, and the number of forbidden maneuvers (change of course greater than 90° , if the distance to the closest obstacle is larger than 0.15 nautical miles). Tuning process of the anti-collision system is determined by the evaluation function. The greater the function result is, the more effective anti-collision system is tuned.

The whole process of tuning the TSK or the FSNA systems is terminated, when the evaluation function reaches a value greater than or equal to 6000, i.e. when the USV reached the target without collision in 60 learning scenarios. In the research presented in the next section, 60,000 iterations were applied as the maximum number of iterations for the tuning process.

NUMERICAL RESEARCH

MODEL OF THE VESSEL MOTION

To simulate horizontal plane motion of the USV and other vessels control-oriented model of marine object was applied [13]. The model was described in the following matrix form:

$$S_V = [P_{ij}]_{6 \times 3} \quad (3)$$

where P_{11} includes the changes of course $\Delta\psi_{kl}$, P_{12} contains the changes of coordinate x : Δx_{kl} , and P_{13} includes the changes of coordinate y : Δy_{kl} .

Elements of the matrices were registered in response to desired course $\psi_k^z = k \cdot \Delta\psi$ (where $k = 1..36$ and $\Delta\psi = 5^\circ$), in l -th time step $t_l = l \cdot \Delta t$ (where $l = 1..60$ and $\Delta t = 0,5$ s), for advance velocities $V_i = i \cdot \Delta V$ (where $i = 1..5$ and $\Delta V = 5$ knots).

For USV and the other vessels motion simulation, 5 discrete advance velocities were applied (5, 10, ..., 25 knots), and the state vector of the vehicle and vessels were reduced to 3 parameters: course, coordinate x and coordinate y . The more details about the model was included in [13].

Parameters of the model were registered based on the classical nonlinear model [2]. To control the course of the USV and the vessels, slide mode controllers were used, which were described in details in [16].

STRUCTURE OF THE TSK AND THE FSNA SYSTEMS

In the structure of the fuzzy system, the following three components should be determined: fuzzy sets, fuzzy rules and fuzzy operation [1,19]. Based on the earlier research [15], fuzzy sets for inputs and outputs, illustrated in Figure 9, were applied. The same universe of discourse was used for all the inputs ($x_1, x_2 \dots x_7$ – distances from obstacles in sectors, ψ_s – desired course to the target) and the same for all the outputs ($\Delta\psi$ – the change of course and ΔV_a – the change of velocity USV). The whole structure of the anti-collision system of USV is illustrated in Figure 8.

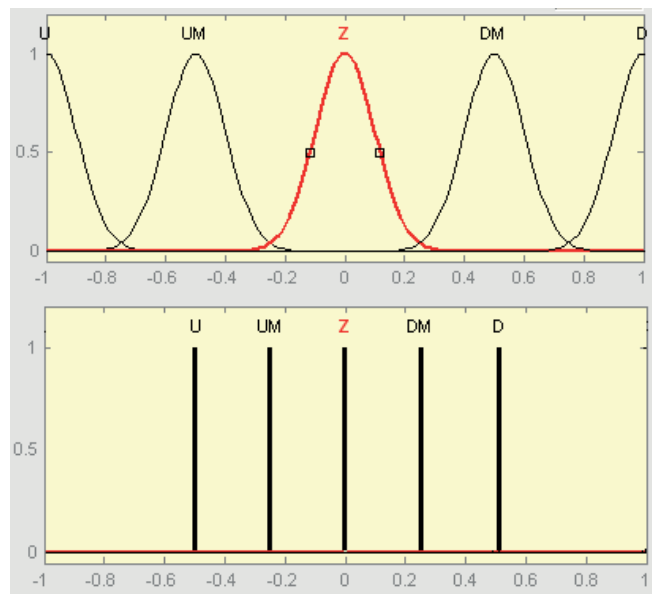


Figure 9. Fuzzy sets for inputs (gaussian functions) and output (singletons) of the TSK anti-collision system

In the TSK anti-collision system, fuzzy rules were tuned by the evolutionary method.

It was assumed that crisp values of the outputs were calculated using a weighted sum of the rules (wtsum) [1]. For this purpose, it is important to calculate the weight of the i -th rule and the crisp value of the output of the i -th implication. Calculation of rules weights is usually carried out using a logical product (min) or an algebraic product (product) [1]. Due to the lack of a proper solution of the TSK system using operation (product), in addition to the operation (min), an algebraic sum (sum) was applied [1] (usually (sum) is used for an alternative of prerequisites). In the case of using singletons on the outputs, the crisp value of the output of the i -th implication is reduced to the constant value of the proper singleton.

For the TSK system mentioned above preliminary studies were carried out for the simpler 30 learning scenarios. Satisfactory results were not received. Therefore, in the TSK system, additional improvement was introduced, i.e. rules with the same singletons were aggregated. For this purpose, two optional operations were applied: a logical sum (max) and the algebraic sum (sum) [1]. In this case, the weighted sum of rules operation (wtsum) was also modified in such a way that it did not work on all the rules, but on the aggregated rules for the same singletons in conclusions. In this case, the maximum number of components of the weighted sum is equal to the number of singletons in the output variable.

According to the description included in Section 2, in the FSNA, both fuzzy sets and rules were tuned in the evolutionary way.

In the FSNA, crisp values on the outputs were achieved in the result of operation of the aggregating neural network. The neural network is “fed” on the inputs with the weights of the fuzzy rules. To calculate the weight of rule, the same operations were applied as for the TSK system, i.e. the logical product (min) for a conjunction of prerequisites or the algebraic sum (sum) for an alternative of prerequisites.

TSK SYSTEM LEARNING AND VALIDATION

The learning phase of the TSK system was divided into two parts. The result of the first part was that the fuzzy systems learned by means of 30 simpler learning scenarios, described in [15]. The results of the second part were presented in the Table 1. The learning process was performed based on 30 simpler and 30 additional learning scenarios (in total 60 learning scenarios).

The main aim of the process was to compare different variants of the fuzzy system. All variants had the same distribution of the fuzzy sets, presented in the Figure 9. The variants differed in the maximum number of fuzzy rules (10 or 20) and applied fuzzy operations (min – sum, sum – sum, min – max, sum – max), respectively for (the calculation of the rules weights – the aggregation rules with the same singletons).

Tab. 1. Results of the learning for TSK system for the anti-collision problem defined by 60 learning scenarios

	Variants of TSK system			Learning	
	Aggregation of prerequisites	Aggregation of identical singletons	Number of rules	Average total evaluation function	Maximal total evaluation function
1	min	sum	10	3416	3607
2	min	max	10	3252	3605
3	sum	sum	10	3299	3606
4	sum	max	10	3393	3606
5	min	sum	20	3466	3506
6	min	max	20	3605	3606
7	sum	sum	20	3112	3606
8	sum	max	20	3436	3606

According to the results of the first part of the learning process, following parameters of the evolutionary method were used: the mutation probability equal to 0.045 and the crossover probability equal to 0.4. Similarly to the previous research [15], each variant of the fuzzy system was evolutionary tuned 30 times. Therefore, the Table 1 presents the results of the evolution in the form of the average and the maximum values of the total evaluation function achieved in 30 runs.

Tab. 2. Results of validating the TSK system for the anti-collision problem in 30 scenarios

	Variants of TSK system			Validation	
	Aggregation of prerequisites	Aggregation of identical singletons	Number of rules	Average total evaluation function	Maximal total evaluation function
1	min	sum	10	1215	1702
2	min	max	10	1462	1704
3	sum	sum	10	1170	1805
4	sum	max	10	1248	1805
5	min	sum	20	1556	1706
6	min	max	20	1605	2303
7	sum	sum	20	1269	2103
8	sum	max	20	1229	1902

Based on the results of evolutionary tuning of the TSK system for 60 learning scenarios (Table 1), this fuzzy system was not able to “learn” new scenarios. Evolution in the best case, stopped at scenario no. 36 and was not able to cope with the collision situation defined by scenario no. 37.

Despite the lack of even one TSK system that would have successfully avoided a collision in all 60 scenarios, to compare the TSK system with the FSNA, it was decided to validate the obtained TSK solutions by means of 30 validating scenarios.

Based on the results of validating tests presented in the Table 2, it is worth noting that the inability to tune the TSK fuzzy system in the learning phase, resulted in achieving poor evaluation in the validation phase.

FSNA LEARNING AND VALIDATION

The learning and validating processes of the FSNA were carried out by means of the learning and validating scenarios, the same as were used for the TSK system. Based on the results of the previous research [15], the subsequent parameters for validation tests were used:

- 1) the mutation probability 0.045,
- 2) the crossover probability 0.4,
- 3) the operation (min) for the aggregation of prerequisites.

The results of tuning 16 FSNA variants were presented in Table 3.

Tab 3. Results of learning the FSNA for the anti-collision problem defined by 60 learning scenarios

	FSNA variants		Learning		
	Number of fuzzy rules	Number of hidden neurons	Average total evaluation function	Maximal total evaluation function	Number of successful runs
1	3	0	4094	5008	4
2		2	4580	5309	0
3		5	5095	6009	0
4		8	1464	2404	2
5	6	0	4521	6009	2
6		2	4735	6011	2
7		5	4581	6011	4
8		8	1957	2404	6
9	8	0	4085	5008	0
10		2	4464	5819	0
11		5	4264	6011	0
12		8	1638	2304	1
13	10	0	4093	5608	0
14		2	3993	4308	0
15		5	5066	6013	0
16		8	1549	2403	2

The variants differed in the number of fuzzy rules (3, 6, 8 and 10) and the number of hidden neurons in the aggregating neural network (0, 2, 5 and 8 neurons).

As in previous studies, each FSNA variant evolved during 30 runs. The results of tuning various options FSNA fuzzy system were illustrated in Table 3 as the average and the maximum overall evaluation functions. In addition, each FSNA variant was evaluated by an additional index, i.e. the number of successful runs (ended without collision).

The best learning result was achieved for the FSNA variant with 6 fuzzy rules and 8 hidden neurons in the aggregation network. For 30 runs of evolution for this variant, 6 runs were successful (the collision was avoided in all 60 learning scenarios), i.e. efficiency of tuning method was 20%.

Based on the results of evolution (Table 3), large influence of neural network for the fuzzy rules aggregation on the operation of the entire FSNA can be seen. Increasing

the number of hidden neurons in these networks leads to better results (the average total evaluation function and the number of successful runs increased). Due to the condition of finishing the tuning process in a specified finite time, no research to a larger number of hidden neurons was performed.

Tab. 4. Results of validating the FSNA for the anti-collision problem in 30 scenarios

	FSNA variants		Validation	
	Number of fuzzy rules	Number of hidden neurons	Average total evaluation function	Maximal total evaluation function
1	3	0	735	1012
2		2	1917	2503
3		5	1946	2604
4		8	1946	2604
5	6	0	1977	2604
6		2	1977	2705
7		5	2037	2606
8		8	2037	2606
9	8	0	1550	2504
10		2	1550	2206
11		5	1449	2103
12		8	1449	2103
13	10	0	2060	2703
14		2	1531	2105
15		5	2018	2704
16		8	2018	2704

The verification tests were carried out for the obtained FSNA by means of 30 validating scenarios, the same as for the TSK system (Table 4). No FSNA was positively verified in all 30 validating scenarios. The best solutions for anti-collision systems managed to avoid collisions in the 27 validating scenarios, i.e. the best solutions of the FSNA achieved an effectiveness of 90%.

It can be concluded that the solutions of FSNA that have evolved in 60 learning scenarios, are able to work effectively on a different data set than the training set. As mentioned earlier, an important element for success of the learning process is the selection of training data. In this case, the learning scenarios could be improved to represent a wider range of learning data.

EXAMPLES OF FSNA OPERATION

In Fig. 10 and 12, the trajectories of the USV and 10 other vessels were illustrated for scenarios no. 14 and 10, respectively with collision and without collision. The USV starting position was marked by a circle, and the starting positions of the other vessels were marked by asterisk. Target position of the USV is the position with coordinates (4000 m, 4000 m), which is placed outside the space visualized in Figure 10.

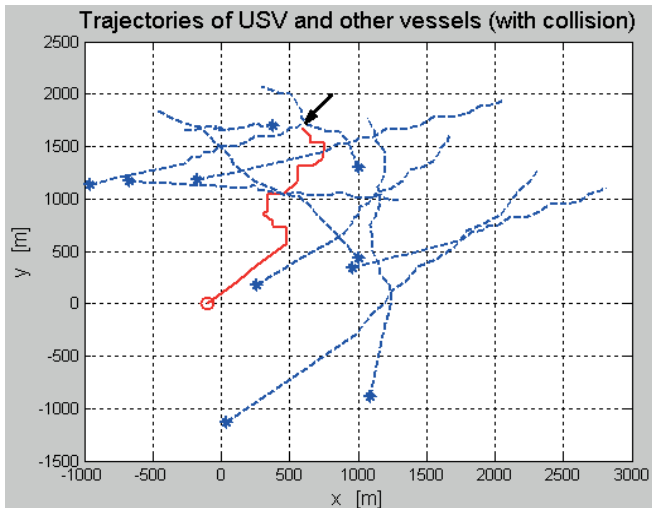


Fig. 10. Trajectories of the USV (red solid line, a circle – starting position), and the vessels (blue dotted lines, asterisks – starting positions) in scenario with collision (black arrow)

In Fig. 11, it can be seen that the USV initially moved straight to the target, then at approx. 170 s of simulation performed a maneuver avoiding a collision with one of the other vessels. Next, for longer than 200 seconds, the USV maneuvered to the port and to the starboard, trying to avoid collision and to cover the shortest path to the target. At approx. 460 s of simulation, the USV collided with one of the other vessels.

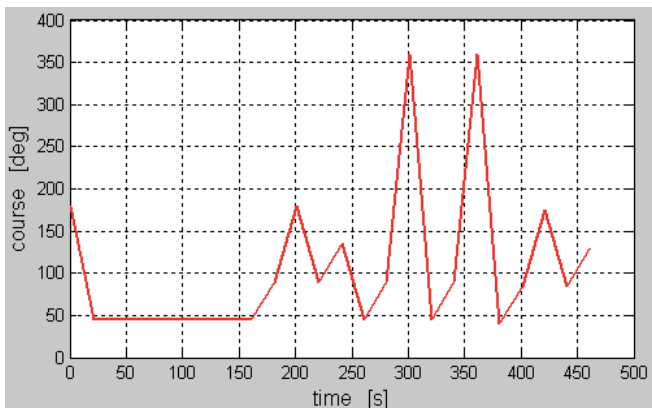


Fig. 11. Change in time of the USV desired course in the scenario with collision

In Fig. 12, it can be seen that the USV made several changes of its course during approx. 500 s of simulation. These manoeuvres enabled the USV to leave the area of potential collisions, and then to reach the target without collision.

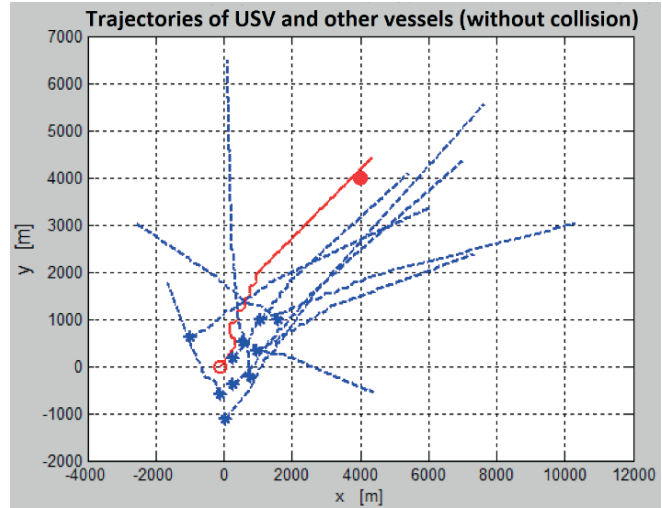


Fig. 12. Trajectories of the USV (red, solid line, a circle – starting position, a wheel – target position) and the vessels (blue, dotted lines, asterisks – starting positions) in the scenario without collision

CONCLUSIONS

In the paper, the new neuro-fuzzy system called FSNA was presented. The FSNA is an improvement of the classical TSK system enriched with (1) integration of fuzzy rules with membership functions, and (2) aggregation of fuzzy rules by an artificial neural network. The FSNA was tuned by the evolutionary method named CCGA-INE. The FSNA correctly learned and then was verified by means of respectively, the learning and validating scenarios in the anti-collision problem.

It is worth mentioning that the CCGA-INE is a quite efficient but a time-consuming method taking into consideration the learning process. The one variant of FSNA was received after 12-24 hours of a one core 3 GHz processor work. The research was conducted using BSD Operating System. Despite the long process of learning, the taught and verified variant of the FSNA can be used as a control system in time close to real using a medium class hardware platform.

The FSNA was compared with its predecessor the classical TSK system. The classical TSK system with base of rules tuned in evolutionary way (CCGA-INE) poorly generalized learned anti-collision behaviour. The classical system showed less effectiveness, both in the learning and validating phases. The selected solutions of FSNA obtained during an evolution process (Table 4) guarantee good behaviour for the validation scenarios. It should be noted that in the case of new scenarios, they always can be used for precise tuning of the FSNA (an additional learning process).

In the future, the following improvements and research are proposed to implement and test:

- 1) Implementation of the FSNA system based on Mamdani type fuzzy system,

- 2) Examination of the impact of an artificial neural network at the input of the fuzzy system, e.g. to aggregate prerequisites of the fuzzy rules,
- 3) FSNA testing in other control problems, e.g. to control a new marine control object – biomimetic underwater vehicle.

REFERENCES

1. D. Driankov, H. Hellendoorn, M. Reinfrank, *An Introduction to Fuzzy Control*, Springer-Verlag, 1996.
2. T.J. Fossen, *Guidance and Control of Ocean Vehicles*, John Wiley and Sons Ltd., 1994.
3. D.E. Goldberg, *Genetic Algorithms in Search, Optimization and Machine Learning*, Addison Wesley, Reading, Massachusetts, 1989.
4. K. Guney, N. Sarikaya, Comparison of Mamdani and Sugeno Fuzzy Inference System Models for Resonant Frequency Calculation of Rectangular Microstrip Antennas, *Progress In Electromagnetics Research B*, Vol. 12, p. 81–104, 2009.
5. C. Hwang, “The integrated design of fuzzy collision-avoidance and H ∞ -autopilots on ships”, *The Journal of Navigation*, Vol. 55(1), pp.117-136, 2002.
6. Z. Kitowski, “Autonomous unmanned surface vehicle Edredon”, *Polish Hyperbaric Research*, Vol. 3(40), 2012, s. 7-22.
7. J. Lisowski, “Sensitivity of Computer Support Game Algorithms of Safe Ship Control”, *International Journal of Applied Mathematics and Computer Science*, Vol. 23, No. 2, 439–446, 2013.
8. E. H. Mamdani, S. Assilian, “An experiment in linguistic synthesis with a fuzzy logic controller”, *International Journal of Man-machine Studies*, Vol. 7, p. 1-13, 1975.
9. K. Naus, M. Wąż, A simplified navigational chart pyramid dedicated to an autonomous navigational system, *Polish Hyperbaric Research*, Vol. 3(40), pp. 99-118, 2012.
10. S. Osowski, *Neural networks for data processing*, in polish, Publishing House of Technology University in Warsaw, 2006.
11. M. A. Potter, K. A. De Jong, “Cooperative coevolution: An architecture for evolving coadapted subcomponents”, *Evolutionary Computation*, Vol. 8(1), p. 1–29, 2000.
12. T. Praczyk, “Neural anti-collision system for Autonomous Surface Vehicle”, *Neurocomputing*, Vol. 149, Part B, p. 559–572, 2015.
13. T. Praczyk, P. Szymak, “Decision System for a Team of Autonomous Underwater Vehicles – Preliminary Report”, *Neurocomputing*, Vol. 74 (17), pp. 3323-3334, 2011.
14. T. Praczyk, P. Szymak, “Using Genetic Algorithms to Fix a Route for an Unmanned Surface Vehicle”, in *Proceedings of the 17th International Conference on Methods and Models in Automation and Robotics*, pp. 487-492, 2012.
15. P. Szymak, T. Praczyk, “Using Neural-Evolutionary-Fuzzy Algorithm for Anti-collision System of Unmanned Surface Vehicle”, in *Proceedings of the 17th International Conference on Methods and Models in Automation and Robotics*, pp. 286-290, 2012.
16. P. Szymak, “Course Control of Unmanned Surface Vehicle”, *Solid State Phenomena*, Vol. 196, pp. 117-123, 2013.
17. T. Takagi, M. Sugeno, “Fuzzy Identification of Systems and its Application to Modelling and Control”, *IEEE Transactions on Systems, Man and Cybernetics*, vol. 15, pp. 116-132, 1985.
18. J. Vieira, F.M. Dias, A. Mota, Neuro-Fuzzy Systems: A Survey, *WSEAS Transactions on Systems*, 3(2), 2004.
19. L. Zadeh, “Fuzzy sets”, *Information and Control*, vol. 8, pp. 338–353, 1965.
20. Y. Zhuo, “An intelligent decision support system to ship anti-collision in multi-ship encounter”, in *Proceedings of the Intelligent Control and Automation 2008*, pp. 1066–1071, 2008.

CONTACT WITH THE AUTHOR

Piotr Szymak

e-mail: p.szymak@amw.gdynia.pl

Polish Naval Academy

Smidowicza 69, 81-127 Gdynia

POLAND

MAPPING SOUTH BALTIC NEAR-SHORE BATHYMETRY USING SENTINEL-2 OBSERVATIONS

Andrzej Chybicki

Gdansk University of Technology, Poland

ABSTRACT

One of the most promising new applications of remote observation satellite systems (RO) is the near-shore bathymetry estimation based on spaceborn multispectral imageries. In recent years, many experiments aiming to estimate bathymetry in optically shallow water with the use of remote optical observations have been presented. In this paper, optimal models of satellite derived bathymetry (SDB) for relatively turbid waters of the South Baltic Sea were presented. The obtained results were analysed in terms of depth error estimation, spatial distribution, and overall quality. The models were calibrated based on sounding (in-situ) data obtained by a single-beam echo sounder, which was retrieved from the Maritime Office in Gdynia, Poland. The remote observations for this study were delivered by the recently deployed European Space Agency Sentinel-2 satellite observation system. A detailed analysis of the obtained results has shown that the tested methods can be successfully applied for the South Baltic region at depths of 12-18 meters. However, significant limitations were observed. The performed experiments have revealed that the error of model calibration, expressed in meters (RMSE), equals up to 10-20% of the real depth and is, generally, case dependent. To overcome this drawback, a novel indicator of determining the maximal SDB depth was proposed. What is important, the proposed SDB quality indicator is derived only on the basis of remotely registered data and therefore can be applied operationally.

Keywords: near-shore satellite, derived, bathymetry, Sentinel, multispectra, observation

INTRODUCTION

Satellite remote multispectral systems provide valuable large- and local-scale observations of optical and thermal properties of Earth's surface. One of the most promising new applications of the remote observation satellite systems (RO) are near-shore bathymetry estimations. RO observations are an interesting approach because they can provide relatively low-cost information on shallow water bathymetry, compared to other known bathymetry retrieval techniques, such as Lidar scanning (LS), multibeam systems (MBS) and single-beam echo sounder (SBE). The above methods, particularly LS and MBS, provide high resolution and accurate data, but surveying in those cases is usually expensive and time consuming [1] [2]. With the development of optical and thermal satellite sensors for land and sea observation imagers, new applications of RO arise.

In recent years many experiments aiming to estimate bathymetry in optically shallow waters with the use of remote optical observation have been presented. Basically, two fundamental models of determining the bathymetry

from optical imagery are defined, namely: the empirical optical band ratio transform algorithm proposed by Stumpf [3] and a more analytical approach proposed by Lyzenga [4, 5] and Philpot [6]. Both of these models assume that the radiation in optical bands is absorbed by water and reflected from the bottom. However, the scale of this process differs depending on the wavelength. Therefore, the ratio of the observed radiances of at least two optical bands is to be used to retrieve the information about the bottom depth.

During this process, many factors constitute limitations of these methodologies. When the bottom reflectance and light attenuation of water is stable over the analysed area, depth estimates can be relatively easily made by modelling the depth of light penetration based on the amount of reflectance measured by the satellite. Having known the multiple visible-wavelength spectral bands, the effects of seafloor reflectance variability and water turbidity can be reduced. However, water turbidity is still one of the most important factors in the process of obtaining satellite derived bathymetry (SDB).

Therefore, most of the experiments made in this area have focused on testing fields and datasets that satisfy the

abovementioned criteria. For instance, Sandidge and Holyer used the Airborn Visible/Infrared scanner to derive the bathymetry for waters of Florida, USA [7]. The observations of optically shallow waters near the Bahama islands were also analysed by Adler-Godlen [8], Sheng Ma [9], and others i.e. [10][11][12][13]. This paper presents optimal models of satellite based bathymetry derivation developed for relatively turbid waters of the South Baltic Sea. The research involved Sentinel-2 data, as well as log-ratio and analytical approaches making use of inverse transform optimization methods. The results obtained using these two models were then compared in terms of depth error estimation, spatial distribution, and quality. The model was calibrated on the basis of the sounding (in-situ) data obtained by a single-beam echo sounder. The calibration data was retrieved from the Maritime Office in Gdynia, Poland, which is the local entity of official Marine Administration in Poland.

METHODS

Bathymetry estimation from satellite observations involves extracting the bottom radiance from the measured water-leaving reflectance. The reflectance R is defined as the ratio of the radiance leaving the water surface to the downwelling irradiance just above the water surface. It is a feature that describes light absorption related optical properties of the surface, as well as scattering properties of the constituents in the water, and bottom albedo and depth. The fundamental physical principle in the process of deriving bathymetry using satellite observations bases on the phenomena of light pass attenuation in the water column, and bottom reflection and scattering (Fig. 1).

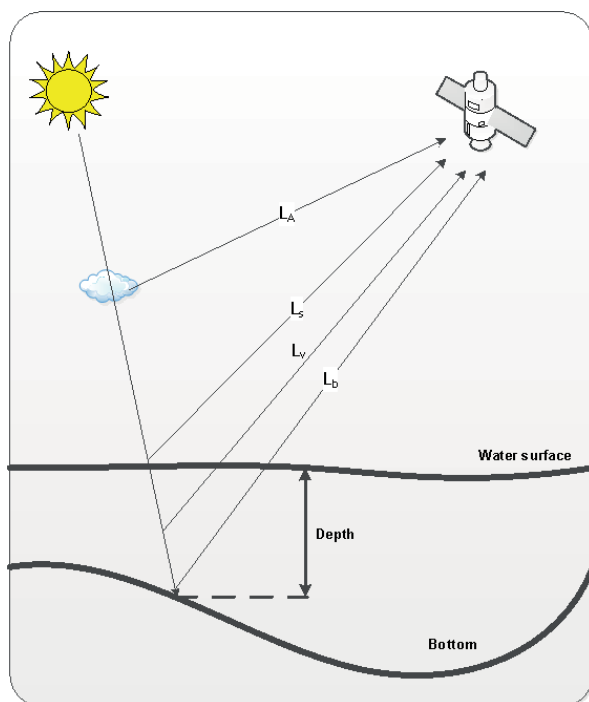


Fig. 1. Physical principle of SDB model

As shown in Fig. 1, this principle can be divided into four basic components of the energy registered at the satellite sensor [14] which are: the bottom radiance L_B , the subsurface volumetric radiance L_v , the specular radiance L_s , and the atmospheric path radiance L_A . This can be written down as:

$$L_{TOA} = L_B + L_V + L_S + L_A \quad (1)$$

where the radiance L_{TOA} registered at the sensor includes the atmospheric scattering L_A and the subsurface volumetric radiance L_v resulting from volume scattering in water and its organic/inorganic constituents (e.g. sediment and chlorophyll). The surface radiance L_s is caused by the reflection of optical energy from the water surface, including possible sunglint effects. Finally, L_B is the result of energy reflection from the seabed, which holds the information about bottom scattering characteristics and water depth. In this context, in order to derive the bottom depth from satellite observation, disaggregating the bottom and volumetric radiance from the total radiance is crucial.

Basically, there are two fundamental models for obtaining SDB. Both of them apply mechanisms to remove L_p and specular effects, and minimize the variability of volumetric scattering effects [15][16]. In most approaches this is achieved by assuming that bottom radiance in fully deep water equals zero. Then, the total radiance (or reflectance) over optically-deep water (L_∞ or R_∞), represents the combined effect of subsurface volumetric radiance, specular radiance, and atmospheric path radiance. After atmospheric and sunglint corrections, the deep-water radiance contains only subsurface volumetric radiance. Assuming that the subsurface volumetric radiance in shallow water and atmospheric absorption is the same as that in the adjacent deep water, the optically deep-water radiance recorded by the remote sensor can be used to correct the subsurface volumetric radiance in shallow water.

In order to minimize depth estimation errors, a possibly largest number of wavelength bands with smallest attenuation should be used. The maximal derivation depth is limited by water turbidity (caused by suspended sediments, chlorophyll, and organic particles) and the wavelength registered by the sensor. Therefore, the basic band used for SBD is blue light spectrum (440 to 540 nm) as it has the smallest attenuation and can penetrate water up to 30m in optimal conditions. Longer wavelengths (green and red) attenuate rapidly in water, as a consequence of which green light (500–600 nm) can penetrate to a maximum depth of approximately 15 m, red light (600–700 nm) to 5 m, and near infrared (700–800 nm) to as little as 0.5 m [17].

OPTICAL BAND RATIO BATHYMETRY RETRIEVAL MODEL

The first of the above described approaches [3], based on a log-ratio equation, is described by the following equation:

$$z_{est} = m_1 \frac{\ln(R(\lambda_i))}{\ln(R(\lambda_j))} + m_0 \quad (2)$$

where z_{est} is the satellite derived bathymetry depth, m_0 and m_1 are the coefficients of the model, and $R(\lambda_i)$ and $R(\lambda_j)$ are the remote sensing radiances for optical bands λ_i and λ_j . In this model, the bottom depth is estimated on the basis of light attenuation phenomena, as the attenuation of the incoming shortwave radiation varies spectrally. This effect can be observed in spectral bands.

ANALYTICAL INVERSION MODEL

The local inversion model is derived directly from the simplified radiation equation for optically shallow waters (3):

$$L_{TOA} = L_{\infty}[1 - e^{-kz}] + A_d e^{-kz} + L_A + L_S \quad (3)$$

where A_d is the upwelling spectral radiance directly reflected from the bottom (before interacting with the overlaying water column), k is the two-way attenuation coefficient, and z is the depth. In this context, the expression $A_d e^{-kz}$ represents the energy attenuation effect resulting from energy passing through the water column of known depth z . Assuming that the ratio of bottom reflectance between two spectral bands is constant for all bottom types within a given scene and the light attenuation variability caused by atmospheric effects is negligible for a given area, the depth estimated with the use of the following model can be expressed as:

$$z_{est} = \alpha_0 + \sum_{i=1}^N \alpha_i \ln[L(\lambda_i) - L_{\infty}(\lambda_i)] \quad (4)$$

where N is the number of spectral bands, α_i ($i=1,2,\dots,N$) are the constant coefficients derived during model calibration, and $L(\lambda_i)$ is the remote sensing radiance after atmospheric and sunglint corrections for spectral band λ_i . The use of natural logarithm in the expression makes the transformation linear to water depth and deepwater-corrected radiances of spectral bands.

MATERIALS

In this section, the description of input data for the algorithms used in the paper is outlined. The proposed algorithms utilize two types of input datasets, which are: multispectral imageries obtained from the Sentinel-2 satellite system that SDB is derived from, and the calibration dataset constructed from SBE surveys.

SENTINEL-2 DATA

Sentinel-2 (S2) is a two polar-orbiting satellite system that is the continuation of the SPOT and Landsat series of

multispectral missions. Its main objective is to deliver high-resolution optical and thermal operational observations for land/sea monitoring, emergency response, and security services [18]. Sentinel-2 is part of the European Space Agency (ESA) Copernicus programme and its data is provided via dedicated data dissemination frameworks, such as SciHub [19] or national Copernicus mirror sites [20][21].

Sentinel-2 provides systematic coverage of the globe between 56°S to 84°N, with relatively high revisit frequency (every five days at the equator under the same viewing conditions). The spatial resolution for optical and NIR (865 ± 10nm) bands equals 10m x 10m per pixel. In the case of the analysed area, data is delivered via the UTM 34N projection grid. Sentinel-2 also delivers six NIR and SWIR bands with 20m x 20m spatial resolution and three 60m resolution bands in optical, NIR and SWIR ranges (Fig. 2).

The observation data from S2 is delivered by the mission Ground Segment, which provides processing schemes in four levels:

- Level-0 (L0) – raw compressed geometrically registered data
- Level-1 (L1) – divided into A, B, C and C sub-stages. The stage L1C provides geocoded uncompressed TOA reflectance after radiometric calibration, data correction, and geometric refinement.
- Level-2 (L2) – the stage can be performed with the use of dedicated processing software ([22][23]) and provides the bottom of the atmosphere reflectance.

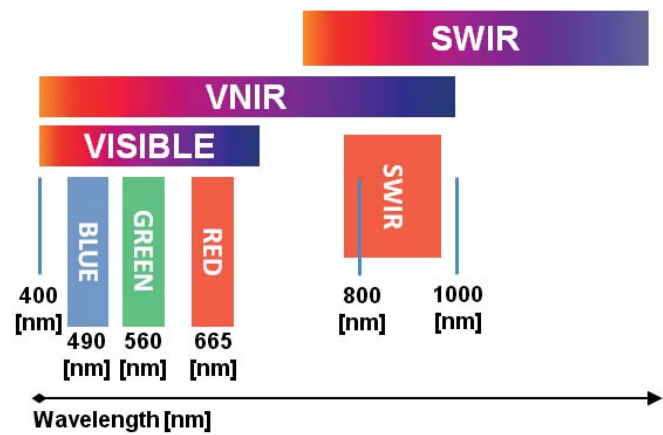


Fig. 2. Sentinel-2 MSI optical band characteristics.

SOUNDING DATA

The data for SDB model calibration was delivered by the Maritime Office in Gdynia (MAG), which is part of national maritime authority in Poland. Its duties cover such activities as: ensuring and monitoring maritime safety and security in the scope of inspections carried out by Flag State Control and Port State Control, monitoring of ships' traffic, sea routes and security of ship and port facilities, monitoring of ships' routes and waterways, management of waters, maritime spatial planning, and others.

In addition to the above stated duties, MAG performs systematic Polish coast bathymetry surveys with the aid of different survey techniques, including SBE, MBS, and Lidar scanning. The data for the presented research was retrieved from near-shore SBE surveys made in 2011. The testing site covers 12 km of the South Baltic coast (Fig. 3).

Each survey is based on acoustic sounding profile depth measures, where each sounding within the profile is spaced by 10-20m. Each profile is perpendicular to the coast and starts 1800-2000m before the coastline, which corresponds to the bottom depth of about 15-20m. The profiles are parallel to each other and spaced by 500m along the coast.

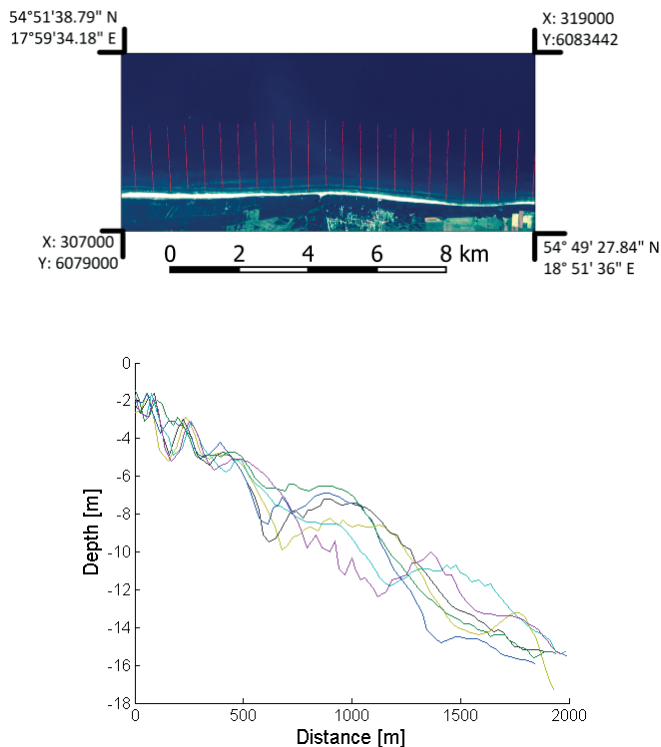


Fig. 3. Upper picture: calibration test site geographically positioned on the basis of composite RGB Sentinel-2 imagery in UTM 34N projection. Red dots represent SBE soundings profiles. Lower picture: plots of selected sounding profiles (the same as in the upper figure) as functions of distance from the shore.

RESULTS

In order to calibrate the proposed models of bathymetry retrieval, the sounding data described in the previous section was used. This process was based on visual and analytical inspection of the calibrating dataset. As it can be observed, the sounding in-situ observations contain not only underwater soundings but also some small number of in-situ measurements along the coast (above the water surface). Because of this, the in-situ observations with depth less than 0.5 m were removed from further analysis. The remaining data was compared to the remote Sentinel-2 observations acquired on 4th March 2016, 9th March 2016, 27th March 2016, and 6th May 2016 under clean-sky conditions.

LOG-RATIO MODEL CALIBRATION

During log-ratio model calibration, for each sounding point the $\langle \text{observation}, \text{model value} \rangle$ pair is built. Then, for each pair the model value is calculated using eq. (2) with initial values of $m_0 = 1$ and $m_1 = 0$. In the next step, this set of pairs is put under second degree polynomial regression in order to obtain optimal m_0 and m_1 values. The root mean square error of calibration and correlation is calculated as the quality indicator. The total number of calibration points equals 2074 (Fig. 4). Figures 4-7 show scatter plots of calibrated SDB corresponding to sounding data for different S2 observations.

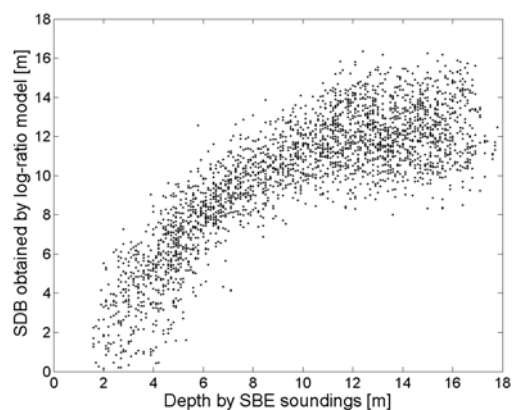


Fig. 4. Scatter plot of results obtained by optimized log-ratio model vs. depths obtained by SBE. Root mean square error was $RMSE = 2.4231 [m]$ and Pearson correlation coefficient was $R = 0.8254$. Model was calibrated on the basis of satellite acquisition made on 4th March 2016.

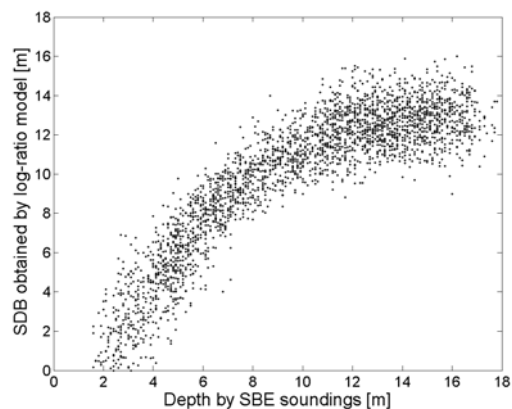


Fig. 5. Scatter plot of results obtained by optimized log-ratio model vs. depths obtained by SBE. Root mean square error was $RMSE = 2.0555 [m]$ and Pearson correlation coefficient was $R = 0.8779$. Model was calibrated on the basis of satellite acquisition made on 9th March 2016.

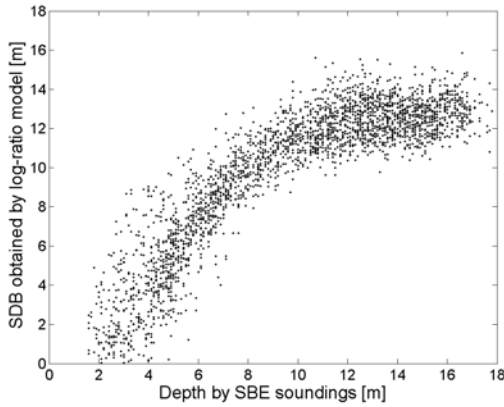


Fig. 6. Scatter plot of results obtained by optimized log-ratio model vs. depths obtained by SBE. Root mean square error was RMSE= 2.079 [m] and Pearson correlation coefficient was $R= 0.8749$. Model was calibrated on the basis of satellite acquisition made on 27th March 2016

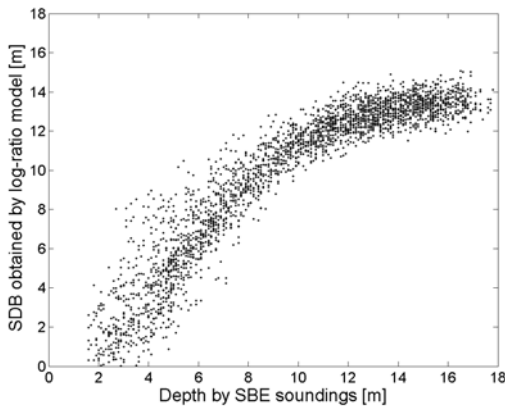


Fig. 7. Scatter plot of results obtained by optimized log-ratio model vs. depths obtained by SBE. Root mean square error was RMSE= 1.653 [m] and Pearson correlation coefficient was $R= 0.9229$. Model was calibrated on the basis of satellite acquisition made on 6th May 2016.

The presented results indicate strong correlation between SDB and the sounding data acquired by SBE. This strong correlation can be particularly observed for mid-range bottom depths. The noise for small bottom depths is caused by optical effects of wave collapse and relatively high temporal bathymetry variation. For deeper sounding, the maximal derived bathymetry differs in different observations, however in most cases it ranges between 12 and 16 meters. Within this range of bottom depth values, the SBE data for deeper optical properties of water becomes equal to that of fully deep water.

Nevertheless, it can be seen that for each observation used to derive bathymetry, SDB depicts the characteristics of the bottom profile lines. In order to present this, selected SBE profiles were plotted in Fig. 8 together with the corresponding SDB profile. The black line represents the calibration data, while the coloured lines represent SDB derived along the selected SBE profile for different acquisition datasets. This result is consistent with previous observations, as the SDB bathymetry profile depicts the shapes of SBE bathymetry,

particularly for mid-range bottom depths. The difference between SBE and SDB increases at points situated deeper than 12-14 meters.

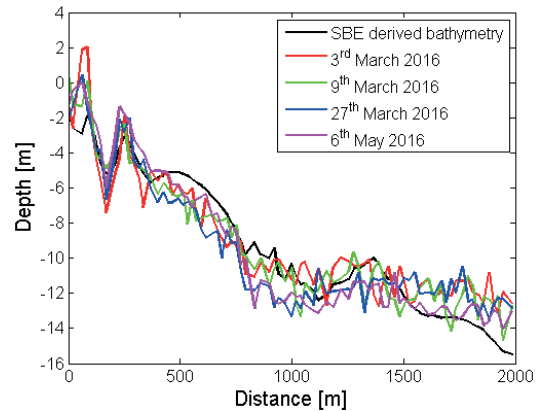


Fig. 8. Comparison of analytical model performance for different calibration datasets recorded for one selected SBE profile.

ANALYTICAL MODEL CALIBRATION

The calibration methodology for the second model was analogical, however this model consists of at least four parameters ($\alpha_0, \alpha_1, \alpha_2, \alpha_4$) which are to be calibrated locally when using Sentinel-2 (for this purpose 3 optical bands: R, G, and B were used). Thus, for the sounding point calibration dataset M eq. 4 takes the form:

$$SDB_{M(k)} = \alpha_0 + \sum_{i=1}^N \alpha_i \ln[L(\lambda_i)_{M(k)} - L_{\infty}(\lambda_i)] \quad (5)$$

where $SDB_{M(k)}$ is the satellite derived bathymetry for the k -th sounding point ($M(k)$), $k(1,2,\dots, K)$, and K is the total number of calibration points. $L(\lambda_i)_{M(k)}$ is the i -th band reflectance corresponding to $M(k)$. Then, for K calibration points, the optimal solution to the above stated optimization problem has the form of matrix equation (6):

$$\hat{\alpha} = [L^T W L]^{-1} L^T z \quad (6)$$

where $\hat{\alpha}$ is the N -element column vector of optimal model parameters (α_i), W is the optional $K \times K$ weight matrix, L is the $K \times N$ matrix, and z is the K -element column vector of sounding depths. Figures 9-12 show a series of scatter plots of calibrated SDB depths against SBE data, analogical to those shown in Figs. 4-7.

Generally, the results are consistent with those obtained in the previous case, however some significant conclusions can be derived. For instance, both models reach a similar maximum depth derivation, which ranges in about 12-16 meters. It can be also observed that higher data noise occurs for small- and maximum-depth ranges, while in mid-depth ranges the noise is relatively low. Moreover, in both models

the SDB obtained from observation made on 6th May 2016 returns the smallest error among all observations. That leads to the conclusion that low water turbidity and other obscuring effects have higher impact on final quality of SDB then the applied model.

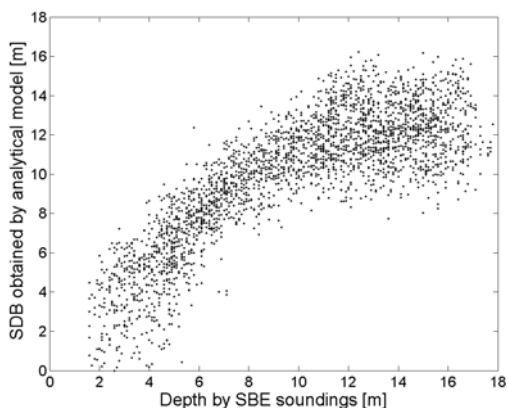


Fig. 9. Scatter plot of results obtained by optimized analytical model vs. depths obtained by SBE. Root mean square error was RMSE= 2.4186 [m] and Pearson correlation coefficient was $R= 0.8262$. Model was calibrated based on satellite acquisition made on 4th March 2016.

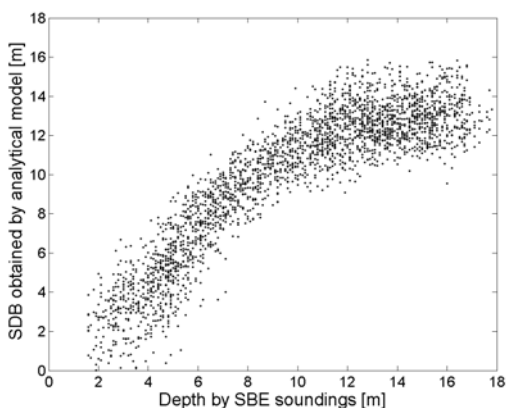


Fig. 10. Scatter plot of results obtained by optimized analytical model vs. depths obtained by SBE. Root mean square error was RMSE= 1.9694 [m] and Pearson correlation coefficient was $R= 0.885$. Model was calibrated based on satellite acquisition made on 9th March 2016.

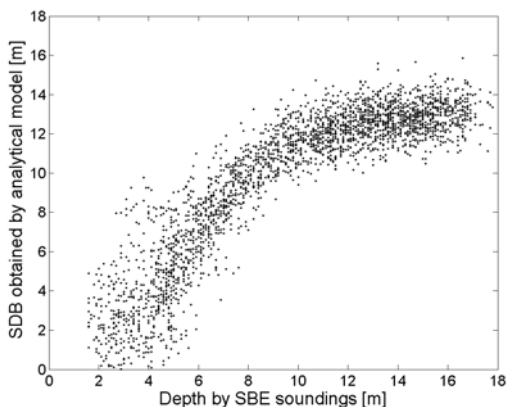


Fig. 11. Scatter plot of results obtained by optimized analytical model vs. depths obtained by SBE. Root mean square error was RMSE= 1.9727 [m] and Pearson correlation coefficient was $R= 0.8881$. 9th March 201. Model was calibrated based on satellite acquisition made on 27th March 2016.

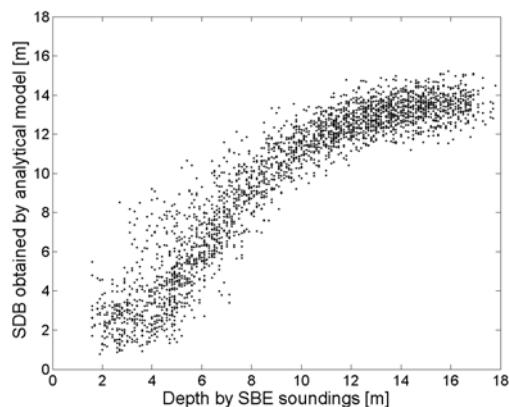


Fig. 12. Scatter plot of results obtained by optimized analytical model vs. depths obtained by SBE. Root mean square error was RMSE= 1.651 [m] and Pearson correlation coefficient was $R= 0.9231$. Model was calibrated based on satellite acquisition made on 6th May 2016.

Detailed comparison of SDB and SBE is given in Fig. 13 for the selected SBE profile (the same as in previous case). In this case, similar conclusions related to SDB errors and maximum derivation depth can be derived. However, additional issues should be discussed. Firstly, both models can be characterized by the repeatability of the obtained SDB profiles. The shapes of the SBE bottom profiles can be observed, for all acquisitions, both in log-ratio and analytical model results. However, in both models, very shallow SDB observation can be derived as exposed over the water surface - this can be particularly seen for the observation made on 3rd March 2016. However, there is no certain method to tell whether this information is true or false. In other words, for this particular observation, some areas placed very near to the shore could be exposed above the water surface due to low sea level or past storm.

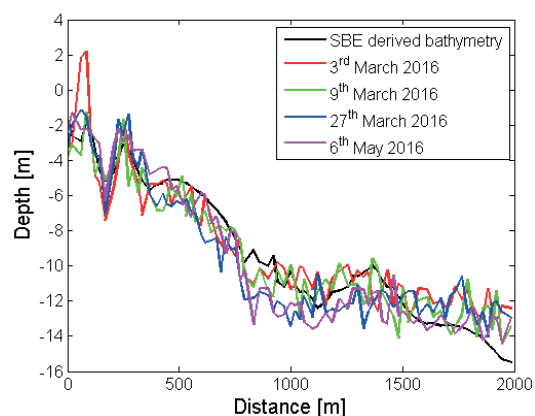


Fig. 13. Comparison of analytical model performance for different calibration datasets recorded for one selected SBE profile.

Overall comparison of model performance for different S2 observations is given in Table 1. This analysis shows that both models preserve satisfactory quality of SDB derived for depths 0-16m. This comparison also confirms earlier conclusions that the observation presented in the 4th row of the table (6th May 2016) is characterized by the highest quality what is confirmed by the lowest RMSE (1.653 m for

the log-ratio model and 1.653 m for the analytical model) and highest correlation from all calibration datasets (0.9229 and 0.9231, respectively).

Tab. 1. Comparison of model performance after calibration with different acquisition datasets

Acquisition date	Log-ratio model		Analytical model	
	R	RMSE	R	RMSE
04.03.2016	0.8254	2.4231	0.8262	2.4186
09.03.2016	0.8779	2.0555	0.885	1.9694
27.03.2016	0.8749	2.079	0.8881	1.9727
06.05.2016	0.9229	1.653	0.9231	1.651

ERROR ANALYSIS

As it was observed, the correlation between SDB and SBE bathymetry is clearly visible, particularly for smaller depths than, approximately, 16 meters. For deeper soundings, the SDB estimator becomes constant and uncorrelated, like for fully deep water. In this context, it is noteworthy that SDB models do not behave evenly for all bottom depths, and model calibration is not efficient for the depths higher than 12-16 meters. Therefore, model calibration making use of calibration points deeper than a particular threshold leads to the decrease of general model performance.

In order to analyse how bottom depth influences the error of SDB, additional analysis of the obtained results was performed. For each remote observation, the bathymetry error was plotted as the function of depth. The results of this analysis are given in Fig. 14-17. In each figure, the upper plot represents the SDB error as the function of depth, the middle graph represents the number of calibration points for each water depth bin (it is a depth histogram of the calibration dataset). The lower plot shows changes of the introduced SDB quality coefficient (SDB_{Qcoef}) that describes the quality of the retrieved SDB. This coefficient is described by the following formula:

$$SDB_{Qcoef} = \frac{\ln(1 + R(\lambda_i))}{\ln(1 + R(\lambda_j))} - \left(\ln\left[\frac{1 + R_w(\lambda_i)}{1 + R_w(\lambda_j)} \right] - 2\sigma \right) \quad (7)$$

where σ is the standard deviation of the selected field with fully deep-water log ratios reflectance for wavelengths λ_i and λ_j . SDB_{Qcoef} enables to determine a threshold to which bathymetry derived by the proposed models can be retrieved with certain quality. Note that this value depends only on the remote observation data, therefore neither bathymetric nor other auxiliary information is necessary to compute it. Consequently, it can be used operationally. The red line in the lower plots (Fig. 14-17) represents the threshold equal to 0. As it can be observed, as SDB_{Qcoef} reaches this threshold, the SDB error is clearly increasing.

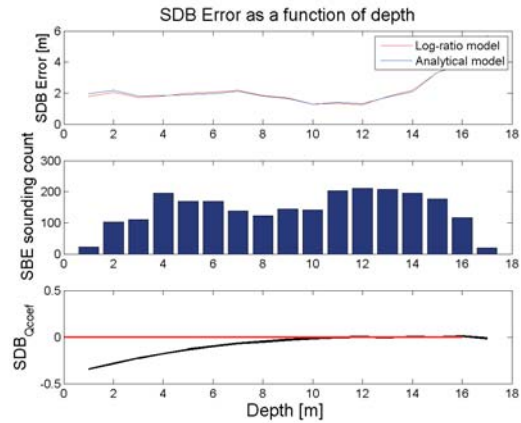


Fig. 14. Error distribution as function of depth (upper picture), SBE sounding count (middle), and SDB quality indicator plot (lower) for 4th March 2016. The red line in the lower plot represents threshold equal to 0.

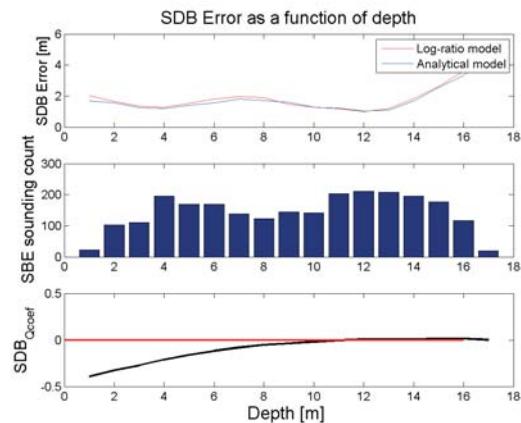


Fig. 15. Error distribution as function of depth (upper picture), SBE sounding count (middle), and SDB quality indicator (SDB_{Qcoef}) plot (lower) for 9th March 2016

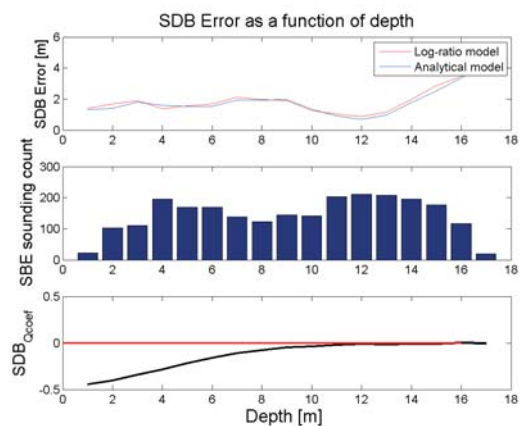


Fig. 16. Error distribution as function of depth (upper picture), SBE sounding count (middle), and SDB quality indicator (SDB_{Qcoef}) plot (lower) for 27th March 2016

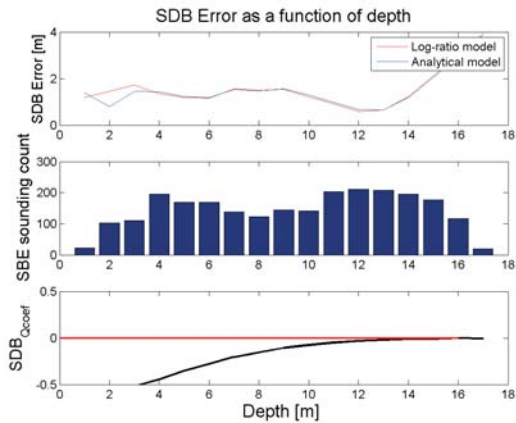


Fig. 17. Error distribution as function of depth (upper picture), SBE sounding count (middle), and SDB quality coefficient (SDB_{Qcoef}) indicator plot (lower) for 6th May 2016

In order to show benefits of using the SDB_{Qcoef} threshold, each model was calibrated with only those observations which met the aforementioned quality criterion, namely where $SDB_{Qcoef} < 0$. In this way, only those observations were used for model calibration which were indicated as valid by the quality indicator. The results of model calibration presented in Tab. 2 reveal significant improvement of model performance. Namely, for each observation dataset, the RMSE values are significantly lower. For the log-ratio model the RMSE was reduced from the range of 1.653-2.4231[m] to 1.0822-1.4319 [m], while for the analytical model the final RMSE values ranged within 1.0681-1.456[m], compared to the initial range of 1.651-2.4186 [m]. Analogically, the increase of the correlation coefficient was observed from 0.8254-0.9229 to 0.8736-0.9346 for the log-ratio model and from 0.8262-0.9231 to 0.869-0.9345 for the analytical model.

Tab. 2. Comparison of model performance after calibration with different SDB acquisition datasets and maximal depth determined by the quality indicator (SDB_{Qcoef}).

Acquisition date	Log-ratio model		Analytical model	
	R	RMSE	R	RMSE
04.03.2016	0.8736	1.4319	0.869	1.456
09.03.2016	0.9065	1.0822	0.9091	1.0681
27.03.2016	0.9083	1.3678	0.9115	1.3447
06.05.2016	0.9346	1.3632	0.9345	1.3643

VERIFICATION OF RESULTS

In order to perform visual inspection of bottom maps generated by the proposed SDB models and visually verify the quality of these models, maps representing the bathymetry derived from remote observations were generated. Figures 18-21 represent SDB images obtained with the use of the log-ratio model and the analytical model. The data is presented as colour coded depths ranging from 0 to 18 meters. The analytical model was calibrated with the use of SDB_{Qcoef} thresholding technique, described in the previous section. The areas above water surface, in SDB and coast, are marked as white pixels.

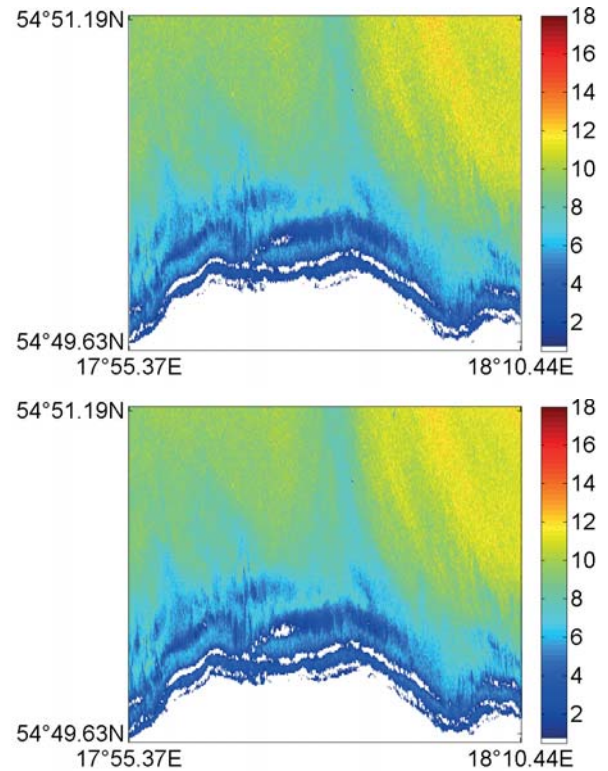


Fig. 18. Comparison of colour coded depth maps obtained by the optimized log-ratio SDB model (upper figure) and the analytical SDB model (lower figure) for 3rd March 2016.

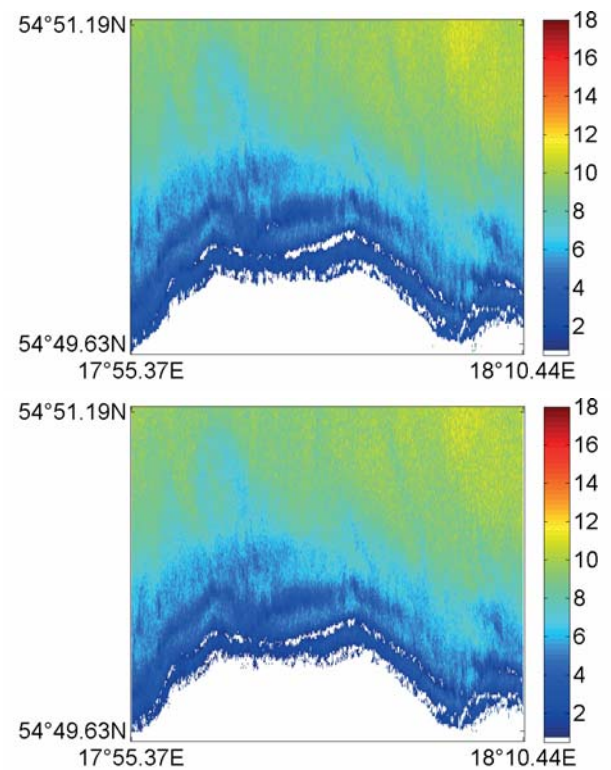


Fig. 19. Comparison of colour coded depth maps obtained by the optimized log-ratio SDB model (upper figure) and the analytical SDB model (lower figure) for 9th March 2016.

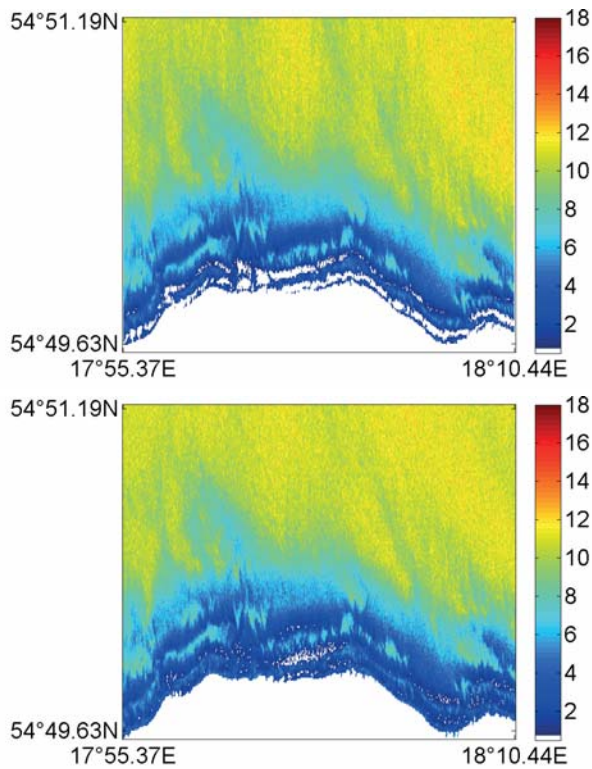


Fig. 20. Comparison of colour coded depth maps obtained by the optimized log-ratio SDB model (upper figure) and the analytical SDB model (lower figure) for 27th March 2016. White pixels represent depths derived as situated above the sea surface.

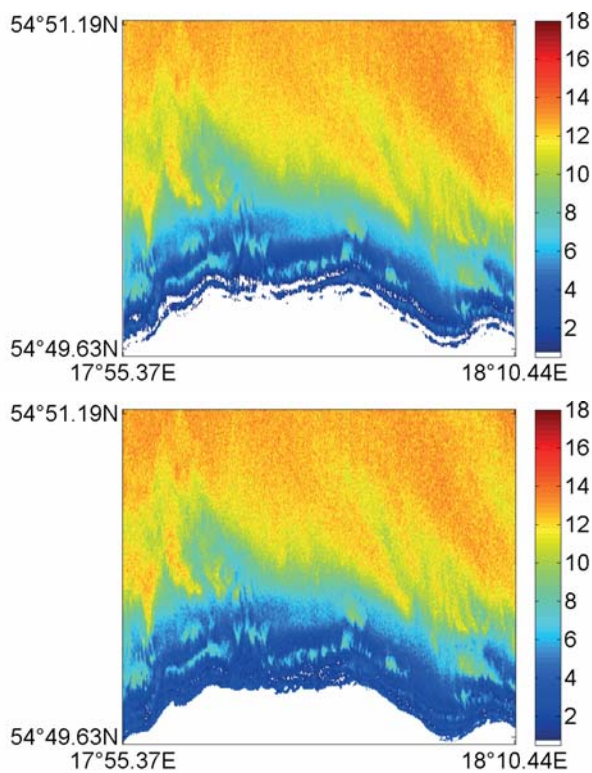


Fig. 21. Comparison of colour coded depth maps obtained by the optimized log-ratio SDB model (upper figure) and the analytical SDB model (lower figure) for 6th May 2016. White pixels represent depths derived as situated above the sea surface.

It can be observed that the corresponding depth maps retrieved from both models are relatively similar to each other, and both techniques enable to obtain similar results in the context of visual analysis. Visible noise levels observed in the scatter plots presented in previous sections (Fig. 4-11) are also noticeable in these maps. Visual inspection of the results also reveals the fact that the examined methods behave relatively poorly for depths exceeding the maximum derivation depth determined by the $SDB_{Q_{coef}}$ factor. However, for shallow and non-turbid waters, even single 3D shapes of underwater bathymetry are easy to retrieve for human eye.

Visual inspection enables to notice only minor differences between the observations acquired at the same time, and both methods can be successfully used in relatively turbid and difficult conditions.

CONCLUSIONS

The paper compares two fundamental methods for bathymetry retrieval from S2 multispectral satellite observations. The results of model performance were obtained using the data acquired for the 12-km long South Baltic coastline. The calibration points acquired from SBE surveys were delivered by the National Maritime Administration.

A detailed analysis of the obtained results shows that both methods can be successfully applied for the South Baltic region. However, some limitations and factors causing obstruction of the results can be observed. It is water turbidity which is most important in this case, therefore the bathymetry can be derived to the depth approximately equal to 12-18 meters. What is also important is the fact that the maximum depth that can be derived from satellite observation varies in time and space and is difficult to be assumed a priori. To overcome this drawback, a novel indicator of determining maximal SDB depth was proposed in the paper. This SDB quality indicator is derived only on the basis of the remotely registered data and can therefore be applied operationally.

During the research, a detailed analysis of errors obtained for different depth ranges was also performed. The obtained results indicate that the error of model calibration, expressed in meters (RMSE), equals up to 10-20% of the real depth and is, generally, case dependent. This value is worse than the results obtained by other authors [1][3-16]. However, there are at least two reasons for this. The first is water turbidity, as the effects of light attenuation and its spatial variety are much more obscuring in the Baltic Sea than in other locations such as presented in [1][3-16], where the testing datasets were related to optically clear waters. Another issue is that bathymetry surveys for this research were not collected at the same time. This is because of the fact that the Polish Maritime office performs SBE surveys periodically and, consequently, exact time co-incidence between remote observation and calibration data acquisitions was unavailable for our test site. Nevertheless, it was shown that the proposed methods, combined with the SDB quality indicator, are not only self-adaptive but can also be used operationally, for instance to

deliver a cost-effective alternative for large scale bathymetry observations. The novelty of the research presented in the paper also relies on the fact that it bases on newly deployed ESA Sentinel-2 observations obtained for relatively difficult turbid Baltic Sea waters.

ACKNOWLEDGEMENTS

The author wishes to thank the Maritime Office in Gdynia, Poland, for providing sounding bathymetry maps used in the research presented in the paper.

REFERENCES

1. D. R. Lyzenga, N. R. Malinas, and F. J. Tanis, "Multispectral bathymetry using a simple physically based algorithm," *IEEE Trans. Geosci. Remote Sens.*, vol. 44, no. 8, pp. 2251–2259, Aug. 2006.
2. A. Chybicki et al., "GIS for remote sensing, analysis and visualisation of marine pollution and other marine ecosystem components," 2008 1st International Conference on Information Technology, Gdansk, 2008, pp. 1-4. doi: 10.1109/INFTECH.2008.4621628
3. Stumpf, R.P., Holderied, K., Sinclair, M., 2003. Determination of water depth with high-resolution satellite imagery over variable bottom types. *Limnology Oceanogr.* 48, 547–556. doi:10.4319/lo.2003.48.1_part_2.0547
4. R. Lyzenga, D., 1981. Remote sensing of bottom reflectance and water attenuation parameters in shallow water using aircraft and Landsat data. *Int. J. Remote Sens.* 2, 71–82.
5. R. Lyzenga, D., 1978. Passive remote sensing technique for mapping water depth. *Appl. Opt.* 17, 379–383.
6. Philpot, W.D., 1989. Bathymetric mapping with passive multispectral imagery. *Appl. Opt.* 28, 1569–1578. doi:10.1364/AO.28.001569
7. J. C. Sandidge, and R. J. Holyer, "Coastal bathymetry from hyperspectral observations of water radiance," *Remote Sens. Environ.*, vol. 65, no. 3, pp. 341–352, Sep. 1998.
8. S. M. Adler-Golden, P. K. Acharya, A. Berk, M. W. Matthew, and D. Gorodetzky, "Remote bathymetry of the littoral zone from AVIRIS, LASH, and QuickBird imagery," *IEEE Trans. Geosci. Remote Sens.*, vol. 43, no. 2, pp. 337–347, Feb. 2005.
9. Sheng Ma, Zui Tao, Xiaofeng Yang, Member, IEEE, Yang Yu, Xuan Zhou, and Ziwei Li, "Bathymetry Retrieval from Hyperspectral Remote Sensing Data in Optical-Shallow Water", *Ieee Transactions on Geoscience and Remote Sensing*, Vol. 52, No. 2, February 2014
10. H. Holden and E. LeDrew, "Measuring and modeling water column effects on hyperspectral reflectance in a coral reef environment," *Remote Sens. Environ.*, vol. 81, nos. 2–3, pp. 300–308, Aug. 2002.
11. Haibin Su, Hongxing Liu, William D. Heyman, "Automated Derivation of Bathymetric Information from Multi-Spectral Satellite Imagery Using a Non-Linear Inversion Model", *Marine Geodesy*, vol. 31, 2008.
12. E. P. Green, P. J. Mumby, A. J. Edwards, and C. D. Clark, "Remote sensing handbook for tropical coastal management," in *Coastal Management Sourcebooks 3*, A. J. Edward, Ed. Paris, France: UNESCO, 2000.
13. Poliyapram V., Venkatesh R., Shinji M., 2016, Satellite-derived bathymetry using adaptive geographically weighted Regression model, *Marine Geodesy*, vol. 39:6, 458-478.
14. Jensen, J. R. 2007. *Remote sensing of the environment: An earth resource perspective*, 2nd ed. Upper Saddle River, NJ: Prentice Hall
15. Mishra, D., S. Narumalani, D. Rundqulst, and M. Lawson. 2006. Benthic habitat mapping in tropical marine environments using QuickBird multispectral data. *Photogrammetric Engineering & Remote Sensing* 72:1037–1048.
16. Lyzenga, D. R., N. P. Malinas, and F. J. Tanis. 2006. Multispectral bathymetry using a simple physically based algorithm. *Geoscience and Remote Sensing, IEEE Transactions on* 44:2251–2259.
17. Green, E. P., P. J. Mumby, A. J. Edwards, and C. D. Clark. 2000. *Remote sensing handbook for tropical coastal management*. Paris: A. J. Edwards, UNESCO
18. Drusch, M. & 14 co-authors (2012). Sentinel-2: ESA's optical high-resolution mission for GMES operational services, *Rem. Sens. Env.* (accepted).
19. Sentinels Scientific Data Hub, Technical Guide, European Space Agency, source: <https://scihub.copernicus.eu/userguide/> (accessed on 22/12/2016)
20. Hellenic National Sentinel Data Mirror Site. Operated by the National Observatory of Athens. Source: <https://sentinels.space.noa.gr/> (accessed on 22/12/2016)
21. National French Copernicus Site, Centre National D'Etudes Spatiales, Source: <https://copernicus.cnes.fr/en/ground-segment-1> (accessed on 22/12/2016)

22. Sentinel Application Platform (SNAP), available at Science Toolbox Exploitation Platform (STEP), European Space Agency, source: <http://step.esa.int/main/toolboxes/snap/> (accessed on 22/12/2016)
23. Sen2cor - Sentinel-2 Level 2A product generation and formatting, available at Science Toolbox Exploitation Platform (STEP), European Space Agency, source: <http://step.esa.int/main/third-party-plugins-2/sen2cor/> (accessed on 22/12/2016)

CONTACT WITH THE AUTHOR

Andrzej Chybicki

e-mail: andrzej.chybicki@eti.pg.gda.pl

Gdansk University of Technology
Narutowicza 1/2, 80-233 Gdansk

POLAND

BEARING ESTIMATION USING DOUBLE FREQUENCY REASSIGNMENT FOR A LINEAR PASSIVE ARRAY

Krzysztof Czarnecki
Wojciech Leśniak
Gdansk University of Technology

ABSTRACT

The paper demonstrates the use of frequency reassignment for bearing estimation. For this task, signals derived from a linear equispaced passive array are used. The presented method makes use of Fourier transformation based spatial spectrum estimation. It is further developed through the application of two-dimensional reassignment, which leads to obtaining highly concentrated energy distributions in the joint frequency-angle domain and sharp graphical imaging. The introduced method can be used for analysing, a priori, unknown signals of broadband, nonstationary, and/or multicomponent type. For such signals, the direction of arrival is obtained based upon the marginal energy distribution in the angle domain, through searching for arguments of its maxima. In the paper, bearing estimation of three popular types of sonar pulses, including linear and hyperbolic frequency modulated pulses, as well as no frequency modulation at all, is considered. The results of numerical experiments performed in the presence of additive white Gaussian noise are presented and compared to conventional digital sum-delay beamforming performed in the time domain. The root-mean-square error and the peak-to-average power ratio, also known as the crest factor, are introduced in order to estimate, respectively, the accuracy of the methods and the sharpness of the obtained energy distributions in the angle domain.

Keywords: Direction of arrival, DOA, instantaneous frequency, short-time Fourier transform, STFT, time-frequency reassignment, intercept and surveillance sonar, crest factor

INTRODUCTION

Bearing estimation is an important issue in sonar and radar techniques [9], [21]. In underwater acoustic systems, the direction of arrival (DOA) of the signal can be estimated, among others, through the use of its spatial spectrum [4], [10], [15]. The considerations presented in the paper exploit and expand this approach by introducing two-dimensional reassignment in a joint frequency-angle domain, which is a novel modification, compared to classical time-frequency reassignment [11]. The main aim of this research is to present the reassignment as a usable method for DOA estimation and to assess its utility in this field. We propose the use of this method especially in order to analyse nonstationary

and multicomponent signals whose parameters are *a priori* unknown, as well as by allowing comprehensive graphical presentation. These issues are particularly important in the considered passive sonar system. Other critical requirements for digital real-time systems include predictable and short durations of their response, as well as their high performance and stability. These requirements can be achieved by using Fast Fourier Transformation (FFT) which is the implementation basis of the proposed method [22].

The reassignment method, initially referred to as “the modified moving window method”, was introduced by Koderá *et al.* in 1976 [11]. In general, this approach is helpful in obtaining highly concentrated energy distributions in the joint time-frequency domain and can be effectively used for

analysing multicomponent and non-stationary signals with components sparsely distributed over the time-frequency plane. Numerous authors have proposed contributions to the aforementioned approach [1], [5], [7], to name but a few. The time-frequency reassignment is accomplished through energy relocation, which employs local group delay (LGD) and channelized instantaneous frequency (CIF). In the paper, we consider the reassignment in the frequency-angle domain, or equivalently, in the frequency-bearing domain. Therefore, we still use the CIF, but the LGD will be knowingly overlooked. Meanwhile, DOA can be obtained by the ratio of CIF and local spatial frequency (LSF). Both, CIF and LSF, may be estimated by differentiating the phase of the extended short-time Fourier transform (STFT). We propose extending the classical STFT to four dimensions: time, frequency, propagation delay, and spatial frequency. This allows us to obtain CIF and LSF by processing a single transform. The proposed method is novel, but there are other contributions to bearing estimation in this particular context, which have also been reported in [3] and [6].

The introduced method and the used linear passive array are presented as elements of a surveillance or intercept sonar system. All the relevant situations and analysed signals are related, in some way, to this area. Nonetheless, the resultant conclusions are universal and may also be applicable to other areas of bearing estimation, where the received signals stored by a linear array consist of a number of omnidirectional sensors. The method is also referred to time-frequency reassignment as its extension to many dimensions.

The paper is organized as follows. In Section II, a general scheme of data acquisition and forming the received signal in a system with linear passive array is presented. In Section III, the concept of a novel method of bearing estimation is introduced. Section IV contains descriptions of its discrete implementations. Finally, in Section V, the results of numerical experiments and analyses of popular types of sonar sounding pulses with and without frequency modulation are presented. The accuracy of the method and the sharpness of the final imaging in the presence of noise are also evaluated in this section.

LINEAR PASSIVE ARRAY

From a military point of view, water depth can be explored by sonars in search of potentially dangerous objects such as submarines, torpedoes, and mines. However, active sonar systems are usually very reluctantly used by the crews of Navy ships during military operations. When functioning, the active sonar easily gives away its location. Furthermore, a sounding signal must have a sufficient amount of energy to allow back and forth propagation between the sonar and the target, and must take into account any losses due to reflection and backscatters. This is the reason why the distance over which a sounding sonar can detect targets is significantly smaller than the distance from which this sonar can be detected by other passive sonar systems. Conversely,

passive systems do not possess this disadvantage and are important equipment used by Navy vessels, especially out on the high seas. However, it should be added that the passive systems are helpless when facing objects which do not emit any acoustic signals, mines for instance. Another source of restrictions in the use of active sonar systems is their adverse effects on underwater fauna [19]. This is particularly true of systems emitting high-power acoustic waves into the natural environment. Therefore, development in this area is crucial and is largely driven by practical considerations [14].

Let us consider a hypothetical passive sonar system with a linear array of omnidirectional hydrophones [12], [20]. This array consists of M hydrophones uniformly distributed along a straight line, at a distance from each other equal to d_{Δ} . In this way, each received acoustic signal can be uniformly sampled in both space and time. This means that the Nyquist-Shannon sampling theorem should be met in all these dimensions. In the time domain, the maximal frequency f_{max} of the signal component in the Fourier spectrum is only limited by the sampling rate r_s , in accordance with $f_{max} < r_s/2$. Respectively, in space, the maximal frequency depends on the distance between the neighbouring hydrophones d_{Δ} , the propagation velocity of the acoustic wave in water v_w , and the direction of arrival ϕ_u of the signal $u(t)$. In the situation under consideration, signal parameters, especially the DOA, are, *a priori*, unknown. Therefore, d_{Δ} should be set taking into account the reception of a signal propagated along the array, due to the fact that this direction is most demanding as regards sampling. Consequently, the greatest satisfactory distance between the neighbouring hydrophones is equal to:

$$d_{\Delta} = v_w / (2f_{max}), \quad (1)$$

where f_{max} is the maximal expected frequency of a considerable component in the Fourier spectrum of the incoming signal. In general, the resolution of bearing estimation in the classical approach is greater if the array is longer. Unfortunately, increasing the number of hydrophones can, simultaneously, increase significantly the overall cost of the entire system. Consequently, d_{Δ} is usually assumed as to be as large as possible, taking into account the fact that it is a relatively inexpensive means to elongate the array, as the total array length is equal to Md_{Δ} as well as the whole delay along the longitudinal section of the array being

$$\tau_{arr} = Md_{\Delta} / v_w. \quad (2)$$

The surveillance sonar under consideration is usually used for receiving signals whose sources are located at a significant distance from the array. This distance should be far greater than the wavelength of the received signal – the array is located in the far acoustic field. The arrival signals, including useful, disturbing, and noise contributions from various sources and directions, are summed and saved into the buffers. The scheme of input sample acquisition is

presented in Figure 1. The saved samples can be treated as the received signal $u(t, \tau)$ of two variables, dependent on time t and delay along the longitudinal section of the array τ as presented in Figure 2.

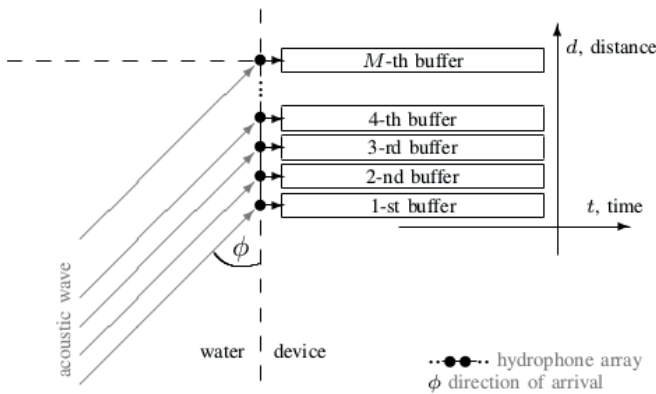


Fig. 1. Schema of data acquisition in a passive array.

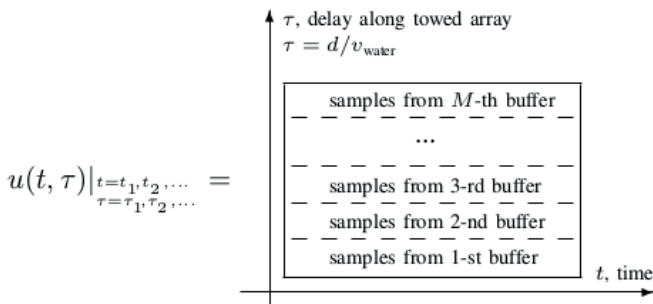


Fig. 2. Schema of received discrete signal forming.

DOUBLE FREQUENCY REASSIGNMENT

Let us consider the following complex-valued four-dimensional variant of the short-time Fourier transform of the function $u(t, \tau)$ of two variables:

$$U_h(t, \tau, \omega, \varpi) = A_h(t, \tau, \omega, \varpi) \exp(j\varphi_h(t, \tau, \omega, \varpi)) \iint u(\zeta, \xi) \bar{h}(\zeta - t, \xi - \tau) \exp(-j(\zeta\omega + \xi\varpi)) d\xi d\zeta. \quad (3)$$

It turns out that $U_h(t, \tau, \omega, \varpi)$ is a function of the following four variables: time t , geometrical location along the array expressed by propagation delay τ , angular frequency ω , and spatial angular frequency ϖ . $A_h(t, \tau, \omega, \varpi)$ is the amplitude and $\varphi_h(t, \tau, \omega, \varpi)$ is the appropriate phase of the Fourier transform. $\bar{h}(t, \tau)$ with a short line over it expresses the conjugated function of the analysing tapering window [6].

The Blackman-Harris (BH) window, which is a function of two variables: time and propagation delay, is used here as the analysing window. It is limited (finite) both in time and in delay. In the situation in question, the range of the window depends on the number and distribution of hydrophones

(sensors), as well as on the observation time (the duration of a single frame). The main reason for employing this window is a comparatively small size of its ambiguity area, which is similar to the Gaussian function (also known as the Gabor window). The ambiguity area of this window is the smallest for all known windows. The size of the ambiguity area is particularly important because it determines the TF resolution of the obtained transforms. However, the corresponding Gabor window has to be infinite in time and in delay, and therefore it is impractical in implementation. The proposed BH window has slightly lower TF resolution, however it allows a real-time implementation. Other important reasons include relatively highly attenuated side-lobes of the chosen BH window and nonzero window derivative, as well as their analytic formulae being both known and fairly simple. There also exists the possibility to use other windows. However, as long as the incoming signals are, *a priori*, unknown, there is no guarantee of any benefit from their use and the proposed BH window is one of the best choices for the considered method.

In regard to works by Kodera's et al. [11] and in relation to (3), the channelized angular instantaneous frequency (CIF) is defined as the partial derivative of the phase $\varphi_h(t, \tau, \omega, \varpi)$ with respect to time, in the following manner:

$$\Omega_h(t, \tau, \omega, \varpi) = \varphi_h(t, \tau, \omega, \varpi) / \partial t \quad (4)$$

Analogously, the local spatial frequency (LSF) expressed in hertz is herein defined as the partial derivative with respect to delay:

$$\Pi_h(t, \tau, \omega, \varpi) = \varphi_h(t, \tau, \omega, \varpi) / \partial \tau \quad (5)$$

where $|\Pi_h(t, \tau, \omega, \varpi)| \leq |\Omega_h(t, \tau, \omega, \varpi)|$, which derives from the geometrical axis of array location with respect to the direction of wave propagation. Subsequently, both the Ω_h and Π_h distributions are used to estimate the DOA as a function of t , τ , ω , and ϖ following:

$$\Phi_h(t, \tau, \omega, \varpi) = \arccos(\Pi_h(t, \tau, \omega, \varpi) / \Omega_h(t, \tau, \omega, \varpi)) \quad (6)$$

Subsequently, the introduced reassignment, which is to be understood as energy relocation, can be performed from the frequency-spatial-frequency (ω - ϖ) domain into the frequency-angle domain for each time t and delay τ as follows:

$$(t, \tau, \omega, \varpi) \rightarrow (t, \tau, \Omega_h(t, \tau, \omega, \varpi), \Phi_h(t, \tau, \omega, \varpi)). \quad (7)$$

Herein, the spectrogram's energy is defined as the squared magnitude of the transform:

$$E_h(t, \tau, \omega, \varpi) = |U_h(t, \tau, \omega, \varpi)|^2 = A_h(t, \tau, \omega, \varpi)^2 \quad (8)$$

to a new space, where the DOA is one of the dimensions. After this reassignment, we obtain a new spectral energy distribution marked by $\mathcal{E}_h(t, \tau, \Omega, \Phi)$. Eq. (7) represents energy relocation from a raster grid to locations related to signal parameters, such as frequency and the arrival angle. Relocation vectors are obtained by processing only the STFT phase. The desired result of this process is local increase of energy concentration near the instantaneous frequency of signal components and close to the directions from which the signals arrive (bearings). The directions are represented by angles with respect to the longitudinal axis of the antenna.

DIRECTIONAL CHARACTERISTIC

In general, the arrival signals received by passive sonar can be broadband, multicomponent, noisy, and nonstationary. However, in the paper, only their DOA is within our area of interest. Therefore, we propose a consideration of the resultant four-dimensional energy distribution $\mathcal{E}_h(t, \tau, \Omega, \Phi)$ through the marginal distribution, which can be interpreted as a directional characteristic and is defined as follows:

$$\mathcal{E}_h(t, \Phi) = \int_{\omega_1}^{\omega_2} \mathcal{E}_h(t, \tau_{arr}/2, \Omega, \Phi) d\Omega, \quad (9)$$

where Ω represents the instantaneous angular frequency of the signal, with ω_1 and ω_2 limiting the considered frequency band. We observe the transform in the middle of the array, where the analysing window has its maximal value, that is to say $\tau = 0.5\tau_{arr}$. Finally, the bearing estimation problem can be solved by working out the argument of energy maximum in the corresponding marginal distribution:

$$\varphi = \underset{\phi}{\operatorname{argmax}} \mathcal{E}_h(t, \Phi). \quad (10)$$

SEPARABILITY

The proposed method is based upon the short-time local-spatial Fourier transform. Consequently, the resolution (separability) of the method is similar to that of the transform. It depends on the number and spatial distribution of sensors, as well as the effective width of the analysing window, and especially as regards the ambiguity function. In the proposed method, a tapering window should be used as the analysing window $h(t, \tau)$. Unfortunately, this window effectively leads to array shortening and lowering in resolution within the bearing domain, compared to methods employing rectangular windows [18]. However, in the proposed method, like in other Fourier transform based methods, we can estimate the energy distributed in the joint frequency-bearing domain. Therefore, signals can be simultaneously clearly separated both in the frequency and direction of arrival. As well as this, the frequency resolution can easily be increased by extending the observation time, which is usually acceptable in passive sonar systems. This should be of assistance in separating

non-coherent sources whose frequencies are even marginally different, especially for continuously functioning sonars, engines, and propellers.

IMPLEMENTATION

The formulae: (3), (4), (5), (6), and (7) introduced in the previous section have continuous representations. Their implementation on any digital machine should provide discrete equivalents. Let us assume the following notation: the values for any discrete function of selected arguments are denoted by the appropriate symbol and adjoining square brackets containing inside them the arguments. As an example, for the time-dependent two-dimensional signal let us give

$$u[n, m] = u(t, \tau)_{t=nT_s, \tau=mY_d}, \quad (11)$$

where $T_s = 1/r_s$ is the sampling interval and $Y_d = d_\Delta/v_w$ is the propagation delay of the acoustic wave between two neighbouring hydrophones. Both, T_s and Y_d , are expressed in seconds. The discrete transform is denoted as follows:

$$U_h[n, m, k, l] = U_h(t, \tau, \omega, \varpi)_{t=nT_s, \tau=mY_d, \omega=k\Omega_\Delta, \varpi=l\Pi_\Delta} \quad (12)$$

where Ω_Δ and Π_Δ are the distances between lines (stems) to respective frequency and spatial frequency domains. $U_h[n, m, k, l]$ can be calculated by a two-dimensional FFT algorithm with zero-padding, so therefore Ω_Δ and Π_Δ may be arbitrarily presumed, also being dependent, as they are, on the number of attached zeros, as well as on the number of signal samples. In the considered method, the zero-padding can be applied in order to elongate the Fourier transform up to a power of two, regardless of the window width, simultaneously increasing the number of pixels in the final imaging. However, the application of this is not necessary. The analysing window is obtained in the following manner:

$$h[n, m] = h(t, \tau)_{t=nT_s, \tau=mY_d}, \quad (13)$$

where

$$h(t, \tau) = h_{time}(t)h_{delay}(\tau) \quad (14)$$

and both $h_{time}(t)$ and $h_{delay}(\tau)$ are the Blackman-Harris windows whose widths are dependent on the observation time and array length, respectively.

There are two discrete implementations of the reassignment which are mainly known to us: interframe and intraframe, where the frame is defined as a windowed part of the signal. Their two-dimensional adaptations are introduced below. They differ particularly in their manners of phase derivative approximation, which were defined in the previous section by Eqs. (4) and (5).

INTERFRAME IMPLEMENTATION

In the interframe approach, also referred to as the cross-spectral method [7], the below solutions are used. Three adjacent (in time and delay) frames, processed by the FFT, are employed here – the middle frame being used for energy estimation based on Eq. (8), while the previous and next frame for CIF and LSF estimations, respectively:

$$\check{\Omega}_h[n, m, k, l] = \frac{\arg U_h[n+1, m, k, l] \bar{U}_h[n-1, m, k, l]}{2T_s} \quad (15)$$

as well as:

$$\check{I}_h[n, m, k, l] = \frac{\arg U_h[n, m+1, k, l] \bar{U}_h[n, m+1, k, l]}{2Y_d}, \quad (16)$$

for $k = -K/2, \dots, -1, 0, 1, \dots, (K-1)/2$ and $l = -L/2, \dots, -1, 0, 1, \dots, (L-1)/2$, where K and L are respectively rounded upwards and downwards. K and L are the sizes of the discrete Fourier transforms.

INTRAFRAME IMPLEMENTATION

In the intraframe method, the phase derivatives are estimated in a different manner through the use of a differentiated window in the time domain [7]. In this method, samples from all available sensors can be used to form each frame, which is in contrast with the interframe, where at least elementary shifts along the array and in time are necessary in order to obtain derivatives.

In the intraframe method, three different analysing windows are required to obtain the Fourier transforms. The first window is a product of two Blackman-Harris windows, in a similar manner to Eq. (13). The second and third windows are obtained using the following formulae:

$$g(t, \tau) = \frac{\partial h(t, \tau)}{\partial t} = \frac{h_{time}(t)}{\partial t} h_{delay}(\tau) \quad (17)$$

and

$$\varrho(t, \tau) = \frac{\partial h(t, \tau)}{\partial \tau} = \frac{h_{delay}(\tau)}{\partial \tau} h_{time}(t) \quad (18)$$

Both $\partial h_{time}(t)/\partial t$ and $\partial h_{delay}(\tau)/\partial \tau$ can be calculated based upon the definition of the Blackman-Harris window. Finally, we obtain the transforms: $U_h[n, m, k, l]$, $U_g[n, m, k, l]$, and $U_\varrho[n, m, k, l]$, which are used for both CIF and LSF estimation in the following manner:

$$\hat{\Omega}_h[n, m, k, l] = \frac{2\pi k}{T_s K} - \Im \frac{U_g[n, m, k, l]}{NT_s \bar{U}_h[n, m, k, l]} \quad (19)$$

as well as:

$$\hat{I}_h[n, m, k, l] = \frac{2\pi l}{Y_d L} - \Im \frac{U_\varrho[n, m, k, l]}{MY_d \bar{U}_h[n, m, k, l]} \quad (20)$$

for $k = -K/2, \dots, -1, 0, 1, \dots, (K-1)/2$ and $l = -L/2, \dots, -1, 0, 1, \dots, (L-1)/2$, where I returns the imaginary part of the subsequent expression and N is the number of window coefficients.

COMPUTER SIMULATION

The properties and performance of the introduced method are evaluated by the peak-to-average power ratio (PAPR) [2] and the root-mean-square error (RMSE). The simulated signals are intentionally degraded by additive white Gaussian noise (AWGN). Afterwards, bearing estimation is performed in accordance with the aforementioned instructions. The difference between the estimated and assumed DOA values is measured for various levels of the signal-to-noise ratios (SNR), as well as for different assumed directions of signal arrival. Moreover, the PAPR is calculated in order to assess the sharpness of the obtained marginal energy distributions and images.

White noise is added within the whole frequency band which is limited by half of the sampling rate $r_s/2$. This process is entirely carried out by computer simulation – at least one thousand noise realizations are considered for each point of the obtained characteristics. SNR is defined as the ratio of the energy of the usable signal to total noise energy. The results are compared to conventional digital beamforming based upon the summation of accordingly delayed signals, performed within the time domain [16].

We consider an intercept sonar system with the aforementioned passive array. This system captures the following types of sounding pulses:

- pulse without frequency modulation (WFM),
- linear frequency modulated (LFM) pulse,
- hyperbolic frequency modulated (HFM) pulse.

The distance between a tracked target and the sonar is far greater than the maximal expected wavelength – the far field condition is thus satisfied. The velocity of wave propagation in the seawater is equal to 1447 m/s, which corresponds to the water temperature equal to approximately 10 °C [8]. The parameters of the received signals are detailed in the appropriate sections. We take into consideration an array which consists of sixteen hydrophones set apart from each other by nine and half centimetres, a distance connected to the frequency of the considered signals. The assumed sampling rate is fifteen kilo samples per second. Graphical results are also presented as visual comparison of the proposed method and conventional beamforming.

In the performed experiment, the introduced method is defined by the following procedure:

1. STFT calculation.
2. Energy, CIF, LSF, and DOA estimation based on STFT.
3. Composition of reassignment vectors using the DOA and CIF as orthogonal components.
4. Energy relocation according to reassignment vectors.
5. Estimation of the new energy density in the frequency-angle domain.

6. Preparation of marginal distribution of this energy in the bearing domain.
7. The argument of the global maximum of the marginal distribution being the final result.

In all variants, the global maximum can be changed to local maxima if additional signals from different directions are anticipated.

CONVENTIONAL BEAMFORMING IN TIME DOMAIN

The proposed method is compared with conventional beamforming performed in the time domain by the sum values of accordingly delayed discrete signals. The signals derived from each hydrophone are interpolated by a four-point digital filter in order to obtain fractional delay corresponding to the appropriate beam and direction [16]. Finally, we specify bearing by looking for the argument of the maximum of the directional characteristic. To this end, we use the golden section search, where the tolerance parameter is assumed equal to one hundredth degree. The resultant characteristic is averaged in such a way that the analysis covers the same parts of the signal in the two compared methods.

ANALYSIS OF WFM PULSES

A pulse without frequency modulation, also known as a mono-tone burst or finite duration impulse, is one of the simplest sounding excitations used in the sonar technique. In the simulation presented in Figure 3, we use a pulse without frequency modulation (WFM) whose constant frequency is equal to five kilohertz and duration equal to ten milliseconds. Furthermore, the Tukey window is applied in order to model the non-zero duration of the rising and falling edges. This window is applied for shaping all the considered pulses in the presented experiments.

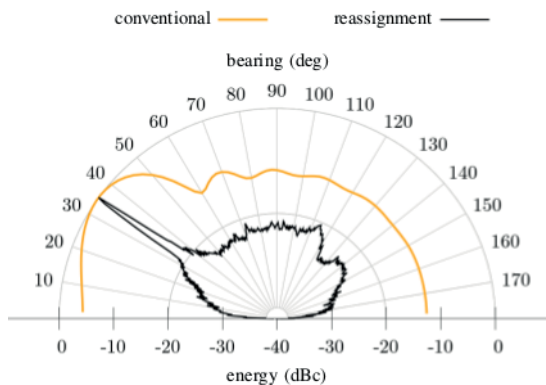


Fig. 3. Comparison of marginal energy distribution after reassignment carried out by the interframe variant (black) with the directional characteristic obtained by conventional beamforming performed in the time domain (orange). A single tone burst in the presence of AWGN is analysed. SNR is equal to approximately 0 decibels. True direction of arrival is assumed equal to 35 degrees.

ANALYSIS OF LFM PULSES

In general, the frequency modulation allows us to efficiently use the pulse compression carried out by matched filtering. However, in the considered simulation we assume that the parameters of the matched filter are unknown. Therefore, optimal pulse compression is not applied at either this, or any subsequent point. We assess the capabilities of the introduced method for LFM signal analysis. The signal parameters which were employed in this experiment are the following:

- duration – 10 ms,
- mean frequency – 5 kHz,
- frequency bandwidth – 5 kHz,
- frequency band – $2.5 \div 7.5$ kHz,

The results of this analysis are shown in Figure 4.

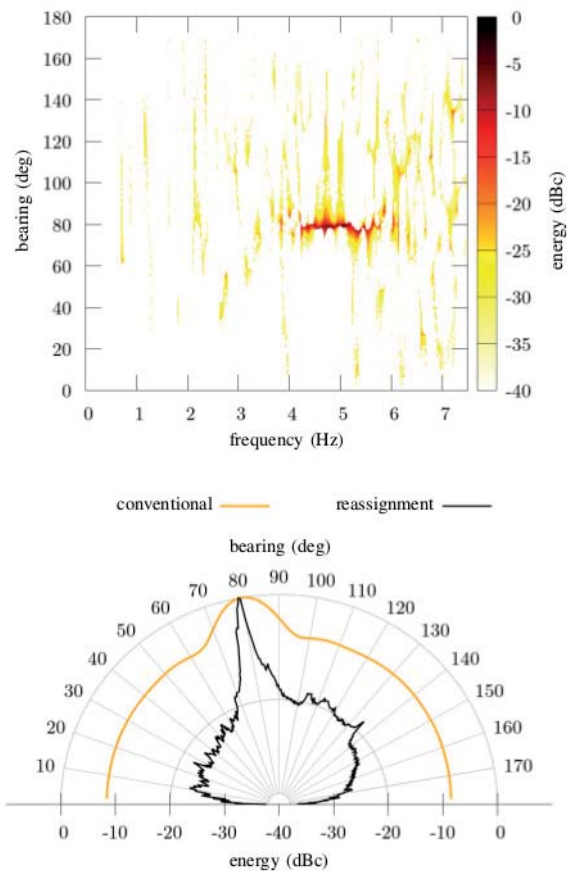


Fig. 4. Reassigned spectrogram estimated by the intraframe variant (top), and the corresponding comparison of marginal energy distributions after reassignment (black; bottom) with the directional characteristic obtained by conventional beamforming performed in the time domain (orange; bottom). A single LFM pulse in the presence of AWGN is herein analysed. SNR is equal to approximately 0 decibels. True direction of arrival is equal to 80 degrees.

ANALYSIS OF HFM PULSES

Hyperbolic frequency modulation is also known as logarithmic phase modulation and linear period modulation. This technique is widely used in wideband active sonars designed for minimizing the degradation caused by Doppler shifting of the return signal, in the instance when the

source and target are in relative motion [17]. In the present simulation, we assumed the same parameters as for the LFM signals considered in Section 5.3. The results of the analysis of this signal are presented in Figure 5.

MULTICOMPONENT SIGNALS

Signal separability is especially important when a number of unknown targets on similar directions have to be detected and specified. In general, conventional beamforming has superior separability in the bearing domain, because a rectangular window is used in this method. However, in some situations the here introduced method can give better results, compared to conventional beamforming, on the condition that no additional selective filtering is applied. This is possible because we base upon separation in the joint frequency-bearing domain. This situation is presented in Figure 6, in which the constant frequency pulse is added as the interfering signal to the LFM pulse. The signals under consideration slightly overlap in the frequency domain. However, both signals are clearly separated by the proposed method and both directions of arrival can be estimated, which is in contrast to the conventional method. The LFM pulse has the same parameters as in Section 5.3. The frequency of the WFM pulse is equal to three and half kilohertz.

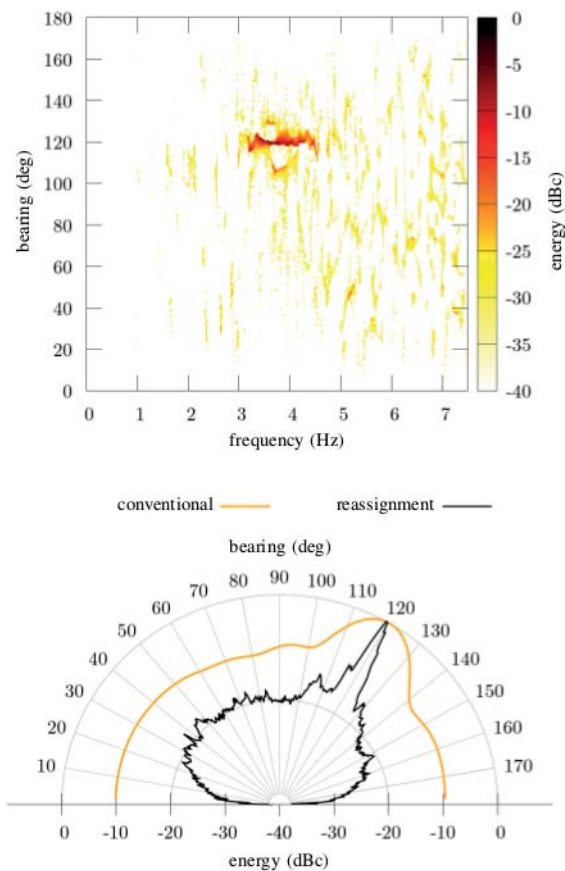


Fig. 5. Reassigned spectrogram estimated by the interframe variant (top), and the corresponding comparison of marginal energy distributions after reassignment (black; bottom) with the directional characteristic obtained by conventional beamforming performed in the time domain (orange; bottom). A single HFM pulse in the presence of AWGN is herein analysed. SNR is equal to approximately 0 decibels. True direction of arrival is equal to 120 degrees.

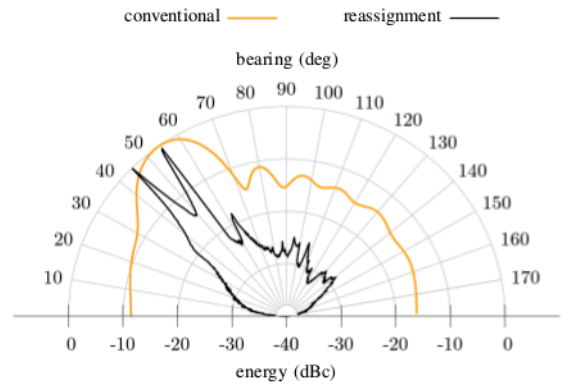


Figure 6. Comparison of marginal energy distributions after reassignment (black) with the directional characteristic obtained by conventional beamforming performed in the time domain (orange). LFM and WFM pulses in the presence of AWGN are herein analysed. SNR is equal to approximately six decibels. True directions of signal arrival are equal to 45 and 55 degrees, respectively.

CREST FACTOR

The peak-to-average power ratio is also referred to as the crest factor, or peak factor. In the considered context, the crest factor is used to assess the sharpness of the obtained distributions and imaging [2]. A high level of this factor is interpreted as constituting either high contrast in the usable signal representation in final imaging, or a clear peak in marginal distribution in the bearing domain. In this experiment, the results of which are shown in Figure 7, as well as in Tables 1 and 2, all three kinds of pulses (WFM, LFM, and HFM) were considered for different directions of arrival, window widths, and SNR levels. In addition, the crest factor can be utilized to find the optimal width of the analysing window in the time domain. The optimal absolute window width is equal to approximately five thousandths of a second for the LFM and HFM pulses, and about two times greater for the WFM pulse. This value corresponds to the duration of the analysed pulses. In general, the optimal window width may vary for different signals and varying parameters. The results in Tables 1 and 2 were obtained for the analysing window whose width is equal to five thousandths of a second, which is close to the optimal value for LFM and HFM pulses. In such a situation, signal parameters are the same as those reported in Sections 5.3 and 5.4. In all rows of these tables, the achieved crest factors are higher for the proposed method based upon reassignment than for conventional beamforming.

Table 1. Crest factor obtained for reassignment and conventional beamforming for selected DOA and for SNR \approx -6 decibels

pulse type	DOA degrees	PAPR	
		conventional dB	reassignment dB
WFM	45	2.362	14.076
LFM	45	3.319	12.828
HFM	45	4.317	12.094
WFM	75	2.449	14.525
LFM	75	3.518	13.471
HFM	75	4.655	12.858

pulse type	DOA degrees	PAPR	
		conventional dB	reassignment dB
WFM	90	2.502	14.669
LFM	90	3.579	13.923
HFM	90	4.699	13.112

Tab 2. Crest factor obtained for reassignment and conventional method for DOA = 75 degrees and for selected SNR levels

pulse type	SNR dB	PAPR	
		conventional dB	reassignment dB
WFM	-5.3	2.667	14.728
WFM	5.8	8.738	21.977
LFM	-5.3	3.503	13.145
LFM	5.8	8.953	20.626
HFM	-5.3	4.991	12.759
HFM	5.8	9.28	20.227

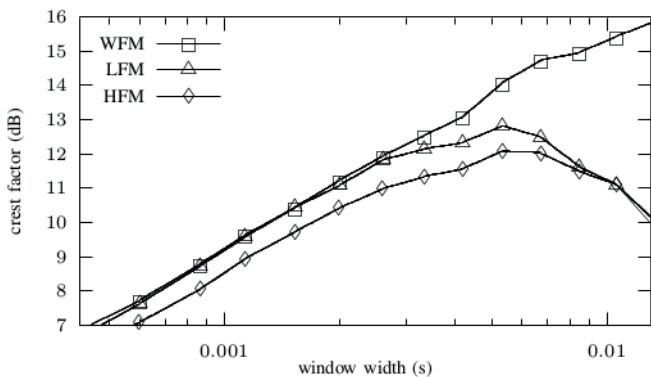


Fig. 7. Comparison of crest factor as a function of absolute window width for WFM, LFM and HFM pulses. Crest factor is calculated for the marginal energy distribution in the presence of noise. SNR is equal to approximately minus six decibels. True direction of arrival is assumed equal to forty-five degrees.

ROOT MEAN SQUARE ERROR

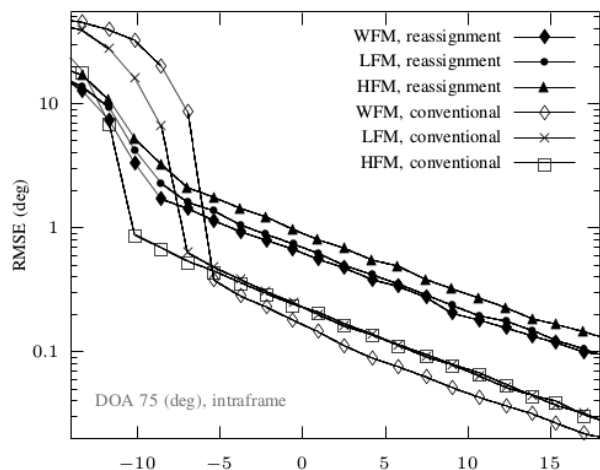
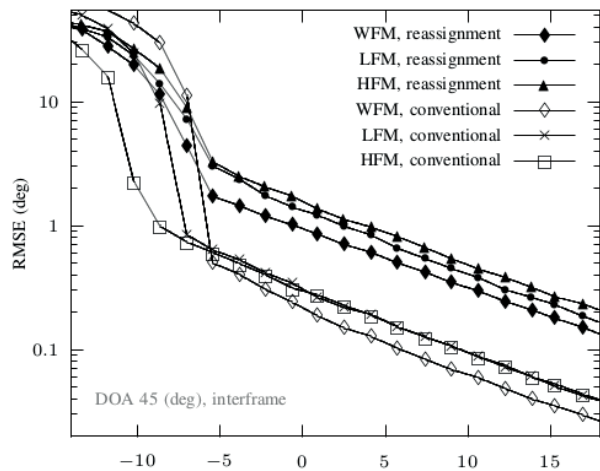
The root mean square error is estimated in order to evaluate the accuracy of the introduced method. The RMSE curves as functions of the signal-to-noise ratio are presented in Figure 8. The simulations were performed for three directions (45, 75, and 90 degrees) and three considered pulses (WFM, LFM, and HFM). The used window had the optimal width being equal to approximately five thousandths of a second, which was estimated in the previous section. In all considered situations, the introduced method has significantly worse accuracy than conventional beamforming, which is its serious drawback. Table 3 collates errors for inter- and intraframe implementations. The DOA is assumed equal to seventy five degrees, and SNR is equal to approximately minus half decibels. The results indicate that the intraframe variant is slightly better.

Tab. 3. Root mean square errors obtained for interframe and intraframe for selected simulation parameters

pulse type	DOA degrees	SNR dB	RMSE	
			interframe degrees	intraframe degrees
WFM	75	-0.5	0.717	0.677
LFM	75	-0.5	1.017	0.742
HFM	75	-0.5	1.175	0.973

DISCUSSION

The performed experiments demonstrate high sensitivity of the introduced method to the influence of noise. The conventional beamformer is significantly superior in this regard. There are two main reasons for this. Namely, the use of the analysing tapering window causes a decrease in the effective length of the array and reduces the final resolution. Therefore, a uniformly distributed AWGN has a greater impact. Unfortunately, it is not recommended to omit the use of the window. Secondly, both CIF and LSF, as well as the STFT energy of different signals derived from different non-coherent sources, in accordance with the Heisenberg-Gabor limit, cannot be completely independent in the considered domain. This is a well-known problem as regards the time-frequency analysis, which is related to the ambiguity function and the choice of the analysing window.



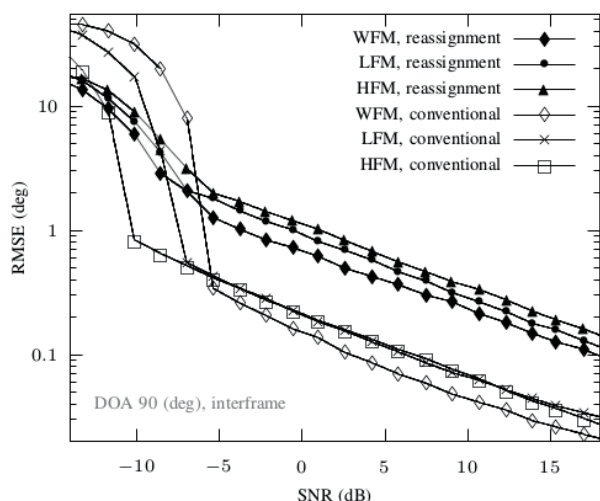


Fig. 8: Comparison of the root mean square error as a function of SNR for both conventional and reassignment methods in the presence of AWGN. True directions of arrival are assumed equal to 45, 75, and 90 degrees, respectively. The interframe and intraframe variants are tested.

On the other hand, in some situations (see for example Fig. 6), the introduced method yields superior results in the separation of two (or more) signals whose frequency bands partially overlap. This is achieved by simultaneous analysis in the joint frequency-bearing domain, while a conventional beamformer only provides separation in the bearing domain. Similar results are also possible for the conventional solution through additional band filtering performed in the time domain. However, this involves complication of the algorithm.

The presented method can be useful especially in passive sonar monitoring to estimate signal parameters, which can be subsequently used for further analysis or processing. Signals which can be analysed in this manner include also noise generated by ships. Comparing the conditions reported in [23], [24] to the results presented in Figure 8 gives us a considerable chance that the method can also be applied online for monitoring coastal waters of the Baltic Sea [25]. This is all the more so that we can find the information in scientific literature about the use of a linear array in the shallow water [20]. We are going to continue our research in this area.

CONCLUSION

The paper demonstrates the possibility of using two-dimensional (double frequency) reassignment for bearing estimation. The reassignment is based upon the Fourier transform and is carried out in the joint frequency-bearing domain, which enables to obtain highly concentrated energy distributions, as well as clear and sharp imaging. We have used the crest factor in order to assess this concentration. The results were compared to conventional beamforming performed in the time domain. In all the experiments, the crest factor is significantly higher than that for the conventional method. This confirms that the resultant images generated by the introduced method are sharper and more clear. The

crest factor was also used to find the optimal width of the analysing window, which is related to parameters of pulses under consideration. In sonar and radar techniques, a high crest factor after pulse compression is usually required to ensure good quality detection [2], [13].

Two implementations of reassignment were examined, which were the interframe and the intraframe. They originate from the time-frequency reassignment and provide very similar results, however the intraframe variant turned out slightly better, as a result of the fact that all sensors were used in calculations of every single Fourier transform. This is in contrast to the interframe, which utilizes at least one less sensor, since elementary shift along the array is necessary in order to estimate the phase derivative. As a result of this, the effective length of the array is fractionally shorter – approximately six percent for sixteen hydrophones.

The introduced method has been regarded as being both fast and efficient, due to the fact that its implementation is based upon a two-dimensional FFT algorithm [22]. The analysis in the frequency and bearing domains was conducted in a single-phase, which may also increase the computing performance in comparison with two-stage processing which includes conventional time and spatial filtering.

ACKNOWLEDGMENT

The authors would like to thank Dr. Mirosław Rojewski and Prof. Roman Salamon for their suggestions and discussion on this topic.

REFERENCES

1. F. Auger, P. Flandrin, Yu-Ting Lin, S. McLaughlin, S. Meignen, T. Oberlin, Hau-Tieng Wu, "Time-frequency reassignment and synchrosqueezing: an overview", *IEEE Signal Proc. Mag.*, vol. 30, no. 6, pp. 32–41, 2013.
2. J.S. Byrnes, "Quadrature Mirror Filters, Low Crest Factor Arrays, Functions Achieving Optimal Uncertainty Principle Bounds, and Complete Orthonormal Sequences – A Unified Approach", *Applied and Computational Harmonic Analysis*, vol. 1, no. 3, pp. 261–266, 1994.
3. Z. Chen, J. Sun, H. Hou, "Phase difference method for DOA estimation", *J. of Marine Science and Application*, vol. 9, no.4, pp.445–450, 2010.
4. C. Chi, Z. Li, Q. Li, "Fast broadband beamforming using nonuniform Fast Fourier Transform for underwater real-time 3-d acoustical imaging", *IEEE J. Ocean. Eng.*, vol.41, no.2, pp.249–246, 2016.
5. K. Czarnecki, "The instantaneous frequency rate spectrogram", *Mech. Syst. Signal Process.*, vol. 66–67, pp.361–373, 2016.

6. K. Czarnecki, W. Leśniak, "The synchrosqueezing method in the bearing estimation of stationary signals for a passive sonar system with a towed array", *Hydroacoustics*, vol. 18, pp. 41–46, 2015.
7. S.A. Fulop, K. Fitz, "Algorithms for computing the time-corrected instantaneous frequency (reassigned) spectrogram, with applications", *J. Acoust. Soc. Amer. (JASA)*, vol. 119, no. 1, pp.360–371, 2006.
8. V.A. Del Grosso, "Tables of the speed of sound in open ocean water (with Mediterranean Sea and Red Sea applicability)", *J. Acoust. Soc. Amer. (JASA)*, vol.53, no.5, pp.1384–1401, 1973.
9. S. Haykin, *Radar array processing for angle of arrival estimation in Array Signal Processing*, pp. 149–292, Prentice-Hall, 1985.
10. L.B. Jackson, H. Chien, "Frequency and bearing estimation by two-dimensional linear prediction", *proc. IEEE International Conference on Acoustics, Speech, and Signal Processing*, vol. 4, pp. 665–668, 1979.
11. K. Kodera, C.D. Villedary, R. Gendrin, "A new method for the numerical analysis of non-stationary signals", *Phys. Earth Planet. In.*, vol.12, pp.142–150, 1976.
12. H. Krim, M. Viberg, "Two decades of array signal processing research", *IEEE Signal Proc. Mag.*, vol. 13, no. 4, pp.67–94, 1996.
13. A. De Maio, Y. Huang, M. Piezzo, S. Zhang, A. Farina, "Design of Optimized Radar Codes with a Peak to Average Power Ratio Constraint", *IEEE Tran. Signal Process.*, vol. 59, no. 6, pp. 2683–2697, 2011.
14. J. Marszał, *Digital signal processing applied to the modernization of Polish Navy sonars*, *Polish Maritime Research*, vol. 21, no. 2, pp. 65–75, 2014.
15. B. Maranda, "Efficient digital beamforming in the frequency domain", *J. Acoust. Soc. Amer.*, vol. 86, no. 5, pp. 1813–1819, 1989.
16. R.G. Pridham, R.A. Mucci, "Digital interpolation beamforming for low-pass and bandpass signals", in *Proceedings of the IEEE*, vol. 67, no. 6, pp. 904–919, 1979.
17. M. Readhead, *Calculations of the sound scattering of hyperbolic frequency modulated chirped pulses from fluid-filled spherical shell sonar targets*, technical note, Maritime Operations Division, Defence Science and Technology Organisation, Australia, 2010.
18. P. Rudnick, "Digital Beamforming in the Frequency Domain", *J. Acoust. Soc. Amer.*, vol. 46, no. 5, pp. 1089–1090, 1969.
19. H. Slabbekoorn, N. Bouton, I. Van Opzeeland, A. Coers, C. ten Cate, A.N. Popper, "A noisy spring: the impact of globally rising underwater sound levels on fish", *Trends in Ecology & Evolution*, vol. 25, no. 7, pp. 419–427, 2010.
20. W. Szymczak, E. Kozaczka, G. Grelowska, I. Gloza, and S. Kozaczka, "The shallow sea experiment with usage of linear hydrophone array", *The Journal of the Acoustical Society of America*, vol. 133, no. 5, pp. 3439–3439, 2013.
21. E. Tuncer, B. Friedlander, *Classical and Modern Direction of Arrival Estimation*, Elsevier, Burlington, MA, 2009
22. J.R. Williams, "Fast beam-forming algorithm", *J. Acoust. Soc. Amer. (JASA)*, vol. 44, no. 5, pp. 1454–1455, 1968.
23. G. Grelowska, E. Kozaczka, S. Kozaczka, W. Szymczak, "Underwater Noise Generated by a Small Ship in the Shallow Sea", *Archives of Acoustics*, vol. 39, no. 3, pp. 351–356, 2013.
24. G. Grelowska, "Study of seasonal acoustic properties of sea water in selected waters of the southern Baltic", *Polish Maritime Research*, vol. 23, no. 1, pp. 25–30, 2016.
25. G. Grelowska, E. Kozaczka, S. Kozaczka, W. Szymczak, "Gdansk Bay sea bed sounding and classification of its results", *Polish Maritime Research*, vol. 20, no. 3, pp. 45–50, 2013.

CONTACT WITH THE AUTHORS

Krzysztof Czarnecki

e-mail: krzycz@eti.pg.gda.pl

Gdansk University of Technology, Narutowicza 11/12,
80-233 Gdańsk

POLAND

Wojciech Lesniak

e-mail: wojlesni1@pg.edu.pl

Gdansk University of Technology, Narutowicza 11/12,
80-233 Gdańsk

POLAND

APPLICATION OF AN AUTONOMOUS/UNMANNED SURVEY VESSEL (ASV/USV) IN BATHYMETRIC MEASUREMENTS

Cezary Specht
Emilian Świtalski
Mariusz Specht
Gdynia Maritime University, Poland

ABSTRACT

The accuracy of bathymetric maps, especially in the coastal zone, is very important from the point of view of safety of navigation and transport. Due to the continuous change in shape of the seabed, these maps are fast becoming outdated for precise navigation. Therefore, it is necessary to perform periodical bathymetric measurements to keep them updated on a current basis. At present, none of the institutions in Poland (maritime offices, Hydrographic Office of the Polish Navy) which are responsible for implementation of this type of measurements has at their disposal a hydrographic vessel capable of carrying out measurements for shallow waters (at depths below 1 m). This results in emergence of large areas for which no measurement data have been obtained and, consequently, the maps in the coastal zones are rather unreliable.

The article presents the concept of bathymetric measurements for shallow waters with the use of an autonomous, unmanned survey vessel (ASV/USV). For this purpose, the authors modernized a typical ASV/USV unit with standard radio remote control system to the fully autonomous mode. As part of the modernization, the route planning software was created. The developed software works based on, alternatively, GNSS measurements of the coastline, or satellite images. The system was supplemented by an own autopilot (adapted for flying drones). Moreover, the method of controlling electric motors was changed thanks to the use of own electronic circuit.

The modernized ASV/USV measuring system was verified by performing bathymetric measurements of the retention reservoir in Gdansk, Poland. Then, the obtained measurement data were used to create a digital bottom model and a bathymetric map of the reservoir.

Keywords: autonomous, unmanned survey vessel (ASV/USV), bathymetric measurements, digital sea bottom model, bathymetric map

INTRODUCTION

The beginning of the 21st century is the era of using unmanned boats in various measurement applications [22, 27, 29]. Modern autonomous and unmanned vessels (*Autonomous Surface Vehicle* – ASV, *Unmanned Surface Vehicle* – USV) offer a variety of design solutions in the construction of the hull and the boat propulsion: single hull, double hull with a screw or screwless propulsion with a small draft. They allow the entry into the reservoir with difficult access caused by the presence of shallow waters [22]. Bathymetric surveys being part of hydrographic measurements which aim at measuring the seabed topography require adequate positioning accuracy [7, 9], hence the use of unmanned boats in hydrography can now be regarded as the beginning of a new era in this field.

Depending on the size and displacement of the unmanned vessel, its equipment is of vital importance (in particular echo sounder transducers of single and multibeam type). Single beam echo sounders, which can be used here, are small devices that usually do not require Motion Reference Units (MRU) to determine the spatial orientation. Hence, they can be mounted on smaller vessels [12]. Whereas multibeam echo sounders are placed on larger survey vessels [14].

An example of an unmanned hydrographic vessel may be a hydrographic survey drone. Its main advantage is small draft, even when loaded with the echo sounder transducer (20-30 cm). This allows to perform not only accurate maps of inland waters (including depths below 1 m), but also to determine the course of the territorial sea baseline, which in the case of e.g. Poland is usually located at a depth of tens

of centimetres below the temporary sea level. Previously, the use of manned hydrographic vessels rendered it impossible to perform that type of measurements due to large draft of boats (0.6-3.3 m) and placing echo sounder transducers on their bows [25, 26]. It resulted in damage to the measuring equipment and the emergence of large areas for which no measurement data were obtained (bathymetric maps in the coastal zone were unreliable due to the effect of linear interpolation between the coastline and the measurements carried out to the 1m contour line) [12]. Therefore, it seems reasonable to make detailed bathymetric measurements for shallow waters to ensure the safety of navigation and transport on these waters [6, 30].

AUTONOMOUS CONTROL OF THE UNMANNED SURVEY VESSEL

The hydrographic survey drone of the Seafloor company required some significant changes to allow for installation of a system ensuring its autonomy. Initially, each of the floats had its own gel battery, along with an RC receiver, a brushless motor propelling the screw, and the Electronic Speed Control (ESC). The output signals from the receiver were inputs for the ESC. Consequently, each of the floats was an independent system, which prevented the introduction of autonomous control. It was therefore decided to change the structure of the electrical connections in the drone (Fig. 1).

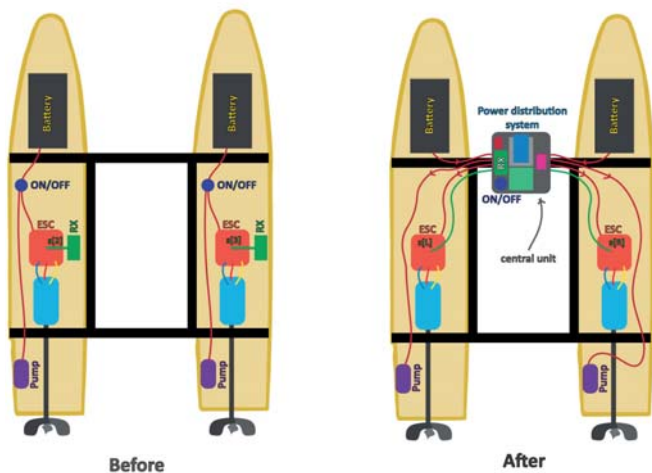


Fig. 1. Differences in electrical connection systems inside the drone (own study)

The designed power distribution system (Figs. 2 and 3) makes it possible to connect 2 gel batteries (terminals + 12V IN), the main power switch (terminals Switch), the power output, as well as peripherals and outputs, enabling it to apply smooth power control or completely shut off the pumps (terminals Channel 1 OUT and Channel 2 OUT). The implemented power distribution system far exceeds the functionality of the original solution by introducing the main power switch for the entire system, which increases power control capabilities and, above all, the possibilities of control

implementation where the work of motors is correlated. The peripherals are powered from a single point, which is beneficial to the distribution of power of the batteries and to the stability of the entire power system.

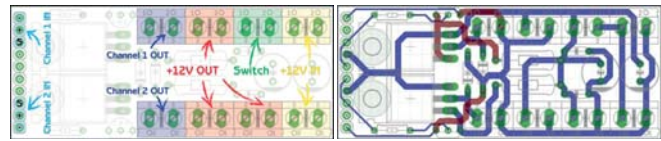


Fig. 2. Connections (left) and paths (right) in the power distribution system (own study)

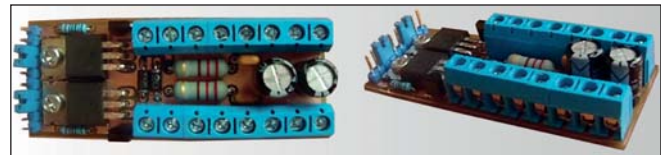


Fig. 3. Power distribution system (own study)

In order to ensure the autonomy of the vessel it was decided to use the Pixhawk autopilot of the 3DR company. For the autopilot to begin sending any signals at the control outputs, all of its components (accelerometer, compass) had to be configured, all peripherals (radio module, GPS receiver) had to be connected, and all security functions related to arming the motors had to be disabled. The mode which seems to be the most optimal for the drone is a „rover” – that is like a car with one engine and a steering axle. However, with 2 engines that proved impossible (due to the lack of a rudder blade). Thus, the authors were forced to build a mixer of control signals which collects power and twist signals, and then, based on these signals, prepares signals for both engines to obtain the desired effect.

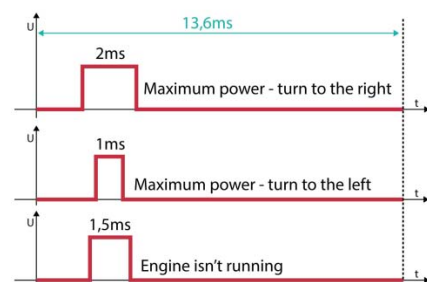


Fig. 4. Interpretation of PPM signals used by ESC (own study)

Most autopilots operate with Pulse Position Modulation (PPM) signals. In the case of service by one channel we are only interested in their width. The pulses may have a width of 1 to 2 ms. 1.5 ms is an average value that in the applied system corresponds with idle (unmoving) screws. At 1 and 2 ms the engines operate at maximum power, but in the opposite direction. The selected autopilot generates signals with a period of 20 ms, while the ESC units work properly for signals with a period of 13.6 ms. Thus, the mixer of control signals must also change their frequency.

The ATmega8 microcontroller was used in the construction of the device, as it is cheap and fully sufficient for the realization of the planned task. A quartz crystal resonator 20 Mhz was used as the clock signal source, while the TIMER2 counter and two external interrupts INT0 and INT1 were used to detect the incoming signals. The following code shows the activation of selected peripherals.

```
int main(void) { ...
MCUCR |= (1<<ISC10)|(1<<ISC00); // interrupt by activating
logic state change
GICR |= (1<<INT1)|(1<<INT0); // activation INT0 and INT1
interrupts
TCCR2 |= (1<<CS22)|(1<<CS20); // activation TIMER2 counter
and setting prescaler at 128
... }
```

Setting the prescaler at 128 causes that a change by 1 in the TCNT2 register occurs at $t_d = 6.4 \mu s$. This makes it possible to measure the time at the t_d accuracy. TIMER2 is an 8-bit register. Therefore, one can measure the time with the difference $t_r = 1.64 ms$. This allows measuring the times of 1 to 2 ms. Below the authors present the support for external interrupts.

```
ISR(INT0_vect) { // support for INT0 interrupt
if (!(PIND & (1<<2))) { take[0] = TCNT2; } // if 0
if (PIND & (1<<2)) { TCNT2 = 176; GICR |= (1<<INTF1)|(1<<INTF0);
} // if 1
ISR(INT1_vect) { // support for INT1 interrupt
if (!(PIND & (1<<3))) { take[1] = TCNT2; } // if 0
if (PIND & (1<<3)) { TCNT2 = 176; GICR |= (1<<INTF1)|(1<<INTF0);
} // if 1
}
```

Here, use is made of the fact that signals start at the same time. The occurrence of the signals is indicated by the appearance of 1 at the inputs. This results in setting the TCNT2 register to 176 and zeroing the interrupt flags so that the second interrupt is not implemented before the TIMER1 adds up to 256 – when it passes the value of $t_0 = 0.512 ms$. When zero occurs at one of the channels, then the current value of the TCNT2 register, which contains full information on the pulse duration, is stored.

Output signals were generated using the TIMER1 counter in PWM operational mode, as its use allows to generate a PPM signal. To activate the PWM the previously written library was used:

```
#include "pwm/pwm.h" ...
int main(void) { ...
PWM_Init(); // using library
... }
```

with parameters loaded at the pwm.h header file:

```
#define PS_PWM 8 // PWM prescaler counter = 8
#define ROZ_PWM 17000 // PWM resolution counter = 17000
#define COM_PWM 1 // filling „ones”
#define ON_PWM outAB // activation OC1A and OC1B
```

The period of the output pulse amounts to $T = 13.6 ms$, which it is exactly what the ESC unit expects. Along with the change of the values of OCR1A and OCR1B registers from 1250 to 2500, the pulse width can vary from 1 to 2 ms.

Before they get to the output, the measured values have to be subjected to appropriate correction, needed when changing an autopilot/telem manipulator. The microcontroller should keep these corrections in the EEPROM memory, and the signals need to be properly mixed and optionally filtered.

ESC units cannot receive signals immediately after the supply of power, so the mixer of control signals waits a few seconds before it starts sending pulses. This device was designed in the Eagle software (Fig. 5a) and physically built (Fig. 5b).

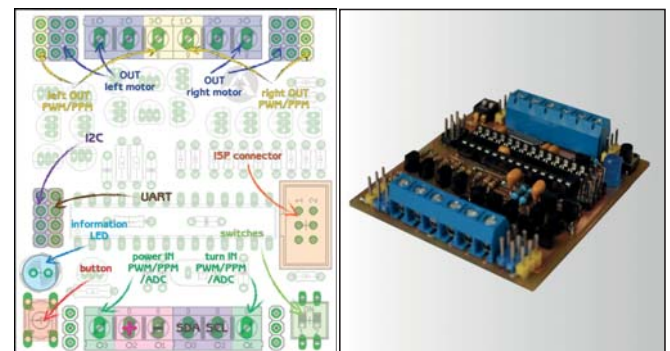


Fig. 5. Outputs (left) and view (right) of the mixer of control signals. (own study)

Both the input and output signals can be different. This fact was taken into account during the design process and the plate is equipped with appropriate infrastructure.

The last built device was a remote switch. Along with the transistorized channels, the switch is used to remotely control the operation of the cooling pumps. It operates as a mixer of control signals, but differs from the mixer in that it uses an ATtiny13A microcontroller and an internal RC resonator 9.6 MHz, and is much simpler. It receives the signal using the INT0 interrupt, but the output signal is an ordinary PWM with a width from 0 to 255. In the programme, the input value (take) is appropriately scaled, limited, and entered in the OCR0A register.

```
while (1) {
power = take;
power *= 2; power += 110; // scaling
if (power < 205) { power = 0; Led_OFF; }
else if (power > 255) { power = 255; Led_ON; }
else { Led_ON; } // limiting
OCR0A = power; }
```

All devices have been properly interconnected and closed in a casing with glands. The RC receiver passed channels 1 to 5 to the PPM encoder, which then prepared the resulting signal and passed it to the autopilot. Channel 5 was used to switching from manual to automatic mode. Depending on the mode, the autopilot passed signals 1, 3 based on the position of analogue sticks in the telemanipulator, or on the GPS signal. These signals were taken by the mixer of control signals, which generated pulses for the ESC. At the same time Channel 6 of the RC receiver wandered to the remote switch, the output of which was connected to the transistorized channels switching on and off the cooling pumps (Fig. 6).

ROUTE PLANNING SOFTWARE

In order to determine the drone route, the software for planning the measurement campaign was created in PHP language. The application requires entering: the coordinates of the selection area, the drone position, the coordinates of the directional point, and the distance between the measurement profiles. Based on the drone position and the coordinates of the directional point the direction vector is calculated. Then the entered coordinates are transformed from the geographic coordinate system to the local cartesian coordinate system (with drone position as the origin), which are in turn converted to the polar coordinate system.

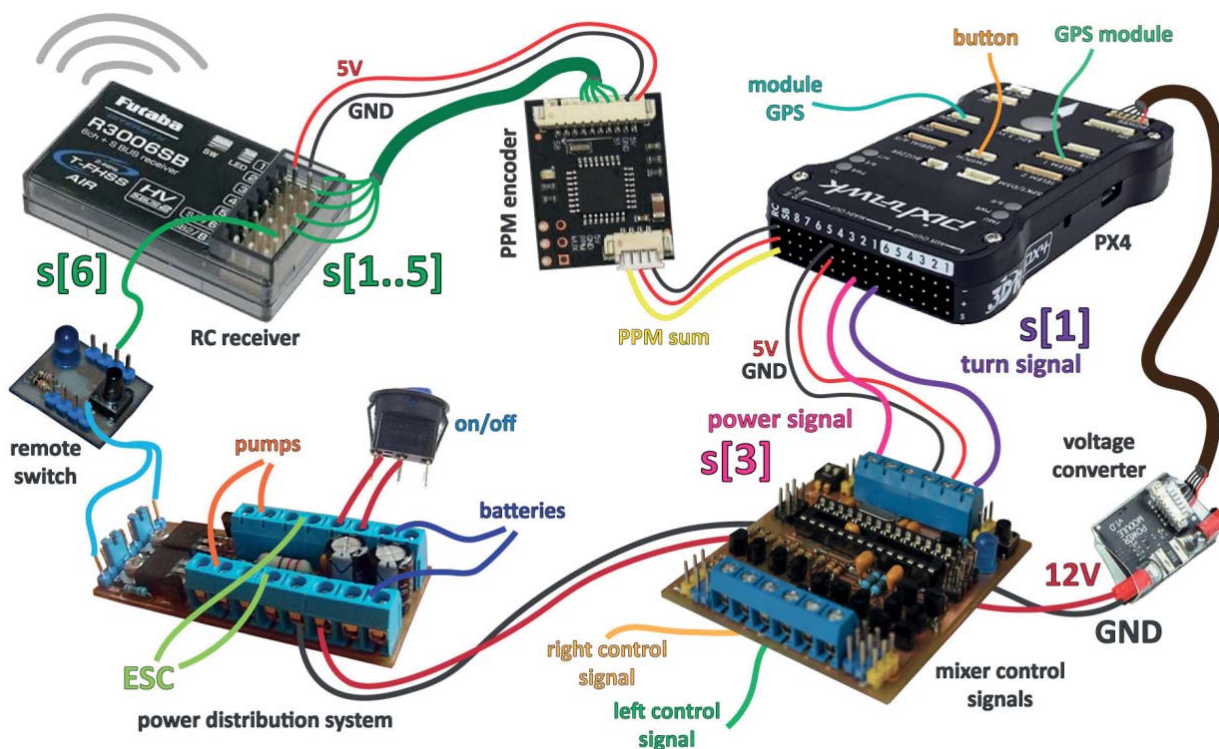


Fig. 6. Schematic diagram of connections in the central unit (own study)

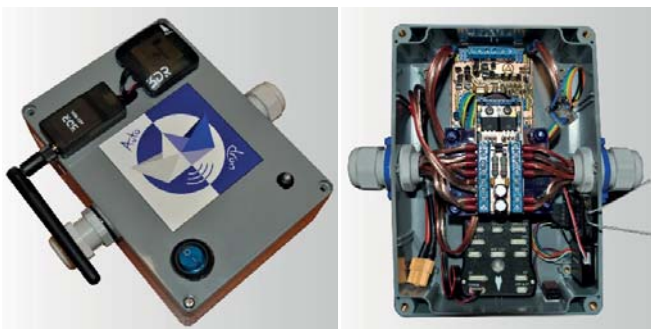


Fig. 7. Central unit (own study)

All points are rotated with respect to the direction vector, that is, the angle formed by that vector with the OX axis is subtracted from each point in the polar system. Then the coordinates are transformed back to the cartesian system. In the system prepared in that way, the coordinates of profile points composing the drone route that are perpendicular to the direction vector are calculated. When this is completed, all operations are carried out in the reverse order until the route in the geographical system is obtained (Fig. 8). The resulting data are prepared in the format suitable for the Mission Planner software of the 3DR company (used to upload the drone route in the autopilot) [25].

coordinate system 2000 [15], the height system Kronstadt 86 [28], and the quasigeoid model PL-geoid-2011 [8].

Country	Poland
System/zone	2000/18
Reference ellipsoid	WGS 84
Ellipsoid semi-major axis	6378137
Ellipsoid flattening	0.00335281067183
Projection	Gauss-Krüger
Latitude of origin	0
Central meridian	18
False Northing	0
False Easting	6 500 000
Scale factor	0.999923
Azimuth	North
Grid orientation	Rising northeast
Transformation of elevation	Geoid
Geoid model	PL-geoid-2011
Reference system	Kronstad

Fig. 10. Report on data processing during measurements of the coastline of the retention reservoir in Gdansk (own study)

The processed measurement data determined the coastline of the artificial water reservoir (Fig. 11). As illustrated in the figure, the outline of the measured retention reservoir does not coincide with that observed in the satellite photo (provided by the Google Earth Pro platform), which was taken on April 11, 2016, by the Landsat 8 satellite under the program for acquisition of satellite imagery of Earth (Landsat). It is noteworthy that the outlines of the reservoir overlap almost entirely, except for the viewing pier which, as seen in Fig. 11, is clearly shifted. The reason for this may be the fact that it is a floating pier so its position can change. What is interesting, at the corner points of the satellite photo of the pier there are steel piles designed to stabilize the floating structure. Therefore, it is almost certain that the pier in the past few months had been deliberately shifted and the satellite images are highly accurate [13]. Such a situation can lead to the damage of the autonomous survey vessel (drone) that uses the route planning software based on satellite images from Google. The only solution to this problem is the most frequent update of satellite images.



Fig. 11. Staking out the coastline point (left) and the coastline of the retention reservoir, measured and obtained from the Google Earth Pro platform (right) (own study).

The results of the research of August 8, 2016, were taken into account when planning the drone route during the next measurement campaign on September 3, 2016. Its objective was to create a digital bottom model based on triangle mesh (Fig. 12) and bathymetric (contour) map of the retention reservoir (Fig. 13). In less than two hours the drone measured 2222 points in autonomous/hand mode. Then the measurement data were processed in the TBC software, using the same parameters as in Fig. 10.

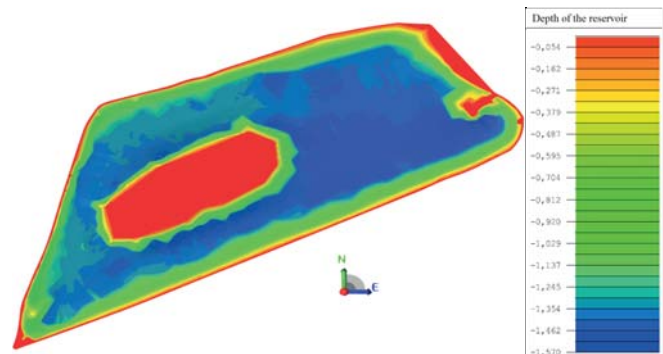


Fig. 12. Digital bottom model of the retention reservoir in Gdansk (own study)

The area of the reservoir is 1.17 ha, the length is 525 m, and the maximum depth is 1.57 m. It is characterized by a steep shore (at a distance of 4-8 meters from the coastline there is a sudden drop in depth to the 1.4 m contour line) and a flat bottom (almost the entire area of the reservoir lies at the depth of 1.4-1.57 m) (Figs. 12 and 13). It is noteworthy that in Figs. 13 and 14 the contour lines are placed at every 10 cm (within the range of 0-1.5 m).

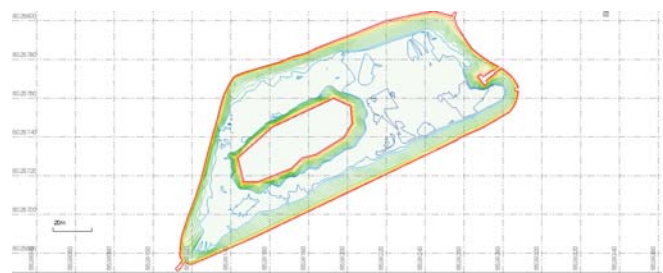


Fig. 13. Bathymetric (contour) map of the retention reservoir in Gdansk in the 2000 system (own study)

Because isometric illustration using the Google platform is widely used today, hence the obtained results were exported to .kmz format, which allows the presentation of the results from the application of this platform.



Fig. 14. Isometric projection of the retention reservoir in Gdansk with the marked coastline and contour lines (own study)

CONCLUSIONS

When modernising the survey vessel and performing bathymetric measurements, the authors encountered a number of difficulties. The applied autopilot was not designed to work in water environment which led to the rounding of measurement profiles. An additional impact here was the inaccurate GPS position (a several-meter error) obtained from the module dedicated to the Pixhawk autopilot. Therefore, in future works the authors intend to change the autopilot and connect it to the GNSS geodetic receiver. It also turned out that the hydrographic drone weighing approx. 20 kg (including the measuring equipment) is characterized by low seakeeping. Consequently, the time of measurements and hydrometeorological conditions played an important role, hence the measurements were carried out in calm weather with little waving. In addition, when planning a further measurement campaign, use will have to be made of most recent satellite images because, as shown by experience gained from the implementation of the project, situations can occur which will lead to the damage of the autonomous survey vessel.

In terms of measuring, the document regulating the conduct of hydrographic surveys is the IHO S-44 standard [7]. This document does not, however, define the method for determining the shape of the bottom of an inland reservoir and does not assign minimum accuracy requirements for this type of measurements. Nevertheless, the accuracy of the proposed solution (bathymetric measurements implemented using a single beam echo sounder and GNSS geodetic networks) can be considered entirely satisfactory [17, 18]. It is noteworthy here that, at present, none of the respective institutions in Poland (maritime offices, Hydrographic Office of the Polish Navy) has a hydrographic vessel capable of carrying out bathymetric measurements for shallow waters (at depths below 1 m).

ACKNOWLEDGEMENTS

This scientific work was financed from the budget for science in years: 2016-2020, as a research project within the frameworks of the „Diamond Grant” programme.

REFERENCES

1. Bakuła M., Przestrzelski P. (2013), Technology of Reliable RTK GPS/GLONASS Positioning, *Geodesic Review*, No. 7, pp. 3-9 (in Polish).
2. Bakuła M., Przestrzelski P., Kaźmierczak R. (2015), Reliable Technology of Centimeter GPS/GLONASS Surveying in Forest Environments, *IEEE Transactions on Geoscience and Remote Sensing*, Vol. 53(2), pp. 1029-1038.
3. Ćwiąkała P., Gabryszuk J., Krawczyk K., Krzyżek R., Leń P., Oleniacz G., Puniach E., Siejka Z., Wójcik-Leń J. (2015), *GNSS Technology and Its Application in Setting Out Surveys and Monitoring*, Rzeszów School of Engineering and Economics Publishing House, Rzeszów (in Polish).
4. Deakin R. E., Hunter M. N., Karney C. F. F. (2010), The Gauss-Krüger Projection, *Proceedings of the 23rd Victorian Regional Survey Conference*, Warrnambool.
5. Elliot W. (2014), *Programming AVR Microcontrollers for Practitioners*, Helion Publishing House, Gliwice (in Polish).
6. Guze S., Neumann T., Wilczyński P. (2017), Multi-Criteria Optimization of Liquid Cargo Transport According to Linguistic Approach to the Route Selection Task, *Polish Maritime Research*, Vol. 24(s1), pp. 89-96.
7. IHO (2008), *IHO Standards for Hydrographic Surveys*, Special Publication No. 44, 5th Edition.
8. Kadaj R. (2014), Design of the Quasigeoid Model PL-geoid-2011, Seminar of the Committee on Geodesy of the Polish Academy of Sciences and the Faculty of Geodesy and Cartography at Warsaw University of Technology: „Realization of Geodetic Control Networks and Geodynamic Problems”, Grybów (in Polish).
9. Kazimierski W., Włodarczyk-Sielicka M. (2016), Technology of Spatial Data Geometrical Simplification in Maritime Mobile Information System for Coastal Waters, *Polish Maritime Research*, Vol. 23(3), pp. 3-12.
10. Makar A. (2002), Shallow Water Geodesy: Survey Errors During Seabed Determination, *Reports on Geodesy*, No. 2(62), pp. 71-78.
11. Makar A. (2008), Method of Determination of Acoustic Wave Reflection Points in Geodesic Bathymetric Surveys, *Annual of Navigation*, No. 14, pp.1-89.

12. Makar A., Naus K. (2003), Obtaining of Data for Digital Sea Bottom Model, Archives of Photogrammetry, Cartography and Remote Sensing, Vol. 13A, pp. 163-170 (in Polish).
13. Mohammed N. Z., Ghazi A., Mustafa H. E. (2013), Positional Accuracy Testing of Google Earth, International Journal of Multidisciplinary Sciences and Engineering, Vol. 4, No. 6, pp.6-9.
14. Moszyński M., Chybicki A., Kulawiak M., Łubniewski Z. (2013), A Novel Method for Archiving Multibeam Sonar Data with Emphasis on Efficient Record Size Reduction and Storage, Polish Maritime Research, Vol. 20(1), pp. 77-86.
15. Osada E. (2016), Geodetic Datums, UxLAN Publishing House, No. 3, Wrocław (in Polish).
16. PN-EN ISO 9875:2005, Vessels and Maritime Technology – Echo Sounders (in Polish).
17. Popielarczyk D. (2012), RTK Water Level Determination in Precise Inland Bathymetric Measurements, Proceedings of the 25th International Technical Meeting of the Satellite Division of the Institute of Navigation (ION GNSS 2012), Nashville, pp. 1158-1163.
18. Popielarczyk D. (2016), Accuracy of Vertical Trajectory Determination of Hydrographic Survey Unit Using Robotized Total Station, Proceedings of the 16th International Multidisciplinary Scientific GeoConference & EXPO SGEM2016, Albena, pp. 39-46.
19. Popielarczyk D., Templin T. (2014), Application of Integrated GNSS/Hydroacoustic Measurements and GIS Geodatabase Models for Bottom Analysis of Lake Hancza: the Deepest Inland Reservoir in Poland, Pure and Applied Geophysics, Vol. 171(6), pp. 997-1011.
20. Popielarczyk D., Templin T., Łopata M. (2015), Using the Geodetic and Hydroacoustic Measurements to Investigate the Bathymetric and Morphometric Parameters of Lake Hancza (Poland), Open Geosciences, Vol. 7(1), pp. 854-869.
21. PRS (2015), Rules for Statutory Survey of Sea-going Ships. Part V – Navigation Devices, Gdansk (in Polish).
22. Romano A., Duranti P. (2012), Autonomous Unmanned Surface Vessels for Hydrographic Measurement and Environmental Monitoring, Proceedings of the FIG Working Week, Rome.
23. Specht C., Koc W., Smolarek L., Grzędziela A., Szmagliński J., Specht M. (2014), Diagnostics of the Tram Track Shape with the Use of the Global Positioning Satellite Systems (GPS/GLONASS) Measurements with a 20 Hz Frequency Rate, Journal of Vibroengineering, Vol. 16(6), pp. 3076-3085.
24. Specht C., Specht M., Dąbrowski P. (2017), Comparative Analysis of Active Geodetic Networks in Poland, Proceedings of the 17th International Multidisciplinary Scientific GeoConference & EXPO SGEM2017, Albena, pp. 163-176.
25. Specht C., Weintrit A., Specht M. (2016), Determination of the Territorial Sea Baseline – Aspect of Using Unmanned Hydrographic Vessels, TransNav – The International Journal on Marine Navigation and Safety of Sea Transportation, Vol. 10, No. 4, pp. 649-654.
26. Specht M. (2016), Determination of the Polish Territorial Sea Baseline, Master's Thesis, Gdynia Maritime University (in Polish).
27. Tuna G., Arkoc O., Koulouras G., Potirakis S. M. (2013), Navigation System of an Unmanned Boat for Autonomous Analyses of Water Quality, Elektronika i Elektrotechnika, Vol. 19, No. 8, pp. 3-7.
28. Wyrzykowski T. (1988), Monograph on Domestic 1st Class Precise Levelling Networks, Institute of Geodesy and Cartography, Warsaw (in Polish).
29. Yan-na Z., Ti-kun S., Fei D., Wei-min Y. (2015), The Design of ARM-Based Control System of Unmanned Research Catamaran, In: Kim J.-H. et al. (eds.), Robot Intelligence Technology and Applications 3, Advances in Intelligent Systems and Computing 345, Springer International Publishing, Cham, pp. 617-623
30. Zienkiewicz M. H., Czaplewski K. (2017), Application of Square M_{split} Estimation in Determination of Vessel Position in Coastal Shipping, Polish Maritime Research, Vol. 24(2), pp. 3-12.

CONTACT WITH THE AUTHORS

Cezary Specht

e-mail: c.specht@geodezja.pl
Akademia Morska w Gdyni
Morska 81-87, 81-225 Gdynia
POLAND

Emilian Świtalski

e-mail: switalski.emilian@gmail.com
Akademia Morska w Gdyni
Morska 81-87, 81-225 Gdynia
POLAND

Mariusz Specht

e-mail: m.specht@wn.am.gdynia.pl
Akademia Morska w Gdyni
Morska 81-87, 81-225 Gdynia
POLAND

PROBLEMS OF THE STARTING AND OPERATING OF HYDRAULIC COMPONENTS AND SYSTEMS IN LOW AMBIENT TEMPERATURE (PART IV)

MODELLING THE HEATING PROCESS AND DETERMINING THE SERVICEABILITY OF HYDRAULIC COMPONENTS DURING THE STARTING-UP IN LOW AMBIENT TEMPERATURE

Ryszard Jasiński

Gdańsk University of Technology, Poland

ABSTRACT

Designers of hydraulically driven machines and devices are obliged to ensure during design process their high service life with taking into account their operational conditions. Some of the machines may be started in low ambient temperature and even in thermal shock conditions (due to delivering hot working medium to cold components). In order to put such devices into operation appropriate investigations, including experimental ones - usually very expensive and time-consuming, are carried out. For this reason numerical calculations can be used to determine serviceability of a hydraulic component or system operating in thermal shock conditions. Application of numerical calculation methods is much less expensive in comparison to experimental ones. This paper presents a numerical calculation method which makes it possible to solve issues of heat exchange in elements of investigated hydraulic components by using finite elements method. For performing the simulations the following data are necessary: ambient temperature, oil temperature, heat transfer coefficient between oil and surfaces of elements, as well as areas of surfaces being in contact with oil. By means of computer simulation method values of clearance between cooperating elements as well as ranges of parameters of correct and incorrect operation of hydraulic components have been determined. In this paper results of computer simulation of some experimentally tested hydraulic components such as axial piston pump and proportional spool valve, are presented. The computer simulation results were compared with the experimental ones and high conformity was obtained.

Keywords: hydraulic drive, hydraulic components, thermal shock, computer simulation

INTRODUCTION

Hydraulic system components operate in various climatic conditions [33-35]. Users of hydraulically driven devices expect their proper work in a.o. low ambient temperature and thermal shock conditions (due to supplying cold components with hot hydraulic liquid).

Development of computer technique made it possible to model various phenomena which occur in hydraulic components of machines and devices. Owing to that it is possible to carry out diagnoses for determining their correct operation in thermal shock conditions. Heating processes of hydraulic devices during such start-up can be modelled by using numerical methods incorporated in NASTRAN, ANSYS, FLUENT and other software systems [13, 20, 21].

In order to perform computer simulation of heating process of cold elements of a hydraulic component after its start-up it is necessary to work out an appropriate model and assume initial and boundary conditions.

Pumps, hydraulic motors and valves are the basic hydraulic system components in which energy losses occur. The losses are classified into volumetric, pressure and mechanical ones and determined for a given hydraulic device in steady conditions with neglecting as a rule impact of heat exchange in such device as that insignificant in total balance of energy losses [1, 17-19, 22-27, 29, 32]. In start-up process of a hydraulic machine or device the heat exchange on the path of working medium, i.e. between elements of hydraulic components and environment, highly influences effectiveness of energy

conversion in the components of devices especially during starting-up cold components supplied with hot working medium as it was proved a.o. in the publications [2-12]. Hence the issues, considered in this paper, of modelling the heating processes during starting-up in thermal shock conditions, which take place in axial piston pump and proportional spool valve, are purposeful and justified. One may be acquainted with operating principles of various hydraulic components as well as results of their tests in low ambient temperature by studying a.o. the publications [1-12, 30].

INTRODUCTION TO ISSUES OF UNSTEADY CONDUCTIVE HEAT TRANSFER

The supplying of hydraulic components with hot working medium results in unsteady heating their parts (elements) [2-12]. Temperature of component parts varies in time. Application of conductive heat transfer differential equation it is possible to determine temperature field distribution in component parts. To determine the differential equation of conductive heat transfer in elements of the component it is necessary to create energy balance equation for elementary volume of its body [21, 28, 31].

The energy balance for a cuboid of dV volume during heating at $d\tau$ time interval, taking into consideration the internal heat source q_V , can be expressed by the following equation [31]:

$$\begin{aligned} dQ_x + dQ_y + dQ_z + q_V dV d\tau = \\ = dQ + dQ_{x+dx} + dQ_{y+dy} + dQ_{z+dz} \end{aligned} \quad (1)$$

where:

dQ – energy increase of cuboid,

dQ_x, dQ_y, dQ_z – heat transported to cuboid surface in the direction of x -, y - and z - axis, respectively,

$dQ_{x+dx}, dQ_{y+dy}, dQ_{z+dz}$ – heat transported from cuboid surface in the direction of x -, y - and z - axis, respectively.

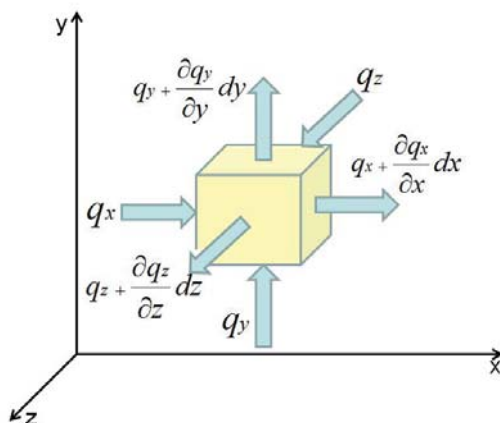


Fig.1. Unsteady conductive heat transfer through elementary volume $dV=dx dy dz$ of solid body [8, 28, 31]

The heat dQ_x, dQ_y, dQ_z is delivered to three surfaces of the cuboid and in the same time the heat $dQ_{x+dx}, dQ_{y+dy}, dQ_{z+dz}$

is transported from the other three surfaces shifted by the distances dx, dy, dz from the initial ones, respectively.

The heat dQ which influences on energy increase of the cuboid of dV volume (Fig. 1) is equal to:

$$\begin{aligned} dQ = q_x dy dz d\tau - \left(q_x + \frac{\partial q_x}{\partial x} dx \right) dy dz d\tau + \\ + q_y dx dz d\tau - \left(q_y + \frac{\partial q_y}{\partial y} dy \right) dx dz d\tau + \\ + q_z dx dy d\tau - \left(q_z + \frac{\partial q_z}{\partial z} dz \right) dx dy d\tau + q_V dV d\tau \end{aligned} \quad (2)$$

The energy increase dQ in the cuboid of dV volume of the solid body can be described as follows:

$$dQ = c_p \rho \frac{\partial T}{\partial \tau} dV d\tau \quad (3)$$

where:

c_p – specific heat at constant pressure,

ρ – density.

After transformation of Eq. 2 and 3 as well as by taking into account value of heat generated inside the volume dV , the following equation was obtained :

$$\frac{\partial T}{\partial \tau} = -\frac{1}{c_p \rho} \left(\frac{\partial q_x}{\partial x} + \frac{\partial q_y}{\partial y} + \frac{\partial q_z}{\partial z} \right) + \frac{q_V}{c_p \rho} \quad (4)$$

The heat flux transported through the hydraulic component elements is proportional to temperature gradient in accordance with Fourier law :

$$q = -\lambda \nabla T \quad (5)$$

where : q - heat flux,

λ - thermal conductivity,

∇ - nabla operator,

T - temperature.

Simultaneous using of the Fourier law and the energy balance leads to the differential equation which describes temperature field in fixed isotropic component elements [28, 31]:

$$\frac{\partial T}{\partial \tau} = \frac{1}{c_p \rho} \left(\frac{\partial}{\partial x} \left(\lambda \frac{\partial T}{\partial x} \right) + \frac{\partial}{\partial y} \left(\lambda \frac{\partial T}{\partial y} \right) + \frac{\partial}{\partial z} \left(\lambda \frac{\partial T}{\partial z} \right) \right) + \frac{q_V}{c_p \rho} \quad (6)$$

The differential equation of unsteady conductive heat transfer through elements of the component without internal heat sources and at $\lambda = idem$ is presented below:

$$\frac{\partial T}{\partial \tau} = a \left(\frac{\partial^2 T}{\partial x^2} + \frac{\partial^2 T}{\partial y^2} + \frac{\partial^2 T}{\partial z^2} \right) = a \nabla^2 T \quad (7)$$

where: $a = \frac{\lambda}{c_p \cdot \rho}$ - thermal diffusivity,
 ∇^2 - Laplace operator.

The calculation of the temperature field from differential equation of unsteady conductive heat transfer is possible if only initial and boundary conditions are known. Initial conditions determine initial distribution of temperature in the considered component. Boundary conditions inform about quantities which determine heat flux on surfaces of hydraulic component elements. To perform computer simulation of heating process of component elements, 3rd type of boundary conditions comprising the oil temperature T_{ol} and the heat transfer coefficient α_w between oil and surfaces of component elements, were used.

The oil temperature T_{ol} was measured by help of temperature sensors. The heat transfer coefficient was determined on the basis of experimental tests [2-12].

EXPERIMENTAL TESTS AND COMPUTER SIMULATION OF HEATING PROCESS IN ELEMENTS OF AXIAL PISTON PUMP

Experimental tests of the axial piston pump with cam-driven commutation unit (shown in Fig. 2) during start-up in thermal shock conditions, were performed in the Hydraulics Laboratory of the Faculty of Mechanical Engineering of the Gdańsk University of Technology.

The Laboratory is equipped with a.o. multipump supply devices with oil temperature stabilization, devices for testing hydraulic components and systems as well as a system for measuring and recording mechanical, hydraulic and thermal quantities.

In low temperature chambers it was possible to cool down hydraulic components up to temperature not lower than $-25\text{ }^\circ\text{C}$ (in one of the chambers – even down to $-38\text{ }^\circ\text{C}$). The tests were conducted without forced air flow. The supply oil temperature was kept in the range from 20 to $60\text{ }^\circ\text{C}$ (usually at $50\text{ }^\circ\text{C}$) by means of an oil temperature stabilizing system.

During start-up of the hydraulic pump, time characteristics of the following quantities were recorded: pressure and temperature (Pt100 sensors) in suction and pressure connections of the pump, rate of flow, pump shaft rotational speed, temperature in low temperature chamber, temperature in many points of the pump in question (thermocouples), pump shaft torque. An Advantech VisiDAQ system was used for transmitting and recording the data in computer.

The tests of the pump were made for the following parameters: oil temperature of about $48\text{ }^\circ\text{C}$, ambient temperature in the range from -21 to $+23\text{ }^\circ\text{C}$, pump shaft rotational speed in the range from 500 to 2500 rpm, pressure in the range from $4,5$ to 12 MPa. For the parameters a dozen or so measuring series of pump start-up in thermal shock conditions were performed [3, 4, 7, 11]. As a result,

characteristics of: temperature changes while heating the fixed and mobile elements, oil inlet and outlet temperature as well as oil leakage temperature, were achieved. Moreover, characteristics of other pump parameters such as e.g. hydraulic-mechanical efficiency, were determined.

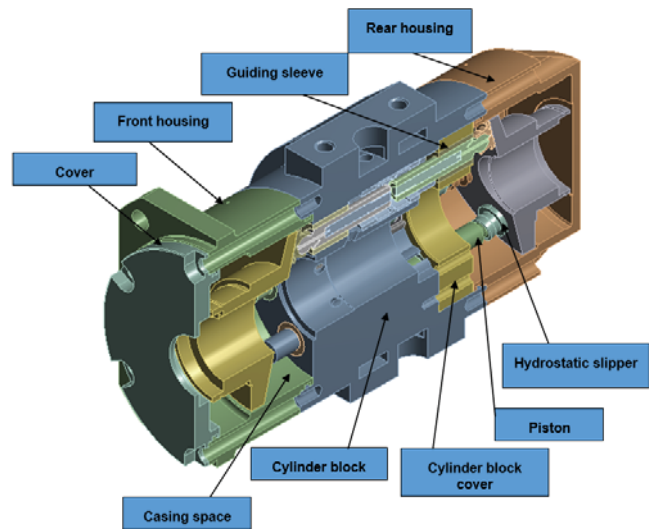


Fig. 2. Elements of axial piston pump [14-16, 33]

It was observed that pump fixed elements (Fig. 2) such as cover, front and rear housing were heated up with some delay in relation to the cylinder block and cylinder block cover in initial phase of start-up.

The delay results from that in the instant of start-up cold oil is present in the internal space of the pump (casing space). At the beginning it becomes warmer as a result of oil mixing due to influence of revolutions of swash plate and to and fro motion of pistons. Additionally, the oil in casing space is heated by leakages from clearance between piston and guiding sleeve as well as slipper and swash plate of the pump. Results of the experimental tests of the pump are described in detail in [3, 4, 7, 11].

Because of different heating rate in the fixed elements of the pump the elements have been split into two groups. The first group contains elements of cylinder block component (cylinder block, cylinder block cover), and the second group comprises elements of housing (cover, front housing, rear housing).

During the experimental tests of the pump two cases of its start-up were considered. In one of the cases uniform rate of heating the pump pistons was applied, in the other - two-phase heating the pistons and hydrostatic slipper was used. The first phase was characterized by fast heating rate of the pistons and hydrostatic slipper (about 30 s). Later the heating process was slower. Results of the experimental tests are described in detail in [3, 4, 7, 11].

For carrying out computer simulation it is necessary to determine heat transfer coefficients from oil to mobile and fixed elements of the pump. It is possible this way to compare real characteristics of heating the pump elements with those obtained as a result of computer simulation.

To determine the heat transfer coefficients $\alpha_w = f(n)$ in function of rotational speed, the experimental test data (temperature characteristics of elements) were used [3, 4, 7, 11, 12].

The characteristics of the heat transfer coefficients in function of pump rotational speed for the cylinder block of component, presented in Fig. 3, can be described by the following straight line equation: $\alpha_{w1n} = 0,321 \cdot n + 92,8$ (n – rotational speed).

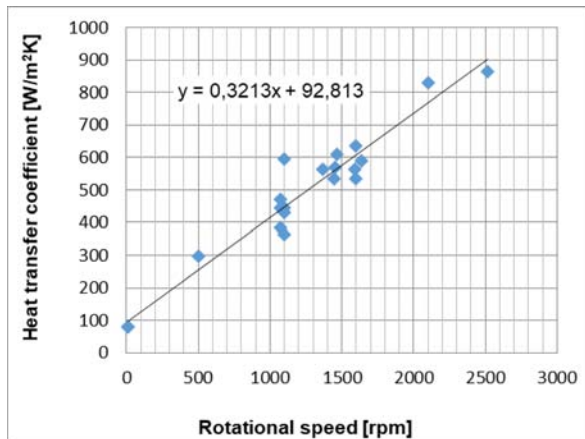


Fig. 3. The heat transfer coefficients from oil to surfaces of cylinder block and cylinder block cover in function of pump rotational speed [12]

Fig. 4 shows the determined characteristics of the heat transfer coefficients in function of pump rotational speed for the following elements: the cover, front housing and rear housing, which can be described by the straight line equation as follows: $\alpha_{w2n} = 0,266 \cdot n + 51,95$.

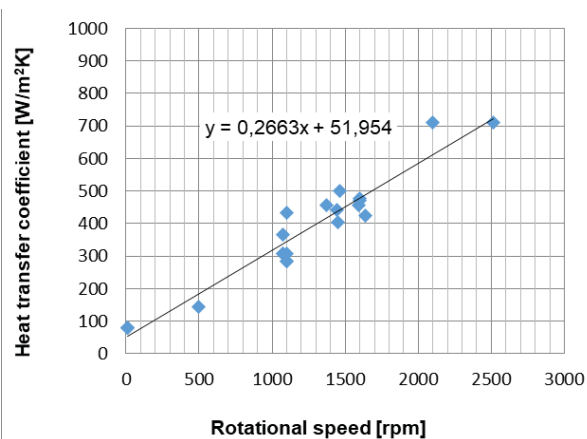


Fig. 4. The heat transfer coefficients from oil to surfaces of cover, front housing and rear housing in function of pump rotational speed [12]

It can be noticed that values of the heat transfer coefficients for the cylinder block component (cylinder block, cylinder block cover) are greater by about 20 % than those for the pump housing elements (cover, front housing, rear housing).

The numerical calculation method based on finite elements makes it possible to solve dynamic issues of heat exchange in investigated model. The data necessary to perform the simulation were the following: ambient temperature, oil

temperature, determined heat transfer coefficient (Fig. 3 and 4) as well as areas of element surfaces being in contact with oil.

Having in one's disposal these data one was able to perform computer simulation of the heating process in elements of the investigated pump during its start-up in thermal shock conditions. The model containing mobile and fixed parts of the pump was split into finite elements. The computer simulations of the heating of pump elements in thermal shock conditions were conducted for a few different sets of parameters. The most interesting results of the simulations carried out for the following parameters: ambient temperature of -20°C , oil temperature of 48°C , rotational speed of 1100 rpm and pressure of 5.2 MPa, are presented below. During the test, temperature was measured in both fixed and mobile elements.

For numerical calculations heat transfer coefficients of the pump elements were assumed on their surfaces (Fig. 5). Tab.1. presents values of definite heat transfer coefficients. The pump was tested for two-phase heating process of piston. In this case two values of the heat transfer coefficient from oil to piston surfaces, were assumed.

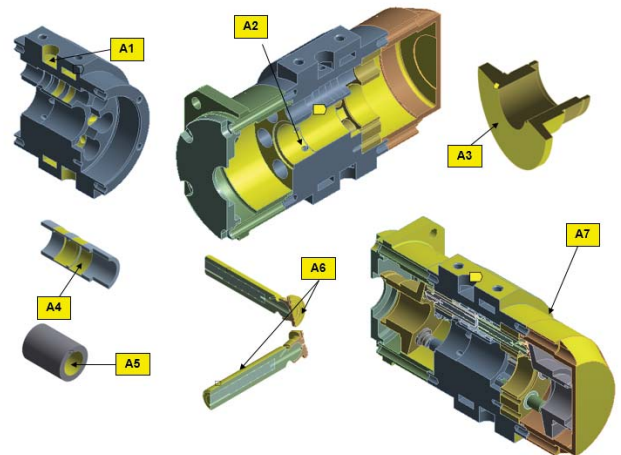


Fig. 5. Defined heat exchange surfaces of the pump

On the surfaces of mobile and fixed elements the following values of the heat transfer coefficient from oil to respective surfaces were assumed:

- for surface of cylinder block - 430 [W/m²K],
- for surface of housing - 285 [W/m²K],
- for surface of swash plate - 115 [W/m²K],
- for surface of piston - 150 [W/m²K] (during the time interval of 0 ÷ 30 s), and 40 [W/m²K] (during the time interval of 31 ÷ 500 s).

Tab. 1. Heat exchange surfaces with assumed heat transfer coefficients from oil to the pump elements (A1-A6) and from the pump elements to the environment (A7).

Heat exchange surface	Heat transfer coefficient	Initial temperature of surface
	[W/m²K]	[°C]
A1	430	48

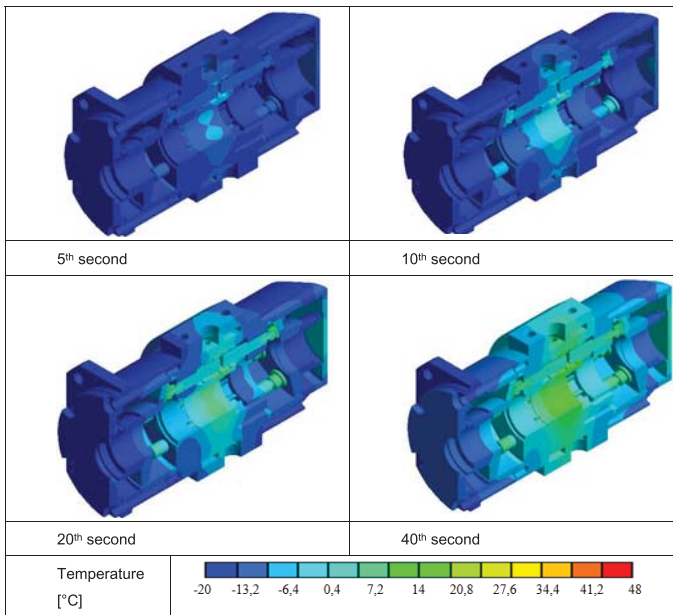


Fig. 6. Temperature distribution in mobile and fixed elements in subsequent seconds of pump start-up in thermal shock conditions for the following working parameters of the pump after its start-up: cooling chamber temperature $t_{oi} = -20^{\circ}\text{C}$, oil temperature $t_{oi} = 48^{\circ}\text{C}$, rotational speed $n = 1100 \text{ rpm}$, pressure $p = 5,2 \text{ MPa}$.

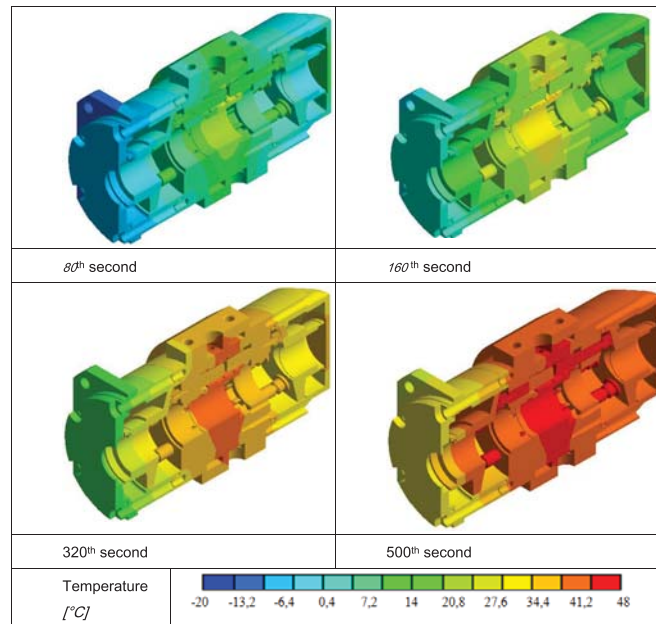


Fig. 7. Temperature distribution in mobile and fixed elements in subsequent seconds of pump start-up process for the following working parameters of the pump after its start-up: cooling chamber temperature $t_{oi} = -20^{\circ}\text{C}$, oil temperature $t_{oi} = 48^{\circ}\text{C}$, rotational speed $n = 1100 \text{ rpm}$, pressure $p = 5,2 \text{ MPa}$.

A2	285	48
A3	115	48
A4	430	48
A5	40	48
A6	150 (0÷30s), 40 (31÷500s)	48
A7	12	-20

Fig. 6 and 7 present temperature distribution in mobile and fixed elements in subsequent seconds of pump start-up in thermal shock conditions.

It can be observed that the pump heating process begins in places which are in direct contact with flowing hot oil. These are surfaces of internal channels of the pump through which hot working medium flux flows. As a result, the cylinder block component of the pump is the element which becomes heated the fastest.

During the first 40 s of the start-up process the difference between the highest and the lowest temperature occurring in fixed elements of the pump is equal to about 35°C . The front housing and cover become heated the slowest. In spite of that the front housing is of similar mass compared to that of the rear housing, the rear housing becomes heated much more fast during later phase of start-up. It results from that the area of the rear housing surface which is washed by oil is greater than that of front housing. Despite the insulation, the heat flows from the front housing to the stand.

COMPARISON OF TEMPERATURE CHARACTERISTICS OF THE ELEMENTS OBTAINED FROM THE EXPERIMENT WITH THOSE RESULTING FROM THE COMPUTER SIMULATION DURING HEATING THE TESTED PUMP

In order to check conformity of heating temperature characteristics of the elements of the experimentally tested pump with those resulting from the numerical calculations, in the model (Fig. 8) points were selected in the same places where temperature were measured by means of the thermocouples T1-T8 in the tested component [3, 4, 7, 11].

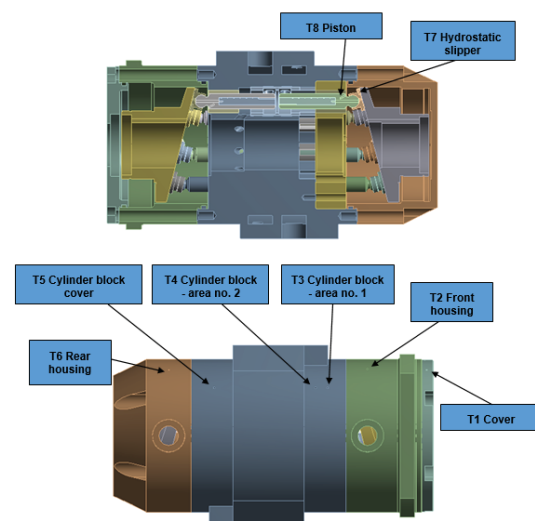


Fig. 8. Points where temperature was recorded during computer simulation of heating process in mobile and fixed elements of the pump

Comparing cover's temperature characteristics obtained from the experiment to ones obtained from computer simulation (Fig. 9), it can be observed that there is high conformity between them. In the initial phase the temperature according to the computer simulation is only slightly higher than that from the experiment. It so happens because during temperature measurement in real conditions heat is transferred to the cover with a delay.

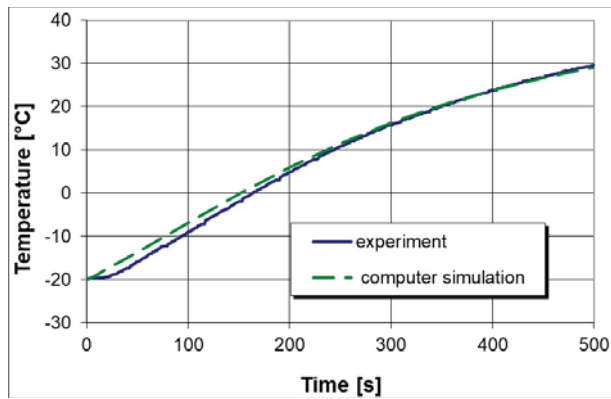


Fig. 9. Temperature of the cover obtained from experimental test and computer simulation (T1 - Fig. 8)

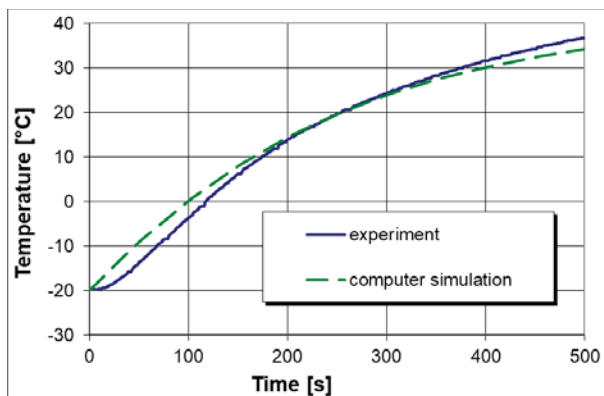


Fig. 10. Temperature of the front housing obtained from experimental test and computer simulation (T2- Fig. 8)

High conformity is observed between the heating characteristics obtained from the computer simulation and the experiment for the front housing (Fig. 10) and cylinder block (Fig. 11).

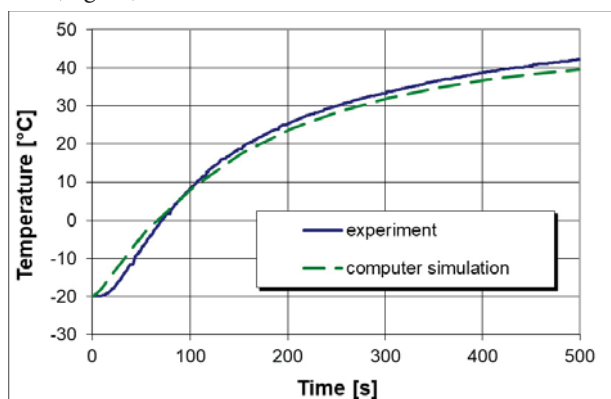


Fig. 11. Temperature of the cylinder block obtained from experimental test and computer simulation (T3- Fig. 8)

Fig. 12 presents the temperature characteristics obtained from the experimental tests and numerical calculations for the cylinder block cover. After about 70 s from the instant of starting up the cold pump, temperature of the cylinder block cover according to the computer simulation is by a few grades lower than that from the experiment. It is consequence of a simplification introduced to the structural computer model of the pump. Additionally, the cylinder block cover is washed by the oil heated in pump casing space chamber due to mechanical friction in ball bearings, internal friction of oil under intensive mixing with that from leakages.

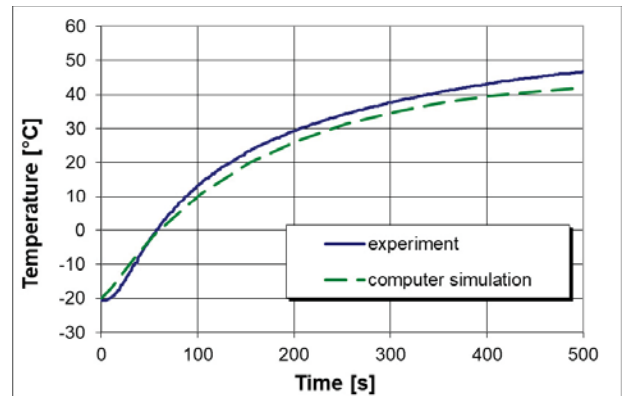


Fig. 12. Temperature of the cylinder block cover obtained from experimental test and computer simulation (T5 - Fig. 8)

For modelling the heating process of piston, two values of the heat transfer coefficient from oil to washed surface of the piston and hydrostatic slipper, were used. This ensured a good conformity of results. The hydrostatic slipper temperature according to the computer simulation is only slightly lower than that from the experimental tests (Fig. 13). One of the reasons is that a lower temperature of oil was assumed in the model. The oil temperature in pump casing space in steady conditions is higher than that of oil delivered to the pump. The higher pumping pressure in the pump the higher oil temperature in its casing space.

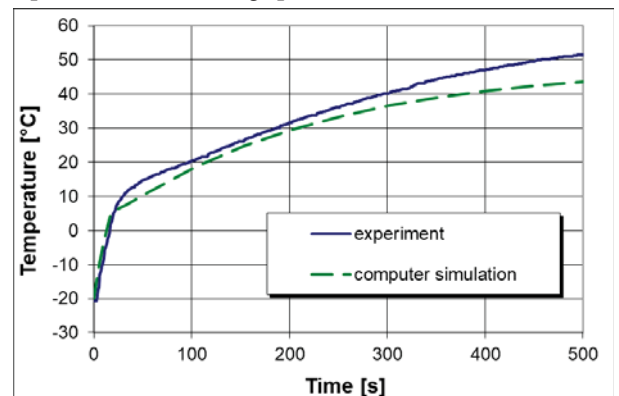


Fig. 13. Temperature of the hydrostatic slipper obtained from experimental test and computer simulation (T7 - Fig. 8)

Summing up the results of the investigation of the axial piston pump performed by using the computer simulation

one is able to state that they are close to those obtained from the experiment. It results from that the values of the heat transfer coefficient from oil to surfaces of mobile and fixed elements, determined on the basis of the experiment results, can be considered correct. It was proved that it is possible to simulate heating processes in the pump elements with high accuracy.

DETERMINATION OF SERVICEABILITY OF AXIAL PISTON PUMP DURING ITS START-UP IN THERMAL SHOCK CONDITIONS ON THE BASIS OF MODEL TESTS WITH THE USE OF COMPUTER SIMULATION

To assess serviceability of axial piston pump (Fig. 2) during its start-up in thermal shock conditions, by means of the computer simulation method, a simplified computer model was worked out especially for this purpose (Fig. 14).

It differs from the model presented in Fig. 8 by a simplified structure. Heat exchange surfaces as well as quantities of mass of the elements only roughly correspond to real ones. As the pump structure is symmetrical only a half of it was modelled (Fig. 14). The model consists of the cylinder block, cylinder block cover, rear housing, swash plate, piston with hydrostatic slipper. The piston contains a hole throughout its length. The pump model was split into finite elements.

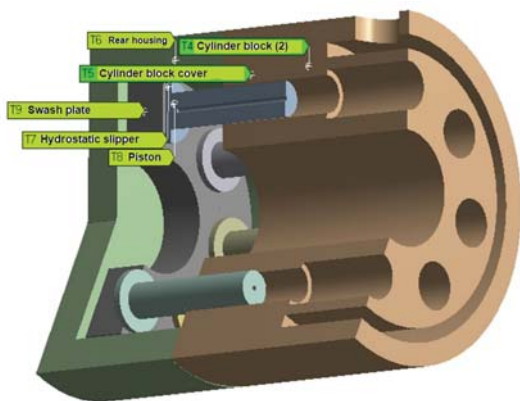


Fig. 14. Arrangement of measurement points in the pump model (the same measurement points are placed in the tested pump – Fig. 2, Fig. 8)

Tests of the pump model (Fig. 14) were carried out for the start-up conditions given in Tab. 1. Its heating process was tested by means of numerical calculations.

Fig. 15 presents results of the computer simulation of the heating of the simplified model in the above mentioned

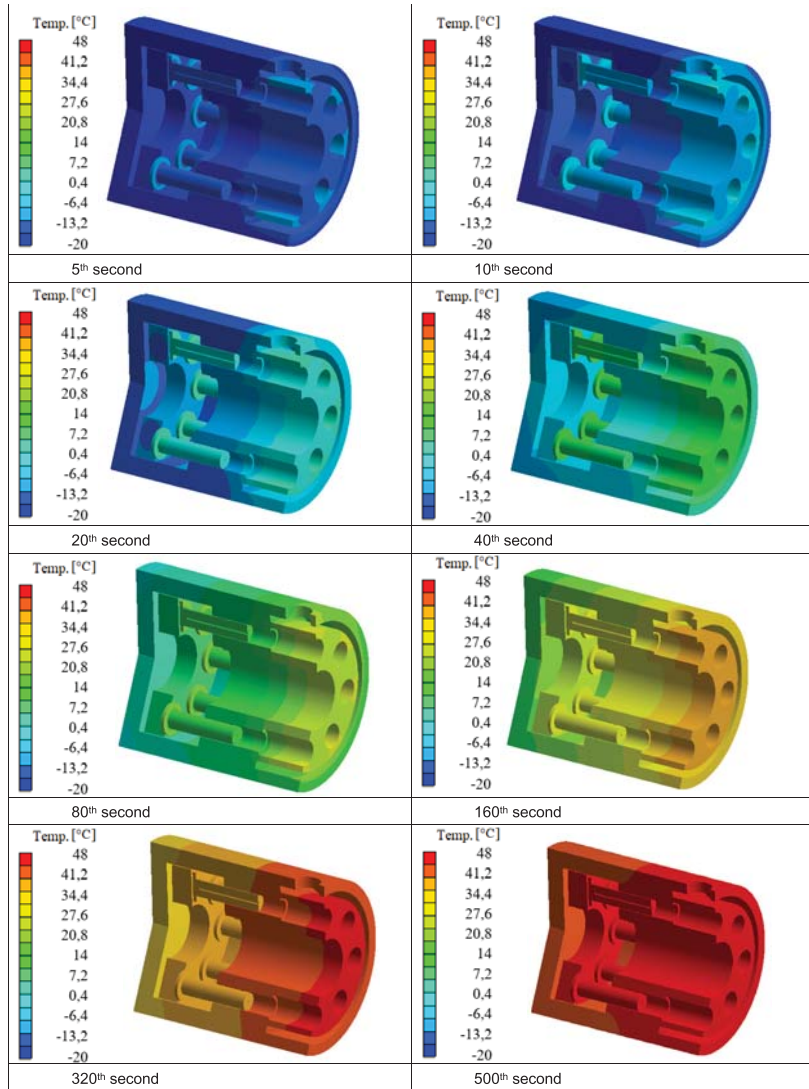


Fig. 15. Temperature distribution in pump model elements in subsequent seconds of pump start-up process for the following working parameters of the pump after its start-up: cooling chamber temperature $t_{ot} = -20$ °C, oil temperature $t_{oi} = 48$ °C, rotational speed $n = 1100$ rpm, pressure $p = 5,2$ MPa

conditions. The temperature distribution in the pump model elements was prepared for 5th, 10th, 20th, 40th, 80th, 160th, 320th and 500th second of the process. On the basis of the obtained temperature fields in the elements (Fig. 15) it was stated that beginning from 30th second the piston and cylinder block were heated almost with the same rate.

The temperature characteristics obtained from the computer simulation are consistent with those measured during the corresponding experimental test of the pump (parameters of the cold pump start-up: the cooling chamber temperature $t_{ot} = -20$ °C, oil temperature $t_{oi} = 48$ °C, rotational speed $n = 1100$ rpm, pressure $p = 5,2$ MPa).

Fig. 16 shows the temperature characteristics of: cylinder block cover, cylinder block, rear housing, piston and hydrostatic slipper. The temperature characteristics of the hydrostatic slipper and piston change their character in 31st second. It is connected with the change in the heat transfer coefficient from oil to surfaces of the slipper and piston.

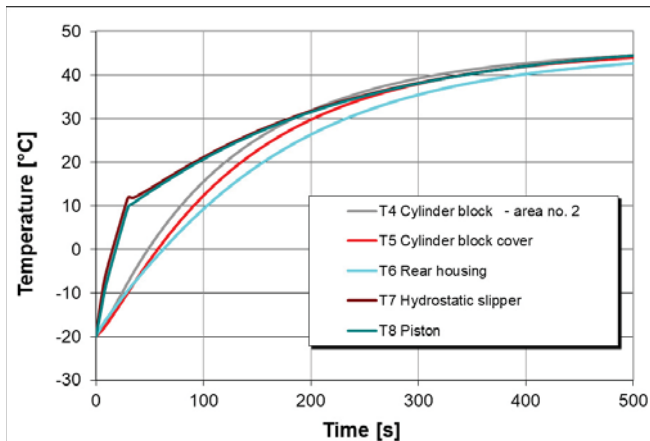


Fig. 16. Temperature of the cylinder block cover, cylinder block, rear housing, piston and hydrostatic slipper for the following initial parameters: oil temperature $t_{oi}=48^{\circ}\text{C}$, ambient temperature -20°C , rotational speed $n=1100\text{ rpm}$, pressure $p=5,2\text{ MPa}$

The temperature characteristic of the hydrostatic slipper obtained from numerical calculations is consistent with that from experimental tests (Fig. 17). As it results, in order to perform computer simulation it is possible to work out a slipper - piston component model which is structurally simplified and made only of one material, e.g. steel.

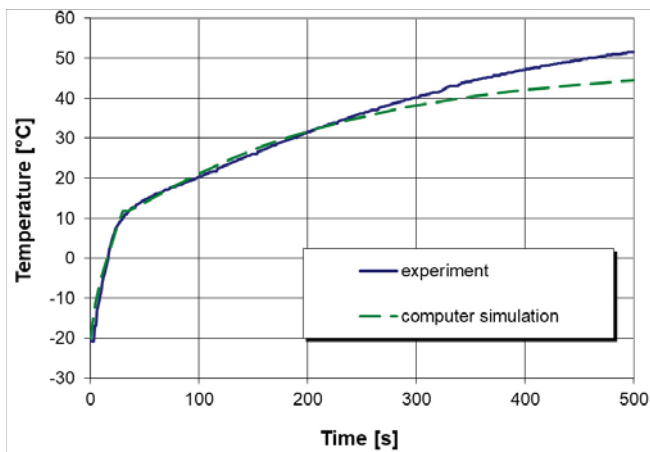


Fig. 17. Temperature of the hydrostatic slipper obtained from experimental test and computer simulation (T 7 - Fig.14)

The structural simplification introduced to the cylinder block model (Fig. 14) did not lower accuracy in determining its temperature characteristic compared to that obtained from the experimental tests. The reached conformity of the temperature characteristics was even greater (Fig. 18) than that resulting from the numerical calculations of the pump (Fig. 12).

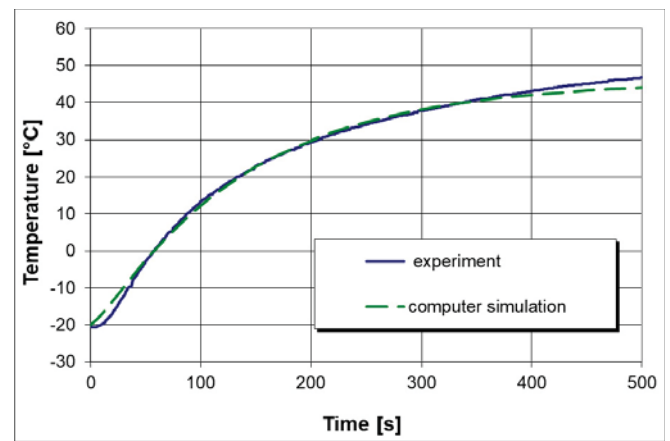


Fig. 18. Temperature of the cylinder block cover obtained from experimental test and computer simulation (T 5 - Fig.14)

During start-up of the cooled pump the pistons are heated from hot oil more fast than the cylinder block (Fig. 16). This is the main cause of change in clearance in these conditions. Change in the effective clearance l_e during start-up can be determine by using the following relation:

$$l_e(\tau) = l_m + \Delta l_p(\tau) - \Delta l_t(\tau) \quad (8)$$

It describes change of the initial clearance l_m by the quantity Δl_p under influence of pressure exerted onto mobile and fixed elements as well as by the quantity Δl_t resulting from thermal expansion of the elements.

The change in clearance by the quantity Δl_t , due to difference in linear thermal expansion of the cooperating component elements, resulting from non-uniform heating during start-up in thermal shock conditions, can be described as follows :

$$\Delta l_t(\tau) = h_R \cdot \beta_R \cdot (T_R(\tau) - T_0) - h_N \cdot \beta_N \cdot (T_N(\tau) - T_0) \quad (9)$$

where:

β_R, β_N - coefficients of linear thermal expansion of the elements: mobile - marked R, fixed - marked N,

$T_R(\tau)$ - temperature of mobile elements,

$T_N(\tau)$ - temperature of fixed elements,

h_R, h_N - linear dimensions of the elements : mobile - marked R, fixed - marked N, determined in the temperature of geometrical measurements T_0 .

Based on the characteristics of temperature difference between piston and cylinder block, the effective clearance between the elements (Fig. 19) was determined under assumption that displacements of cooperating elements resulting from influence of pressure are rather not large. In 31st second from the instant of pump start-up the maximum decrease takes place in the effective radial clearance between piston and guiding sleeve hole. Starting from 250th second the heating process of piston, hydrostatic slipper as well as fixed elements (cylinder block cover) becomes uniform (Fig. 17,

Fig. 18). In this phase the effective clearance does not change almost at all and maintains on the level of $10\ \mu\text{m}$ (Fig. 19).

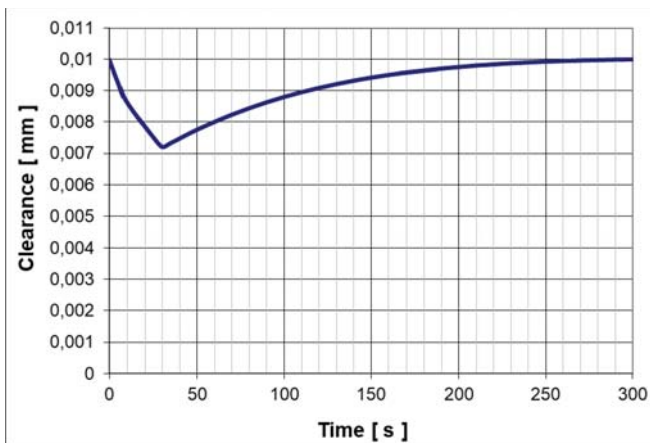


Fig. 19. Change of the clearance between piston and guiding sleeve for the following working parameters of the pump after its start-up: oil temperature $t_{ol}=48^{\circ}\text{C}$, ambient temperature -20°C , rotational speed $n=1100\ \text{rpm}$, pressure $p=5,2\ \text{MPa}$.

The characteristic of the effective clearance between piston and guiding sleeve, obtained from the model tests of the pump by using the computer simulation (Fig. 19), is consistent with that achieved from the experimental tests [4, 7, 11].

INVESTIGATIONS OF HEATING PROCESSES IN ELEMENTS OF THE PROPORTIONAL SPOOL VALVE IN THERMAL SHOCK CONDITIONS WITH THE USE OF COMPUTER SIMULATION METHOD AND COMPARISON OF THEIR RESULTS WITH EXPERIMENTAL DATA

A proportional spool valve was tested in various supply conditions [3-6, 30]. A dozen or so measurement series were conducted in total. The difference between oil temperature and initial temperature of the component was contained within the range of $20\div 75\ \text{K}$. In several cases of operation in thermal shock conditions, apart from a delayed steering reaction, an incorrect operation of the spool valve was observed.

The thermocouples T1 and T2 (Fig. 20) were placed in the spool. The thermocouples T8, T9, T10, T11 and T12 (Fig. 20) were located in the fixed elements of the spool valve: T12 - in the cover, T9 - in the housing to record its temperature close to heat source, and T10 - in the place where the largest amount of housing material is. Temperature of the connection plate was measured by using T11 thermocouple.

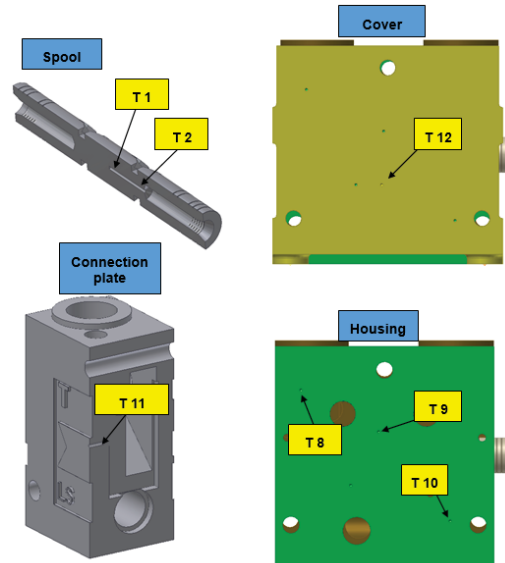


Fig. 20. Arrangement of holes to install the thermocouples T1, T2, T8, T9, T10, T11, T12 in the elements of proportional spool valve model: spool, connection plate, cover and housing

On the basis of the temperature characteristics recorded in the spool valve fixed and mobile elements, values of the heat transfer coefficient from oil to surfaces of the elements were determined in function of flow rate. They can be found in the publication [5].

One of the experimental tests was performed for the following parameters: the flow rate $Q=39\ \text{dm}^3/\text{min}$, ambient temperature of -10°C , oil temperature of 37°C . Numerical calculations were conducted to compare results of heating the spool valve elements. To this end, the following values of the heat transfer coefficient were assumed: from oil to spool surface - $2540\ \text{W}/\text{m}^2\text{K}$, from oil to surfaces of internal channels of the spool valve - $1760\ \text{W}/\text{m}^2\text{K}$, from the external surface of the spool valve to the environment - $12\ \text{W}/\text{m}^2\text{K}$.

To determine the clearance between spool and hole in housing it is necessary to know changes in temperature of the elements.

On the basis of the numerical calculations of the heating process in the spool valve, the temperature distribution in spool valve elements was achieved (Fig. 21) for the rise of the flow rate $Q=39\ \text{dm}^3/\text{min}$ and the initial difference of temperature between oil and the spool valve equal to $57\ \text{K}$.

The calculated temperature characteristic of the spool T1 presented in Fig. 22 differs only slightly from that determined experimentally. The difference between the characteristics obtained from the experiment and computer simulation after 20 s from the start-up instant, is not greater than $3\ \text{K}$.

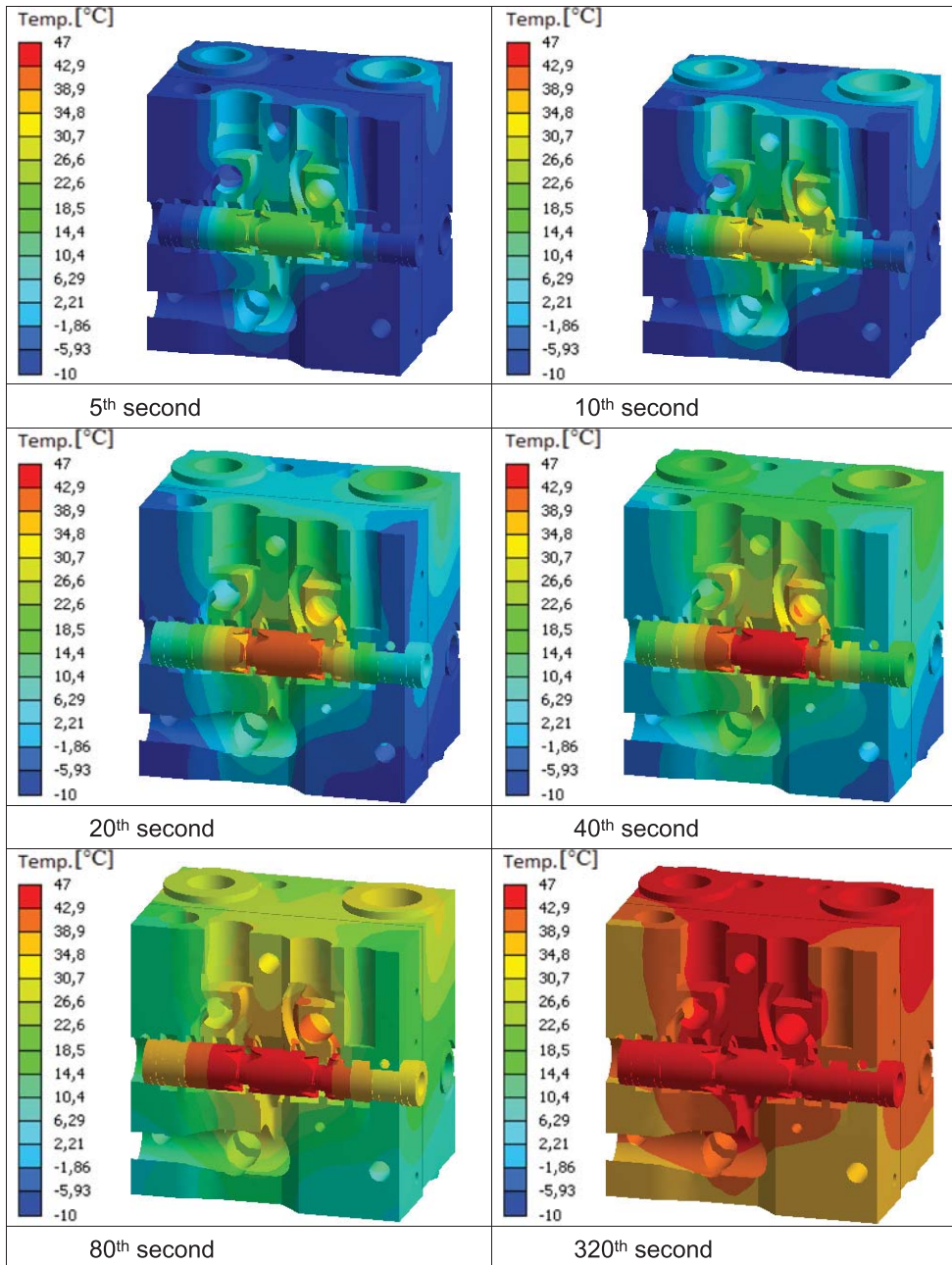


Fig. 21. Temperature distribution in heating elements of proportional spool valve (initial temperature of -10°C , oil flow rate of $39\text{ dm}^3/\text{min}$) counted in 5th, 10th, 20th, 40th, 80th and 320th s after supply of oil in 47°C temperature

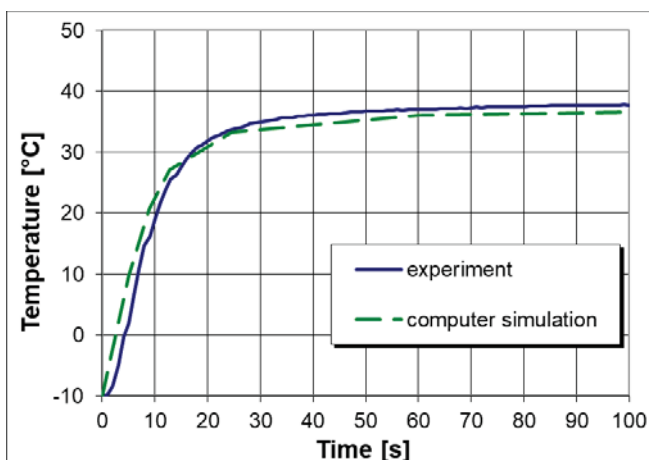


Fig. 22. Temperature of the spool obtained from experimental test and computer simulation (initial temperature of -10°C , oil temperature of 37°C , oil flow rate of $39\text{ dm}^3/\text{min}$)

To determine permissible parameters of correct operation of the spool valve, three series of calculation of heating its elements at the subsequent temperature difference of 47 K, 52 K and 57K between oil and the spool valve (and the assumed ambient temperature of -10°C), were performed. By making use of Eq. (8) the effective clearance values were calculated under assumptions that displacements of the spool and housing resulting from pressure action are rather not big.

The characteristics of the effective clearance between the cooperating elements (i.e. spool and housing of the spool valve) are presented in Fig. 23.

At the initial difference equal to 52 K of temperature between delivered oil and the spool valve (Fig. 23) an instantaneous loss of the clearance between spool and housing takes place in 25th second after start-up of the system including the spool valve. Whereas at the temperature difference of 57 K

(Fig. 23) an instantaneous jamming of the spool in the spool valve housing occurs between 15th and 55th second.

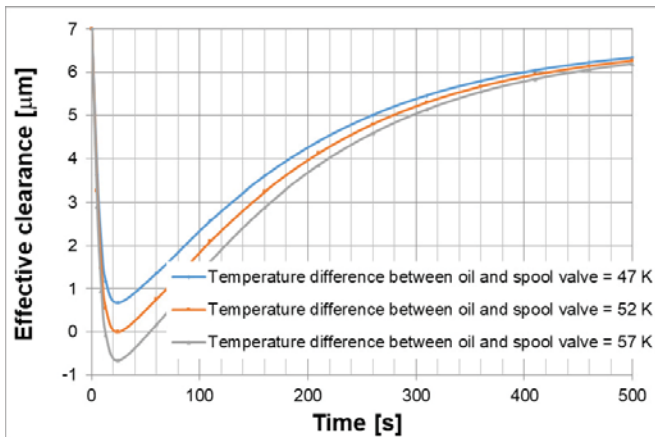


Fig. 23. Effective clearance between the spool and hole in the housing of the proportional spool valve in function of time for the following initial parameters: spool valve temperature of -10 °C, oil temperature of 37, 42, 47 °C, respectively, oil flow rate of 39 dm³/min)

The quantity of the clearance determined on the basis of the numerically calculated characteristics of temperature in the spool valve elements is in high conformity with results of the experiment.

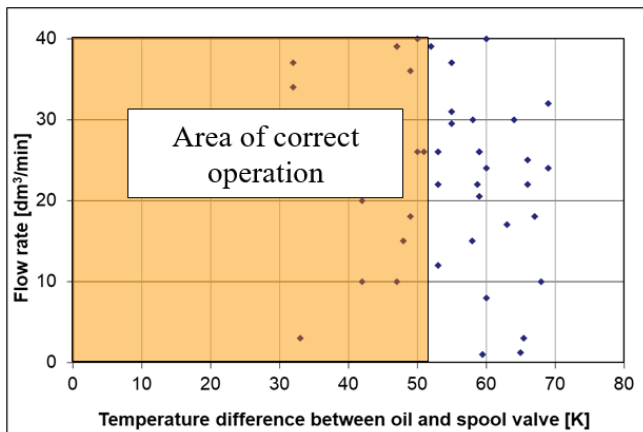


Fig. 24. Areas of correct and incorrect operation of the proportional spool valve with the clearance of 7 µm between the spool and the hole in the housing

The tested proportional spool valve in which the clearance between its spool and hole in the housing equals 7 µm, is resistant to operation in thermal shock conditions at the difference of temperature of hot oil and cold spool valve equal up to 52 K (Fig. 24).

CONCLUSIONS

The temperature characteristics in mobile and fixed elements of the tested hydraulic components, determined by means of computer simulation show high conformity with the characteristics obtained from experimental tests. This means that the experimentally determined heat transfer coefficients

from oil to elements of the components can be considered correct. It was also demonstrated that it is possible to obtain credible results in case of carrying out computer simulation of heating process in elements of hydraulic components in order to determine their serviceability for different initial supply parameters, e.g. a given magnitude of flow rate.

The method worked out by this author for determining the serviceability of hydraulic components in hydraulic shock conditions (Fig. 25) consists in making use of experimentally determined data base containing heat transfer coefficients from oil to surfaces of elements of the components. The coefficients are necessary for carrying out computer simulation of heating processes in components of hydraulic systems. On the basis of temperature characteristics in the elements, the effective clearance between cooperating elements of the hydraulic components and the area of correct operation of the component (and even the whole hydraulic system), was determined.

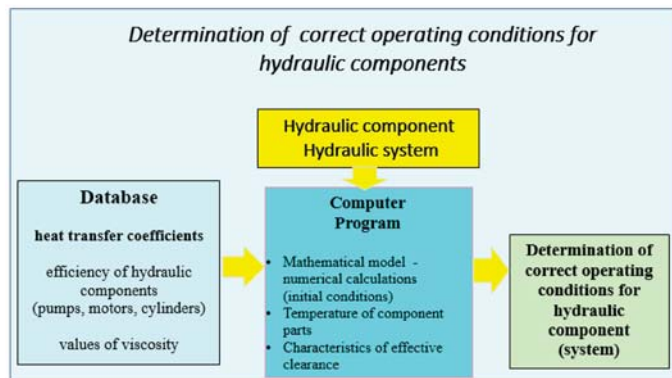


Fig. 25. Assessment of serviceability of hydraulic components and systems on the basis of database containing heat transfer coefficients [9, 10]

The computer simulation method which makes use of numerical calculations (finite elements method) for determining serviceability of hydraulic (system) component consists in determining the area of initial parameters in the start-up instant: ambient temperature, working medium temperature and flow rate (rotational speed) at which the component would operate correctly.

The computer simulation method makes it possible to determine values of clearance between cooperating elements as well as areas of parameters of correct start-ups of hydraulic components with a greater accuracy than that available from the analytical method presented in the publications [5, 6, 8].

BIBLIOGRAPHY

- Balawender A.: Energy analysis and testing methods of slow-speed hydraulic motors (in Polish). Zeszyty Naukowe PG. Gdańsk 1988.
- Jasiński R.: Operation of selected slow-speed hydraulic motors in thermal shock conditions (in Polish). Doctorate

thesis, supervisor: A. Balawender. Gdańsk 2002.

3. Jasiński R.: Problems of the starting and operating of hydraulic components and systems in low ambient temperature (Part I). *Polish Maritime Research*, 4/2008.
4. Jasiński R.: Problems of the starting and operating of hydraulic components and systems in low ambient temperature (Part II). Determining the clearance between cooperating elements during the hydraulic components start-up in extremely low ambient temperatures on the grounds of experimental research. *Polish Maritime Research*, 1/2009.
5. Jasiński R.: Problems of the starting and operating of hydraulic components and systems in low ambient temperature (Part III). Methods of determining parameters for correct start-ups of hydraulic components and systems in low ambient temperatures. *Polish Maritime Research*, 4/2009.
6. Jasiński R.: Research and method for assessment of operation of hydraulic drive components started in low ambient temperature and supplied with hot working medium (in Polish). Report on execution of the research project financed by Polish Ministry of Science and Higher Education (in Polish) , No. 4 T07C042 30, Gdańsk 2010.
7. Jasiński R.: Operation of hydraulic drives in low ambient temperatures. Part II (in Polish). *Hydraulika i Pneumatyka*, 2/2011.
8. Jasiński R.: Operation of hydraulic drives in low ambient temperatures. Part V (in Polish). *Hydraulika i Pneumatyka*, 6/2011.
9. Jasiński R.: Determination of ability of machines with hydraulic drive during start-up in low ambient temperatures. *Journal of KONES Powertrain and Transport*, Vol 1, No. 16, 2009.
10. Jasiński R.: Determination of ability of hydrotronic systems to start in low ambient temperatures. *Solid State Phenomena*. - Vol. 164, 2010.
11. Jasiński R.: Experimental tests of axial piston pump PWK 27 from HYDROTOR company in low ambient temperatures (in Polish). *Napędy i Sterowanie*, 4/2008.
12. Jasiński R., Lewandowski P.: Modelling the heating process of axial piston pump PWK 27 from HYDROTOR company during start-up in low ambient temperatures (in Polish). *Napędy i Sterowanie*, 6/2008.
13. Kleiber M.: Introduction to finite elements method (in Polish). PWN, Warszawa-Poznań, 1989.
14. Landvogt B.; Osiecki L.; Patrosz P.; Zawistowski T.; Zylinski B.: Numerical simulation of fluid-structure interaction in the design process for a new axial hydraulic pump. *Progress in Computational Fluid Dynamics*. Vol. 14, No. 1, 2014. doi: 10.1504/PCFD.2014.059198.
15. Osiecki A., Osiecki L.: Development efforts on new design of axial piston pumps (in Polish). *Hydraulika i Pneumatyka* 4/1998, pp. 4–9.
16. Osiecki L., Patrosz P., Zawistowski T., Landvogt B., Piechna J., Żyliński B.: Compensation of pressure peaks in PWK-type hydraulic pumps. *Key Engineering Materials*. Vol. 490., (2012), s.33-44. doi: 10.4028/www.scientific.net/KEM.490.33.
17. Paszota Z.: Energy losses in hydrostatic drive. LABERT Academic Publishing, 2016.
18. Paszota Z.: Energy losses in the hydraulic rotational motor - definitions and relations for evaluation of the efficiency of motor and hydrostatic drive. *Polish Maritime Research* 2(65)/2010.
19. Pobędza J., Sobczyk A.: Properties of high pressure water hydraulic components with modern coatings. *Advanced Materials Research*. Trans Tech Publications Ltd, 849/2014. doi: 10.4028/www.scientific.net/AMR.849.100.
20. Rusiński E.: Finite elements method. COSMOS/M System (in Polish). Wydawnictwa Komunikacji i Łączności, Warszawa 1994.
21. Szargut J.: Numerical modelling of temperature fields (in Polish). WNT, Warszawa 1992.
22. Śliwiński P.: The influence of water and mineral oil on the mechanical losses in a hydraulic motor. *Chinese Journal of Mechanical Engineering*. Article accepted for publication.
23. Śliwiński P.: Influence of water and mineral oil on the leaks in satellite motor commutation unit clearances. *Polish Maritime Research*. Article accepted for publication.
24. Śliwiński P.: The influence of water and mineral oil on volumetric losses in a hydraulic motor. *Polish Maritime Research*, vol. 24, 2017. Doi: 10.1515/pomr-2017-0041.
25. Śliwiński P.: The basics of design and experimental tests of the commutation unit of a hydraulic satellite motor. *Archives of Civil and Mechanical Engineering*, No. 16/2016, DOI: 10.1016/j.acme.2016.04.003.
26. Śliwiński P.: The flow of liquid in flat gaps of satellite motors working mechanism. *Polish Maritime Research*, No. 2/2014.

27. Śliwiński P.: New satellite pumps. *Key Engineering Materials*, No. 490/2012.
28. Wiśniewski S., Wiśniewski T.: Heat exchange (in Polish). WNT, Warszawa 2000.
29. Walczak P., Sobczyk A.: Simulation of water hydraulic control system of francis turbine. *American Society of Mechanical Engineers*, 2014. doi: [dx.doi.org/10.1115/FPNI2014-7814](https://doi.org/10.1115/FPNI2014-7814).
30. Rutkiewicz Ł.: Experimental tests of operation of a proportional spool valve in low ambient temperature conditions (in Polish). Diploma thesis, supervisor: R. Jasiński, Gdańsk University of Technology, Gdańsk, 2006.
31. Staniszewski B.: Heat exchange (in Polish). PWN, Warszawa, 1980.
32. Złoto T., Nagorka A.: An efficient FEM for pressure analysis of oil film in a piston pump. *Applied Mathematics and Mechanics*, Vol.30, No. 1/2009.
33. Catalogues from Hydrotor company.
34. Catalogues from Parker company.
35. Catalogues from Sauer-Danfoss company.

CONTACT WITH THE AUTHOR

Ryszard Jasiński

Gdańsk University of Technology
11/12 Narutowicza St.
80 - 233 Gdańsk
POLAND

INFLUENCE OF WATER AND MINERAL OIL ON THE LEAKS IN SATELLITE MOTOR COMMUTATION UNIT CLEARANCES

Paweł Śliwiński

Gdańsk University of Technology, Poland

ABSTRACT

The article describes the flow rates of mineral oil and water flowing, as working media, through the commutation unit of a hydraulic satellite motor. It is demonstrated that geometrical dimensions of commutation unit clearances change as a function of the machine shaft rotation angle. Methods for measuring the rate of this flow and the pressure in the working chamber are presented. The results of pressure measurements in the working chamber during the transition from the filling cycle to the emptying cycle are included. The pressure in the motor's working chamber changes linearly as a function of the shaft rotation angle, which has a significant effect on the leakage in the commutation unit clearances. The paper presents new mathematical formulas in the form: $Q=f(\Delta p^\gamma)$ to calculate the flow rate of water and mineral oil in the commutation unit clearances. The γ factor is described as a function of fluid viscosity and clearance length (the motor shaft rotation angle). The coefficients used in these formulas were determined based on the results of laboratory tests of a motor supplied with water and mineral oil.

Keywords: flow in clearances, commutation unit, satellite motor, degree of flow laminarity, water, oil

INTRODUCTION

The hydraulic motor is the executive element in the hydraulic system. Its purpose is to convert hydraulic energy into mechanical energy. The energy carrier in hydraulic systems is liquid, and its type is conditioned by certain requirements imposed on these systems. In most hydraulic systems, mineral oil is commonly used [35]. However, in some industrial sectors, the basic requirements can include non-flammability of the liquid (mining, steel mills, etc.), or its non-toxicity to the environment and human health (food industry). The liquid which is non-flammable and non-toxic, and certainly suitable for energy transfer in hydraulic systems is water [25].

Throughout the world, there is a growing trend towards research and development of components and hydraulic systems supplied with water [14,25,30].

Such studies are also of particular importance in the marine technology, where hydraulic power circuits are frequently used and water is generally available as working

liquid [4]. In comparison to mineral oil, water has very low viscosity and low lubricating properties [14,15]. These features adversely influence the efficiency of energy conversion in hydraulic systems [28,29]. Despite this, attempts are made to develop innovative components and hydraulic systems supplied with water [6,25,27,30].

So far, each hydraulic device is dedicated to a specific type of working liquid. For example, a hydraulic motor dedicated for oil systems should not be used in systems where the working medium is water [26,28,29].

Both the pump and the hydraulic motor are hydraulic system components in which large energy losses are generated, including volumetric, mechanical and pressure losses [1,16,17,20,21,22,23,35]. The scale of these losses is affected by both engine design parameters and liquid properties [2, 3,5,7,8,9,10,11,12,13,18,19,20,24,25,30,33,34]

The main source of volumetric losses in a hydraulic motor are clearance leakages in the working mechanism and in the commutation unit [21,24,27,35]. The results of the past research have proved that the type of working liquid has

influence on all types of losses. In general, the motor supplied with low viscosity liquid generates greater energy losses than the motor supplied with oil [27,28]. The influence of water (as a low viscosity liquid) and mineral oil on the flow in flat gaps of the working mechanism was studied in [28]. This article extends the subject to studying the influence of these media on the flow in the motor's commutation unit clearances.

There is no specific information about hydraulic motors which can be alternatively supplied with water and mineral oil. There is only a rich literature on flows in orifices and other simple openings. Furthermore, no comprehensive studies can be found in the literature that compare the influence of the type of liquid on flow characteristics in the commutation unit clearances.

Therefore, from the scientific and cognitive point of view, the research and description of the influence of water and mineral oil on the flow rate in commutation unit clearances of a hydraulic motor is appropriate and justified. Developing a mathematical model to describe the flow in the motor commutation unit which can be supplied either by high or low viscosity liquid is also appropriate and reasonable. Therefore, the influence of the type of working liquid on the losses in the commutation unit of a hydraulic motor is a new issue and represents an important scientific problem.

The present article focuses on the following objectives:

- detailed analysis of the flow in the commutation unit clearances of the satellite working mechanism;
- comparing results of experimental tests of the flow in the commutation unit clearances of the motor supplied with mineral oil and water;
- developing a mathematical model to describe the flow of water and oil in the satellite motor commutation unit and comparing the results of the experimental research with the mathematical model.

OBJECT OF RESEARCH – SATELLITE MOTOR

The experimental research of the influence of mineral oil and water as working media on the flow rate in the commutation unit clearances was carried out on a prototype hydraulic satellite motor, marked with the symbol SM-0,75/25. The most recent design of this motor, developed by the author, is shown in Fig. 1.

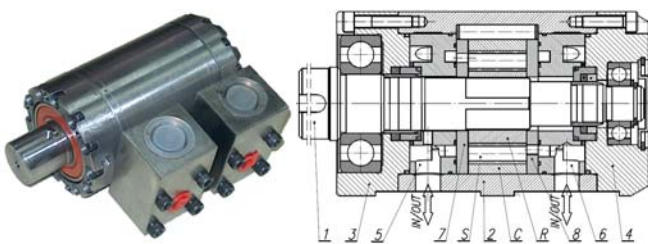


Fig. 1. General view and axial cross section of SM-06 motor: C – curvature, S – satellite, R – rotor, 1 – shaft, 2 – casing, 3 – front casing, 4 – rear casing, 5 and 6 – inlet and exit manifold, 7 and 8 – compensation (commutation) plates [28,29].

The toothed unit, shown in Fig. 2, is the satellite working mechanism of the motor. It consists of a toothed rotor R (4 humps), toothed curvature C (6 humps), and 10 wheels S (satellite).

The principle of operation of the satellite mechanism is the following: when the rotor rotates, the volume of the space between the satellites changes. This space forms the working chamber. When its volume increases, the filling cycle takes place, while when it decreases, we have the emptying cycle. 24 cycles correspond to one shaft revolution. The chambers in the satellite mechanism are closed by the commutation plates (Fig. 1 – elements 7 and 8, and Fig. 3), which also play the role of compensation plates. Thus, the satellite motor has the ability to compensate axial clearances of the rotor and the satellites. This limits the volumetric losses in the working mechanism [24,26,27,28,29].

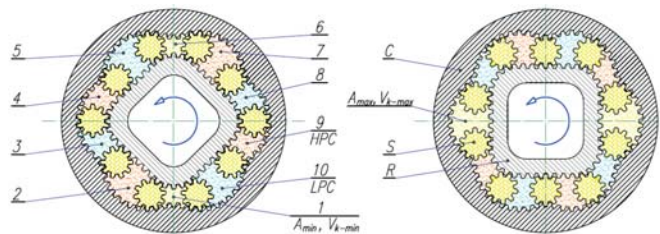


Fig. 2. The working mechanism of the satellite motor: C – stator, R – rotor, S – satellite, 1÷10 – working chambers, LPC – low pressure working chamber, HPC – high pressure working chamber, V_{k-min} – working chamber with minimum area A_{min} (dead chamber), V_{k-max} – working chamber with maximum area A_{max} [24,26,27,28,29].

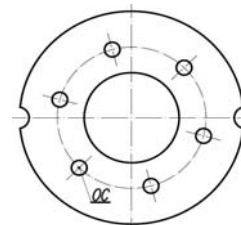


Fig. 3. Distribution plate: OC – inflow/outflow hole [24,26,27,28,29]

The theoretical displacement of the prototype satellite motor used for laboratory tests is $q_t = 32,94 \text{ cm}^3/\text{rev}$. The motor was tested using:

- Total Azolla 46 oil ($\nu_o = 40 \text{ cSt}$, $\rho_o = 873 \text{ kg/m}^3$, $\mu_o = 35 \text{ mPas}$);
- water ($\nu_w = 0,853 \text{ cSt}$, $\rho_w = 996 \text{ kg/m}^3$).

COMMUTATION UNIT IN SATELLITE MOTOR

During the motor shaft rotation, the satellites are moving and properly lock up the inflow holes or open the outflow holes in the compensation plates 7 and 8 (Fig. 1). Correct selection of geometrical dimensions of these holes is very important. The size of the holes has an impact on the volumetric losses.

The holes in the satellite motor compensation plates have a circular shape (Fig. 3).

Oversized holes (the so-called negative overlap of holes by satellites) cause an unwanted flow of liquid Q_{Cm} (so-called flow breakdown) from the high-pressure channel to the low-pressure channel by the death volume (Fig. 4). As a result, the loaded motor generates greater volumetric losses and has, consequently, lower volumetric efficiency. When the stream of liquid supplied to the motor is suitably small, it may even stop the motor. On the other hand, an excessively small diameter of the channels in the compensation plate (the so-called positive overlap of holes by satellites) causes incomplete filling of the working chamber and increases the flow resistance to and from the working chambers. Therefore, a desirable goal is the zero overlap in the satellite motors [27].

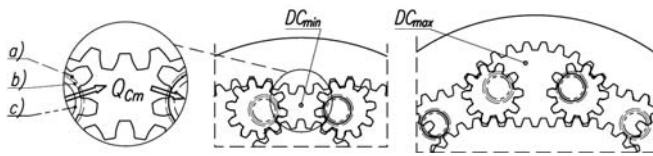


Fig. 4. Overlap of inflow and outflow channels by satellites: a) negative overlap, b) zero overlap, c) positive overlap; Q_{Cm} - instantaneous flow in commutation unit clearances and by death volume DC_{min} .

In the working satellite mechanism, there is a chamber with the minimum death volume

DC_{min} and that with the maximum death volume DC_{max} (Fig. 4).

Methodology of flow rate measurement in commutation unit clearances

In order to experimentally determine the value of Q_{Cm} in short clearances (at the moment of closing the inflow and outflow channels by satellites) it is necessary to measure the instantaneous flow rate Q_m at small constant velocity n and constant pressure drop Δp in the motor. It is possible to keep the rotational speed of the motor low only when it is coupled with the worm gear (Fig. 5). This gear is self-locking and therefore it is required by an electric motor drive.

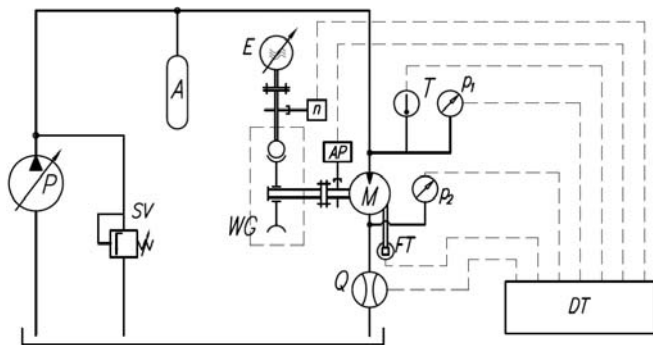


Fig. 5. Scheme of the measuring system: M - tested motor, P - pump, A - accumulator, E - electric motor with frequency converter, SV - safety valve, WG - worm gear, DT - measurement data recorder, Q - flow meter, FT - force sensor (for moment measurement), p_1 and p_2 - pressure sensors, T - temperature sensor, n_1 - rotational speed sensor, AP - sensor measuring angular position of the shaft

The pressure in the working chambers in the tested motor was measured as well. The pressure sensor location is shown in Fig. 6.

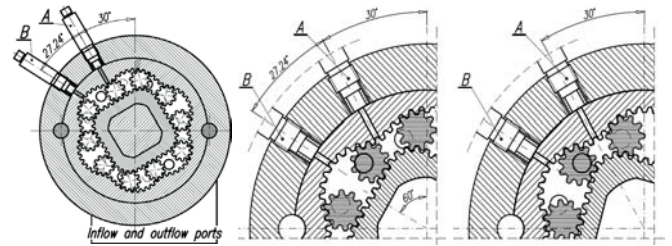


Fig. 6. Method for measuring pressure in motor working chambers: A and B - pressure sensors [27]

RESULTS OF EXPERIMENTAL RESEARCH

The tests of the motor were conducted at a very low constant speed equal to 1 rpm. The results of the flow rate at constant pressure drop were registered for one full rotation of the motor shaft. As a result, the characteristics of the instantaneous flow rate Q_m in the motor as a function of the motor shaft rotation angle α were obtained. Q_m is a sum:

$$Q_m = \frac{q_t \cdot n}{Q_t} + \frac{Q_{Lfgm} + Q_{Cm}}{Q_{Lm}} \quad (1)$$

where:

- q_t - theoretical motor displacement;
- n - rotational speed of the motor shaft;
- Q_t - theoretical flow rate in the motor;
- Q_{Lm} - instantaneous volumetric losses;
- Q_{Lfgm} - instantaneous flow rate in flat clearances;
- Q_{Cm} - instantaneous flow rate in clearances when the inflow and outflow channels are closed by the satellites.

Due to the fact that the engine speed n is very small, the pressure drop Δp_{ich} in the internal channels of the motor can be omitted and then the pressure drop Δp_i in the working chambers is equal to:

$$\Delta p_i = \Delta p = p_1 - p_2 \quad (2)$$

During one full rotation of the shaft, a 12-peak flow rate Q_{Cm-H} of large values and a 12-peak flow rate Q_{Cm-L} of small values (Fig. 7) (24 peaks in total) are observed. Thus, as many as there are filling and emptying cycles in the working chambers per one shaft rotation. It can be shown that:

- smaller peaks Q_{Cm-L} occur when the death volume DC_{min} is formed;
- largest peaks Q_{Cm-H} occur when the death volume DC_{max} is formed.

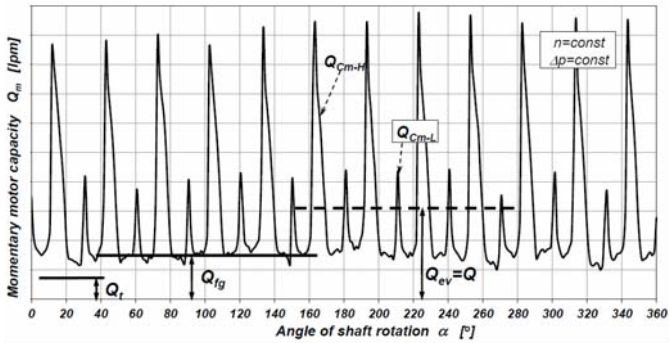


Fig. 7. Characteristic of instantaneous flow rate Q_m in the motor vs. shaft rotation angle α : Q_{Cm-H} - flow rate by maximum death volume, Q_{Cm-L} - flow rate by minimum death volume, $Q_{fg} = Q_t + Q_{Lfgm}$

This is due to:

- satellite movement within the backlash;
- the overlap in the commutation unit. The lowest values of the peaks or no peak at all are observed for positive overlap;
- the accuracy of the shape of rotor and satellite curvatures.

In the satellite mechanism, the death volumes are implemented in pairs. Thus, the peaks of the flow Q_{Cm} shown in Fig. 7 refer to a pair of death volumes.

The characteristics of the course of pressure changes in the working chambers are shown in Fig. 8, while Fig. 9 shows pressure change characteristics caused by changing the commutation unit phasing. It is assumed here that $\alpha=0^\circ$ corresponds to the position of the operating mechanism for which the maximum death volume or the minimum death volume, optionally, exists. Then, for the zero overlap, the fields A_1 and A_2 (Fig. 15) are equal to zero. Q_{Cm} forms in a small range of the shaft rotation angle α . Fig. 8 and Fig. 9 show that the angle α for which the peak grows or decreases is not greater than 2° .

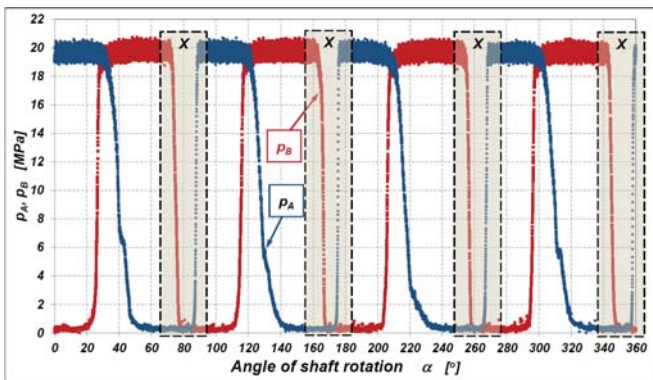


Fig. 8. Characteristics of $p_A=f(\alpha)$ and $p_B=f(\alpha)$: p_A, p_B - pressure measured by sensor A and B, respectively, X - area of sudden pressure drop caused by moving through the dead volume. Inflow and outflow hole diameter 3,8mm. Supply pressure 20 MPa.

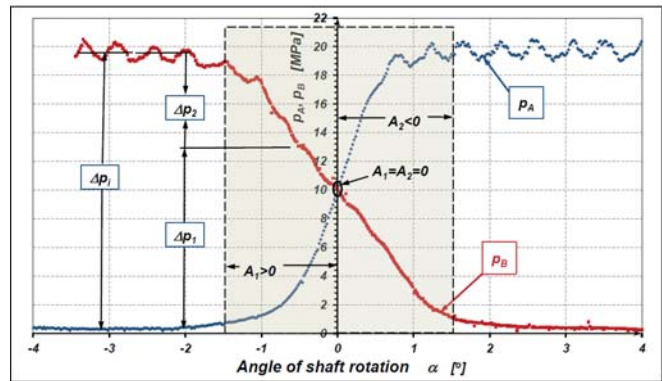


Fig. 9. Area X from Fig. 8. Characteristics of $p_A=f(\alpha)$ and $p_B=f(\alpha)$.

Changing the commutation unit phase results in a linear pressure change in the chambers (Fig. 9). Δp_1 and Δp_2 can be described as:

$$\Delta p_1 = \frac{\Delta p}{2} \cdot \left(1 - \frac{\alpha}{1,3}\right) \quad (3)$$

$$\Delta p_2 = \frac{\Delta p}{2} \cdot \left(1 + \frac{\alpha}{1,3}\right) \quad (4)$$

Further analysis is carried out for the flow rate Q_{Cm-H} (for the flow rate Q_{Cm-L} the analysis is the same). Q_{Cm} is used instead of Q_{Cm-H} for simplification

The experimental characteristics of $Q_{Cm}=f(\alpha>0)$ are shown in Fig. 10. For $\alpha<0$ the shape of the characteristics $Q_{Cm}=f(\alpha<0)$ is a mirror image of the characteristics $Q_{Cm}=f(\alpha>0)$. Fig. 11 shows the characteristics $Q_{Cm}=f(\Delta p)$, which can be described by the equation:

$$Q_{Cm} = C \cdot \Delta p_i^\gamma \quad (5)$$

The values of factors C and γ are shown in Fig. 12 for oil and water, respectively.

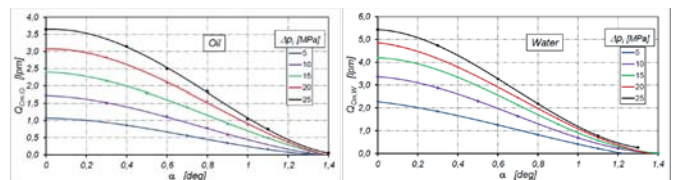


Fig. 10. Characteristics of $Q_{Cm}=f(\alpha)$. Motor supplied with oil (left) and water (right).

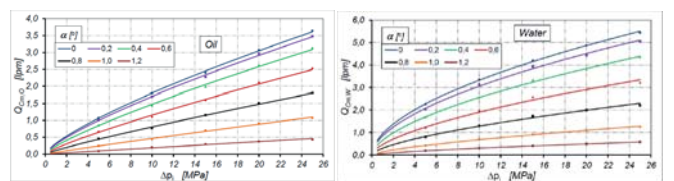


Fig. 11. Characteristics of $Q_{Cm}=f(\Delta p)$. Motor supplied with oil (left) and water (right).

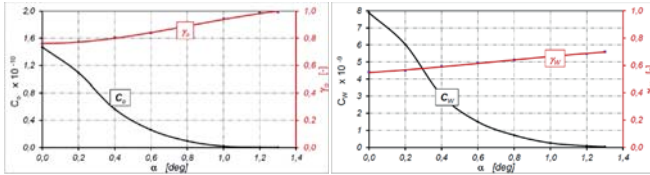


Fig. 12. Characteristics of $C=f(\alpha)$ and $\gamma=f(\alpha)$. Motor supplied with oil (left) and water (right).

The results of the research show (Fig. 13) that the ratio of water flow rate $Q_{Cm,W}$ to oil flow rate $Q_{Cm,O}$ (for $\alpha=const.$), can be written as the empirical equation:

$$\frac{Q_{Cm,W}}{Q_{Cm,O}} = E \cdot \Delta p_i^F \quad (6)$$

where E and F are factors. The values of E and F are shown in Fig. 14 in the form of characteristics. These factors are functions of the shaft rotation angle α (and the clearance length).

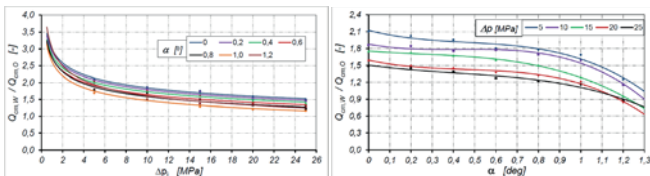


Fig. 13. Characteristics of $Q_{Cm,W}/Q_{Cm,O}=f(\Delta p)$ (left) and $Q_{Cm,W}/Q_{Cm,O}=f(\alpha)$ (right).

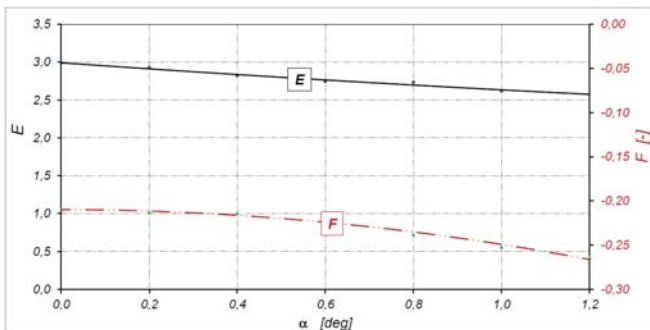


Fig. 14. Characteristics of $E=f(\alpha)$ and $F=f(\alpha)$.

MECHANISM OF Q_{CM} FLOW RATE FORMATION IN COMMUTATION UNIT CLEARANCES

The mechanism of flow rate Q_{Cm} formation in commutation unit clearances is shown in Fig. 15.

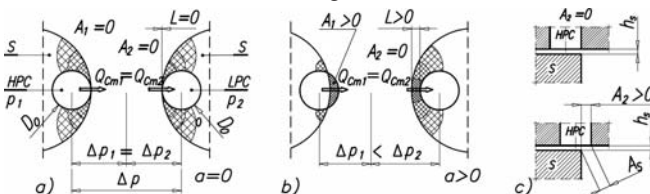


Fig. 15. Position of satellites relative to high pressure hole HPC and low-pressure hole LPC. Zero overlap: a) typical position of satellites for maximum or minimum death volume; b) process of filling the working chamber; c) clearance dimensions for the characteristic position of the satellite.

As shown in Fig. 15, the clearances are arranged in series. For such a case:

$$Q_{Cm1} = Q_{Cm2} = Q_{Cm} \quad (7)$$

$$\Delta p_1 + \Delta p_2 = \Delta p_i = \Delta p \quad (8)$$

For $\alpha=0$ the flow area A_1 is proportional to hole diameter D_o and to clearance height h_s :

$$A_1 = C_2 \cdot D_o \cdot h_s \quad (9)$$

where C_2 is the coefficient of proportionality. To simplify further discussion, $C_2=1$ is adopted.

In the tested satellite motor, the angle range is $\alpha=(0^\circ;2^\circ)$, and A_2 is expressed as:

$$A_2 = 0,107 \cdot m^2 \cdot |\alpha| \quad (10)$$

Therefore, for $\alpha>0$, the flow cross-sectional area A_s is:

$$A_s = \sqrt{A_1^2 + A_2^2} = \sqrt{D_o^2 \cdot h_s^2 + 0,107^2 \cdot m^4 \cdot \alpha^2} \quad (11)$$

For $\alpha>0$ the length L of the clearance is a function of the teeth module m and the shaft rotation angle α . In the satellite mechanism, for $\alpha=(0^\circ;2^\circ)$, the following relationship is true:

$$L = 0,213 \cdot m \cdot \alpha \quad (12)$$

KNOWN METHODS DESCRIBING THE FLOW IN SHORT CLEARANCES

In the literature, the flow in the commutation unit is treated as:

- an average value, independent of the shaft rotation angle [1,21,22];
- a turbulent volumetric loss component, related to the theoretical capacity q_t of the motor [1];

$$Q_C = C_t \cdot \sqrt{\frac{2}{\rho} \cdot \Delta p} \cdot \sqrt[3]{\left(\frac{q_t}{2 \cdot \pi}\right)^2} \quad (13)$$

where:

- C_t - coefficient of proportionality,
- ρ - density of liquid.

The liquid flow in the commutation unit clearances is a typical case of the flow in:

- a sharp-edged clearance (orifice type);
- a flat clearance with a very small length.

In [31,32] the flow rate in short clearances is described by the following formula:

$$Q = C_{d\infty} \cdot \left(1 + a \cdot e^{\frac{-\delta_1}{C_{d\infty}} \sqrt{Re}} + b \cdot e^{\frac{-\delta_2}{C_{d\infty}} \sqrt{Re}} \right) \cdot A \cdot \sqrt{\frac{2}{\rho} \cdot \Delta p} \quad (14)$$

where:

- A – cross-sectional area of the clearance,
- a, b, δ_1 , δ_2 – specific flow dependent coefficients,
- $C_{d\infty}$ – turbulent discharge coefficient.

For clearance types shown in Fig. 16, A and Re are [31]:

$$A = w \cdot x \quad (15)$$

$$Re = 2 \cdot \frac{Q \cdot \rho}{w \cdot \mu} \quad (16)$$

respectively,



Fig. 16. Different types of holes: orifice and short clearances [32].

while for the type shown in Fig. 17, A is [31]:

$$A(x) = \frac{w \cdot x}{1 - e^{-\frac{x}{d_0}}} \quad (17)$$

In the above equations:

- w – clearance width,
- x – dimension of the clearance opening,
- d_0 – clearance height for $x=0$.

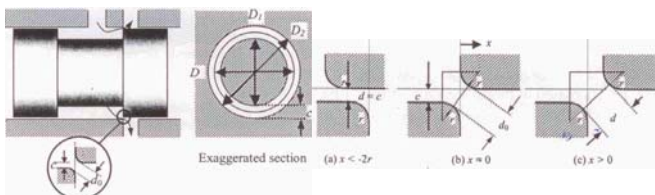


Fig. 17. Flow in rectangular orifice of directional valve spool (left) and enlarged scenario of spool and sleeve chamfers (right) [31].

Equation (14) cannot be used to describe the flow in motor commutation unit clearances because:

- it is an implicit equation;
- there is a laminar flow component at low flow rates of liquid in the clearance. Consequently, describing a partially turbulent flow as function $\Delta p^{0.5}$ is not appropriate;
- clearances change their dimensions during motor shaft rotation, i.e. the clearance dimensions are a function of the shaft rotation angle α .

Therefore, a detailed analysis of the flow in short clearances of the satellite mechanism commutation unit is justified, as it will allow to simulate more accurately the characteristics of volumetric losses in the hydraulic motor.

MATHEMATICAL MODEL OF FLOW RATE IN COMMUTATION UNIT CLEARANCES

Based on the above experimental results, it has been concluded that the flow in both clearances (Fig. 15) is turbulent and not fully developed.

For $\alpha > 0$ the first clearance (Fig. 15) has the cross-sectional area $A_s = f(\alpha)$. It is assumed that:

$$Q_{Cm1} = Q_{Cm} = \underbrace{A_s \cdot \left(\frac{2}{\zeta \cdot \rho} \right)^{0.5}}_{C_1} \cdot \Delta p_1^{0.5} \quad (18)$$

and

$$\zeta = \frac{K_1}{Re \beta_1} \quad (19)$$

$$Re = \frac{c_1 \cdot A_s^{0.5}}{\nu} \quad (20)$$

The relations between c_1 and A_s is:

$$c_1 = \frac{Q_{Cm1}}{A_s} \quad (21)$$

Taking into account Equations (3) and (11), the flow rate is:

$$Q_{Cm1} = \underbrace{(D_o^2 \cdot h_s^2 + 0.1072 \cdot m^4 \cdot \alpha^2)^{\frac{1}{4}}}_{c_1} \cdot \underbrace{\left(\frac{2}{K_1 \cdot \rho \cdot \nu \beta_1} \right)^{\frac{1}{4}}}_{\left(\frac{1}{\Delta p_1} \right)^{\frac{1}{4}}} \cdot \underbrace{\left(\frac{1.3 - \alpha}{2.6} \cdot \Delta p \right)^{\frac{1}{4}}}_{\Delta p_1^{\frac{1}{4}}} \quad (22)$$

In the second slot, the flow can be described by the formula [5]:

$$Q_{Cm2} = Q_{Cm} = \left(\frac{1}{\nu} \right)^{\frac{\beta_2}{2 - \beta_2}} \cdot \left(\frac{1}{K_2 \cdot \rho} \right)^{\frac{1}{2 - \beta_2}} \cdot b \cdot \left(\frac{2 \cdot h_s^3}{L} \right)^{\frac{1}{2 - \beta_2}} \cdot \Delta p_2^{\frac{1}{2 - \beta_2}} \quad (23)$$

Assuming $b = D_o$ and taking into account the relationship (4) and (12) we get:

$$Q_{Cm2} = D_o \cdot \underbrace{\left(\frac{9.39 \cdot h_s^3}{m \cdot \alpha \cdot K_2 \cdot \rho \cdot \nu \beta_2} \right)^{\frac{1}{2 - \beta_2}}}_{C_2} \cdot \underbrace{\left(\frac{1.3 + \alpha}{2.6} \cdot \Delta p \right)^{\frac{1}{2 - \beta_2}}}_{\Delta p_2} \quad (24)$$

There are two unknowns in each of Equations (22) and (24), which are: K_1 , β_1 , K_2 and β_2 . Nonetheless, for the flow:

- $b_1 = 0$ cannot be accepted in the first clearance;
- $b_2 = 1$ cannot be accepted in the second clearance.

If α increases, then:

- A_s increases in the first clearance;
- Δp_1 decreases and Δp_2 increases;
- length L of the second clearance increases;
- the low rate in both clearances decreases.

Therefore, the flow becomes less disturbed in both clearances. Hence, γ is growing in both cases. It is proposed to assume that:

$$\gamma_1 = \gamma_2 = \gamma \quad (25)$$

which leads to:

$$\beta_1 = \beta_2 \quad (28)$$

Due to the fact that $Q_{Cm1} = Q_{Cm2} = Q_{Cm}$, and comparing (22) and (24) to (5) we arrive at:

$$C_1 \cdot \left(\frac{1,3-\alpha}{2,6}\right)^Y = C_2 \cdot \left(\frac{1,3+\alpha}{2,6}\right)^Y = C \quad (29)$$

The above analysis shows that the flow rate Q_{Cm} in satellite motor commutation unit clearances can be described both by formula (22) and formula (24).

Taking into account C_1 and C_2 from equations (22) and (24), the coefficients K_1 and K_2 can be calculated as:

$$K_1 = \frac{(1,3-\alpha)}{1,3} \cdot \frac{(D_o^2 \cdot h_s^2 + 0,1072 \cdot m^4 \cdot \alpha^2)^{(0,5 + \frac{1}{4} \gamma)}}{C^{\left(\frac{1}{\gamma}\right)} \cdot \rho \cdot \nu^{(2 - \frac{1}{\gamma})}} \quad (30)$$

$$K_2 = 3,61 \cdot \left(1 + \frac{1,3}{\alpha}\right) \cdot \left(\frac{D_o}{C}\right)^{\left(\frac{1}{\gamma}\right)} \cdot \frac{h_s^3}{m \cdot \rho \cdot \nu^{(2 - \frac{1}{\gamma})}} \quad (31)$$

These coefficients are functions of the motor shaft rotation angle. Therefore, they depend on the length of the clearances. The values of these coefficients are shown in Fig. 18.

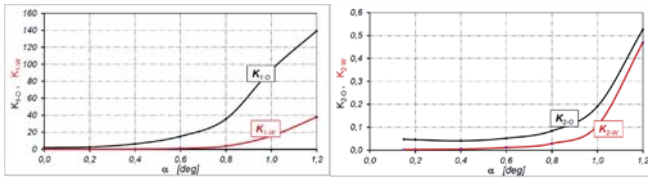


Fig. 18. Characteristics: $K_{1,0}=f(\alpha)$ and $K_{2,0}=f(\alpha)$ for motor supplied with oil; $K_{1,W}=f(\alpha)$ and $K_{2,W}=f(\alpha)$ for motor supplied with water.

AVERAGE VALUE OF PEAK FLOW

The average value of one peak flow is:

$$Q_{Cm-av} = \frac{1}{\alpha} \cdot \int_0^\alpha Q_{Cm} d\alpha \quad (32)$$

The average value of the flow in clearances during one shaft rotation is:

$$Q_C = \frac{z_C \cdot z_R}{720} \cdot \left(\int_0^{\alpha_H} Q_{Cm-H} d\alpha + \int_0^{\alpha_L} Q_{Cm-L} d\alpha \right) \quad (33)$$

where:

- z_R – number of rotor humps,
- z_C – number of curvature humps;
- α_H – angle at which a higher flow peak [deg] disappears or is formed;

- α_L – angle at which a lower flow peak [deg] disappears or is formed.

The experimental research (Fig. 7) has shown that:

$$\frac{Q_{Cm-H-av}}{Q_{Cm-L-av}} \approx 2,5 \quad (34)$$

Thus, for $z_R=4$ and $z_C=6$

$$Q_C = \frac{33,6}{360} \cdot \int_0^{\alpha_H} Q_{Cm-H} d\alpha \quad (35)$$

Due to the fact that coefficient β depends on the shaft rotation angle, the integral in Equation (35) has no solution. Therefore, it is proposed to simplify the problem and assume that the average value:

a) for a single higher peak is equal to:

$$Q_{Cm-H-av} = \frac{(Q_{Cm-H})_{\alpha=0}}{2} \quad (36)$$

b) for a single lower peak is equal to (according to (34)):

$$Q_{Cm-L-av} = \frac{(Q_{Cm-H})_{\alpha=0}}{5} \quad (37)$$

c) during one rotation of the shaft, for $z_R=4$ and $z_C=6$, in analogy to (33):

$$Q_C = 0,0932 \cdot \alpha_{max} \cdot (Q_{Cm-H-av})_{\alpha=0} \quad (38)$$

Here, α_{max} is the angle for which the peak is equal to zero. In this case $\alpha_{max}=1,3$. In addition, for $\alpha=0$ the coefficient:

- $\beta_{1,0}=0,684$ and $\beta_{1,W}=0,183$;
- $K_{1,0}=1,792$ and $K_{1,W}=0,0144$.

Hence:

- for oil:

$$Q_{C,O} = 0,077 \cdot (D_o \cdot h_s)^{1,26} \cdot \left(\frac{1}{\rho_O \cdot \nu_O^{0,684}}\right)^{0,76} \cdot \Delta p^{0,76} \quad (39)$$

- for water:

$$Q_{C,W} = 1,25 \cdot (D_o \cdot h_s)^{1,05} \cdot \left(\frac{1}{\rho_W \cdot \nu_W^{0,183}}\right)^{0,55} \cdot \Delta p^{0,55} \quad (40)$$

The characteristics of $Q_{C,O}$ and $Q_{C,W}$ obtained based on experimental data and calculated from formulas (39) and (40) are compared in Fig. 19.

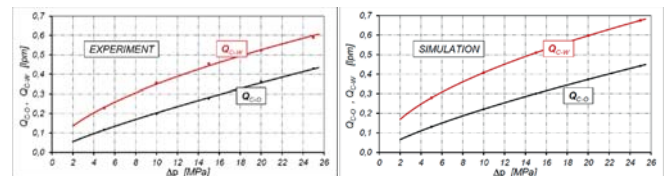


Fig. 19. Characteristics of $Q_{C,W}=f(\Delta p)$ and $Q_{C,O}=f(\Delta p)$ experimentally obtained (left) and calculated from equations (39) and (40) (right).

DISCUSSION

The research results have proved that for a given pressure drop, in short clearances of the motor working mechanism (i.e. commutation unit clearances), the flow rate of water is at most 3,5 times greater than that of oil (Fig. 13). This ratio decreases with the increasing Δp in the motor. Thus, the flow of both water and oil is not a fully developed turbulent flow within, practically, the whole pressure drop range in the motor. For a high pressure drop in the motor (25 MPa), the water/oil flow rate ratio does not exceed 1.5.

The research results have also shown (according to Fig. 19), that:

a) for $\Delta p=5$ MPa $\frac{Q_{C,W}}{Q_{C,O}} \cong 2;$

d) for $\Delta p=25$ MPa $\frac{Q_{C,W}}{Q_{C,O}} \cong 1,4.$

Thus, the use of water instead of oil leads to the increase in volumetric losses in short clearances, for example, by about 40% at $\Delta p=25$ MPa. For comparison, in flat clearances of the motor working mechanism, the flow rate of the 1% HFA-E emulsion is at least more than ten times greater than the flow rate of oil [28]. It was also observed that with the increasing shaft rotation angle, flow disturbances in both clearances of the commutation unit became smaller. Therefore, the description of the flow rate in short clearances of the commutation unit may base on both formula (22) and formula (24). Formula (22) is more suitable as it can describe the flow in a commutation unit with negative overlap, i.e. for the case $\alpha=0$ when we have $A_1>0$ and $A_2>0$.

It follows from both formula (22) and formula (24) that the flow rate Q_{cm} in short commutation unit clearances depends on the clearance height h_s and the diameter D_o of the inflow and outflow hole from the working chambers. It can therefore be assumed that coefficient ζ is a function of fluid viscosity and geometrical dimensions of the clearance. The value of this coefficient increases with the increasing shaft rotation angle α , as the value of the coefficient K_1 is also increasing (Fig. 18).

For a large rotation angle (here about $1,2^\circ$) Q_{Cm} nears zero, and then:

$$\frac{K_{2,O}}{K_{2,W}} \approx \frac{\rho_W}{\rho_O} = 1,14 \quad (41)$$

which is a typical value for the flow in flat clearances of the satellite working mechanism [28].

The experimental research has shown that for both oil and water, the coefficient γ is a function of the shaft rotation angle α , i.e. the length L of the clearance (Fig. 12). Furthermore, this coefficient is dependent on the viscosity μ of the liquid. Hence, $\gamma=f(\mu,L)$. Theoretically, the function describing the relationship between γ , μ and L should take the asymptotic value of 0.5 and 1. Such features have modified the function arctan, respectively. Thus, it is proposed as [27]:

$$\gamma = 0,5 \cdot \left(2,5 \cdot \frac{\mu}{\mu_R}\right)^{\frac{\alpha}{4}} \cdot \arctg \left(\left(0,1 + \frac{\alpha}{\alpha_R}\right)^{\left(\frac{\mu_R}{5\mu}\right)^2} - 0,5 \right) + 0,75 \quad (42)$$

where:

- μ – dynamic viscosity of the liquid [mPas];
- μ_R – reference dynamic viscosity, here assumed as $\mu_R = 100$ mPas;
- α – shaft rotation angle [°].

The above mathematical formula was determined empirically. The characteristics of coefficient γ , plotted according to (42) for oil and water, are shown in Fig. 20. These characteristics are somewhat different from the experimental data. Greatest difference occurs for oil and is about 8.5%. As a result, the flow rate Q_{Cm} , calculated according to (22) (Fig. 20) will also be inaccurate. For oil, within the range of $\alpha=0,2$, this error reaches 38%.

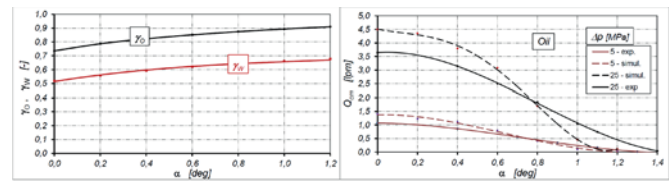


Fig. 20. Characteristics of $\gamma_o=f(\alpha)$ and $\gamma_w=f(\alpha)$ calculated according to formula (42) for motor supplied with oil and water (left). Characteristics $Q_{Cm,o}=f(\alpha)$ calculated according to formula (22) for motor supplied with oil (right).

The values of the average oil flow rate $Q_{C,O}$ and the average water flow rate $Q_{C,W}$ in commutation unit clearances, calculated from the relation (39) and (40) respectively, are higher than those determined experimentally. The smallest differences are observed for the motor supplied with oil and, for example, for $\Delta p = 25$ MPa they amount to only 3%, compared to 15% for water and the same pressure drop.

In the operating mechanism of the motor, the flow rate in commutation unit clearances is one of volumetric loss sources. Other sources include:

- the liquid flow rate in flat clearances of the working mechanism [28];
- the liquid flow rate in the spaces between the teeth of the working mechanism;
- the liquid flow rate caused by cyclic elastic deformation of the working chambers [1];
- the liquid flow rate depending on liquid compressibility [1].

In the overall balance of volumetric losses in the motor supplied with oil, the error of 3% in the calculation of $Q_{C,O}$ is very small. On the other hand, the error of 15% in the calculation of $Q_{C,W}$ in the motor supplied with water seems to be large. However, the flow rate $Q_{C,W}$ in comparison to the flow rate $Q_{L,fg,W}$ of the water in working mechanism flat clearances is at least four times lower. Furthermore, the experiments have shown that the flow rate of the liquid pumped by the spaces between the teeth of the operating mechanism depends on the speed and represents the highest value. Therefore, the $Q_{C,W}$ calculation error at the level of 15% is acceptable.

SUMMARY

The article presents the methodology and experimental results of examination of the flow rate in short clearances in the commutation unit of the working mechanism of a satellite motor. These clearances change their length during motor shaft rotation. The experimental studies have shown that both the oil flow and the water flow in these clearances are turbulent and not fully developed. The mathematical model presented in the article will be used to build a model of volumetric losses in the motor. This model will be the subject of a further publication.

The mathematical model described in the paper will be used to describe the flow rate in satellite pump commutation unit clearances.

The other planned publication will describe the results of CFD calculations of the liquid flow in short clearances of the motor working mechanism. These results will be compared with the results of the experiment and calculations based on the here presented mathematical model.

ACKNOWLEDGMENT

The article was developed in the framework of the project LIDER/35/102/L-2/10/NCBiR/2011, entitled: *New study of hydraulic satellite machines for drives with bioliquids and non-flammable liquids* and funded by the National Centre for Research and Development in Poland.

REFERENCES

1. Balawender A.: Physical and mathematical model of losses in hydraulic motors. Developments in mechanical engineering, Gdansk University of Technology Publishers. Gdansk 2005.
2. Bing X., Junhui Z., Huayong Y., Bin Z.: Investigation on the Radial Micro-motion about Piston of Axial Piston Pump. Chinese Journal of Mechanical Engineering, Vol. 26, No. 2, 2013. DOI: 10.3901/CJME.2013.02.325.
3. Deptula A., Osinski P., Partyka M.: Identification of influence of part tolerances of 3PWR-SE pump on its total efficiency taking into consideration multi-valued logic trees 60. Polish Maritime Research, 1(93)/2017, vol. 24. DOI: 10.1515/pomr-2017-0006
4. Dymarski C., Dymarski P.: Developing Methodology for Model Tests of Floating Platforms in Low-Depth Towing Tank. Archives of Civil and Mechanical Engineering, No 1/2016, DOI: dx.doi.org/10.1016/j.acme.2015.07.003
5. Gao J., Huang W., Quan L., Huang J.: The distributed parameter model of hydraulic axial piston motor and its application in hydraulic excavator swing systems. Proceedings of the Institution of Mechanical Engineers Part I Journal of Systems and Control Engineering, April 2017. DOI: 10.1177/0959651817704098
6. Gelesz P., Karczewski A., Kozak J., Litwin W., Piatek L.: Design Methodology for Small Passenger Ships on the Example of the Ferryboat Motława 2 Driven by Hybrid Propulsion System. Polish Maritime Research, special issue S1 (93) 2017, vol. 24. DOI: 10.1515/pomr-2017-0023
7. Guzowski A., Sobczyk A.: Reconstruction of hydrostatic drive and control system dedicated for small mobile platform. American Society of Mechanical Engineers, 2014. DOI: dx.doi.org/10.1115/FPNI2014-7862.
8. Jasinski R.: Problems of the starting and operating of hydraulic components and systems in low ambient temperature (Part I). Polish Maritime Research, No 4/2008. DOI: 10.2478/v10012-007-0095-9.
9. Jasinski R.: Problems of the starting and operating of hydraulic components and systems in low ambient temperature (Part II). Polish Maritime Research, No 1/2009. DOI: 10.2478/v10012-008-0012-x.
10. Jasinski R.: Problems of the starting and operating of hydraulic components and systems in low ambient temperature (Part III). Methods of determining parameters for correct start-ups of hydraulic components and systems in low ambient temperatures. Polish Maritime Research, No 4/2009. DOI: 10.2478/v10012-008-0052-2.
11. Ke M., Ding F., Li B., Chen Z.: Exploration of the influence of backing pressure on the efficiency of hydraulic motor. Nongye Jixie Xuebao/Transactions of the Chinese Society of Agricultural Machinery, 37(10), October 2006.
12. Kollek W., Osinski P., Wawrzynska U.: The influence of gear micropump body asymmetry on stress distribution. Polish Maritime Research, 2(65)/2010. DOI: 10.1515/pomr-2017-0007.
13. Landvogt B., Osiecki L., Patrosz P., Zawistowski T., Zylinski B.: Numerical simulation of fluid-structure interaction in the design process for a new axial hydraulic pump. Progress in Computational Fluid Dynamics, Vol. 14, Issue 1, 2014. DOI:doi.org/10.1504/PCFD.2014.059198.
14. Litwin W., Olszewski A.: Water-Lubricated Sintered Bronze. Journal Bearings - Theoretical and Experimental Research. Tribology Transactions, vol. 57, No 1/2014.

15. Lubinski J., Sliwinski P. Multi parameter sliding test result evaluation for the selection of material pair for wear resistant components of a hydraulic motor dedicated for use with environmentally friendly working fluids. *Solid State Phenomena* Vol. 225(2015). DOI: 10.4028/www.scientific.net/SSP.225.115.
16. Maczyszyn A.: Evaluation of losses in a hydraulic motor based on the SWSB - 63 motor tests. *Polish Maritime Research*, 4(17)/2010. DOI: 10.2478/v10012-010-0035-y.
17. Maczyszyn A.: Method of Sum of Power Losses as a Way for Determining the k_i Coefficients of Energy Losses in Hydraulic Motor. *Polish Maritime Research*, 2(23)/2016. DOI: 10.1515/pomr-2016-0021.
18. Osiecki L., Patrosz P., Landvogt B., Piechna J., Zawistowski T., Zylinski B.: Simulation of fluid structure interaction in a novel design of high pressure axial piston hydraulic pump. *Archive of Mechanical Engineering. The Journal of Committee on Machine Building of Polish Academy of Sciences*, Vol. 60, Issue 4, 2013. DOI: 10.2478/meceng-2013-0031.
19. Osiecki L., Patrosz P., Zawistowski T., Landvogt B., Piechna J., Zylinski B.: Compensation of pressure peaks in PWK type hydraulic pumps. *Key engineering materials*, Vol. 490, 2011. DOI: 10.4028/www.scientific.net/KEM.490.33.
20. Osinski P., Deptula A., Partyka M.: Discrete optimization of a gear pump after tooth root undercutting by means of multi-valued logic trees. *Archives of Civil and Mechanical Engineering*, No 4/2013, DOI: 10.1016/j.acme.2013.05.001.
21. Paszota Z.: *Energy losses in hydrostatic drive*. LAP LAMBERT Academic Publishing, 2016.
22. Paszota Z.: Energy losses in the hydraulic rotational motor - definitions and relations for evaluation of the efficiency of motor and hydrostatic drive. *Polish Maritime Research*, 2(65)/2010. DOI: 10.2478/v10012-010-0017-0.
23. Paszota Z.: Power of energy losses in hydrostatic drive system elements – definition, relationships, ranges of changes, energy efficiencies. Part 1 – hydraulic motor. *Drives and Control*, 11/2007, Poland.
24. Patrosz P.: Deformation in the axial clearance compensation node in the satellite pump unit. *Hydraulics and Pneumatics* 1/2014, Poland.
25. Pobedza J., Sobczyk A.: Properties of high pressure water hydraulic components with modern coatings. *Advanced Materials Research*. Trans Tech Publications Ltd, 849/2014. DOI: 10.4028/www.scientific.net/AMR.849.100.
26. Sliwinski P.: New satellite pumps. *Key Engineering Materials*, No 490/2012. DOI: 10.4028/www.scientific.net/KEM.490.195.
27. Sliwinski P.: The basics of design and experimental tests of the commutation unit of a hydraulic satellite motor. *Archives of Civil and Mechanical Engineering*, No 16/2016, DOI: 10.1016/j.acme.2016.04.003.
28. Sliwinski P.: The flow of liquid in flat gaps of satellite motors working mechanism. *Polish Maritime Research* 2/2014. DOI: 10.2478/pomr-2014-0019.
29. Sliwinski P.: The influence of water and mineral oil on volumetric losses in a hydraulic motor. *Polish Maritime Research*, special issue S1 (93) 2017, vol. 24. DOI: 10.1515/pomr-2017-0041.
30. Walczak P., Sobczyk A.: Simulation of water hydraulic control system of Francis turbine. *American Society of Mechanical Engineers*, 2014. doi: dx.doi.org/10.1115/FPNI2014-7814.
31. Wu D., Burton R., Schoenau G., Bitner D.: Modeling of orifice flow rate at very small openings. *International Journal of Fluid Power*, vol. 4, No. 1, April 2003.
32. Wu D., Burton R., Schoenau G.: An empirical discharge coefficient model for orifice flow. *International Journal of Fluid Power*, vol. 3, No. 3, December 2002.
33. Xiaogang Z., Long Q., Yang Y., Chengbin W., Liwei Y.: Output Characteristics of a Series Three-port Axial Piston Pump. *Chinese Journal of Mechanical Engineering*, Vol. 25, No. 3, 2012. DOI: 10.3901/CJME.2012.03.498.
34. Yu H., Luo C., Wang H.: Performances of a Balanced Hydraulic Motor with Planetary Gear Train. *Chinese Journal of Mechanical Engineering*, Vol. 25, No. 4, 2012. DOI: 10.3901/CJME.2012.04.760.
35. Zloto T., Nagorka A.: An efficient FEM for pressure analysis of oil film in a piston pump. *Applied Mathematics and Mechanics*, vol. 30, No 1/2009.

CONTACT WITH THE AUTHOR

Paweł Śliwiński

e-mail: pawel.sliwinski@pg.gda.pl

Gdansk University of Technology
Narutowicza 11/12
80-233 Gdansk
POLAND

MODERN MODELING OF WATER HAMMER

Kamil Urbanowicz

West Pomeranian University of Technology, Poland

ABSTRACT

Hydraulic equipment on board ships is common. It assists in the work of: steering gear, pitch propellers, watertight doors, cargo hatch covers, cargo and mooring winches, deck cranes, stern ramps etc. The damage caused by transient flows (which include among others water hammer) are often impossible to repair at sea. Hence, it is very important to estimate the correct pressure runs and associated side effects during their design. The presented study compares the results of research on the impact of a simplified way of modeling the hydraulic resistance and simplified effective weighting functions build of two and three-terms on the estimated results of the pressure changes. As it turns out, simple effective two-terms weighting functions are able to accurately model the analyzed transients. The implementation of the presented method will soon allow current automatic protection of hydraulic systems of the adverse effects associated with frequent elevated and reduced pressures.

Keywords: hydraulic system, cavitation, water hammer, wall shear stress, weighting function

INTRODUCTION

Incompetent accelerating, stopping and sudden changes in direction of fluid flow in hydraulic systems are responsible for periodic pressure spikes. These spikes are referred to in hydraulics as water hammer and are directly related to the conversion of kinetic energy of flowing fluid into pressure energy. Pressure amplitudes at the moment when the aforementioned phenomenon occurs far outweigh the average working values and can easily lead to a leak in piping components.

One should be aware that the occurrence of a severe water hammer in hydraulic systems installed on ships (hydraulic systems for steering gear, pitch propellers, watertight doors, cargo hatch covers, cargo and mooring winches, deck cranes, stern ramps etc.) is not acceptable [4,12]. It is almost always associated with the occurrence of minor or major damage. Repairing the damage at the sea, is often impossible due to the lack of spare parts and if done temporarily it can quickly prevent the further safe travel of the ship.

Quick closing valves are the main element of hydraulic systems responsible for the impact force. Their installation must be preceded by a number of design tests. Due to the complexity of unsteady fluid flow in pressure lines, resulting from the superposition of the effects associated with many accompanying phenomena: cavitation [1,3,5,6,9,14,17], FSI – fluid structure interaction [5,7,10,25], frequency dependent resistance [2,8,13,15,16,17,19,21-23,26] or viscoelastic properties of polymer pipes [6,10,11,25]; it is necessary to use the help of numerical methods in the design calculations. They make it possible to solve partial differential equations, which describe the type of flow analyzed. The simplest method is the so-called method of characteristics [24], the use of which in this area has been known for over half a century. It has gained global application only after the development of personal computers. The main drawback of this method is its opacity, resulting from the complexity of the issue of modelling unsteady hydraulic resistance. This paper attempts to use a simplified method of calculating time-varying hydraulic resistance. Wall shear stress was presented as the

sum of the quasi-steady and time-varying (expressed in a simplified manner) expressions.

NEED FOR RAPID SIMULATION OF WATER HAMMERS

Unsteady flow of fluids in pipes under pressure is described mathematically using a pair of continuity (1) and motion (2) equations [24]:

$$\frac{\partial p}{\partial t} + \rho c^2 \frac{\partial v}{\partial x} = 0 \quad (1)$$

$$\frac{\partial p}{\partial x} + \rho \frac{\partial v}{\partial t} + \rho g \sin \gamma + \frac{2}{R} \tau_w = 0 \quad (2)$$

where: p – pressure, t – time, ρ – density, c – speed of pressure wave propagation, v – flow velocity, x – axis coordinate, g – acceleration due to gravity, γ – pipe tilt, R – inner radius, τ_w – wall shear stress.

The key parameter of hydraulic resistance in the equations written out above is wall shear stress τ_w occurring in the motion equation. In this work, this stress is calculated from the sum of two expressions:

$$\tau_w = \tau_q + \tau_u \quad (3)$$

The subscript “ q ” means that the expression is calculated using the quasi-steady method, while the expression with subscript “ u ” is directly related to the non-stationarity of flow. The accuracy of the simulated pressure runs depends on the method of expressing the unsteady expression τ_u and the number of simplifications assumed in the numerical solution of the system in the aforementioned equations. The method of characteristics is a widely known and recognized method for solving these equations. The calculations applied in this method are carried out on all calculation nodes, distributed evenly along the length of the pipe. They represent subsequent cross-sections of the analyzed pressure line for discrete moments of time, evenly occurring from the appearance of non-stationarity, until the final analysis. The more nodes (in cross-sections along the length of the pipe) are included in the calculations, the more instantaneous values of the basic parameters (pressure and velocity) describing the flow will need to be determined. Numerical calculations therefore take much more time. Current advanced control systems, to effectively protect systems against possible adverse events occurring at the time of the emergence of non-stationary conditions, necessitate continuous development of numerical methods. In terms of control, the ideal situation would take place at a time when a simple computer controlling a hydraulic system would be able to predict basic flow parameters, in advance, through a simplified computer simulation. This

will allow for finding an early correct answer regarding the appropriate controls for the given system. Systems will then be protected using follow-up control against too high and too low pressures. High pressure can cause damage due to leaks, low pressure is responsible for the occurrence of cavitation areas causing rapid erosion of the inner surface of the piping. Application of follow-up control methods discussed above eliminates the need to install currently known and used expensive damping devices (air water tanks or modern bleed valves) which role is to protect hydraulic systems against damaging effects associated with a pressure surge.

As noted above, increasing the speed of modelling pressure in the piping is a very important issue, which will enable further systematic development of control methods. During the modelling of unsteady hydraulic resistance, the use of simplified weighting functions, constructed from only two or three exponential expressions, in combination with a method lumping unsteady friction [8] only in the boundary nodes (the inlet and outlet of the pipe), will allow to considerably unburden the numerical mathematical process.

It remains to be checked if the results of simulated runs will have a sufficient accuracy with such a large number of simplifications? This paper will try to answer this question, especially in the next chapter, where results of the research carried out will be described.

RESEARCH SCOPE AND RESULTS

The weighting functions, composed of multiple exponential expressions, significantly increase operating time of a computer, as the number of expressions describing them is also the upper summation index necessary to determine the unsteady part of wall shear stress in each node of the characteristic grid. Refinement of effective numerical solution of the convolution integral:

$$\tau_u = \frac{2\mu}{R} \int_0^t w(t-u) \frac{\partial v}{\partial t}(u) du \quad (4)$$

where: μ – dynamic viscosity, $w(t-u)$ – weighting function, describing the unsteady expression of wall shear stress, presented in the paper by Urbanowicz and Zarzycki [18], made it possible to limit the scope of applicability representing the effective weight function used from the previously recommended range $[10^{-3} \Delta \hat{t}; \infty)$ to $[\Delta \hat{t}; \infty)$. Subsequent research has shown that this range may be further limited to $[\Delta \hat{t}; 10^3 \Delta \hat{t}]$ without noticeably decreasing the accuracy of the calculations [19]. Two and three expression functions used in the simulations carried out in this project will feature this narrow range. The number of expressions representing an effective weighting function is related to the numerical solution of the convolution integral used for calculating wall shear stress in the calculation nodes for the method of characteristics in the following way [18]:

$$\tau_{w(t+\Delta t)} = \frac{\rho \lambda_{(t+\Delta t)} V_{(t+\Delta t)} |V_{(t+\Delta t)}|}{8} + \frac{2 \cdot \mu}{R} \cdot \sum_{i=1}^j \left[\underbrace{y_{i(t+\Delta t)} \cdot A_i + \eta \cdot B_i \cdot [V_{(t+\Delta t)} - V_{(t)}]}_{y_{i(t+\Delta t)}} + [1 - \eta] \cdot C_i \cdot [V_{(t)} - V_{(t-\Delta t)}] \right] \quad (5)$$

where: λ – hydraulic resistance coefficient, η – weighting function correction factor, Δt – numerical time step.

Constants in the above equation (5) are calculated as follows:

$$A_i = e^{-n_i \cdot \Delta t}; B_i = \frac{m_i}{\Delta t \cdot n_i} \cdot [1 - A_i]; C_i = A_i \cdot B_i \quad (6)$$

where n_i and m_i – coefficients describing the effective weighting functions, Δt – dimensionless time step.

Simulations implemented in this project on a large scale were designed to determine:

A) The effect of the method of calculating wall shear stress using the method of characteristics. Numerical research was carried out using the standard method SM (shear stress calculated at each numerical node using equation (5)) and the simplified method LFM (full calculation only in boundary nodes) [8], in which the shear stress in all internal nodes of the grid of characteristics is calculated using a simple quasi-steady formula:

$$\tau_{w(t+\Delta t)} = \frac{\rho \lambda_{(t+\Delta t)} V_{(t+\Delta t)} |V_{(t+\Delta t)}|}{8} \quad (7)$$

B) The impact of the construction and the scope of the effective weighting functions applicability on the results obtained. In particular, simple functions composed of only two and three exponential expressions (Fig. 1) were tested. For comparison, a highly accurate function, consisting of 10 exponential expressions, was also estimated. All functions were estimated using the method presented in [20]. In the numerical process, the coefficients of these estimated functions were scaled using assumptions about their universality [17]. Specific values of the coefficients are listed in the Appendix.

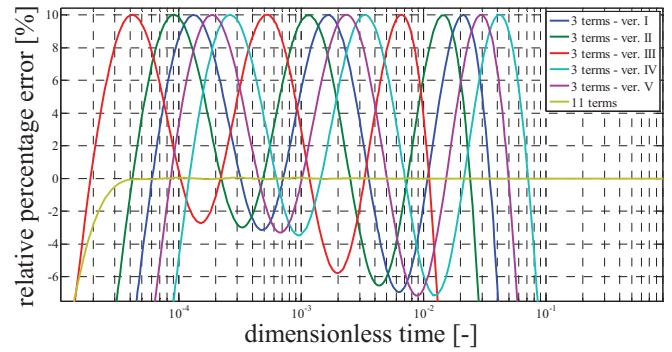
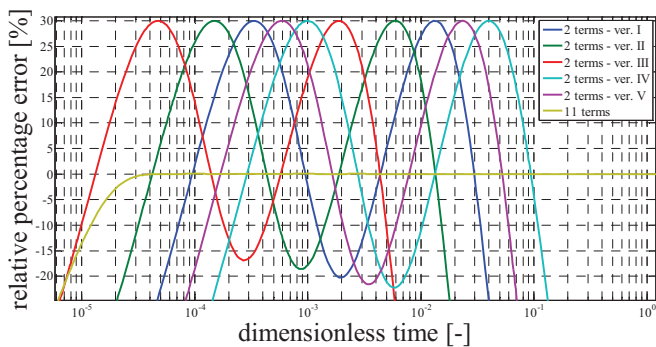


Fig. 1. Errors of the estimated effective weighting functions

C) The impact of the initial flow velocity. Detailed tests were carried out for six pressure fluctuation cases (initial flow velocities: 0.45 m/s, 0.82 m/s, 1.02 m/s, 1.7 m/s, 1.9 m/s, 2.76 m/s), which are the result of a sudden shut off of flow by closing a valve in a simple hydraulic system (used experimental results are described in the works by Adamkowski and Lewandowski [2,3]).

In total, as a result of examination of the impact of the aforementioned three decisive factors (simulation methods, the shape of the eff. weighting function and initial velocity), a series of numerical tests has been implemented, consisting of as many as one hundred and thirty-two computer simulations (Fig. 2).

METHODS	EFF. WEIGHTING FUNCTION	CASES	TOTAL NUMBER OF SIMULATION
2	*	11	*
		6	= 132

Fig. 2. Number of simulations

Since the pressure decreased in most simulations to the vapor pressure, the cavitation model according to Adamkowski and Lewandowski [1] has been used. Using this model, in general situation for pipe segment filled with liquid and vaporous zones discretely distributed along its length in several sections (Fig. 3), shifting of cavity volumes from intermediate zones to the main vaporous zone are needed. The equations for mean velocities calculated in all cross sections of pipe in which the cavity volumes were moved to the main vapor cavity is:

$$v_j = \text{sgn} \left[0.5(v_j^+ |v_j^+| + v_j^- |v_j^-|) + \Delta Z_i \right] \cdot \sqrt{0.5 \left[(v_j^+)^2 + (v_j^-)^2 \right] + \Delta Z_i} \quad (8)$$

where:

$$\text{for } j < k: \Delta Z_i = g \sum_{i=1}^j (V_{\text{cav},i} \sin \beta_i) / A_i$$

$$\text{for } j > k: \Delta Z_i = g \sum_{i=j}^n (V_{\text{cav},i} \sin \beta_i) / A_i$$

For the main vapor cavity the velocities at the left and right sides are calculated using equations:

$$\begin{cases} v_k^- = \text{sgn}[v_k^- |v_k^-| + 2\Delta Z_{j-}] \sqrt{(v_k^-)^2 + 2\Delta Z_{j-}} \\ v_k^+ = \text{sgn}[v_k^+ |v_k^+| + 2\Delta Z_{j+}] \sqrt{(v_k^+)^2 + 2\Delta Z_{j+}} \end{cases} \quad (9)$$

where:

$$\Delta Z_{j-} = g \sum_{j=1}^{k-1} (V_{\text{cav},j} \sin \beta_j) / A_j \text{ and}$$

$$\Delta Z_{j+} = g \sum_{j=k+1}^n (V_{\text{cav},j} \sin \beta_j) / A_j$$

For each executed simulation, for the purpose of simple quantitative reasoning, two parameters were determined representing the error of compatibility of the simulated pressure run with the experimental one.

The first parameter represents the mean absolute percentage error of simulated maximum pressure values on the subsequent pressure amplitudes (Fig. 4). It is calculated from the following simple formula:

$$E_p = \frac{\sum_{i=1}^k \left| \frac{p_{is} - p_{ie}}{p_{ie}} \right| \cdot 100\%}{k} \quad (10)$$

where: k – number of analyzed pressure amplitudes, p_{is} – the maximum pressure on the i -th analyzed amplitude in the simulated graph; p_{ie} – the maximum pressure on the i -th analyzed amplitude in the experimental graph.

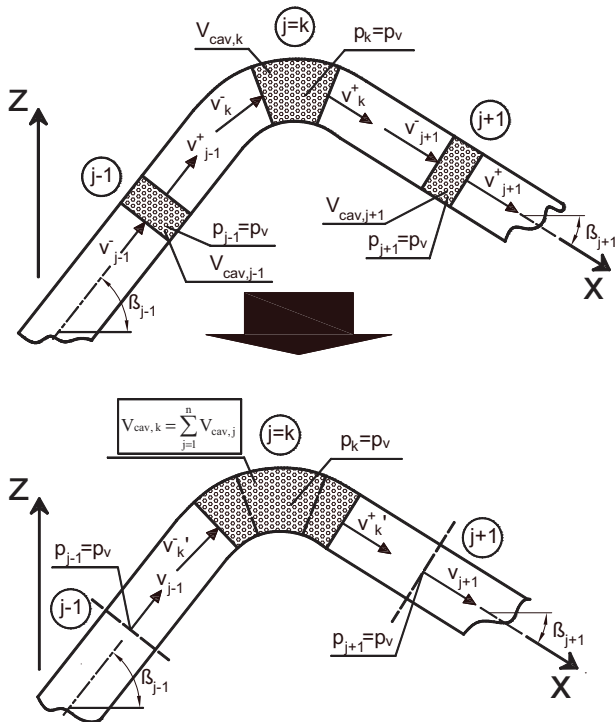


Fig. 3. Schematic diagram of the Adamkowski-Lewandowski model [1]

The second parameter describes the mean absolute percentage error for the time of occurrence of consecutive pressure peaks (Fig. 4). It is calculated similarly:

$$E_t = \frac{\sum_{i=1}^k \left| \frac{t_{is} - t_{ie}}{t_{ie}} \right| \cdot 100\%}{k} \quad (11)$$

where t_{is} – time of occurrence of the maximum pressure on the i -th analyzed amplitude from the the simulated graph; t_{ie} – time of occurrence of the maximum pressure on the i -th analyzed amplitude from the experimental graph.

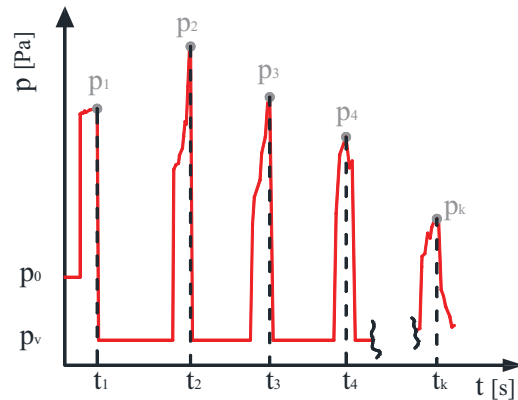


Fig. 4. Analyzed pressure values in the quantitative method

The smaller the values of the above parameters E_p and E_t , the better was the accuracy of the simulation.

For better readability of next chapter, it is worth to present an example comparison (Fig. 5) of the simulated pressure run with the experimental one. Achieved result were received using a standard model of SM computation for a case with initial liquid velocity $v_0 = 2.76$ m/s and effective weighting function in ver. 5. Such comparisons enabled the determination of the parameters E_p and E_t analyzed in details in following subchapter.

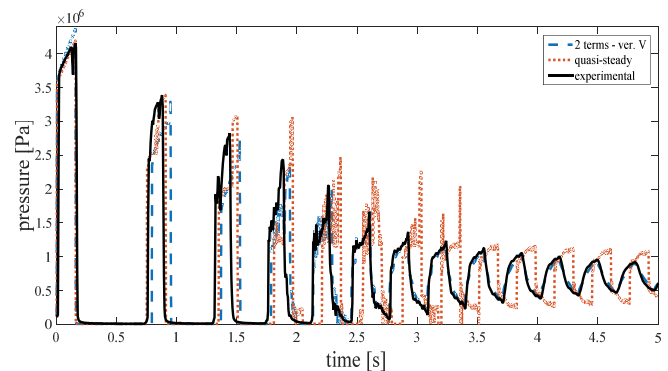


Fig. 5. Examples of the results of simulations

DISCUSSION OF SIMULATIONS RESULTS

The results of the numerous simulations are presented in the following group charts (Fig. 6, Fig.7). Fig. 6a features the results which show the change in the relative percentage error Ep for the analyzed effective functions composed of only two exponential expressions at different initial velocities of unsteady flow and when the simulations were performed using the standard method. It can be seen that good results, with a low value of the Ep parameter (less than 10%), were obtained for low flow velocities ($v_0 = 0.45$ m/s and $v_0 = 0.82$ m/s) using ver. IV of the weighting function. A little worse results using this function in comparison with other results were reported by simulating the flow starting at higher flow rates – an error of about 5 percent for the initial velocity equal to 1.02, 1.7, 1.9, and 2.76 meters per second. To unambiguously determine which version of two-terms effective weighting function during simulations carried out using the classical method (determination of quasi-steady and unsteady components of shear stress in all nodes of the grid of characteristics along the length of the pipe) has a minimal error, the errors obtained for different flow velocities were added (Tab. 1).

Tab. 1. Sum of errors parameters for 2 terms functions (for all v_0 cases: 0.45, 0.82, 1.02, 1.7, 1.9, 2.76)

Type of weighting function	Standard unsteady friction – SM		Lumped unsteady friction – LFM	
	ΣEt	ΣEp	ΣEt	ΣEp
2 terms – v. I	19,84	55,29	14,63	48,79
2 terms – v. II	17,02	48,26	14,55	54,87
2 terms – v. III	15,51	42,66	13,89	44,65
2 terms – v. IV	15,39	38,31	16,26	40,94
2 terms – v. V	17,24	42,57	14,03	37,68

According to the data from the above table, the assumptions resulting from the qualitative analysis of the curves in Fig. 6a are confirmed. During standard numerical simulations using the effective weighting function composed of two exponential expressions, ver. 4 of the weighting function

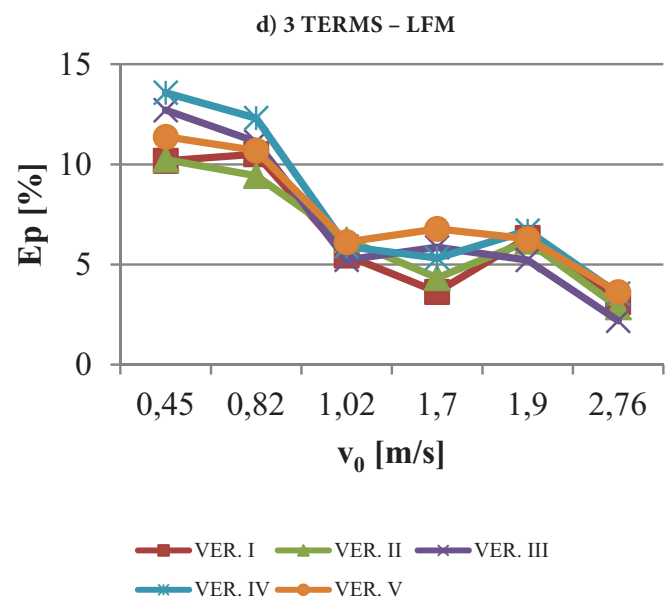
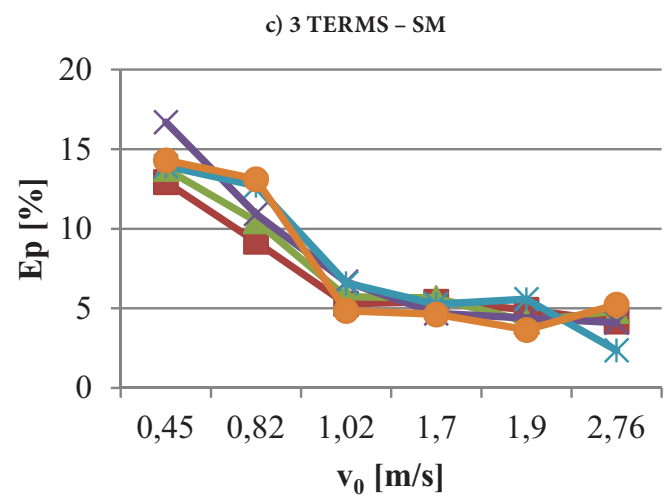
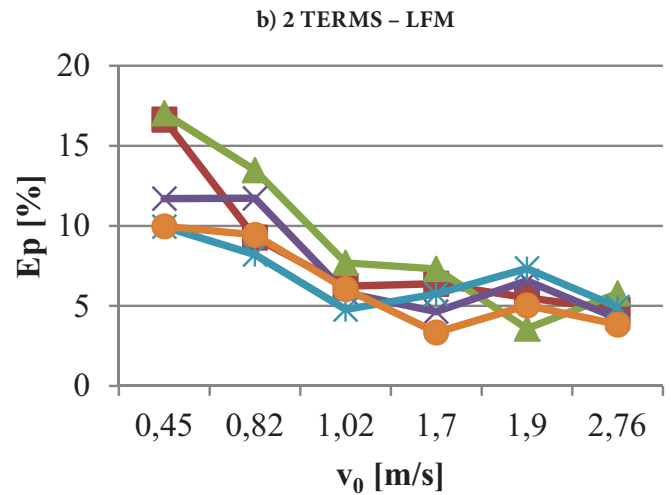
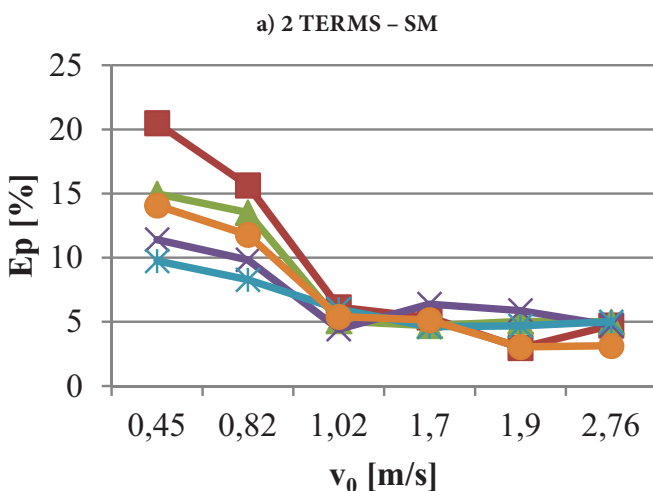


Fig. 6. Results of Ep [%] variation

($\Sigma Ep=38.31\%$) turned out to be the best. This result was, what is worth noting, as much as 6.1% lower than the summary

result obtained for a very precise effective 10-expression weighting function (Tab. 2).

Tab. 2. Sum of errors parameters for 10 terms function (for all v_0 cases: 0.45, 0.82, 1.02, 1.7, 1.9, 2.76)

Type of weighting function	Standard unsteady friction – SM		Lumped unsteady friction – LFM	
	ΣEt	ΣEp	ΣEt	ΣEp
10 terms	17,64	44,41	16,51	51,47

The results indicate that the amount of components is not responsible for the quality of the estimation of the maximum pressure (occurring in successive amplitudes of pressure graphs which are the results of water hammer) as well as the time of their emergence, as confirmed by the data related to the Et parameters included in Tab. 1 and Tab. 2.

Then, analyzing the results shown in Fig. 6b, it seems that even better results were obtained using the effective weighting function composed of two expressions marked as ver. 5, in combination with the method focusing non-stationary components of wall shear stress only in the boundary nodes of the pipe (at the inlet and outlet – Johnston’s method [8]). The total estimation error of the maximum pressure for all analyzed graphs amounted to $\Sigma Ep=37.68\%$ (Tab. 1). Interestingly, this result was lower than that obtained using the very precise effective weighting function (10-component) for this series of tests, up to approx. 13%. This clearly confirms the need for using simple weighting functions instead of multi-expression ones representing a high correlation with the classical weighting functions (according to Zielke [26] or Vardy-Brown [21-23]) and additionally it supports not accounting for unsteady resistance in the internal nodes.

The analysis of plots for the same simulations but using more accurate weighting functions composed of three exponential expression is shown in Fig. 6c and Fig. 6d. On the basis of Fig. 6c, it can be expected that the best results were obtained using the effective weighting function composed of three exponential expressions in ver. I when the calculations were performed by standard computing. In contrast, when the calculations were carried out by focusing the unsteady resistance only in the boundary nodes of the grid of characteristics, it can be concluded from Fig. 6d that the smallest errors were found in the simulations using the 3-expression effective weighting function in ver. II. Additionally, analyzing the quality results obtained by using functions composed of three expressions (Fig. 6c and Fig. 6d) and the results for the two-component functions (Fig. 6a and Fig. 6b) it can be seen that in the case of a more accurate functions (with 3 expressions), dispersion error for equal initial flow velocities and different used versions of the weighting function is smaller. Thus, it seems that in this case a slightly better matching of the simulated results to the experimental ones should occur. However, the analysis from Tab. 3 with the final quantitative results does not confirm the last conclusion made regarding the better compliance, because the results for the Ep parameters obtained with the weighting function which is the best for modelling maximum pressure

– ver. I (both in standard and lumped simulation – Tab. 3) are slightly higher than the best ones obtained using the effective 2-expression functions (Tab. 1). Using the solutions lumping the resistances in boundary nodes, we can also see that very good results are obtained using the 3-component weight function in ver. II (Tab. 3).

Tab. 3. Sum of errors parameters for 3 terms functions (for all v_0 cases: 0.45, 0.82, 1.02, 1.7, 1.9, 2.76)

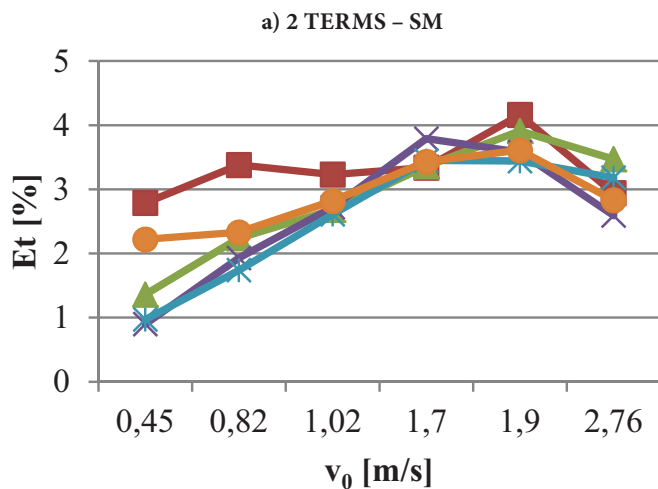
Type of weighting function	Standard unsteady friction – SM		Lumped unsteady friction – LFM	
	ΣEt	ΣEp	ΣEt	ΣEp
3 terms – v. I	16,1	41,91	14,91	39,23
3 terms – v. II	16,47	44,62	14,3	39,26
3 terms – v. III	17,68	47,46	15,59	42,34
3 terms – v. IV	16,09	46,42	14,95	47,34
3 terms – v. V	15,96	45,76	15,2	44,87

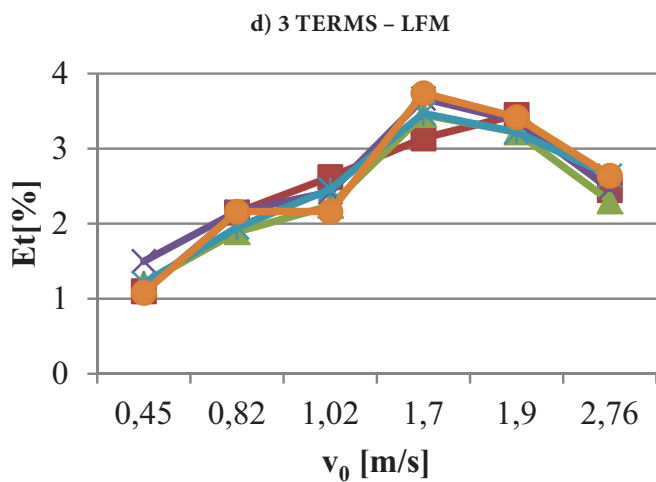
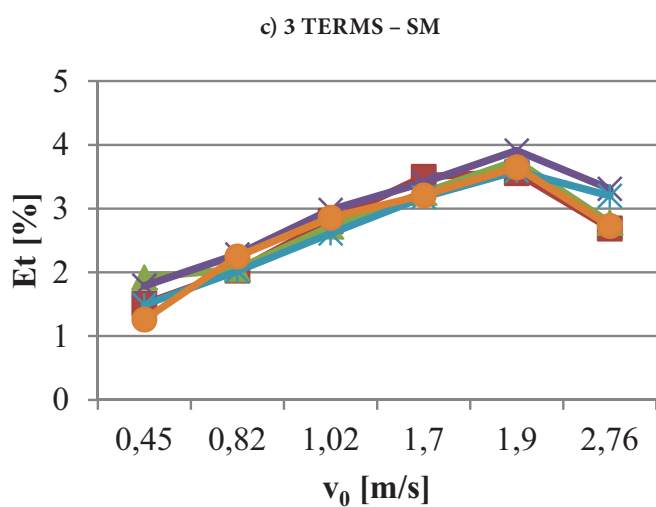
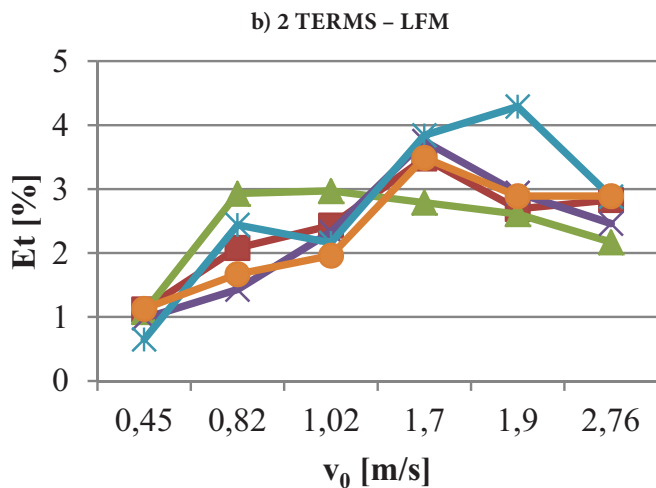
The above presented analysis showed no significant influence of the number of exponential expressions (thus decreasing the degree of compliance with the exact weighting function) on the final results of changes in the pressure graph.

The results presented in figure 7 illustrate the variation of the coefficient Et , the responsibility of which is to determine the time (phase) compliance of simulate pressure amplitudes. It can be seen from them that it is difficult to identify one weighting function (among 10 analyzed ones: 2 terms – ver. I–V, 3 terms – ver. I–V), as well as one method of friction modelling (SM, LFM) from which the best simulation results are being obtained.

However, it can be clearly concluded that the dispersion of the obtained results is much smaller at the time of applying more accurate effective weighting functions being constructed from three terms (this is particularly visible in Fig. 7c).

The maximum Et errors in the performed simulations being analyzed occurred in the modelled courses with the initial velocities $v_0 = 1.7$ m/s and $v_0 = 1.9$ m/s. Interestingly, the results being obtained in the course with the highest initial velocity $v_0 = 2.76$ m/s were characterized by a decrease in the Et error.





■ VER. I ▲ VER. II ✕ VER. III
✱ VER. IV ● VER. V

Fig. 7. Results of E_t [%] variation

It is possible that it has something to do with a decreasing importance of unsteady shear stress τ_u together with the

increasing Reynolds number. It is therefore unfortunate that the tests were not accomplished within a broader range of Reynolds numbers (range from 40000 to 100000) as the analysis of such results would allow for a wider verification of the above formulated hypothesis. The error variation itself may be considered independent of the applied weighting function (2 terms or 3 terms), as well as of the used method of resistance modelling (SM or LFM), because the course illustrating the distribution of errors in the function of change in the initial velocity of flow is very similar (Fig. 7a – Fig. 7d).

When comparing qualitatively the results obtained for the SM model only, it can be seen that final errors for 2 and 3 term weighting functions in version IV (having the same range of application in the domain of dimensionless time) are very similar with a slight predominance of two term weighting function (see: Fig. 7a, Fig. 7c and Tab. 1, Tab. 3).

When using the LFM model, good results were obtained (Fig. 7b) applying 2 term weighting function – ver. II because the E_t error was below 3% for all accomplished simulations. Unfortunately, for the courses with low initial velocities (from $v_0 = 0.45$ up to $v_0 = 1.02$ m/s) it was much greater than applying other weighting functions. When looking at the quantitative results (Tab. 1 and Tab. 3), it can be seen that cumulatively 2 term weighting function in ver. III and 3 term weighting function in ver. II, respectively, were characterized by the smallest errors in these simulations with the use of the LFM model.

To determine the stability of the results obtained depending on the number of exponential expressions representing the effective weighting function, the distribution of errors R_{E_t} and R_{E_p} was calculated for all the tests carried out (Tab. 4 and Tab. 5):

$$R_{E_t} = E_{t_{\max}} - E_{t_{\min}} \quad \text{and} \quad R_{E_p} = E_{p_{\max}} - E_{p_{\min}} \quad (12)$$

The tables presented below show that:

- increasing the number of exponential expressions affects the stability of the solutions, as there is a significant decline in the value of errors distribution for three-component weighting functions;
- the use of the method concentrating unsteady expression of friction in the boundary nodes of the grid of characteristics in the graphs with low Reynolds numbers ($v_0 = 0.45$ and $v_0 = 0.82$) increases the stability of the solutions as it reduces the value of the distribution. At higher Reynolds numbers, however, there was a slight increase in the distribution when applying this simplified method.

Tab. 4. Range of error E_t results

v_0 [m/s]	2 terms weighting functions R_{E_t} [%]		3 terms weighting functions R_{E_t} [%]	
	SM	LFM	SM	LFM
0.45	1.89	0.48	0.66	0.42
0.82	1.64	1.5	0.26	0.27
1.02	0.62	1.01	0.37	0.46
1.7	0.45	1.05	0.32	0.60

v_0 [m/s]	2 terms weighting functions R_{Et} [%]		3 terms weighting functions R_{Et} [%]	
	SM	LFM	SM	LFM
1.9	0.72	1.68	0.35	0.23
2.76	0.88	0.72	0.62	0.34

Tab. 5. Range of error Ep results

v_0 [m/s]	2 terms weighting functions R_{Ep} [%]		3 terms weighting functions R_{Ep} [%]	
	SM	LFM	SM	LFM
0.45	10.74	7.08	3.76	3.40
0.82	7.35	5.27	3.93	2.88
1.02	1.71	2.92	1.83	1.01
1.7	1.77	3.97	1.02	3.15
1.9	2.91	3.76	1.92	1.47
2.76	1.87	1.94	2.87	1.43

As can be concluded from the tests conducted, further research is necessary to enable the easy calculation of the coefficients in effective two-component weight functions: m_1 , m_2 , n_1 and n_2 .

CONCLUSIONS

The simplified method of estimating the instantaneous wall shear stress presented in the paper is an important issue when solving equations describing unsteady fluid flow in pressure lines. The presented solution increases the speed of calculations while maintaining the necessary accuracy for estimating the pressure runs. At the moment, it is becoming possible to estimate the pressure variations occurring in simple systems in real time – which gives great opportunities for the design of control systems.

The series of numerical tests carried out as part of this project proved that:

- the effective weighting functions need not be composed of multiple components and thus represent a high correlation with the classical functions (Zielke or those from Vardy-Brown). Proper modelling of wall shear stress is obtained using two components,
- the simplified method concentrating unsteady friction only in boundary nodes can be successfully used,
- gentle shift of the lower limit of the applicability of the effective weighting function affects the simulated results. However, at the present stage of research it would be hard to look for any distinct trend.

Another problem, which should be addressed in the near future has been revealed by the analysis of the courses of Ep errors obtained in the simulations carried out (Fig. 6). Model of unsteady flow with cavitation according to Adamkowski and Lewandowski [1] used in this paper, with too large error (about 10%), models the flows in the range of low Reynolds numbers ($v_0=0.45$ m/s and $v_0=0.82$ m/s). Therefore, it requires

modifications in order to more accurately simulate the transitional flows. Probably, the inclusion of gas cavitation (and not just vapor cavitation) will allow for a significant improvement in the quality of the modelled functions.

Lack of a detailed definition of an optimal lower range of applicability (for low dimensionless times) for the effective weighting function forces the implementation of further quantitative research. Without a clearly defined optimal lower limit of the applicability for the effective weighting functions, it is not possible to optimize the process of safe automatic control of hydraulic systems.

ACKNOWLEDGMENT

Some part of this work was presented at the 12th International Conference on Pressure Surges, 18-20 November 2015, Dublin, Ireland

BIBLIOGRAPHY

- Adamkowski A., Lewandowski M.: *A new method for numerical prediction of liquid column separation accompanying hydraulic transients in pipelines*, J. Fluids Eng., 131, 7, 2009.
- Adamkowski A., Lewandowski M.: *Experimental examination of unsteady friction models for transient pipe flow simulation*, J. Fluids Eng., 128, pp. 1351-1363, 2006.
- Adamkowski A., Lewandowski M.: *Investigation of hydraulic transients in a pipeline with column separation*, J. Hydraulic Eng., 138, 11, pp. 935-944, 2012.
- Górski Z.: *Construction and operation of marine hydraulic machinery*, Trademar, Gdynia, 2008.
- Hadj-Taïeb L., Hadj-Taïeb E.: *Modelling vapour cavitation in pipes with fluid-structure interaction*, International Journal of Modelling and Simulation, 29, 3, pp. 263-270, 2009
- Hadj-Taïeb L., Hadj-Taïeb E.: *Numerical simulation of transient flows in viscoelastic pipes with vapour cavitation*, International Journal of Modelling and Simulation, 29, 2, pp. 206-213, 2009.
- Henclik S.: *A numerical approach to the standard model of water hammer with fluid-structure interaction*, Journal of Theoretical and Applied Mechanics, 53, 3, pp. 543-555, 2015.
- Johnston D.N.: *Efficient methods for numerical modelling of laminar friction in fluid lines*. J. Dynamic Systems Measurement and Control, ASME, 128, 4, pp. 829 – 834, 2006.

9. Karadžić U. et al.: *Valve-induced water hammer and column separation in a pipeline apparatus*, *Strojniški Vestnik – Journal of Mechanical Engineering*, 60, 11, pp. 742-754, 2014.
10. Keramat A. et al.: *Fluid-structure interaction with pipe-wall viscoelasticity during water hammer*, *Journal of Fluids and Structures*, 28, 1, pp. 434-456, 2012.
11. Pezzinga G.: *Evaluation of time evolution of mechanical parameters of polymeric pipes by unsteady flow runs*, *Journal of Hydraulic Engineering*, 140, 12, paper 04014057, 2014.
12. Qiu Y. et al.: *Suppressing water hammer of ship steering systems with hydraulic accumulator*. *Proc IMechE Part E: J Process Mechanical Engineering*, Vol. 228 (2), pp. 136-148, 2014
13. Reddy H.P. et al.: *Estimation of decay coefficients for unsteady friction for instantaneous, acceleration-based models*, *Journal of Hydraulic Engineering*, 138, pp. 260-271, 2012
14. Soares A.K. et al.: *Investigation of transient vaporous cavitation: experimental and numerical analyses*, *Procedia Engineering*, 119, pp. 235-242, 2015.
15. Storli P., Nielsen T.: *Transient friction in pressurized pipes. I: investigation of Zielke's model*, *Journal of Hydraulic Engineering*, 137, 5, pp. 577-584, 2011.
16. Storli P., Nielsen T.: *Transient friction in pressurized pipes. II: two-coefficient instantaneous acceleration-based model*, *Journal of Hydraulic Engineering*, 137, 6, pp. 679-695, 2011.
17. Urbanowicz, K. et al.: *Universal weighting function in modeling transient cavitating pipe flow*, *J. Theoretical and Applied Mechanics*, 50, 4, pp. 889-902, 2012.
18. Urbanowicz, K., Zarzycki, Z.: *Convolution Integral in Transient Pipe Flow*, *Proc. of the XXth Fluid Mechanics Conference KKMP2012*, Gliwice, Poland, 17-20 September, on CD, 2012.
19. Urbanowicz, K., Zarzycki, Z.: *Improved lumping friction model for liquid pipe flow*, *J. Theoretical and Applied Mechanics*, 53, 2, pp. 295-305, 2015.
20. Urbanowicz, K.: *New approximation of unsteady friction weighting functions*. *Proc. of the 11th International Conference on Pressure Surges*, Lisbon, Portugal, October 24-26, pp. 477 – 492, 2012.
21. Vardy, A.E., Brown, J.M.B.: *Approximation of turbulent wall shear stresses in highly transient pipe flows*, *Journal of Hydraulic Engineering*, 133, 11, pp. 1219-1228, 2007.
22. Vardy, A.E., Brown, J.M.B.: *Transient turbulent friction in fully rough pipe flows*, *Journal of Sound and Vibration*, 270, pp. 233-257, 2004.
23. Vardy, A.E., Brown, J.M.B.: *Transient turbulent friction in smooth pipe flows*, *Journal of Sound and Vibration*, 259, pp. 1011-1036, 2003.
24. Wylie, E.B., Streeter, V.L.: *Fluid transients in systems*, Prentice-Hall Inc., Englewood Cliffs, New Jersey, 1993.
25. Zanganeh R. et al.: *Fluid-structure interaction with viscoelastic supports during waterhammer in a pipeline*, *Journal of Fluids and Structures*, 54, April, pp. 215-234, 2015
26. Zielke W.: *Frequency-dependent friction in transient pipe flow*, *Journal of Basic Engineering*, ASME, 90, pp. 109-115, 1968.

CONTACT WITH THE AUTHOR

Kamil Urbanowicz
e-mail: kurbanowicz@zut.edu.pl
 West Pomeranian University of Technology
 Piastow 19, 70-310 Szczecin
POLAND

APPENDIX

Coefficients describing effective weighting functions tested in the project are summarized in the following tables A1, A2, A3. These coefficients were scaled at the moment of turbulent flows occurrence using assumptions about their universality [17].

Tab. A1. Coefficients of effective two-component weighting functions

L.p.	m_1	m_2	n_1	n_2
2 terms – ver. I	4.0951	28.6939	64.7685	2051.9391
2 terms – ver. II	6.6203	43.1553	119.9504	4542.6744
2 terms – ver. III	12.6592	77.0123	323.2014	14255.3890
2 terms – ver. IV	2.0902	16.3239	34.0614	713.6440
2 terms – ver. V	2.8889	21.5009	44.7999	1183.8544

Tab. A2. Coefficients of effective three-component weighting functions

L.p.	m_1	m_2	m_3	n_1	n_2	n_3
3 terms – ver. I	2.6242	9.7852	34.972	48.007	559.25	6962.4
3 terms – ver. II	3.2982	11.849	42.078	61.214	796.30	10047.2
3 terms – ver. III	5.2734	17.691	62.299	110.32	1707.5	21933.6
3 terms – ver. IV	1.7214	6.7670	24.693	33.398	295.12	3509.8
3 terms – ver. V	2.1201	8.1537	29.394	39.376	404.41	4940.6

Tab. A3. Coefficients of an effective ten-component weighting function

L.p.	m_1	m_2	m_3	m_4	m_5	m_6	m_7	m_8	m_9	m_{10}
10 terms	1	0.999651	1.0047	1.2446	2.328	4.43	8.0761	14.341	25.15	43.867
	n_1	n_2	n_3	n_4	n_5	n_6	n_7	n_8	n_9	n_{10}
	26.3744	70.8493	135.072	226.194	417.598	946.783	2492.23	7100.19	20955.3	62745

MAGNETOHYDRODYNAMIC FLOW OF VISCOUS FLUID IN A SLOT BETWEEN FIXED SURFACES OF REVOLUTION

Jerzy Sawicki

UTP University of Science and Technology in Bydgoszcz, Poland

ABSTRACT

The paper considers stationary magnetohydrodynamic flow of viscous fluid in the slot between fixed curvilinear surfaces of revolution exposed to azimuthal magnetic field. To solve the problem, the equations of boundary layer in the curvilinear coordinate system. x, θ, y , were applied. The equations of the boundary layer were solved analytically with the use of the small-parameter method. The formulas determine the field of velocity and pressure.

Keywords: laminar flow, incompressible magnetohydrodynamic flow, method of perturbation

INTRODUCTION

Magnetohydrodynamics is a section of fluid mechanics covering the aspects of the movement of fluids allowing the flow of an electrical current in magnetic and electrical field [1,11]. Especially magnetohydrodynamics (MHD) uses the laws of fluid mechanics and electrical engineering to determine the interaction of the fluid and electromagnetic field [14].

In the second half of the 20th century research was launched on the use of the phenomena of magnetohydrodynamics for the design of MHD drive of submarines.

The magnetohydrodynamic submarine drive is currently at the phase of R&D work.

The appearance of superconductors decreased the amount of energy necessary for generating the right magnetic field for designed drive systems (MHD). Superconductive magnets can generate a very strong magnetic field allowing for producing a thrust capable of moving a submarine [15].

Before appearance of controlled rheological fluids reacting to external magnetic and electric field in technology, only

solid materials existed in practice. In contemporary industry the control of magnetic and electric field is used in many technical devices [14].

There are known applications of magnets and electromagnets, controlled magnetoreological fluids not allowing the flow of an electrical current, electrorheological and Newton fluids allowing the flow of an electrical current (e.g. electrolytes, ionised seawater, non-magnetic liquid metals).

In the process of design, manufacture and assembly the application of such fluids requires the knowledge of effects which appear both as a result of external effect of the magnetic and electrical field and the effects being a result of the flow itself in the construction element.

In construction systems we can deal with a laminar flow characteristic for the so-called narrow slot and turbulent flow.

Laminar viscous fluid flows allowing the flow of an electrical current in the slots of technical devices exposed to stationary and non-stationary magnetic and electrical fields have triggered much interest [1,5,14,16]. The studies of viscous fluid flows exposed to magnetic and electrical fields as well as an effect of those fields on various physical and chemical processes have been performed for many years [4,10,11,13].

Interestingly, research in that field is still essential for practical purposes.

A new potential offered by fluids allowing the flow of an electrical current in solving numerous design and operational issues (plain bearings, clutches, sealings, dampers etc.) in terms of friction, wear and lubrication, especially under extreme working conditions, determines the need of research of such flows [3,5,6,8,9,17].

The aim of this paper has been an analysis of the effect of magnetic and electrical field as well as inertia effects on the flow of fluid allowing the flow of an electrical current in the slot between fixed curvilinear rotating surfaces exposed to an external azimuthal magnetic and orthogonal field to the surfaces inhibiting the flow of electrical field.

BASIC EQUATIONS

The motion of electro-conductive viscous fluids flowing through a slot between the curvilinear surfaces of revolution presented in Fig. 1, is assumed to be laminar, steady and isothermal.

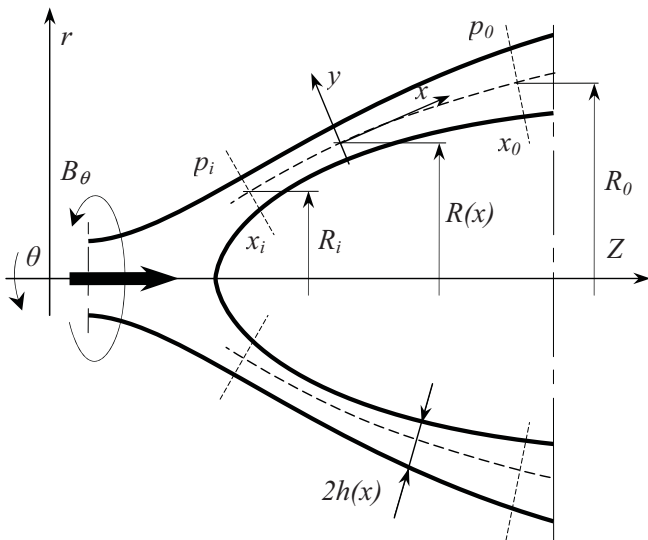


Fig. 1. Magnetohydrodynamic fluid flow area

The flow occurs in the presence of external stationary magnetic $(0, B_\theta, 0)$ and electrical $(0, 0, E_y)$ fields in a slot bounded by electrically conducting surfaces. The magnetic Reynolds number is assumed to be much less than unity, $Re_m \ll 1$, that makes it possible to disregard the effect of the magnetic field induced by the motion of the fluid.

On the base of the general laws of conservation of the mass and momentum, the equations of motion take the following form [1,2,4,7]:

The continuum equation:

$$\nabla V = 0 \quad (1)$$

The momentum equation:

$$\rho(V\nabla)V = -\nabla p + \mu\Delta V + \mathbf{j} \times \mathbf{B} \quad (2)$$

where: $V, \mathbf{j}, B, p, \rho, \mu$ – stands for the vector of viscous fluid velocity, current density vector, magnetic induction vector, pressure, density, dynamic viscosity, respectively.

In order to “close” the set of Eqs (1) and (2) the additional equations of the electromagnetic field is necessary [1]:

$$\nabla \times \mathbf{E} = 0 \quad (3)$$

$$\nabla \mathbf{E} = 0 \quad (4)$$

$$\nabla \times \mathbf{B} = \mu_0 \mathbf{j} \quad (5)$$

$$\nabla \mathbf{B} = 0 \quad (6)$$

$$\nabla \mathbf{j} = 0 \quad (7)$$

$$\mathbf{j} = \sigma(\mathbf{E} + \mathbf{V} \times \mathbf{B}) \quad (8)$$

where: $\mathbf{E}, \mu_0, \sigma$: electrical field vector, magnetic permeability, electrical conductivity, respectively.

Writing Eqs. (1), (2), (8) in the curvilinear system of coordinates x, θ, y and applying the estimations typical for flows occurring in thin layers, $h \ll R(x)$, we obtain [12, 17]:

$$\frac{1}{R} \frac{\partial(Rv_x)}{\partial x} + \frac{\partial v_y}{\partial y} = 0 \quad (9)$$

$$\rho \left(v_x \frac{\partial v_x}{\partial x} + v_z \frac{\partial v_x}{\partial y} \right) = -\frac{\partial p}{\partial x} + \mu \frac{\partial^2 v_x}{\partial y^2} - j_y B_\theta \quad (10)$$

$$\frac{\partial p}{\partial y} = 0 \quad (11)$$

$$j_y = \sigma(E_y + v_x B_\theta) \quad (12)$$

where: $v_x, v_y, p, E_y, B_\theta$: velocity components, pressure, component of magnetization, component of magnetic field, respectively.

Thus, from Eq. (11) we have:

$$p = p(x) \quad (13)$$

The boundary conditions for velocity components and pressure are:

– velocity components

$$v_x(x, \mp h) = 0, \quad v_y(x, \mp h) = 0, \quad (14)$$

– pressure

• at the inlet:

$$p = p_i \quad \text{for } x = x_i$$

- at the outlet

$$p = p_0 \quad \text{for } x = x_0 \quad (15)$$

where: x_i – denotes the inlet coordinate, x_0 – the outlet coordinate.

SOLUTION OF THE EQUATIONS OF MOTION

Introducing the following dimensionless quantities:

$$\tilde{x} = \frac{x}{R_o}, \quad \tilde{y} = \frac{y}{h_o}, \quad \tilde{R} = \frac{R}{R_o}, \quad (16)$$

$$\tilde{v}_x = \frac{v_x}{v_o}, \quad \tilde{v}_y = \frac{v_y R_o}{v_o h_o}, \quad \tilde{p} = \frac{p h_o}{\mu v_o R_o}$$

we can present the equations of motion (9) – (11) in the form:

$$\frac{1}{\tilde{R}} \frac{\partial(\tilde{p}_e R \tilde{v}_x)}{\partial \tilde{x}} + \frac{\partial(\tilde{p}_e \tilde{v}_y)}{\partial \tilde{y}} = 0 \quad (17)$$

$$\lambda \left(\tilde{v}_x \frac{\partial \tilde{v}_x}{\partial \tilde{x}} + v_y \frac{\partial \tilde{v}_x}{\partial \tilde{y}} \right) = -\frac{\partial \tilde{p}}{\partial \tilde{x}} + \frac{\partial^2 \tilde{v}_x}{\partial \tilde{y}^2} - \tilde{j}_y \tilde{B}_\theta Ha \quad (18)$$

$$0 = \frac{\partial \tilde{p}}{\partial \tilde{y}} \quad (19)$$

where:

$$Ha = B h_o \sqrt{\frac{\sigma}{\mu}}, \quad \tilde{B}_\theta = \frac{B_\theta}{B}, \quad \tilde{j}_y = j_y \frac{h_o}{v_o} \sqrt{\frac{\sigma}{\mu}}, \quad \lambda = Re \frac{h_o}{R_o}, \quad Re = \frac{2\rho v_o h_o}{\mu}$$

The quantities marked ‚zero’ are average values within the discussed flow domain; λ – is the modified Reynolds number which satisfies the condition:

$$\lambda < 1 \quad (20)$$

In Eqs. (17), (18), (19) describing motion of electro-conductive fluid, if condition (20) is satisfied, λ is a small parameter of the system.

Thus, the solution can be sought for in the form of power series with respect to λ :

$$\tilde{v}_x = \sum_{i=0}^{\infty} \lambda^i \tilde{v}_x^i, \quad \tilde{v}_y = \sum_{i=0}^{\infty} \lambda^i \tilde{v}_y^i, \quad \tilde{p} = \sum_{i=0}^{\infty} \lambda^i \tilde{p}^i \quad (21)$$

Introducing the series (21) into Eqs. (17), (18) and grouping the terms with the same powers of λ , confining the considerations to linear approximation and returning to the previous dimensional form, we get the following equations:

$$\frac{1}{R} \frac{\partial(Rv_x^0)}{\partial x} + \frac{\partial v_y^0}{\partial y} = 0 \quad (22)$$

$$0 = -\frac{\partial p^0}{\partial x} + \mu \frac{\partial^2 v_x^0}{\partial y^2} - j_y^0 B_\theta \quad (23)$$

$$\frac{1}{R} \frac{\partial(Rv_x^1)}{\partial x} + \frac{\partial v_y^1}{\partial y} = 0 \quad (24)$$

$$\rho \left[v_x^0 \frac{\partial v_x^0}{\partial x} + v_y^0 \frac{\partial v_x^0}{\partial y} \right] = -\frac{\partial p^1}{\partial x} + \mu \frac{\partial^2 v_x^1}{\partial y^2} - j_y^0 B_\theta \quad (25)$$

The boundary conditions in accordance with Eqs. (14) and (15), have the form:

for

$$v_x^0 = v_x^1 = v_y^0 = v_y^1 = 0 \quad \text{for } y = \mp h \quad (26)$$

for

$$p^0 = p_i \quad p^1 = 0 \quad \text{for } x = x_i \quad (27)$$

$$p^0 = p_0 \quad p^1 = 0 \quad \text{for } x = x_0$$

Integrating Eqs. (22)–(25) with the boundary conditions (26)–(27) we have:

$$v_x^0 = \frac{1}{2\mu R h^3} \frac{p_i - p_0 - B_i + B_0}{(A_i - A_0) - (M_i - M_0)} (y^2 - h^2) \quad (28)$$

$$v_y^0 = \frac{h'}{2\mu R h^4} \frac{p_i - p_0 - B_i + B_0}{(A_i - A_0) - (M_i - M_0)} (h^2 y - y^3) \quad (29)$$

$$p^0 = B(x) + \frac{[A(x) - A_0](p_i - B_i)[1 + Z(x)] - [A(x) - A_i](p_0 - B_0)[1 + W(x)]}{(A_i - A_0) + (M_i - M_0)} \quad (30)$$

$$v_x^1 = \frac{1}{840} \frac{\rho C^2 (R h')}{\mu^3 R^3 h^7} (35 h^2 y^4 - 7 y^6 + 5 h^6 - 33 h^4 y^2) \quad (31)$$

$$v_y^1 = \frac{1}{840} \frac{\rho C^2}{\mu^3 R^3} \left\{ \left[\frac{(R h)'}{R^2 h^7} \right] (y^7 - 7 h^2 y^5 - 5 h^6 y + 11 h^4 y^3) + \frac{(R h)'}{R^2 h^7} (44 h^3 y^3 - 14 h y^5 - 30 h^5 y) \right\} \quad (32)$$

$$p^1 = D(x) - \frac{[A(x) - A_0] D_i - [A(x) - A_i] D_0}{A_i - A_0} \quad (33)$$

where:

$$R' = \frac{dR}{dx}, \quad h' = \frac{dh}{dx}, \quad C = \frac{p_i - B_i - (p_0 - B_0)}{(A_i - A_0) + (M_i - M_0)},$$

$$A(x) = \int \frac{dx}{R h^3}, \quad A_i = A(x_i), \quad A_0 = A(x_0),$$

$$B(x) = -\sigma E_y B R_i \int \frac{dx}{R}, \quad B_i = B(x_i), \quad B_0 = B(x_0),$$

$$Z(x) = \frac{(M(x) - M_0)}{(A(x) - A_0)}, \quad W(x) = \frac{(M(x) - M_i)}{(A(x) - A_i)},$$

$$M(x) = \frac{1}{3} H a^2 R_i^2 \int \frac{dx}{(R h)^3}, \quad M_i = M(x_i), \quad M_0 = M(x_0),$$

$$E_y = \frac{J}{2\pi\sigma \left[s(x) - \frac{1}{3} Ha^2 R_i^2 ss(x) \frac{(A_i - A_0)}{(A_i - A_0) + (M_i - M_0)} \right]} + \frac{h^2}{3\mu\sigma} Ha R_i ss(x) \frac{(p_i - p_0)}{(A_i - A_0) + (M_i - M_0)}$$

$$s(x) = \int_{x_i}^{x_0} R dx, \quad ss(x) = \int_{x_i}^{x_0} \frac{dx}{R},$$

$$D(x) = \int \frac{6\rho C^2 (Rh)'}{35\mu^2 R^3 h^3} dx, \quad D_i = D(x_i), \quad D_0 = D(x_0).$$

The complete solution to the magnetohydrodynamic fluid flow problem inside a slot between (in general) curvilinear surfaces consists of the sum of partial solutions v^0 and v^1 .

HYDROMAGNETIC FLUID FLOW BETWEEN FIXED CONICAL SURFACES

The parameters describing the geometry of the considered flow region can be written as follows (Fig. 2):

$$R(x) = x \sin(\alpha), \quad R_i = x_i \sin(\alpha), \\ R_0 = x_0 \sin(\alpha), \quad R' = \sin(\alpha)$$

Introducing the dimensionless quantities into Eqs. (28)–(32):

$$\xi = \frac{x}{R_0}, \quad \eta = \frac{y}{h}, \quad \bar{R}' = 1,$$

$$\bar{v}_x = \frac{v_x}{v_{xmax}^0}, \quad \bar{v}_y = \frac{v_y}{v_{xmax}^0} \frac{R_0}{h},$$

$$v_{xmax}^0 = \frac{p_0 h^2 (\bar{p}_i - 1)}{2x\mu R_0 (a_0 - a_i)}$$

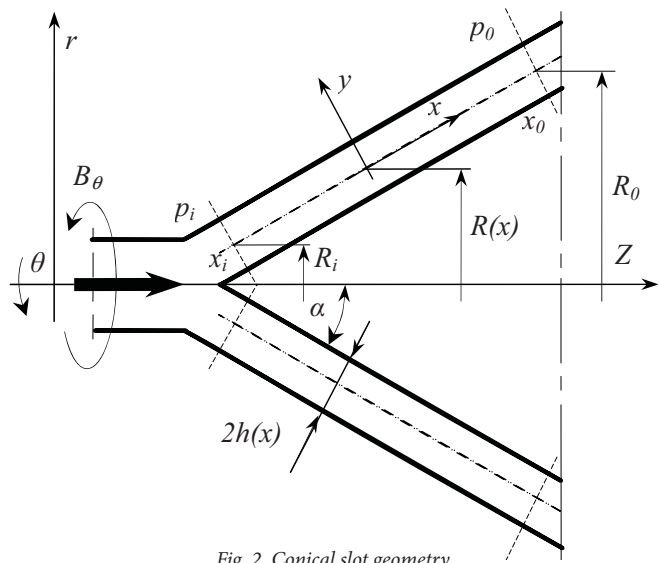


Fig. 2. Conical slot geometry

we obtain the formulae representing the motion of the MHD fluid inside the slot between the fixed conical surfaces:

$$\bar{v}_x^0 = \left(\frac{1 - \frac{\bar{B}_i - \bar{B}_0}{\bar{p}_i - 1}}{1 + \frac{m_i - m_0}{a_i - a_0}} \right) (1 - \eta^2), \quad (34)$$

$$\bar{v}_y^0 = 0, \quad (35)$$

$$\bar{p}^0 = \bar{B}(x) + \frac{[a(x) - a_0](\bar{p}_i - \bar{B}_i)[1 + z(x)] - [a(x) - a_i](1 - \bar{B}_0)[1 + w(x)]}{(a_i - a_0) + (m_i - m_0)} \quad (36)$$

$$\bar{v}_x^1 = -\frac{1}{420\xi^2} \Lambda c \frac{a_i - a_0}{\bar{p}_i - 1} \frac{[\bar{p}_i - 1 - \bar{B}_i + \bar{B}_0]^2}{\left[1 + \frac{(m_i - m_0)}{(a_i - a_0)}\right]^2} (5 - 7\eta^6 + 35\eta^4 - 33\eta^2) \quad (37)$$

$$\bar{v}_y^1 = \frac{1}{240\xi^3} \Lambda c \frac{a_i - a_0}{\bar{p}_i - 1} \frac{[\bar{p}_i - 1 - \bar{B}_i + \bar{B}_0]^2}{\left[1 + \frac{(m_i - m_0)}{(a_i - a_0)}\right]^2} (\eta^7 - 7\eta^5 + 11\eta^3 - 5\eta) \quad (38)$$

$$\bar{p}^1 = \bar{D}(x) - \frac{[a(x) - a_0]\bar{D}_i - [a(x) - a_i]\bar{D}_0}{a_i - a_0} \quad (39)$$

where:

$$a(x) = \ln(\xi), \quad a_i = a(\xi_i), \quad a_0 = a(\xi_0),$$

$$\bar{B}(x) = -EHax_i \ln(\xi), \quad \bar{B}_i = \bar{B}(\xi_i), \quad \bar{B}_0 = \bar{B}(\xi_0), \quad Ha = Bh_0 \sqrt{\frac{\sigma}{\mu}},$$

$$E = \frac{1}{\frac{1}{2}(1 - \xi_i^2) + \frac{1}{3} \frac{Ha^2 \xi_i^2 m(\xi_i)}{1 + \frac{(m_i - m_0)}{(a_i - a_0)}}} \left[I - \frac{1}{3} Ha \xi_i \ln(\xi_i) \frac{\bar{p}_i - 1}{(a_i - a_0) + (m_i - m_0)} \right],$$

$$m(x) = -\frac{1}{6} Ha^2 \frac{\xi_i^2}{\xi^2}, \quad m_i = m(\xi_i), \quad m_0 = m(\xi_0),$$

$$z(x) = 1 + \frac{(m(x) - m_0)}{(a(x) - a_0)}, \quad w(x) = 1 + \frac{(m(x) - m_i)}{(a(x) - a_i)}$$

$$I = \frac{J\sqrt{\mu}}{2\pi h p_0 x_0 \sin \alpha \sqrt{\sigma}}, \quad E = \frac{E_y x_0 \sin \alpha \sqrt{\sigma \mu}}{h p_i},$$

$$\bar{D}(x) = -\frac{3}{35} \Lambda c \frac{(\bar{p}_i - 1 - \bar{B}_i + \bar{B}_0)^2}{\xi^2 \left[1 + \frac{(m_i - m_0)}{(a_i - a_0)}\right]^2},$$

$$\bar{D}_i = \bar{D}(\xi_i), \quad \bar{D}_0 = \bar{D}(\xi_0), \quad \Lambda c = \frac{\rho p_0 h^4}{\mu^2 R_0^2 (a_i - a_0)^2}.$$

The above given formulae have been illustrated in Fig. 3 and Fig. 6.

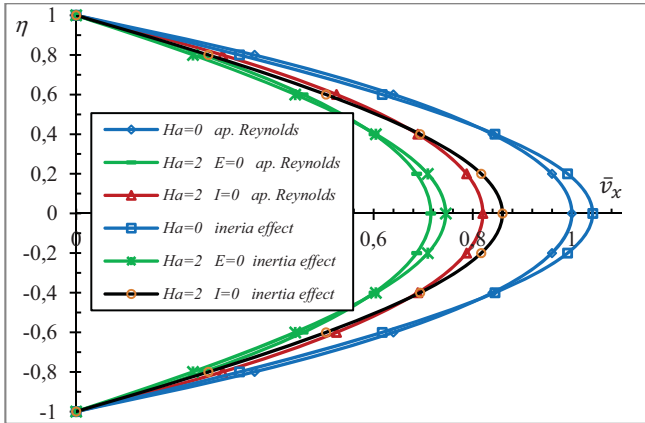


Fig. 3. Effect of magnetic field (Hartmann number (Ha)) and inertia effects on the profile of the velocity component \bar{v}_x

$$(\xi = 0,6, \bar{p}_i = 5, \Lambda c = 0,05)$$

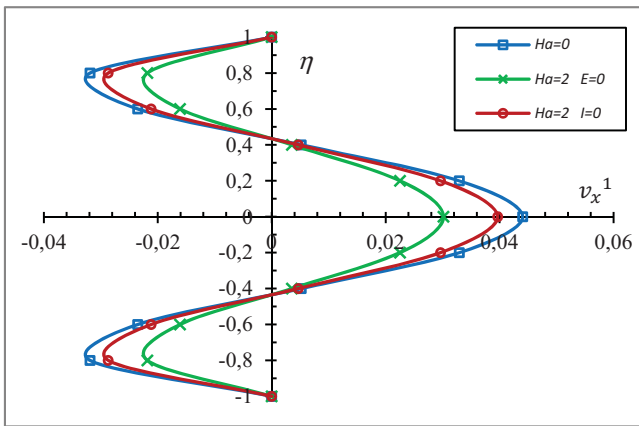


Fig. 4. Effect of magnetic field (Hartmann number (Ha)) and inertia effects on the profile of the velocity component \bar{v}_x^1

$$(\xi = 0,6, \bar{p}_i = 5, \Lambda c = 0,05)$$

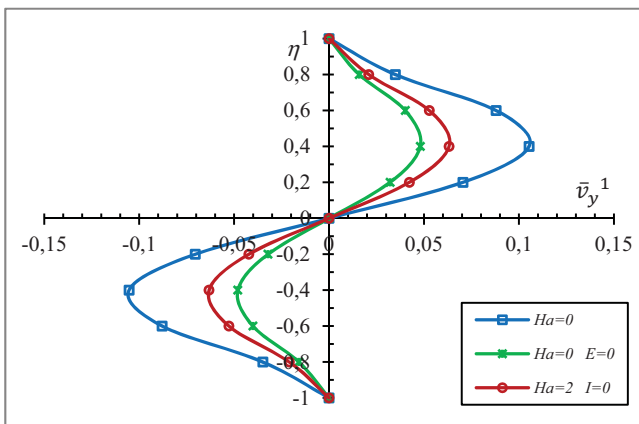


Fig. 5. Effect of magnetic field (Hartmann number (Ha)) and inertia effects on the profile of the velocity component \bar{v}_y^1

$$(\xi_i = 0,2, \xi_0 = 0,6, \bar{p}_i = 5, \Lambda c = 0,05)$$

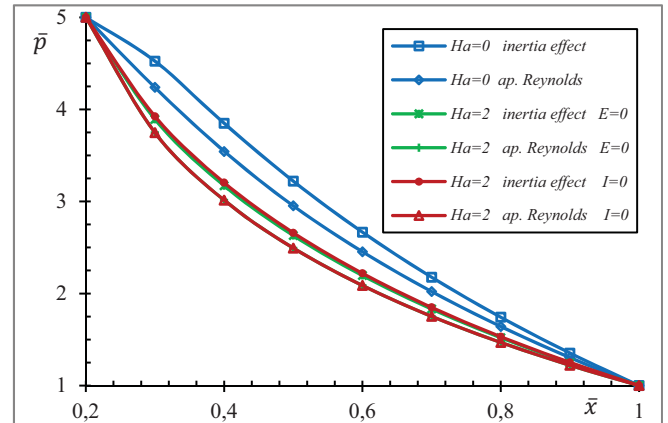


Fig. 6. Effect of magnetic field (Hartmann number (Ha)) and inertia effects on the pressure distribution \bar{p}

$$(\xi_i = 0,2, \xi_0 = 1, \bar{p}_i = 5, \Lambda c = 0,05,)$$

HYDROMAGNETIC FLUID FLOW BETWEEN FIXED SPHERICAL SURFACES

The parameters describing the geometry of the flow region can be written as follows (Fig. 7):

$$R(x) = R_k \sin(\varphi), \quad R_i = R_k \sin(\varphi_i),$$

$$R_0 = R_k \sin(\varphi_0),$$

$$R' = \cos(\varphi), \quad \varphi = \frac{x}{R_k}.$$

After introducing the functions used for describing the geometry of the flow area (Fig. 7) in Eqs. (28)–(32) and providing the dimensionless quantities:

$$\eta = \frac{y}{h}, \quad \bar{R} = \frac{R(x)}{R_0}, \quad \bar{R}' = \cos(\varphi)$$

$$\bar{v}_x = \frac{v_x}{v_{xmax}^0}, \quad \bar{v}_y = \frac{v_y}{v_{xmax}^0} \frac{R_k \sin(\varphi_0)}{h},$$

$$v_{xmax}^0 = \frac{p_0 h^2 (\bar{p}_i - 1)}{2\mu \sin(\varphi) (a_0 - a_i) R_0}$$

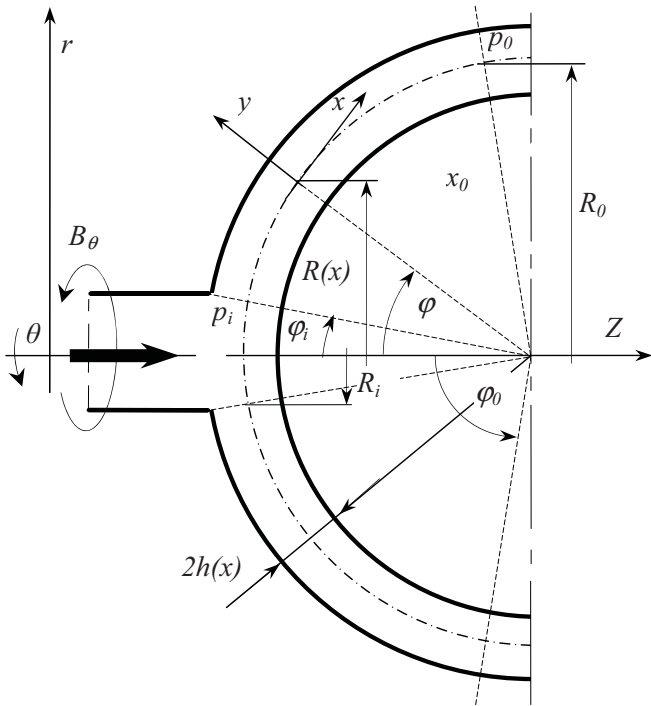


Fig. 7. Spherical slot geometry

we obtain the formulas representing the motion of the MHD fluid inside the slot between the fixed spherical surfaces:

$$\bar{v}_x^0 = \left(\frac{1 - \frac{\bar{B}_i - \bar{B}_0}{\bar{p}_i - 1}}{1 + \frac{m_i - m_0}{a_i - a_0}} \right) (1 - \eta^2), \quad (40)$$

$$\bar{v}_y^0 = 0, \quad (41)$$

$$\bar{p}^0 = \bar{B}(\varphi) + \frac{[\alpha(\varphi) - a_0](\bar{p}_i - \bar{B}_i)[1 + z(\varphi)] - [\alpha(\varphi) - a_i](1 - \bar{B}_0)[1 + w(\varphi)]}{(a_i - a_0) + (m_i - m_0)}, \quad (42)$$

$$\bar{v}_x^1 = -\frac{1}{420} \Lambda s \frac{a_i - a_0}{\bar{p}_i - 1} \frac{[\bar{p}_i - 1 - \bar{B}_i + \bar{B}_0]^2 \cos(\varphi)}{\left[1 + \frac{(m_i - m_0)}{(a_i - a_0)}\right]^2 \sin^2(\varphi)} (5 - 7\eta^6 + 35\eta^4 - 33\eta^2) \quad (43)$$

$$\bar{v}_y^1 = \frac{1}{720 \sin^3(\varphi)} \Lambda s \frac{a_i - a_0}{\bar{p}_i - 1} \frac{[\bar{p}_i - 1 - \bar{B}_i + \bar{B}_0]^2}{\left[1 + \frac{(m_i - m_0)}{(a_i - a_0)}\right]^2} [1 + \cos^2(\varphi)] (\eta^7 - 7\eta^5 + 11\eta^3 - 5\eta) \quad (44)$$

$$\bar{p}^1 = \bar{D}(\varphi) - \frac{[\alpha(\varphi) - a_0] \bar{D}_i - [\alpha(\varphi) - a_i] \bar{D}_0}{a_i - a_0} \quad (45)$$

where:

$$a(\varphi) = \ln \left| \tan \left(\frac{\varphi}{2} \right) \right|, \quad a_i = a(\varphi_i), \quad a_0 = a(\varphi_0),$$

$$\bar{B}(\varphi) = -E H \sin(\varphi) \ln \left(\tan \left(\frac{\varphi}{2} \right) \right),$$

$$\bar{B}_i = \bar{B}(\varphi_i), \quad \bar{B}_0 = \bar{B}(\varphi_0), \quad Ha = B h_0 \sqrt{\frac{\sigma}{\mu}},$$

$$E = \frac{1}{\frac{1}{2}(\cos(\varphi_i) - \cos(\varphi_0)) + \frac{1}{3} \frac{Ha^2 \sin^2 \varphi_i \left[\tan \left(\frac{\varphi_0}{2} \right) - \tan \left(\frac{\varphi_i}{2} \right) \right]}{1 + \frac{(m_i - m_0)}{(a_i - a_0)}}} \left[I - \frac{1}{3} Ha E H \sin(\varphi_i) \left[\left| \tan \left(\frac{\varphi_0}{2} \right) \right| - \left| \tan \left(\frac{\varphi_i}{2} \right) \right| \right] \frac{\bar{p}_i - 1}{(a_i - a_0) + (m_i - m_0)} \right],$$

$$m(\varphi) = -\frac{1}{6} Ha^2 \sin^2(\varphi) \int \frac{d\varphi}{\sin^3(\varphi)},$$

$$m_i = m(\varphi_i), \quad m_0 = m(\varphi_0),$$

$$z(\varphi) = 1 + \frac{(m(\varphi) - m_0)}{(a(\varphi) - a_0)}, \quad w(\varphi) = 1 + \frac{(m(\varphi) - m_i)}{(a(\varphi) - a_i)}$$

$$I = \frac{J \sqrt{\mu}}{2\pi h p_0 R_0 \sin(\varphi_0) \sqrt{\sigma}}, \quad E = \frac{E_y R_0 \sin(\varphi_0) \sqrt{\sigma \mu}}{h p_0},$$

$$\bar{D}(\varphi) = -\frac{3}{35} \Lambda s \frac{1}{\sin^2(\varphi)} \frac{(\bar{p}_i - 1 - \bar{B}_i + \bar{B}_0)^2}{\left[1 + \frac{(m_i - m_0)}{(a_i - a_0)}\right]^2},$$

$$\bar{D}_i = \bar{D}(\varphi_i), \quad \bar{D}_0 = \bar{D}(\varphi_0), \quad \Lambda s = \frac{\rho p_0 h^4}{\mu^2 R_0^2 (a_i - a_0)^2}.$$

Since the diagrams of the MHD fluid flow velocity distribution along the slot between the fixed spherical surfaces show no substantial differences from the magnetohydrodynamic flow velocity distribution in the slot between the fixed conical surfaces, only the formulas for pressure profiles are illustrated in the diagram (Fig. 8).

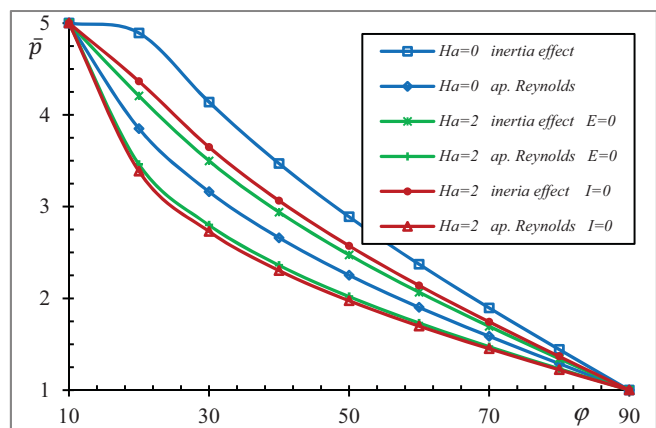


Fig. 8. Effect of magnetic field (Hartmann number (Ha)) and inertia effects on the pressure distribution \bar{p}

$$(\varphi_i = 10^\circ, \quad \varphi_0 = 90^\circ, \quad \bar{p}_i = 5, \quad \Lambda c = 0,05)$$

DISCUSSION OF THE RESULTS

On the basis of the diagram and equations describing the components of the field of velocity and pressure it is possible to formulate the following conclusions:

For the longitudinal velocity \bar{v}_x (Fig. 3):

- the main profile of the velocity \bar{v}_x^0 is a parabolic profile identical to traditional Poisseuille flow profile caused by a steady gradient of pressure (constant pressure difference) characteristic for the so-called Reynolds approximation,
- the so-called secondary profile symmetric to the slot symmetry axis formed due to the occurrence of the flow inertia effects agrees with the main velocity profile \bar{v}_x (Fig. 4),
- increase in the intensity of magnetic field expressed by an increase in the value of the Hartmann number, results in inhibiting the longitudinal velocity component \bar{v}_x ,
- a short circuit in external electrical circuit ($E=0$), as compared with open electrical circuit ($I=0$), results in a greater deceleration of the velocity component \bar{v}_x .

For the transverse velocity \bar{v}_y (Fig. 5):

- distribution of the transverse velocity \bar{v}_y is the result of inertia effects occurring in the flow,
- an increase in the intensity of magnetic field expressed by an increase in the value of the Hartmann number, results in decelerating the velocity component \bar{v}_y ,
- a short circuit in external electrical circuit ($E=0$), as compared with the open electrical circuit ($I=0$), results in a greater deceleration of the velocity component \bar{v}_y .

For the pressure p (Fig. 6 and Fig. 8):

- inertia effects ($\Lambda_c, \Lambda_s > 0$) cause a minimum pressure increase along the slot,
- an increase in the intensity of magnetic field, expressed by an increase in the value of the Hartman number Ha , results in a pressure drop along the slot, characteristic for the supply with constant pressure \bar{p}_i at the inlet (it decreases the effect of inertia),
- a short circuit in the external electric circuit ($E=0$), as compared with open electric circuit ($I=0$) results in a higher drop of the pressure \bar{p} .

The flow through slots with curvilinear profiles is less susceptible to inertia effects.

REFERENCES

1. Batažin A.B.: Ljubimow G.A., Regirer C.A., *Magnitogidrodinamiczeskije teczenia w kanałach* (in Russian), Nauka, CCCP, 1979,
2. Batchelor G. K.: *An Introduction to Fluid Dynamics*, Cambridge Press, Cambridge, 1967,
3. Bujurke N. M., Kudenatti R.B.: *MHD lubrication flow between rough rectangular plates*, Fluid Dynamic Research, 2007, 39, p. 4,
4. Cowling T. G.: *Magnetohydrodynamics*, Interscience, New York, 1957,
5. Chang C.L., Li Y.M., Huang H.H., Leong J.C.: *Analysis of fluid film lubrication of an MHD journal bearing subjected to an axially applied external magnetic field*, Applied Mechanics and Materials, 2013, p. 437,
6. Hughes W.F., Elco R.A.: *Magnetohydrodynamic lubrication flow between parallel rotating disks*, Journal of Fluid Mechanics, 1962, 13, p. 1,
7. Hughes W.F., Young F.J.: *Electromagnetodynamics of fluids*, J. Wiley, London, 1964,
8. Hamza E.A.: *Magnetohydrodynamic effects on a fluid film squeezed between two rotating surfaces*, Journal of Physics, 1991, 24, p. 4,
9. Kirillov I, R, Reed C.B.: *MHD-flow in slotted channels with conducting walls*, Fusion Engineering and Design, 1995, 27, p.1
10. Mohanty H.K.: *Hydromagnetic flow between two rotating discs with noncoincident parallel axes of rotation*, Physics of Fluids, 1972, 15, p. 8
11. Pai S. I.: *Magnetogas dynamics and Plasma Dynamics*, Springer-Verlag, Viena, Prentice Hall, Englewood Cliffs, 1962,
12. Sawicki J.: *Magnetohydrodynamic flow of viscous fluid in a slot between curvilinear surfaces of revolution*, PAN-IPPT Engineering Transactions, 1996, 44 (1),
13. Stephenson C.J.: *Magnetohydrodynamic flow between rotating coaxial disks*, Journal of Fluid Mechanics, 1969, 38, p. 2,
14. Sutton C.W., Sherman A.: *Engineering magnetohydrodynamics*, Mc. Graw-Hill, New York, 1969,
15. Swallom D.W., Sawovnik I., Gibbs J.S., Bergh H.H.: *Magnetohydrodynamic submarine propulsion system*, 103(4), 2009
16. Volkan Ersoy H.: *MHD flow of Oldroyd-B fluid between eccentric rotating disks*, 1999, 37, p.15,
17. Walicki E., Sawicki J., Ziejewski M.: *Inertia effect in magnetic fluid throughflow in a slot between fixed surfaces of revolution*, Mec. Applique, 23, 6, 1978.

CONTACT WITH THE AUTHOR

Jerzy Sawicki

e-mail: jerzy.sawicki@utp.edu.pl

UTP University of Science and Technology in Bydgoszcz

Al. Prof. S. Kaliskiego 7

85-796 Bydgoszcz

POLAND

AN OPTIMIZATION STUDY ON AN ECO-FRIENDLY ENGINE CYCLE NAMED AS DUAL-MILLER CYCLE (DMC) FOR MARINE VEHICLES

Guven Gonca

Yildiz Technical University, Turkey

ABSTRACT

The diesel engine is an indispensable part of technology and it is commonly used in land and marine vehicles. However, diesel engines release NO_x emissions due to high combustion temperatures. They have harmful effects on the environment such as sources of photo-chemical fog and climate changes. Therefore, they must be reduced and limited. The Miller cycle application is a NO_x control method and it is popular in the recent years to abate NO_x produced from the internal combustion engines (ICEs). A performance investigation of a Dual-Miller cycle (DMC) engine in terms of power (PO), power density (PD) and effective efficiency (EE) has been performed using a new finite-time thermodynamics modeling (FTTM) in this study. The effects of engine design and operating parameters on the engine performance (EPER) have been examined. Additionally, the energy losses have been determined resulting from incomplete combustion (IC), friction (FR), heat transfer (HT) and exhaust output (EO). The results presented could be an essential tool for DMC marine engine designers.

Keywords: Dual-Miller cycle engine, Engine performance, Power density, Finite-time thermodynamics

INTRODUCTION

The ICEs are commonly used in the transport sectors. However, they release pollutant emissions to the atmosphere. One of these pollutant emissions is NO_x and it is formed at high combustion temperatures. Miller cycle (MC) application is a method used to abate NO_x emission. Miller (1947) developed and applied the MC in a diesel engine to abate compression work. MC was also applied in a gas engine by Miller and Lieberherr (1957). Stebler et al. (1996) performed a numerical and experimental study to show that the MC could abate the NO_x produced from a Diesel engine. Clarke and Smith (1997) applied the MC in a diesel engine using an intake control valve. Shimogata et al. (1997) implemented the MC into a gas engine co-generation system and enhanced thermal efficiency and power output of the system. Okamoto et al. (1998) applied the MC and EGR combinations at the different ratios into a gas engine in order to examine the performance variation of the gas engine at stoichiometric combustion conditions. Anderson et al. (1998) analyzed the performance

of a MC gasoline engine based on the first and second law of thermodynamics. Wang and Ruxton (2004) reported that NO_x formation could be slowed down by the application of the MC and it is more eco-friendly compared to other engine cycles. Wang et al. (2005) conducted an experimental work to obtain abatement in NO_x of a diesel engine. The NO_x formation of a petrol engine by applying the MC with late intake valve closing version (LIVC) was decreased (Wang et al. 2007; Wang et al. 2008). Mikalsen et al. (2009) assessed the potential benefits of the MC application in a natural gas combined system. The cycle performances of the reversible MC with constant specific heats of working fluid (Al-Sarkhi et al. 2002) and the cycle performance of the reversible and irreversible MC engines considering temperature-dependent specific heats were analyzed (Al-Sarkhi et al. 2006; Al-Sarkhi et al. 2007). Zhao and Chen (2007) changed pressure ratios of a irreversible MC to assess the cycle performance. The effects of engine speed and temperature-dependent specific heats, relative air-fuel ratio and stroke length on the performance of a reversible MC were examined (Ebrahimi

2011a; Ebrahimi 2012). According to Rinaldini et al. (2013) study, NOx and soot would be minimized simultaneously in a high-speed DI Diesel engine by applying the MC. Li et al. (2014) proved that MC application could diminish the specific fuel consumption of a gasoline engine. Ge et al. (2005a) used a FTTM so as to examine the effects of FR and HT losses on the performance of an air standard MC. Wu et al. (2003) applied the MC to a supercharged gasoline engine and attained a considerable increase in thermal efficiency. It was proved that the MC application can provide a noticeable reduction in NO formation based on experimental and theoretical studies (Gonca et al. 2013a; Gonca et al. 2013b; Gonca and Sahin 2014; Gonca et al. 2015a; Gonca et al. 2015b; Gonca et al. 2015c; Gonca et al. 2015d; Gonca et al. 2015e). Ust et al. (2015) compared the exergetic performance of the Otto-Miller, Diesel-Miller and Dual-Miller cycle cogeneration systems. Martins and Lanzanova (2015) applied the MC and EGR together in a gasoline engine fuelled with ethanol and increased the brake efficiency by 47%. Gonca (2016a) compared the performances of the Otto MC, diesel MC and dual MC engines. Gonca (2016b) carried out thermodynamic analysis for the Dual-Atkinson cycle and derived the performance maps. Gonca and Sahin (2016) compared the performance and emission formations of the turbocharged and steam injected MC. Many performance analyses for Dual, Miller and other cycles by using FTT were also performed by the engine researchers described in the literature (Chen et al. 1999; Wu et al. 1999; Wang et al. 2002; Chen and Sun 2004; Ge et al. 2005b; Ge et al. 2005c; Chen 2005; Chen et al. 2006; Ge et al. 2009; Chen et al. 2010; Chen et al. 2011; Gahruei et al. 2013; Chen and Xia 2016; Chen et al. 2016; Ge et al. 2016).

The effects of the engine design and operating parameters on the performance characteristics and energy losses of an DMC engine are reported in this work. Apart from former works, comprehensive comparisons for the engine design parameters are shown by using the included figures. Furthermore, energy losses arising from EO, HT, FR and IC. In this report, realistic performance characteristics named as EE, PO and PD have been used for the DMC engine. The presented results could be assessed by an engine designer to optimize the performance of DMC engines running at lower NOx emissions.

THEORETICAL MODEL

This study presents a comprehensive analysis for DMC which is depicted in Fig. 1. A numerical simulation of EE, PO and PD is conducted by using a FTTM. In the performance computations, intake temperature (T_1), intake pressure (P_1), cycle temperature ratio ($T_6 / T_1 - \alpha$), engine speed (N), friction coefficient (μ), residual gas fraction (RGF), cylinder wall temperature (T_w), cylinder bore (d) and stroke (L) are defined as follow; 300 K, 100 kPa, 3600 rpm, 8, 12.9 Ns/m, 0.05, 400 K, 0.072 m, 0.062 m respectively, at the standard conditions.

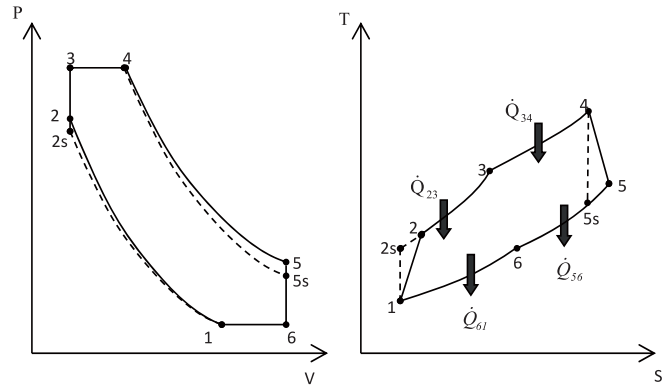


Fig. 1. P-v diagram for the irreversible Dual-Miller cycle (Gonca et al. 2013b).

The PO, PD and EE could be written as:

$$P_{ef} = \dot{Q}_{in} - \dot{Q}_{out} - P_f, P_d = \frac{P_{ef}}{V_T}, \eta_{ef} = \frac{P_{ef}}{\dot{Q}_f} \quad (1)$$

Where, the total heat addition (\dot{Q}_{in}), the total heat rejection (\dot{Q}_{out}) and loss power by friction (P_f) (Gonca et al. 2013a; Ge et al. 2008) are given as:

$$\dot{Q}_m = \dot{Q}_{f,e} - \dot{Q}_{ht} = \dot{m}_r \left[\int_{T_2}^{T_3} C_v dT + \int_{T_3}^{T_4} C_p dT \right] = \dot{m}_r \left(\left[\left(2.506 \cdot 10^{-11} \frac{T^3}{3} + 1.454 \cdot 10^{-7} \frac{T^{2.5}}{2.5} - 4.246 \cdot 10^{-7} \frac{T^2}{2} + 3.162 \cdot 10^{-5} \frac{T^{1.5}}{1.5} + 1.0433T - 1.512 \cdot 10^4 \left(-\frac{T^{-0.5}}{0.5} \right) + 3.063 \cdot 10^5 (-T^{-1}) - 2.212 \cdot 10^7 \left(-\frac{T^{-2}}{2} \right) \right]_{T_2}^{T_3} \right) + \left(\left[\left(2.506 \cdot 10^{-11} \frac{T^3}{3} + 1.454 \cdot 10^{-7} \frac{T^{2.5}}{2.5} - 4.246 \cdot 10^{-7} \frac{T^2}{2} + 3.162 \cdot 10^{-5} \frac{T^{1.5}}{1.5} + 1.3301T - 1.512 \cdot 10^4 \left(-\frac{T^{-0.5}}{0.5} \right) + 3.063 \cdot 10^5 (-T^{-1}) - 2.212 \cdot 10^7 \left(-\frac{T^{-2}}{2} \right) \right]_{T_3}^{T_4} \right) \right) \quad (2)$$

$$\dot{Q}_{out} = \dot{m}_r \left[\int_{T_5}^{T_6} C_v dT + \int_{T_6}^{T_1} C_p dT \right] = \dot{m}_r \left(\left[\left(2.506 \cdot 10^{-11} \frac{T^3}{3} + 1.454 \cdot 10^{-7} \frac{T^{2.5}}{2.5} - 4.246 \cdot 10^{-7} \frac{T^2}{2} + 3.162 \cdot 10^{-5} \frac{T^{1.5}}{1.5} + 1.0433T - 1.512 \cdot 10^4 \left(-\frac{T^{-0.5}}{0.5} \right) + 3.063 \cdot 10^5 (-T^{-1}) - 2.212 \cdot 10^7 \left(-\frac{T^{-2}}{2} \right) \right]_{T_5}^{T_6} \right) + \left(\left[\left(2.506 \cdot 10^{-11} \frac{T^3}{3} + 1.454 \cdot 10^{-7} \frac{T^{2.5}}{2.5} - 4.246 \cdot 10^{-7} \frac{T^2}{2} + 3.162 \cdot 10^{-5} \frac{T^{1.5}}{1.5} + 1.3301T - 1.512 \cdot 10^4 \left(-\frac{T^{-0.5}}{0.5} \right) + 3.063 \cdot 10^5 (-T^{-1}) - 2.212 \cdot 10^7 \left(-\frac{T^{-2}}{2} \right) \right]_{T_6}^{T_1} \right) \right) \quad (3)$$

$$P_f = \mu \bar{S}_p^2 = \frac{\left[Z + 48 \left(\frac{N}{1000} \right) + 0.4 \bar{S}_p^2 \right] V_s N}{1200} \quad (4)$$

where Z is a constant relation to friction (Gonca et al. 2013a) and its minimum value is 75 for the diesel engines, where μ is the friction coefficient, \bar{S}_p is the average piston velocity which is :

$$\bar{S}_p = \frac{L \cdot N}{30} \quad (5)$$

where L and N are stroke length (m) and speed (rpm). \dot{Q}_f is the total heat potential of the fuel injected into the combustion chamber and it is obtained as:

$$\dot{Q}_f = \dot{m}_f H_u \quad (6)$$

where H_u is the lower heat value (LHV). \dot{m}_f is the time-dependent fuel mass and it can be expressed as follows:

$$\dot{m}_f = \frac{m_f N}{120} \quad (7)$$

where m_f is fuel mass per cycle (kg). $\dot{Q}_{f,c}$ is the heat released by combustion; \dot{Q}_{ht} is the heat loss by heat transfer into cylinder wall and they are given as below:

$$\dot{Q}_{f,c} = \eta_c \dot{m}_f H_u \quad (8)$$

$$\dot{Q}_{ht} = h_{tr} A_{cyl} (T_{me} - T_W) = h_{tr} A_{cyl} \left(\frac{T_2 + T_4}{2} - T_W \right) \quad (9)$$

where, η_c is the combustion efficiency. It can be written as (Ebrahimi 2011a; Ebrahimi 2011b; Ebrahimi 2012):

$$\eta_c = -1,44738 + 4,18581 / \phi - 1,86876 / \phi^2 \quad (10)$$

ϕ is equivalence ratio and it can be written as:

$$\phi = \frac{(m_f / m_a)}{F_{st}} \quad (11)$$

where, m_a is air mass per cycle (kg). F_{st} is stoichiometric fuel-air ratio and they are given as follows:

$$m_a = \rho_a V_a = \rho_a (V_T - V_{rg}) \quad (12)$$

$$V_T = V_s + V_c = \frac{(V_s r)}{r-1} \quad (13)$$

$$V_c = \frac{V_T}{r} = \frac{\pi d^2 L}{4} \frac{1}{r-1} \quad (14)$$

$$F_{st} = \frac{\varepsilon \cdot (12.01 \cdot \alpha + 1.008 \cdot \beta + 16 \cdot \gamma + 14.01 \cdot \delta)}{28.85} \quad (15)$$

$$\rho_a = f(T_1, P_1) \quad (16)$$

where V_T , V_a , V_{rg} , V_s , and V_c are volume of total cylinder, air, residual gas, stroke and clearance.

ρ_{rg} is density of residual gas which is given as:

$$\rho_{rg} = f(T_{mix}, P_1) \quad (18)$$

T_{mix} is average temperature of air-steam mixture. They are given as:

$$T_{mix} = \frac{\dot{m}_a T_a R_a + \dot{m}_{rg} T_{rg} R_{rg}}{\dot{m}_a R_a + \dot{m}_{rg} R_{rg}} \quad (20)$$

R_a and R_{rg} are gas constants of air and residual gas. Their values are considered in the calculations as 0.287kJ/kg.K

The compression ratio (r) is given as:

$$r = V_1 / V_2 \quad (21)$$

Where f means function for the eq. 18. The functional expressions are obtained by using EES software (EES 2016). Fuel used in the model is diesel and its chemical formula is given as $C_{14.4}H_{24.9}$ (Ferguson 1986). Where $\alpha, \beta, \gamma, \delta$ are atomic numbers of carbon, hydrogen, oxygen, nitrogen in fuel, respectively. ε is the molar fuel-air ratio (Ferguson 1986):

$$\varepsilon = \frac{0,21}{\left(\alpha - \frac{\gamma}{2} + \frac{\beta}{4} \right)} \quad (22)$$

where, h_{tr} is the heat transfer coefficient and it is stated as (Hohenberg 1979):

$$h_{tr} = 130 V_T^{-0.06} P_1^{0.8} T_{mix}^{0.4} (\bar{S}_p + 1.4)^{0.8} \quad (23)$$

\dot{m}_T , \dot{m}_a , \dot{m}_{rg} and A_{cyl} are flow rate of air-fuel mixture (kg/s), air (kg/s), residual gas (kg/s) and heat transfer area of the cylinder (m²), respectively, they are stated as follows:

$$\dot{m}_T = \dot{m}_a + \dot{m}_f + \dot{m}_{rg} \quad (24)$$

$$\dot{m}_a = \frac{m_a N}{120} = \frac{\dot{m}_f F_{st}}{\phi} \quad (25)$$

$$\dot{m}_{rg} = \frac{m_{rg} N}{120} = \dot{m}_a RGF \quad (27)$$

$$A_{cyl} = \pi dL \frac{r}{r-1} + \frac{\pi d^2}{2} \quad (28)$$

where m_s and m_{rg} are air masses per cycle (kg). RGF is the residual gas fraction. d and r are cylinder bore (m) and compression ratio, respectively. T_{me} and T_w are average combustion temperature and cylinder wall temperature. C_p and C_v are the specific heats of constant pressure and constant volume processes, they are given as (Ge et al. 2008):

$$C_p = 2.506 \cdot 10^{-11} T^2 + 1.454 \cdot 10^{-7} T^{1.5} - 4.246 \cdot 10^{-7} T + 3.162 \cdot 10^{-5} T^{0.5} + 1.3301 - 1.512 \cdot 10^4 T^{-1.5} + 3.063 \cdot 10^5 T^{-2} - 2.212 \cdot 10^7 T^{-3} \quad (29)$$

$$C_v = C_p - R \quad (30)$$

The equations for reversible adiabatic processes (1-2s) and (4-5s) are respectively as follows (Lin et al. 1999):

$$C_{V_1} \cdot \ln \left| \frac{T_{2s}}{T_1} \right| = R \ln |r|, \quad C_{V_2} \cdot \ln \left| \frac{T_{5s}}{T_4} \right| = R \cdot \ln \left| \frac{1}{r} \right| \quad (31)$$

where,

$$C_{V_1} = 2.506 \cdot 10^{-11} T_{2s1}^2 + 1.454 \cdot 10^{-7} T_{2s1}^{1.5} - 4.246 \cdot 10^{-7} T_{2s1} + 3.162 \cdot 10^{-5} T_{2s1}^{0.5} + 1.0433 - 1.512 \cdot 10^4 T_{2s1}^{-1.5} + 3.063 \cdot 10^5 T_{2s1}^{-2} - 2.212 \cdot 10^7 T_{2s1}^{-3} \quad (32)$$

$$C_{V_2} = 2.506 \cdot 10^{-11} T_{5s4}^2 + 1.454 \cdot 10^{-7} T_{5s4}^{1.5} - 4.246 \cdot 10^{-7} T_{5s4} + 3.162 \cdot 10^{-5} T_{5s4}^{0.5} + 1.0433 - 1.512 \cdot 10^4 T_{5s4}^{-1.5} + 3.063 \cdot 10^5 T_{5s4}^{-2} - 2.212 \cdot 10^7 T_{5s4}^{-3} \quad (33)$$

$$T_{2s1} = \frac{T_{2s} - T_1}{\ln \frac{T_{2s}}{T_1}}, \quad T_{5s4} = \frac{T_{5s} - T_4}{\ln \frac{T_{5s}}{T_4}} \quad (34)$$

$$\beta = P_3 / P_2 = T_3 / T_2 \quad (35)$$

β is named as pressure ratio. For irreversible conditions, T_2 and T_5 could be written as (Rashidi et al 2013; Rashidi et al 2014a; Rashidi et al 2014b; Rashidi et al 2014c; Rashidi et al 2014d; Mousapour et al. 2016; Gonca 2017b; Gonca 2017c; Gonca 2017d; Gonca and Sahin 2017b) :

$$T_2 = \frac{T_{2s} + T_1 (\eta_C - 1)}{\eta_C} \quad (36)$$

$$T_5 = T_4 + \eta_E (T_{5s} - T_4) \quad (37)$$

Where η_C and η_E are isentropic compression and expansion efficiencies, respectively. In this work, the other dimensionless engine design parameters used in the analysis are cycle temperature ratio (CTR- α), cycle pressure ratio

(CPR- λ) and cut-off ratio (ψ). They may be expressed respectively as:

$$\alpha = \frac{T_{max}}{T_{min}} = \frac{T_4}{T_1} = \frac{\lambda}{r} \quad (38)$$

$$\lambda = P_{max} / P_{min} = P_3 / P_1 \quad (39)$$

$$\psi = v_4 / v_3 = T_4 / T_3 \quad (40)$$

Energy losses could be expressed as percentage of fuel's energy by combustion in combustion chamber of the engine (Lin et al. 2008). In this work, similar approach is used to obtain the energy losses dependent on heat transfer to cylinder wall, exhaust, friction and incomplete combustion presented as:

$$L_{ht} = \frac{\dot{Q}_{ht}}{\dot{Q}_{fuel}} \cdot 100, \quad L_{ex} = \frac{\dot{Q}_{out}}{\dot{Q}_{fuel}} \cdot 100, \quad L_{fr} = \frac{P_u}{\dot{Q}_{fuel}} \cdot 100, \quad L_{ic} = (1 - \eta_c) \cdot 100 \quad (41)$$

RESULTS AND DISCUSSION

In this study, a FTTM has been applied to a DMC engine to evaluate PO, PD and EE. Fig. 2 shows the effects of cycle temperature ratio on the performance characteristics. The maximum EE, PO and PD increase with increasing CTR owing to more energy input into a cylinder.

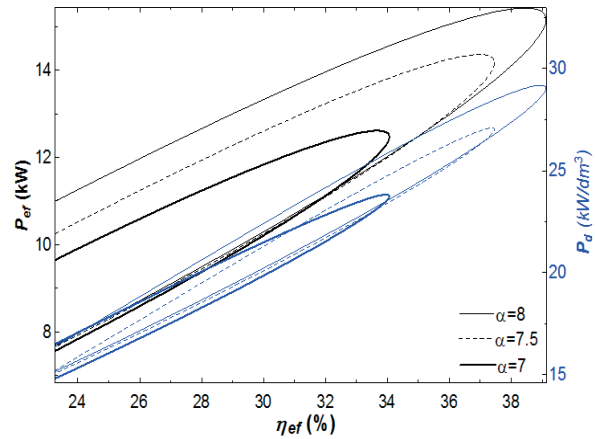


Fig. 2. The variation of P_{ef} - P_d - η_{ef} with respect to α .

Fig. 3 shows the effects of friction coefficient on the performance parameters. The friction coefficient is related to lubrication oil and in-cylinder surfaces in which friction occurs. Friction losses increase with increasing the friction coefficient, hence performance parameters decrease remarkably since irreversibility increases.

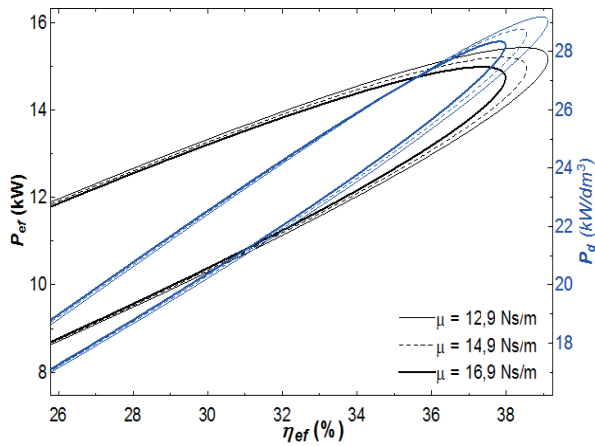


Fig. 3. The variation of $P_{ef} - P_d - \eta_{ef}$ with respect to μ .

Fig. 4 illustrates the effects of the engine speed on the performance characteristics. As expected, the PO and PD rise with enhancing speed. However, the effective efficiency is slightly lower at higher engine speeds as the friction losses rise with augmenting engine speeds. It is clear that the raise ratio of fuel energy is slightly higher compared to that of PO and PD.

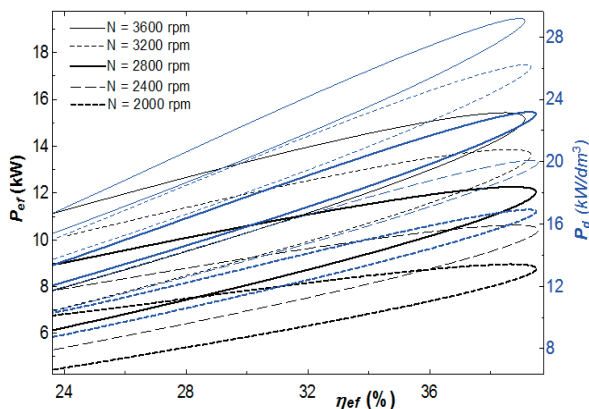


Fig. 4. The variation of $P_{ef} - P_d - \eta_{ef}$ with respect to N .

Figs. 5 show the influence of mean piston speed on the engine performance. Fig. 5a is plotted at constant engine speed condition. In this figure, it is shown that the performance characteristics rise simultaneously with enhancing mean piston speed because engine dimensions (stroke length and bore) enhance together. Fig. 5b is plotted at constant stroke length condition. As the effective efficiency decreases, the PO and PD increase with increasing mean piston speed at this condition, since engine speed raises. It is clearly seen that PD change at constant stroke length condition is greater than that at constant engine speed condition, as the change in engine dimensions has similar trend as the change in PO at the constant stroke length condition.

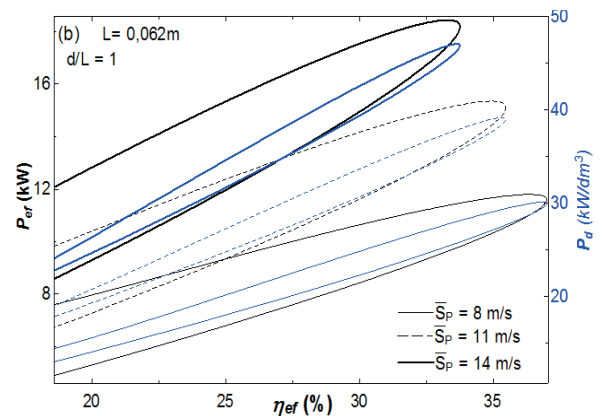
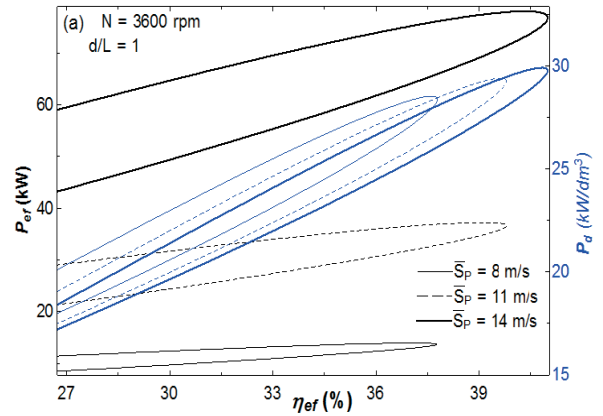


Fig. 5. The variation of $P_{ef} - P_d - \eta_{ef}$ with respect to \bar{S}_p at constant a) N , b) L .

Fig. 6 shows the effects of stroke length on the engine performance characteristics. It is clear from the figure that the PO increases while the EE and PD decrease with enhancing stroke length. The main reason of this result is that the friction losses and engine dimensions increase with respect to stroke length. Although engine power increases, engine dimensions increase more. Therefore, power density decreases with increasing power. Also, it is seen from the figure that the ratio of power change is higher than that of power density.

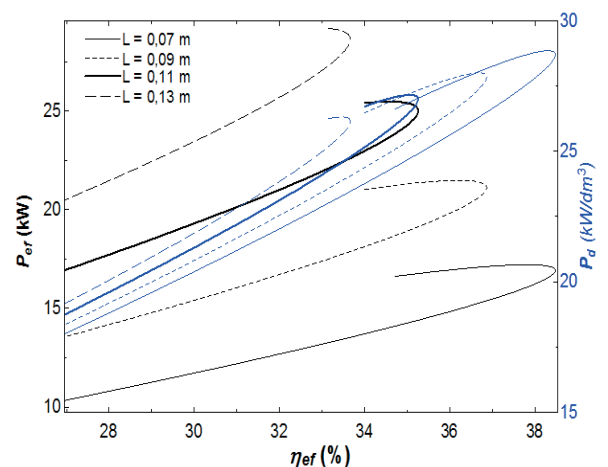


Fig. 6. The variation of $P_{ef} - P_d - \eta_{ef}$ with respect to L .

Fig. 7a and 7b show the effects of intake temperature on the engine performance at two different conditions. Fig. 7a is plotted at constant CTR condition. The performance characteristics increase while intake temperature increases since maximum combustion temperature and energy input increase. Fig. 7b is plotted at constant maximum combustion temperature condition. The performance parameters minimize with increasing intake temperature since air mass introduced into cylinder minimizes.

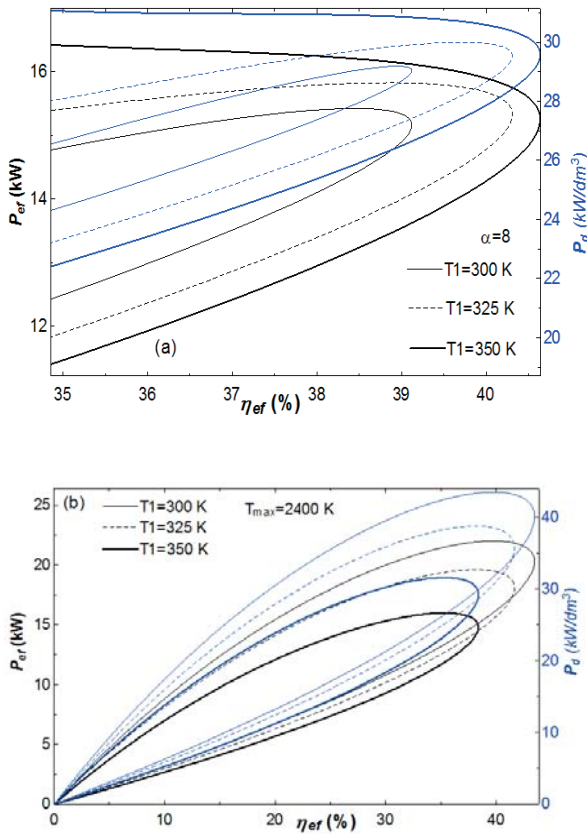


Fig. 7. The variation of P_{ef} - P_d - η_{ef} with respect to T_1 at constant a) α and b) T_{max} .

Fig. 8a, 8b, 8c and 8d illustrate the influences of equivalence ratio and compression ratio on the CTR and the performance characteristics. The CTR and the performance characteristics enhance with rising compression ratio. However, they rise to a certain value and then begin to abate with rising equivalence ratios. There are optimum values of equivalence ratio which give maximum CTR, PO, PD and EE. Their optimum values are observed at different equivalence ratios. The maximum values of CTR, PO and PD are between 1 and 1.2 of equivalence ratio while the maximum value of EE is between 0.8 and 1 of the equivalence ratio.

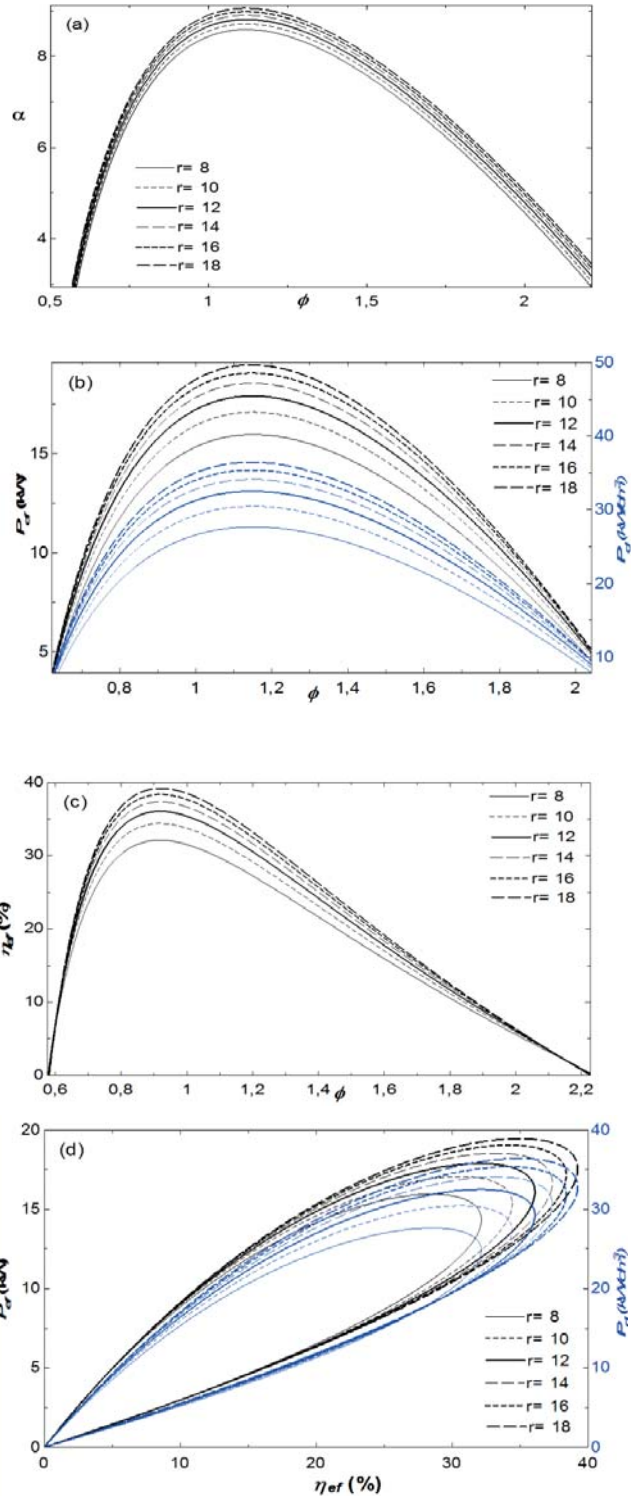


Fig. 8. The variation of a) α , b) P_{ef} - P_d , c) η_{ef} and d) P_{ef} - η_{ef} with respect to r and ϕ .

Fig. 9 shows the influence of equivalence ratio on the engine performance. Similar to previous figures, the performance parameters increase to certain values of equivalence ratio and then start to reduce. The maximum effective efficiency is seen at 0.9 of equivalence ratio while the maximum power is seen at 1.2 of equivalence ratio.

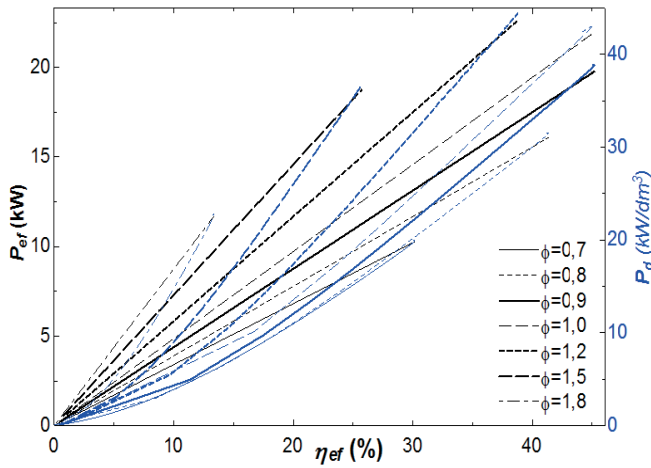


Fig. 9. The variation of $P_{ef} - P_d - \eta_{ef}$ with respect to ϕ .

Fig. 10 shows the effects of cylinder wall temperature on the engine performance. There are no noticeable changes in maximum power and power density depending on cylinder wall temperature. However, maximum effective efficiency decreases with decreasing cylinder wall temperature since heat transfer loss increases with decreasing wall temperature.

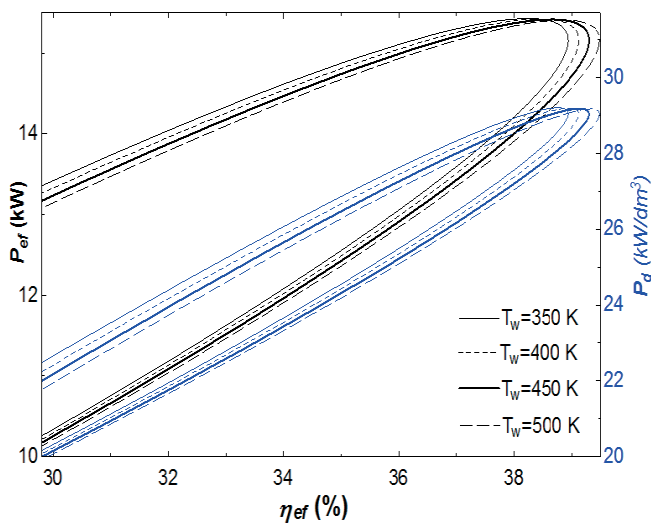


Fig. 10. The variation of $P_{ef} - P_d - \eta_{ef}$ with respect to T_w .

Fig. 11 demonstrates the influence of intake pressure on the engine performance. It is known that more air mass is introduced into the cylinder at higher pressure conditions. Thus, performance parameters increase with raising intake pressure.

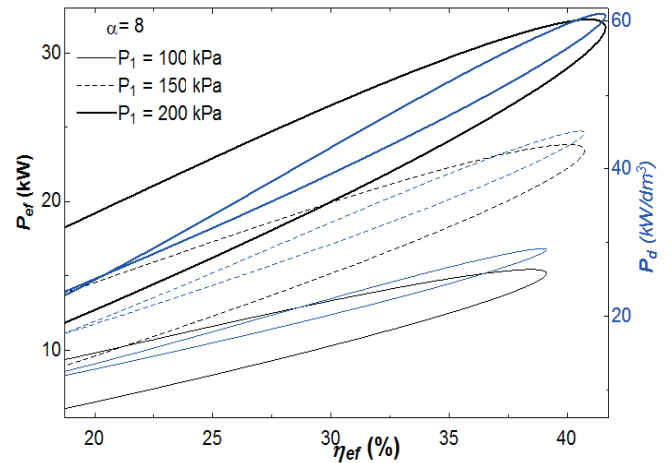


Fig. 11. The variation of $P_{ef} - P_d - \eta_{ef}$ with respect to P_1 .

The influences of the ratio of bore to stroke (d/L) on the performance characteristics are demonstrated in Fig.12. It is clear that the performance characteristics rise with raising d/L due to increasing engine dimensions.

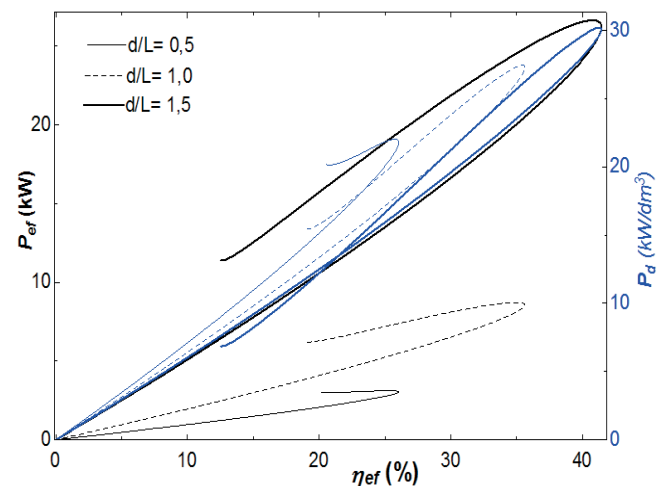


Fig. 12. The variation of $P_{ef} - P_d - \eta_{ef}$ with respect to d/L .

Figs. 13a-c show the effects of d/L on the performance characteristics at constant cylinder volume for three different conditions. Fig. 13a is plotted at constant CTR and stroke length condition. The performance parameters enhance to a determined value and then begin to abate with rising d/L . Fig. 13b is plotted at constant equivalence ratio and stroke length condition. The performance parameters raise with increasing d/L . Fig. 13c is plotted at constant equivalence ratio and compression ratio condition. This figure shows similar characteristics to previous figure. Same increase trend can be observed.

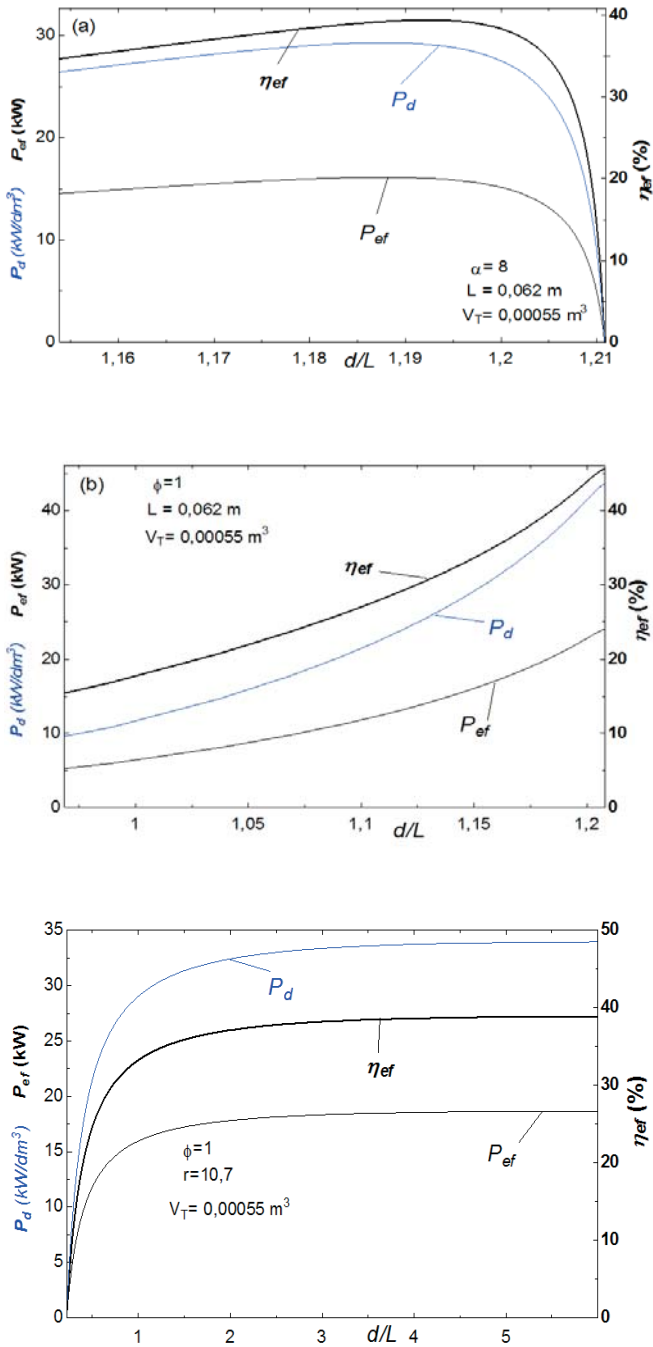


Fig. 13. The effects of d/L on P_{ef} - P_d - η_{ef} variation at constant a) α and L , b) ϕ and L , c) ϕ and r .

Figs. 14a-b demonstrate the influence of r on losses as fuel's energy for two different conditions. Fig. 14a is depicted at constant cycle temperature ratio condition. Incomplete combustion loss (L_{ic}) and exhaust energy loss (L_{ex}) decrease while heat transfer loss (L_{ht}) increase and friction loss (L_{fr}) remains constant with increasing r . Total cylinder volume and equivalence ratio change with respect to changing of r at this condition. L_{ic} is related to equivalence ratio and it changes with changing equivalence ratio. It decreases as fuel energy input decreases with increasing r . Fig. 14b is

depicted at constant equivalence ratio condition. L_{ic} and L_{fr} are constant, L_{ht} increases and L_{ex} decreases with respect to rising compression ratio. Cylinder volume enhances with increasing r , hence L_{ht} increases. Useful work increases with increasing r and so L_{ex} abates. L_{fr} changes with respect to stroke and speed which are constant at both of these conditions. Therefore, L_{ic} does not change.

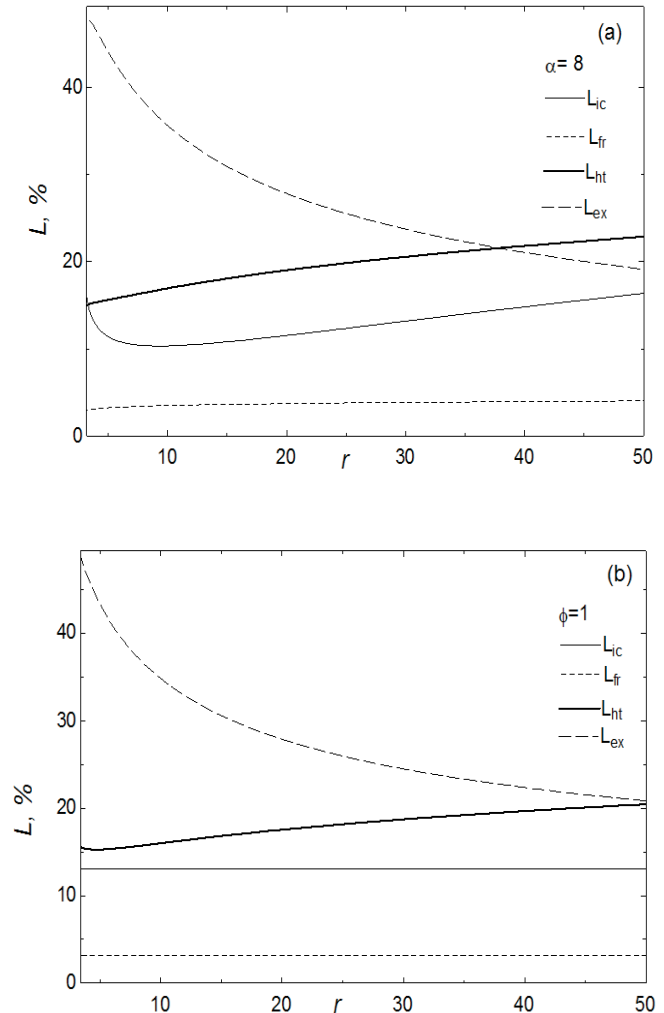


Fig. 14. The variation of energy loss percentages with respect to r for constant a) α and b) ϕ .

Figs. 15a-c demonstrate the effects of RGF on the performance parameters for three different conditions. The figures are plotted at constant cycle temperature condition, constant equivalence ratio condition and at constant compression ratio condition. Similar trends are seen for all conditions. The performance characteristics abate with increasing RGF as expected. Because, intake temperature rises and air mass introduced into the cylinder diminishes with increasing RGF.

CONCLUSION

The influences of the engine design and operating parameters on the performance characteristics and energy losses of a diesel engine have been investigated using a FTTM. Comprehensive parametrical comparisons have been performed. In the parametrical studies, the influences of CTR (α), CPR (λ), friction coefficient (μ), engine speed (N), mean piston speed (\bar{S}_p), stroke length (L), intake temperature (T1), intake pressure (P_1), equivalence ratio (ϕ), compression ratio (r), bore-stroke length ratio (d/L) and residual gas fraction (RGF) on the performance parameters have been examined. The results show that the performance parameters increase with increasing cycle temperature ratio (α), cycle pressure ratio (λ) and intake pressure (P_1). The engine performance abates with friction coefficient (μ). On the other hand, the PO, PD and EE rise with rising mean piston speed for constant engine speed conditions. However, as the PO and PD increase, the EE diminishes with rising mean piston speed for constant stroke length conditions. While the PO and PD increase, the EE abates with rising stroke length and engine speed. The PO, PD and EE increase up to a determined value and then begin to abate with rising equivalence ratio and compression ratio. The energy losses with respect to heat transfer increase, as incomplete combustion and exhaust output losses decrease with increasing compression ratio for constant α conditions. At this condition, friction losses are constant. However, the losses dependent on friction and incomplete combustion are constant, while exhaust output losses decrease and heat transfer losses increase at the constant equivalence ratio conditions. Scientifically valuable results have been obtained and they can be used by eco-friendly engine designers.

REFERENCES

1. Al-Sarkhi, A., Akash, B.A. & Jaber, J.O., 2002. Efficiency of Miller Engine at Maximum Power Density. *Int Commun Heat Mass*, 29, pp.1159-1167.
2. Al-Sarkhi, A., Jaber, J.O., Probert, S.D., 2006. Efficiency of a Miller engine. *Appl Energy*, 83, pp.343-351.
3. Al-Sarkhi, A., Al-Hinti, I., Abu-Nada, E., Akash, B., 2007. Performance evaluation of irreversible Miller engine under various specific heat models. *Int Commun Heat Mass*, 34, pp.897-906.
4. Anderson, M., Assanis, D., Filipi, Z., 1998. First and second law analyses of a naturally-aspirated, Miller cycle, SI engine with late intake valve closure. *SAE Technical Paper Series*, 980889, pp.1-16.

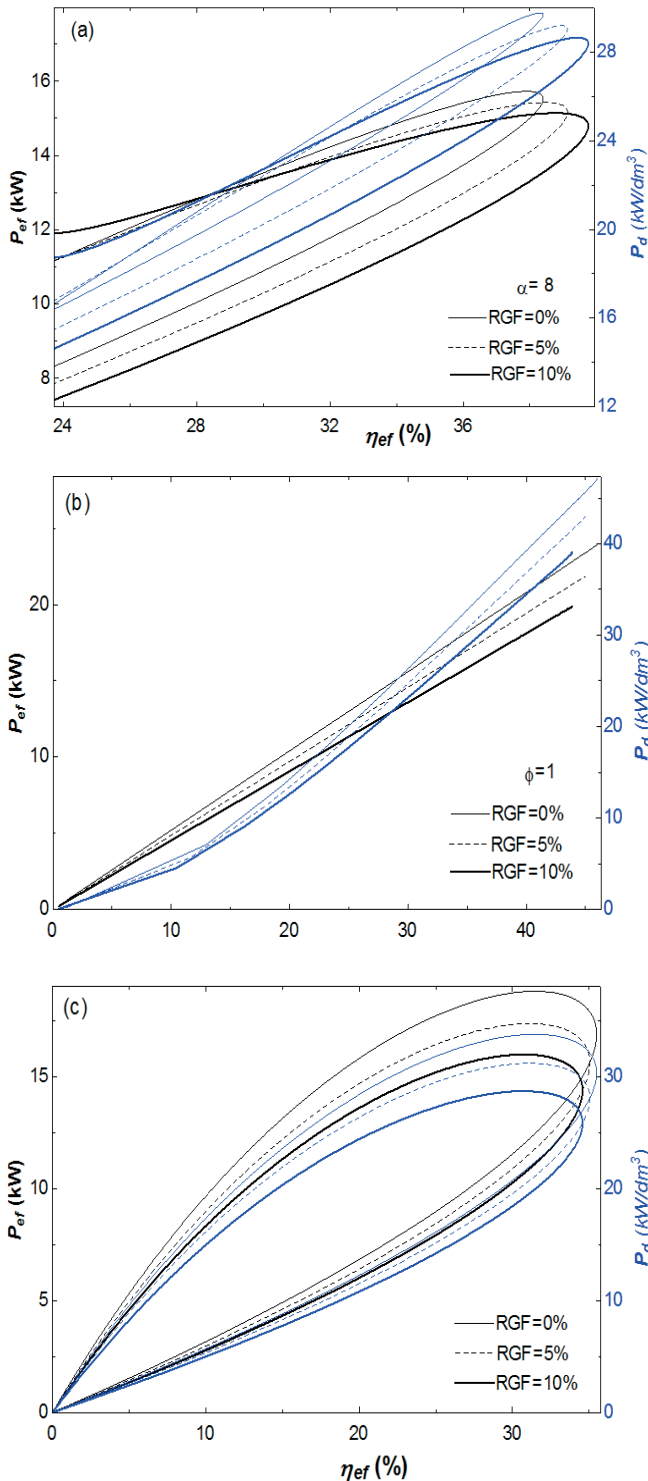


Fig. 15. The effects of RGF on $P_{ef} - P_d - \eta_{ef}$ variation at constant a) α , b) ϕ , c) r .

In this work, the curves are obtained with respect to the variation of the equivalence ratio. The operating points of the engine can be determined to acquire the maximum efficiency or maximum power conditions.

5. Benajes, J., Molina, S., Novella, R., Belarte, E., 2014. Evaluation of massive exhaust gas recirculation and Miller cycle strategies for mixing-controlled low temperature combustion in a heavy duty diesel engine. *Energy*, 71, 355-366.
6. Chen, L., Wu, C. & Sun, F.R., 1999. Finite time thermodynamic optimization or entropy generation minimization of energy systems. *J. Non-Equilib. Thermodyn.*, 24(4), pp.327-359. Chen, L. & Sun, F.R., 2004. *Advances in Finite Time Thermodynamics: Analysis and Optimization*. New York: Nova Science Publishers,
7. Chen, L., 2005. *Finite-Time Thermodynamic Analysis of Irreversible Processes and Cycles*. Beijing: High Education Press. (in Chinese).
8. Chen, L., Ge, Y., Sun, F., & Wu, C., 2006. Effects of heat transfer, friction and variable specific heats of working fluid on performance of an irreversible Dual cycle. *Energy Convers. Manage.*, 47(18/19), pp.3224-3234.
9. Chen, L., Ge, Y., Sun, F., & Wu, C., 2010. The performance of a Miller cycle with heat transfer, friction and variable specific heats of working fluid. *Termotehnika*, 14(2), pp.24-32.
10. Chen, L., Ge, Y., Sun, F., & Wu, C., 2011. Finite time thermodynamic modeling and analysis for an irreversible Miller cycle. *Int. J. Ambient Energy*, 32(2), pp.87-94.
11. Chen, L. & Xia, S.J., 2016. *Generalized Thermodynamic Dynamic-Optimization for Irreversible Processes*. Beijing: Science Press. (in Chinese).
12. Chen, L., Xia, S.J. & Li, J., 2016. *Generalized Thermodynamic Dynamic-Optimization for Irreversible Cycles*. Beijing: Science Press. (in Chinese).
13. Clarke, D., & Smith, W.J., 1997. Simulation, implementation and analysis of the Miller cycle using an inlet control rotary valve, Variable valve actuation and power boost. *SAE Special Publications*, 1258(970336), pp. 61–70.
14. Ebrahimi, R., 2011a. Thermodynamic modeling of performance of a Miller cycle with engine speed and variable specific heat ratio of working fluid. *Computers and Mathematics with Applications*, 62, pp.2169–2176.
15. Ebrahimi, R., 2011b. Effects of mean piston speed, equivalence ratio and cylinder wall temperature on performance of an Atkinson engine. *Mathematical and Computer Modelling*, 53, pp.1289-1297.
16. Ebrahimi, R., 2012. Performance analysis of an irreversible Miller cycle with considerations of relative air–fuel ratio and stroke length. *Applied Math Modeling*, 36, pp.4073–4079.
17. EES Academic Professional Edition, 2016. V.10.112-3D, USA, F-Chart Software.
18. Ferguson, C.R., 1986. *Internal combustion engines – applied thermosciences*. New York: John Wiley & Sons Inc.
19. Gahruei, M.H., Jeshvaghani, H.S., Vahidi, S., & Chen, L., 2013. Mathematical modeling and comparison of air standard Dual and Dual-Atkinson cycles with friction, heat transfer and variable specific-heats of the working fluid. *Applied Mathematical Modelling*, 37(12-13), pp.7319-7329.
20. Ge, Y., Chen, L., Sun, F., & Wu, C., 2005a. Reciprocating heat-engine cycles. *Appl. Energy*, 81, pp.397–408.
21. Ge, Y., Chen, L., Sun, F., & Wu, C., 2005b. Effects of heat transfer and friction on the performance of an irreversible air-standard Miller cycle. *Int. Comm. Heat Mass Transfer*, 32(8), pp.1045-1056.
22. Ge, Y., Chen, L., Sun, F., & Wu, C., 2005c. Effects of heat transfer and variable specific heats of working fluid on performance of a Miller cycle. *Int. J. Ambient Energy*, 26(4), pp.203-214.
23. Ge, Y., Chen, L., Sun, F., & Wu, C., 2008. Finite-Time Thermodynamic Modelling and Analysis of an Irreversible Otto-Cycle. *Appl Energy*, 85, pp.618-24.
24. Ge, Y., Chen, L., & Sun, F., 2009. Finite time thermodynamic modeling and analysis for an irreversible Dual cycle. *Math. Comput. Model.*, 50(1-2), pp.101-108.
25. Ge, Y., Chen, L., & Sun, F., 2016. Progress in finite time thermodynamic studies for internal combustion engine cycles. *Entropy*, 18(4), pp.139.
26. Gonca, G., 2016a. Comparative performance analyses of irreversible OMCE (Otto Miller cycle engine)-DiMCE (Diesel miller cycle engine)-DMCE (Dual Miller cycle engine). *Energy*, 109, pp.152–159.
27. Gonca, G., 2016b. Thermodynamic analysis and performance maps for the irreversible Dual–Atkinson cycle engine (DACE) with considerations of temperature-dependent specific heats, heat transfer and friction losses. *Energy Conversion and Management*, 111, pp.205–216.
28. Gonca, G., 2017a. Thermo-Ecological Analysis of Irreversible Dual-Miller Cycle (DMC) Engine Based on the Ecological Coefficient of Performance (ECOP) Criterion, *Iran J Sci Technol Trans Mech Eng (In press.)*, doi:10.1007/s40997-016-0060-2.
29. Gonca, G., 2017b. Exergetic and ecological performance analyses of a gas turbine system with two intercoolers and two re-heaters. *Energy*, 124, pp. 579-588.

30. Gonca, G., 2017c. Effects of engine design and operating parameters on the performance of a spark ignition (SI) engine with steam injection method (SIM). *Applied Math. Model.*, 44, pp. 655-675.
31. Gonca, G., 2017d. Performance Analysis of A Spark Ignition (SI) Otto Cycle (OC) Gasoline Engine Under Realistic Power (RP) and Realistic Power Density (RPD) Conditions. *Journal of Polytechnic*, 20(2), pp.475-486. Gonca, G., Sahin, B., Ust, Y., & Parlak A., 2013a. A study on late intake valve closing Miller cycled diesel engine. *Arab J Sci Eng*, 38, pp.383-393.
32. Gonca, G., Sahin, B., & Ust, Y., 2013b. Performance maps for an air-standard irreversible dual-Miller cycle (DMC) with late inlet valve closing (LIVC) version. *Energy*, 5, pp.285-290.
33. Gonca, G., & Sahin, B., 2014. Performance Optimization of an Air-Standard Irreversible Dual-Atkinson Cycle Engine Based on the Ecological Coefficient of Performance Criterion. *The Scientific World Journal*, 815787, pp.1-10.
34. Gonca, G., Sahin, B., Ust, Y., Parlak, A., & Safa, A., 2015a. Comparison of Steam Injected Diesel Engine and Miller Cycled Diesel Engine By Using Two Zone Combustion Model. *J Energy Inst*, 88(1), pp.43-52.
35. Gonca, G., Sahin, B., Parlak, A., Ust, Y., Ayhan, V., Cesur, I., & Boru, B., 2015b. Theoretical and experimental investigation of the Miller cycle diesel engine in terms of performance and emission parameters. *Appl. Energy*, 138, pp.11-20.
36. Gonca, G., Sahin, B., & Ust, Y., 2015c. Investigation of heat transfer influences on performance of air-standard irreversible dual-Miller cycle. *J. Thermophys Heat Trans*, 29(4), pp.678-683.
37. Gonca, G., Sahin, B., Parlak, A., Ayhan, V., Cesur, I., & Koksall, S., 2015d. Application of the Miller cycle and turbo charging into a diesel engine to improve performance and decrease NO emissions. *Energy*, 93, pp.795-800.
38. Gonca, G., Sahin, B., Ust, Y., & Parlak, A., 2015e. Comprehensive performance analyses and optimization of their reversible thermodynamic cycle engines (TCE) under maximum power (MP) and maximum power density (MPD) conditions. *Appl Thermal Eng*, 85, pp.9-20.
39. Gonca, G., & Sahin, B., 2016. The influences of the engine design and operating parameters on the performance of a turbocharged and steam injected diesel engine running with the Miller cycle. *Applied Mathematical Modelling*, 40, pp.3764-3782.
40. Gonca, G., & Sahin, B., 2017a. Effect of turbo charging and steam injection methods on the performance of a Miller cycle diesel engine (MCDE). *Applied Thermal Engineering*, 118, pp.138-146.
41. Gonca, G., & Sahin, B., 2017b. Thermo-ecological performance analysis of a Joule-Brayton cycle (JBC) turbine with considerations of heat transfer losses and temperature-dependent specific heats. *Energy Conversion and Management* 138, pp. 97-105.
42. Gonca, G., Sahin, B., Parlak, A., Ayhan, V., Cesur, I., & Koksall, S., 2017. Investigation of the effects of the steam injection method (SIM) on the performance and emission formation of a turbocharged and Miller cycle diesel engine (MCDE). *Energy*, 119, pp.926-937.
43. Hohenberg, G., 1979. *Advanced Approaches for Heat Transfer Calculations*. SAE, 790825.
44. Imperato, M., Kaario, O., Sarjovaara, T., Larmi, M., 2016. Split fuel injection and Miller cycle in a large-bore engine. *Applied Energy*, 162, pp.289-297.
45. Li, T., Gao, Y., Wang, J., & Chen, Z., 2014. The Miller cycle effects on improvement of fuel economy in a highly boosted, high compression ratio, direct-injection gasoline engine: EIVC vs LIVC. *Energy Convers and Manage*, 79, pp.59-65.
46. Li, T., Wang, B., Zheng, B., 2016. A comparison between Miller and five-stroke cycles for enabling deeply downsized, highly boosted, spark-ignition engines with ultra expansion. *Energy Conversion and Management*, 123, pp.140-152.
47. Lin, J., Chen, L., Wu, C., & Sun, F., 1999. Finite-Time Thermodynamic Performance of a Dual Cycle. *Int J Energy Res*, 23(9), pp.765-772.
48. Lin, J.C., & Hou, S.S., 2008. Effects of Heat Loss As Percentage of Fuel's Energy, Friction And Variable Specific Heats Of Working Fluid On Performance of Air Standart Otto Cycle. *Eng Convers Manage*, 49, pp.1218-27.
49. Luo, Q., Sun, B., 2016. Effect of the Miller cycle on the performance of turbocharged hydrogen internal combustion engines. *Energy Conversion and Management*, 123, pp.209-217.
50. Martins, M.E.S., & Lanzanova, T.D.M., 2015. Full-load Miller cycle with ethanol and EGR: Potential benefits and challenges. *Applied Thermal Engineering*, 90, 274-285.
51. Mikalsen, R., Wang, Y.D., & Roskilly, A.P., 2009. A comparison of Miller and Otto cycle natural gas engines for small scale CHP applications. *Applied Energy*, 86, pp.922-927.

52. Miller, R.H., 1947. Supercharging and internal cooling cycle for high output, *Transactions of ASME*, 69, pp.453–457.
53. Miller, R.H., & Lieberherr, H.U., 1957. The Miller supercharging system for diesel and gas engines operating characteristics, CIMAC, Proceedings of the 4th International Congress on Combustion Engines, Zurich, June 15–22, pp. 787–803.
54. Mousapour, A., Hajipour, A., Rashidi, M.M., Freidoonimehr, N., 2016. Performance evaluation of an irreversible Miller cycle comparing FTT (finite-time thermodynamics) analysis and ANN (artificial neural network) prediction. *Energy*, 94, pp.100-109.
55. Okamoto, K., Zhang, F.R., Morimoto, S., & Shoji, F., 1998. Development of a high-performance gas engine operating at a stoichiometric condition – effect of Miller cycle and EGR, Proceedings of CIMAC Congress, Copenhagen, pp. 1345–1360.
56. Rashidi, M.M., Mousapour, & A., Hajipour, A., 2014. The effects of heat transfer on the exergy efficiency of an air-standard Otto cycle. *Heat Mass Transfer*, 50, pp.1177–83.
57. Rashidi, M.M., & Hajipour, A., 2013. Comparison of Performances of Air-Standard Atkinson, Diesel and Otto Cycles with Constant Specific Heats. *Int J Advanced Design and Manufacturing Technology*, 6, pp.57–62.
58. Rashidi, M.M., Hajipour, A., Mousapour, A., Ali, M., Xie, G., & Freidoonimehr, N., 2014. First and Second-Law Efficiency Analysis and ANN Prediction of a Diesel Cycle with Internal Irreversibility, Variable Specific Heats, Heat Loss, and Friction Considerations. *Advances in Mechanical Engineering*, 359872, pp.1–16.
59. Rashidi, M.M., Hajipour, A., & Fahimirad, A., 2014. First and Second-Laws Analysis of an Air-Standard Dual Cycle With Heat Loss Consideration. *International Journal of Mechatronics, Electrical and Computer Technology*, 4, pp.315-332.
60. Rashidi, M.M., Hajipour, A., & Baziar, P., 2014. Influence of Heat Loss on the Second-Law Efficiency of an Otto Cycle. *International Journal of Mechatronics, Electrical and Computer Technology*, 4, pp.922-933.
61. Rinaldini, C.A., Mattarelli, E., & Golovitchev, V.I., 2013. Potential of the Miller cycle on a HSDI diesel automotive engine. *Applied Energy*, 112, pp.102-119.
62. Shimogata, S., Homma, R., Zhang, F.R., Okamoto, K., & Shoji, F., 1997. Study on Miller cycle gas engine for co-generation systems-numerical analysis for improvement of efficiency and power. SAE Paper No. 971709, pp. 61–67.
63. Stebler, H., Weisser, G., Horler, H., & Boulouchos, K., 1996. Reduction of NOx emissions of D.I. Diesel engines by application of the Miller-system: an experimental and numerical investigation, SAE Paper No. 960844, pp. 1238–1248.
64. Ust, Y., Arslan, F., Ozsari, I., & Cakir, M., 2015. Thermodynamic performance analysis and optimization of DMC (Dual Miller Cycle) cogeneration system by considering exergetic performance coefficient and total exergy output criteria. *Energy*, 90, pp.552–559.
65. Wang, W.H., Chen, L., Sun, F., & Wu, C., 2002. The effects of friction on the performance of an air standard Dual cycle. *Exergy, An Int. J.*, 2(4), pp.340-344.
66. Wang, Y.D., & Ruxton, T., 2004. An experimental investigation of NOx emission reduction from automotive engine using the miller cycle. Proceedings of ICEF2004, ASME Internal Combustion Engine Division, Fall Technical Conference, Long Beach, CA, USA, October 24–27.
67. Wang, Y., Zeng, S., & Huang, J., 2005. Experimental investigation of applying Miller cycle to reduce NOx emission from diesel engine. *Proc. IMechE, Part A: J. Power and Energy*, 219, pp.631-638.
68. Wang, Y., Lin, L., & Roskilly, A.P., 2007. An analytic study of applying Miller cycle to reduce NOx emission from petrol engine. *Appl Therm Eng*, 27, pp.1779–1789.
69. Wang, Y., Lin, L., & Zeng, S., 2008. Application of the Miller cycle to reduce NOx emissions from petrol engines. *Appl. Energy*, 85, pp.463– 474.
70. Wang, Y., Zu, B., Xu, Y., Wang, Z., Liu, J., 2016. Performance analysis of a Miller cycle engine by an indirect analysis method with sparking and knock in consideration. *Energy Conversion and Management*, 119, pp.316–326.
71. Wu, C., Chen, L.G. & Chen, J.C., 1999. *Recent Advances in Finite Time Thermodynamics*. New York: Nova Science Publishers,
72. Wu, C., Puzinauskas, P.V. & Tsai, J.S., 2003. Performance analysis and optimization of a supercharged Miller cycle Otto engine. *Appl Therm Eng*, 23, pp.511-521.
73. Tavakoli, S., Jazayeri, S.A., Fathi, M., Jahanian, O., 2016. Miller cycle application to improve lean burn gas engine performance. *Energy*, 109, pp.190-200.
74. Zhao, Y., & Chen, J., 2007. Performance analysis of an irreversible Miller heat engine and its optimum criteria. *Appl Therm Eng*, 27, pp.2051–2058. Zhao, J., 2017. Research and application of over-expansion cycle (Atkinson and Miller) engines– A review. *Applied Energy*, 185, pp.300–319.

75. Zhu, S., Deng, K., Liu, S., Qu, S., 2015. Comparative analysis and evaluation of turbocharged Dual and Miller cycles under different operating conditions. *Energy*, 93, pp.75-87.

CONTACT WITH THE AUTHOR

Güven Gonca

e-mail: guvengca@gmail.com

Yildiz Technical University

Barbaros, 34349 Istanbul

TURKEY

THE INFLUENCE OF DIESEL OIL IMPROVERS ON INDICES OF ATOMISATION AND COMBUSTION IN HIGH-EFFICIENCY ENGINES

Ireneusz Pielecha¹⁾

Jacek Pielecha¹⁾

Maciej Skowron¹⁾

Aleksander Mazanek²⁾

¹⁾ Poznan University of Technology, Poland

²⁾ Oil and Gas Institute – National Research Institute, Poland

ABSTRACT

The process of fuel combustion in a diesel engine is determined by factors existing during liquid fuel injection and atomisation. The physicochemical properties of the fuel to a large extent decide upon the quality of this phase of cylinder fuelling. So it is important to ensure appropriate properties of a fuel affecting its atomisation and, as a result, combustion. The paper deals with the topic of diesel oil improvers and the analysis of their influence on atomisation and combustion indices. In the studies base diesel oil and a diesel fuel improved by a package of additives, were used. The process of conventional and improved fuel injection was analysed by using optical examinations. The amount of released heat was evaluated during the studies carried out on combustion. Significant aspects of the applied improvers in relation to fuel injection and its combustion have been indicated.

Keywords: diesel oil, diesel engine, improvers, fuel injection, fuel combustion

INTRODUCTION

The development of diesel engines is determined mainly by the fuel injection system and combustion system. Because of the low diversification of combustion systems, possibilities to increase the engines' efficiency are sought to be made through modifications of the fuelling system. A multiple division of fuel charge is used here and – by utilising a missing division – so-called rate shaping (a change of nozzle needle lift during the fuel injection) [5,8,10]. The use of substitute fuels or conventional fuel additives are the next possibilities to change the combustion process parameters.

Based on the research of different fuels, Lamas et al. [7] concluded that natural gas is the best alternative fuel for marine engines due to its low cost and high availability. However, the main disadvantage of this fuel is the knock risk. Research conducted by Kowalski [6] showed an increase in exhaust gas temperature when injector nozzle holes are damaged (increased cross-section) and require recalibration.

Blocked (clogged) injector holes cause a drop in combustion pressure, and increase CO emissions by more than 70% with an average engine load [6]. In addition, these studies reported that amounts of nitrogen oxides emission increased at low loads by more than 30% [6]. The reason of this may be contamination of fuel or lack of cleaning substances in the diesel fuel [1, 16], petrol fuel [4] and oil [12]. This paper deals with the issue of diesel fuel improvers.

ANALYSIS OF THE STATE OF KNOWLEDGE

Diesel fuel is improved mainly by oxygen and detergent additives. The application of the first method, e.g. in the form of fatty acid methyl esters (FAME), results in improvement in fuel combustion and in the reduction of harmful pollutant emission into the atmosphere. Ethanol is used here as an additive to diesel fuel. The literature analyses presented by Burnus [3] do not show the occurrence of positive effects of

such fuel. It was shown that despite a small drop in power, the emission of all toxic flue gas components was not limited.

The study carried out by Rodríguez-Fernández et al. [15] shows that the use of an e-diesel fuel (10% of ethanol addition) increases the possibilities of smooth oxidation in the DPF (diesel particulate filter). The higher chemical activity of the modified fuel (this activity is related mainly to the alcohol group) is the reason.

Detergent-dispersing improvers are the second group of additives. Beck et al. [2], in a study on improvers, showed that detergent-dispersing additives can be used to improve the oxidation resistance of pure diesel oil and bio-diesel mixtures with diesel oil. In the case of the studied fuel samples – biodiesel, diesel fuel and their mixtures, the reduced oxidation stability due to long-term storage may be partly offset by the application of selected detergent-dispersing additives. Such additives prevent from the formation of free radicals and neutralise carboxylic acids, and therefore increase the sample's oxidation stability.

Žak et al. [17], when analysing the influence of detergent-dispersing additives, showed that they have a significant impact both on the state of diesel engines' fuelling systems and the reduction of the flue gas emission (mainly particulate matter).

The review of the subject literature is related primarily to influence of the fuel additives on the effects of combustion engine operation. This paper particularly emphasises the initial stages of engine fuelling: injection and atomisation of various fuels (without and with additives) were analysed, including the additives' impact on combustion.

METHODOLOGY

STUDIED FUELS

Base diesel oil (B7) and a diesel fuel improved by a package of additives were used in the studies.

The second diesel fuel was improved by a package of additives (by dosing about 300 mg of additive per 1 kg of fuel), containing a detergent-dispersing additive with an alkene-succinate-imide-amide structure synthesised at the INiG-PIB and the following commercial additives: demulsifiers, a defoamer, an anti-corrosive additive, a biocide and a solvent (the package composition was protected at the Patent Office, application No P.413866). Tab. 1 presents the properties of both diesel oil types.

Tab. 1. Selected properties of the base and modified diesel oils

Test type	Unit	Test result	
		B7 DO	Improved DO INIG
Cetane index	–	57.6	57.8
Cetane number	–	53.3	54.7

Test type	Unit	Test result	
		B7 DO	Improved DO INIG
Density at 15 °C	kg/m ³	828.7	828.6
Content of polynuclear aromatic hydrocarbons	% (m/m)	1.1	
Sulphur content	mg/kg	less than 5	less than 3.0
Ignition temperature	°C	88	87.5
Coking residue (of 10% distillation residue)	% (m/m)	0.062	0.074
Incineration residue	% (m/m)	0.001	0.004
Water content	% (m/m)	0.005	0.0005
Pollutant content	mg/kg	2.1	6.7
Test of corrosive effect on steel (3 h at 38°C)	degree of corrosion	trace B++	corrosion trace
Test of corrosive effect on copper (3 h at 50°C)	class	1a	1a
Fatty acid methyl esters (FAME)	% (V/V)	5.6	–
Oxidation resistance	h g/m ³	35.9 7	2.0
Lubricity, adjusted diameter of the wear trace (WS 1.4) at 60°C	µm	180	337
Kinematic viscosity at 40°C	mm ² /s	2.7175	2.711
Fractional composition up to 250 °C distils	% (V/V)	27.3	26.3
up to 350 °C distils	% (V/V)	97.7	97.2
95% (V/V) distils up to	°C	333.0	328.0

RESEARCH INSTRUMENTS

A number of experiments were applied to comparative analysis of the used fuels, aimed at describing basic practical parameters crucial from a combustion engine operation point of view. Scope of the experiment comprised two main parts: fuel injection and atomisation, and combustion. For each test point 3 iterations were carried out during the first and the second phases to eliminate a gross error from the obtained results.

The first phase of the experiment, related to characteristic parameters of the fuel spray and chamber filling with it, was carried out by using a fast LaVision HSS5 camera working with DaVis software of the same company. A constant volume chamber (CVC) was used as the space being registered [9,13,14], which allowed the setting of a backpressure, thereby simulating conditions existing in the combustion chamber during injection in a diesel engine (2 MPa backpressure). Optical access to the chamber combined with halogen lighting enabled the registration of drops. The same injector which

featured an 8-nozzle sprayer with an angle of spray flare of 162° was used for both fuels. Tests were carried out at working points occurring in a combustion engine. The first point featured 35 MPa injection pressure of and 0.5 ms time of injector opening. The second point was described by the values of 100 MPa and 0.3 ms, respectively. The recorded images were subject to software processing and analysis. On this basis parameters of the fuel spray were determined by using proprietary subroutines.

The second phase of the experiment consisted in using a Rapid Compression Machine (RCM) [13] to carry out combustion of both fuels. The machine allows to carry out one combustion cycle simulating the combustion cycle in a combustion engine. The piston (diameter = 80 mm and stroke = 81 mm) is pneumatically driven, and a combustion pressure gauge is installed in the direct injection combustion chamber (displacement volume is 407 cm³). The AVL instrument for quickly varying measurements was used for recording. The instrument was working with the AVL IndiCom software, and the AVL Concerto software was used to analyse course of the obtained values.

STUDIES ON FUEL INJECTION AND ATOMISATION

Fuel atomisation in the form of atomised fuel sprays was analysed basing on video material recorded at the frequency $f = 10$ kHz. Studies carried out at two values of fuel pressure and different injection times are presented in Tab. 2.

Tab. 2. Picture sequences of fuel atomisation for the analysed injectors

t_{inj} [ms]		0	0.1	0.2	0.3	0.4	0.5	0.6
$P_{inj} = 35$ MPa $t_{inj} [ms] = 0.5$ ms	DO							
	INIG							
$P_{inj} = 100$ MPa $t_{inj} [ms] = 0.3$ ms	DO							
	INIG							

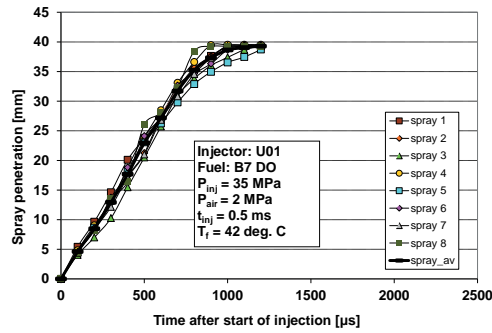
Such analysis does not allow to fully identify the video material at simultaneous shortage of quantitative data on changes in the structure of fuel atomisation. Therefore, by using macros created in the DaVis 7 Command Language editor, the range of individual fuel sprays (based on paper [11]) and their surface areas were analysed (Fig. 1). Determination of such area is based on assuming a flat exposure represented by the recorded image.

Based on the video material processing, quantitative information was obtained, allowing to perform evaluation of the fuel atomisation indices. Because of small deviations of individual fuel spray ranges, the average range and surface area of spray was analysed (Fig. 2). At the same time value of the coefficient of variation (CoV) was determined – Fig. 3, defined as:

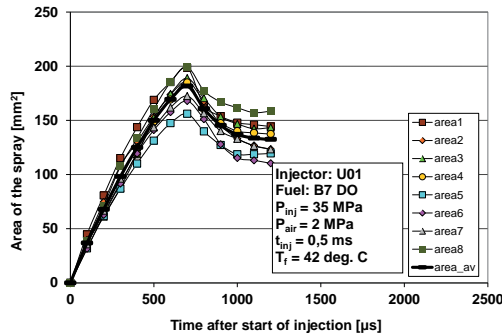
$$\text{CoV}(S) = \frac{\sigma}{S_{av}} \quad (1)$$

where: S_{av} – average value of range in the given time t , σ – standard deviation of the sample mean.

Determination of the range variability shows the fact that the value achieves its maximum value at the beginning of atomisation (errors resulting from processing the image with a small spray range), and then gradually diminishes to around 5–6%. This is the value that allows to use the mean range of the spray and the average value of the spray surface area in the further part of the paper.



a)



b)

Fig. 1. Determination of values of fuel injection characteristics : a) values of each fuel spray range, b) values of each fuel spray area

The stream range observed in Fig. 2 reaches 40 mm in a linear manner. It is clear that a significant slowdown in the stream development process occurs after 1 ms, indicating the stream's limitation. However, the value of the resulting area indicates that a steep development of the stream (surface area increase) occurs up until 0.6 ms, but after this time a decrease in surface area is observed, which indicates an increase in evaporation.

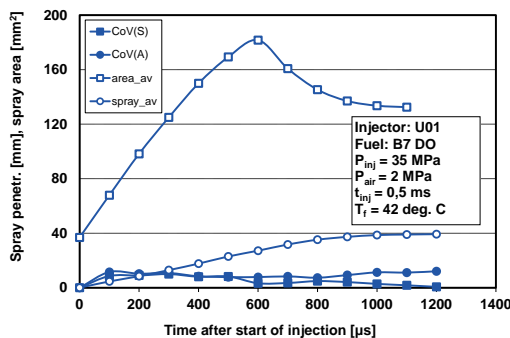
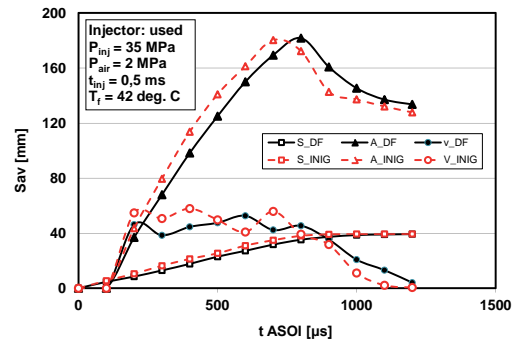


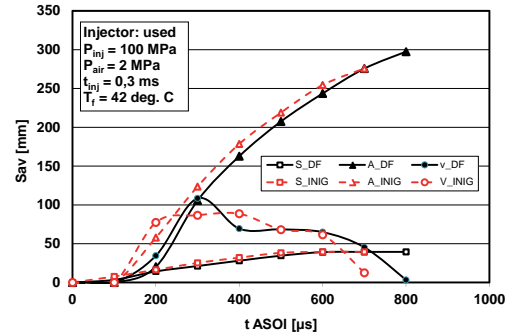
Fig. 2. Determination of values of fuel injection spray characteristics : average values and values of coefficient of variation

By using the presented analyses, the mean ranges of the fuel spray during its injection into a chamber of constant backpressure value, were compared (Fig. 3).

The analysis of the data from Fig. 3 shows the fact that slightly different values of range of the analysed fuels occur.



a)

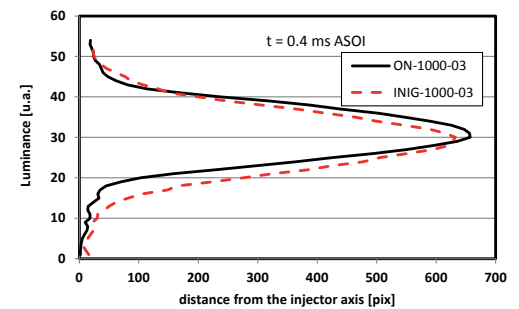


b)

Fig. 3. Geometrical indices of a (mean) fuel spray from the operating injectors fuelled with DF and INIG fuels at: a) $P_{inj} = 35 \text{ MPa}$ and $t_{inj} = 0.5 \text{ ms}$, b) $P_{inj} = 100 \text{ MPa}$ and $t_{inj} = 0.3 \text{ ms}$

INIG fuel has a slightly longer range and larger spray area. The increase in the spray area is not directly a result of the lower density of this fuel since the densities of the fuels, as shown in Tab. 1, have similar values. Therefore this result comes from the used fuel additives. Higher fuel spray values were noted at lower fuel pressure values, i.e. within the range of small loads and low engine speeds. This indicates the potential benefit of using the considered fuel in low speed engine systems at relatively low injection pressure values.

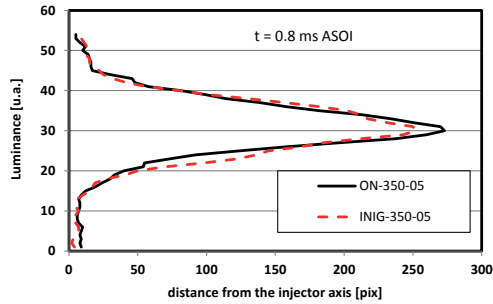
The observation encouraged the authors to look for further differences in the fuels' atomisation. Further on – based on recorded images – a cross-section of the selected fuel spray was made perpendicularly to the spray axis. The distribution of luminance (spray brightness) was this way determined for both fuels at different injection pressures of them (Fig. 4 and Fig. 5).



a)

STUDIES ON THE COMBUSTION PROCESS

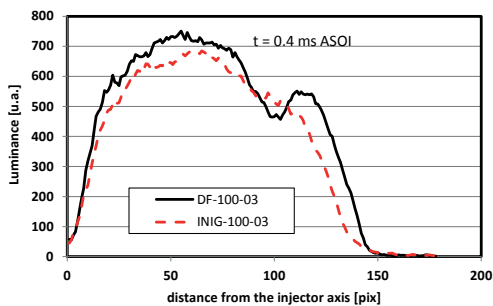
Studies on the combustion process were carried out at the pressure of 100 MPa and injection time of a piezoelectric injector, equal to $t_{inj} = 0.6$ ms. This is the time at which it is possible to obtain a large fuel dose, and the process course can indicate significant changes during the analysis. Short injection times and low pressures implemented during studies in a constant volume chamber are not applicable during combustion. The INIG fuel combustion features lower maximum pressures of the process. To obtain correct combustion, trials were repeated twice. Fig. 6a shows repetitions which are identical during the combustion of a standard diesel oil. Small differences were recorded during the INIG fuel combustion. However, they are related to the combustion and expansion phase.



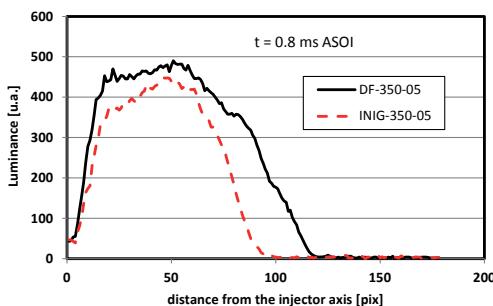
b) *Fig. 4. Analysis of cross-section of fuel sprays at a distance of 30 mm from the injector axis for various times from the injection start at constant value of fuel pressure $P_{inj} = 100$ MPa and $t_{inj} = 0.3$ ms: a) for time $t = 0.4$ ms after start of injection, b) for $t = 0.8$ ms after start of injection*

The initial atomisation of INIG fuel spray (for $t = 0.4$ ms after the injection start – Fig. 4a) results in its larger width, resulting from a smaller fuel concentration in the spray core. This means easier evaporation and may prove to have a larger spray surface area. The observed trend disappears during the spray development (Fig. 4b). It may be related to the evaporation of lighter fuel fractions. Such situation means that the images are similar and the algorithm computing the spray areas calculates a similar number of pixels of present luminance (light intensity).

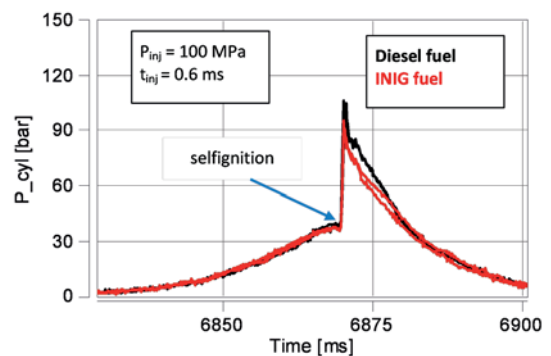
The analysis of the longitudinal cross-section of the spray confirms the previous conclusions on the faster evaporation of the INIG fuel. The spray luminance in the longitudinal cross-section (Fig. 5) shows its smaller intensity during the INIG fuel analysis. This indicates that the considered fuel has a slightly larger spray cone because concentration in the core is smaller. The observed trend is also confirmed during a larger development of fuel spray (Fig. 6b for time $t = 0.8$ s after the start of fuel injection).



a) *Fig. 5. Analysis of longitudinal cross-section in the fuel spray axis for various times from the start of injection at constant value of fuel pressure $P_{inj} = 100$ MPa and $t_{inj} = 0.3$ ms: a) for time $t = 0.4$ ms after start of injection, b) for $t = 0.8$ ms after start of injection*



b) *Fig. 5. Analysis of longitudinal cross-section in the fuel spray axis for various times from the start of injection at constant value of fuel pressure $P_{inj} = 100$ MPa and $t_{inj} = 0.3$ ms: a) for time $t = 0.4$ ms after start of injection, b) for $t = 0.8$ ms after start of injection*



a) *Fig. 6. Combustion pressure (during two combustion trials) (a); and conditions of electric signals course during this process (b)*

Fig. 6b presents the conditions of injector operation, specifying the value of control voltage (140 V) and a characteristic course of a piezoelectric injector with 8 A peak [=peak?] value.

The analysis of the combustion process shows a similar course of pressure growth after spontaneous ignition (Fig. 7a) but a slightly smaller value of the maximum released heat (Fig. 7b). This may prove a slightly worse combustion or slightly lower calorific value of the new fuel.

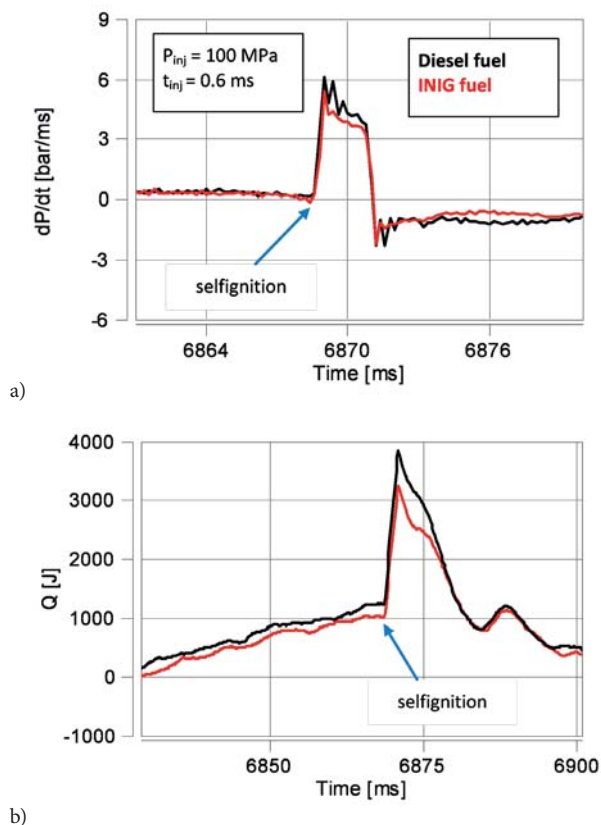


Fig. 7. Thermodynamic parameters of the combustion : a) rate of pressure change in the cylinder, b) amount of heat released during combustion

SUMMARY

The studies on comparison of fuels selected by the authors were carried out in the form of characteristics trials, providing the grounds for the assessment of the injection system, combustion system, and the fuel properties. Because of the nature of individual analyses, the conclusions were divided - in accordance with the aim of the carried out studies- into those dealing with blend [= mixture?] preparation and combustion.

The studies on fuel-air mixture ? preparation in a constant volume chamber showed no visible differences during standard analysis. The extension of the analysis scope by means of direct image comparisons allowed to indicate conditions for the blend preparation of a new fuel. A larger exposure area proves a potential for faster evaporation due to a greater filling of the analysed area and facilitation of substances mixing. The luminance-based analysis of liquid phase concentration within the spray became the argument confirming this thesis. It showed a greater share of gaseous fuel fraction combined with a better spatial distribution.

The second group of conclusions applies to combustion, showing slightly smaller values of pressure change rates inside the cylinder. Compared to the commercial diesel fuel, the course of dP/dt indicates less deflagration and thereby a smaller share of kinetic combustion phase.

These observations allow to determine the new fuel's potential:

- it is expected to reduce fuel consumption due to the increase in the spray rate values in the area occupied by the fuel stream. This beneficially affects its evaporation, that in consequence leads to a reduction in the injected fuel weight,
- it is possible to reduce the emission of HC and CO components as better spraying and faster evaporation will lead to partial elimination of incomplete combustion (reduced combustion losses). The negative effect of using this fuel may be an increase in the emission of nitrogen oxides (improvement of the fuel-air mixture preparation process), which could be corrected by changing the injection timing setting.

Reduced fuel consumption and increased combustion efficiency can be achieved not only through the search for new alternative fuels, but also by using suitable fuel additives to increase the charge preparation process indicators and controlling the course of the combustion process itself.

BIBLIOGRAPHY

1. Abe M., Hirata S., Komatsu H. et al.: *Thermodynamic selection of effective additives to improve the cloud point of biodiesel fuels*. Fuel, 171, 2016, pp. 94–100.
2. Beck Á., Pölczmán G., Eller Z. et al.: *Investigation of the effect of detergent–dispersant additives on the oxidation stability of biodiesel, diesel fuel and their blends*. Biomass and Bioenergy, 66, 2014, pp. 328–336.
3. Burnus Z.: *Badania jakościowe paliw oxydiesel techniką chromatografii gazowej z systemem detekcji (O-FID)*. Nafta-Gaz, 09, 2010, pp. 849–857.
4. Ferreira da Silva M.P., Rodrigues e Brito L., Honorato F.A et al.: *Classification of gasoline as with or without dispersant and detergent additives using infrared spectroscopy and multivariate classification*. Fuel, 116, 2014, pp.151–157.
5. Herrmann H.-O., Gorbach A., Lettmann H., Chebli E.: *The (R)evolution of Daimler's heavy duty diesel engine platform*. 37. Internationales Wiener Motorensymposium 2016.
6. Kowalski J.: *An experimental study of emission and combustion characteristics of marine diesel engine with fuel injector malfunctions*. Polish Maritime Research, 23(1), 2016, pp. 77–84.
7. Lamas M.I., Rodríguez C.G., Telmo J., Rodríguez J.D.: *Numerical analysis of emissions from marine engines using alternative fuels*. Polish Maritime Research, 22(4), 2015, pp. 48–52.

8. Le D., Pietrzak B.W., Shaver G.M.: *Dynamic surface control of a piezoelectric fuel injector during rate shaping*. Control Engineering Practice, 30, 2014, pp. 12–26.
9. Mazanek A.: *Ocena parametrów użytkowych wtryskiwaczy piezo-elektrycznych na podstawie badań wizualizacyjnych procesu rozpylania paliwa*. Nafta-Gaz, 4, 2016, pp. 279–284.
10. Mohan B., Yang W., Yu W. et al.: *Numerical investigation on the effects of injection rate shaping on combustion and emission characteristics of biodiesel fueled CI engine*. Applied Energy, 160, 2015, pp. 737–745.
11. Naber J., Siebers D.: *Effects of gas density and vaporization on penetration and dispersion of diesel sprays*. SAE Technical Paper 960034, pp.1996.
12. Nassar A.M., Ahmed N.S., Abdel-Hameed H.S. et al.: *Synthesis and utilization of non-metallic detergent/dispersant and antioxidant additives for lubricating engine oil*. Tribology International, 93, Part A, 2016, pp. 297–305.
13. Pielecha I., Wiśłocki K., Borowski P., Cieślik W.: *Thermodynamical evaluation of usefulness of future hydrocarbon fuels for use in compression ignition engines*. Journal of Thermal Analysis and Calorimetry, 122, 2015, pp. 473–485.
14. Pielecha I., Wiśłocki K., Cieślik W. et al.: *Problems of determining of fuel spray geometric parameters when based on optical investigations*. Combustion Engines, 162(3), 2015, pp. 307–315.
15. Rodríguez-Fernández J., Hernández J.J., Sánchez-Valdepeñas J.: *Effect of oxygenated and paraffinic alternative diesel fuels on soot reactivity and implications on DPF regeneration*. Fuel, 185, 2016, pp. 460–467.
16. Zhang X., Peng G., Du G. et al.: *Investigating the microstructures of piston carbon deposits in a large-scale marine diesel engine using synchrotron X-ray microtomography*. Fuel, 142, 2015, pp. 173–179.
17. Żak G., Ziemiański L., Stępień Z., Wojtasik M.: *Engine testing of novel diesel fuel detergent–dispersant additives*. Fuel, 122, 2014, pp. 12–20.

CONTACT WITH THE AUTHORS

Ireneusz Pielecha

e-mail: ireneusz.pielecha@put.poznan.pl
 Poznan University of Technology
 Piotrowo 3, 60965 Poznan
POLAND

Jacek Pielecha

e-mail: jacek.pielecha@put.poznan.pl
 Poznan University of Technology
 Piotrowo 3, 60965 Poznan
POLAND

Maciej Skowron

e-mail: maciej.skowron@put.poznan.pl
 Poznan University of Technology
 Piotrowo 3, 60965 Poznan
POLAND

Aleksander Mazanek

e-mail: mazaneka@inig.pl
 Oil and Gas Institute - National Research Institute
 Lubicz 25A, 31-503 Cracow
POLAND

PRELIMINARY FIELD TESTS AND LONG-TERM MONITORING AS A METHOD OF DESIGN RISK MITIGATION: A CASE STUDY OF GDAŃSK DEEPWATER CONTAINER TERMINAL

Mikołaj Miśkiewicz

Gdansk University of Technology, Faculty of Civil and Environmental Engineering, Poland

Oskar Mitrosz

Keller Polska Sp. z o.o.

Tadeusz Brzozowski

Keller Polska Sp. z o.o.

ABSTRACT

Appropriate risk assessment plays a fundamental role in the design. . The authors propose a possible method of design risk mitigation, which follows recommendations included in Eurocode 7. The so-called “Observational Method” (OM) can produce savings in costs and programmes on engineering projects without compromising safety. The case study presented is a complex design solution that deals with the heavy foundations of a gantry crane beam as one of the elements of a Deepwater Container Terminal extension. The paper presents a detailed process of the design of the rear crane beam being a part of the brand new berth, together with its static analysis, as well as the long-term results of observations, which have revealed the real performance of the marine structure. The case presented is based on excessive preliminary field tests and technical monitoring of the structure, and is an example of a successful OM implementation and design risk mitigation.

Keywords: monitoring, field test, Observational Method, CFA piles, micropiles, geotechnics

INTRODUCTION

Geotechnical Eurocode 7 (EC7) [6] recommends verification of limit states by one or a combination of four possible methods: **use of calculations**, adoption of prescriptive measures, experimental models and load tests or an **Observational Method (OM)**. In addition, on the basis of geotechnical design the European code introduces geotechnical categories of structures from 1 to 3, from relatively simple structures to structures involving abnormal risks, unusual or exceptionally difficult ground and loading conditions. The geotechnical categories are in line with local regulations [13].

More and more often in geoen지니어ing the risk matter and its appropriate management are now being considered.

Topolnicki [19] has classified available methods of ground improvement, paying particular attention to risk factor, and has introduced three categories of increasing hazard from A (low hazard) to C (high hazard).

In 2002, a European geotechnical forum was set up for the exchange of best practice ideas and innovations in geotechnical engineering, called GeoTechNet [15]. This forum published a document promoting modern design tools, including the application of the Finite Element Method (FEM) and the observational method, which can reduce costs and programmes on engineering projects without compromising safety. It also shows how the geotechnical community can benefit from developing scientific knowledge.

In current everyday design practice, however, most designs are based on engineering calculations only, with

no or marginal use of the observational method. The aim of this study is to illustrate, taking recently completed extension of the Deepwater Container Terminal in Gdańsk as an example, how the design process can be improved by effective implementation of the observational method, leading to mitigation of risk and optimized engineering solution.

OBSERVATIONAL METHOD

The forerunner of the observational method in geotechnics was Peck [16]. In a recent work on OM, published by the Construction Industry Research and Information Association's Report 185 (CIRIA) [12], the definition of OM approach reads: "The Observational Method in ground engineering is a continuous, managed, integrated, process of design, construction control, monitoring and review that enables previously defined modifications to be incorporated during or after construction as appropriate. All these aspects have to be demonstrably robust. The objective is to achieve greater overall economy without compromising safety."

Traditional ground engineering projects are usually based on a single, robust design and there is often no intention of varying the design during the construction phase [17]. Optional monitoring, if carried out, plays a very passive role to check only if the original predictions are still valid and provide confidence to all parties involved in the process (eg. client, contractor, designer). In comparison, in the OM monitoring plays an active role in both the design and during construction, allowing planned modifications to be carried out within an agreed contractual framework.

The enhancement of OM is also described in the Eurocode 7, but should only be considered whenever prediction of geotechnical behavior is "difficult" or the complexity of the interaction between the ground and the structure makes it "difficult to design". This code sets some general rules for OM that are required before construction is started. However, as stated by Patel et al. [15], EC7 is inconsistent and is lacking in any detailed instructions the geo-engineers shall follow. Moreover, the code doesn't concentrate on the advantages OM can bring to a typical construction processes, but recommends the method as one of the optional, alternative approaches to design. A totally different scientific approach is represented by the promoters of the observational method, who prove the effectiveness of appropriately implemented OM in major European projects [15]. The method requires full consciousness of the construction process and active participation and management by client, designer and contracting teams. Significantly more time is dedicated to designing and planning than constructing, but this leads to an efficient and effective organization of the engineering projects.

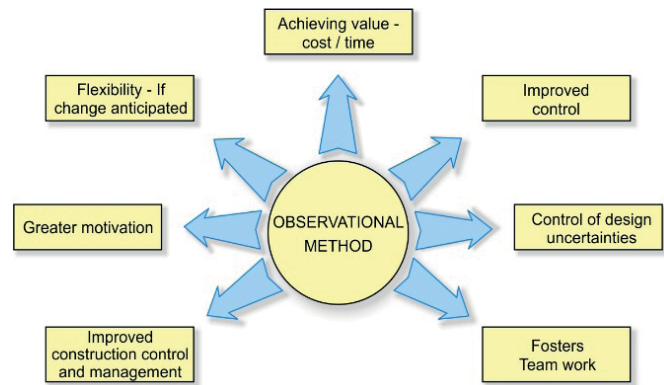


Fig. 1. Potential benefits of the OM [12]

The latest and more promising technologies like Building Information Modelling (BIM) can serve the observational method as a professional tool supporting the integrated process of planning, building and operating the investments.

Topolnicki [18] describes the high accuracy of BIM application in geotechnics and advocates the use of GeoBIM upgrade of the system that will take into account soil-structure interaction affecting the construction process. Due to its digital character and high management effectiveness, BIM can accelerate the preparation process of error-free design documentation and improve the execution process consequently optimizing the global cost of the project.

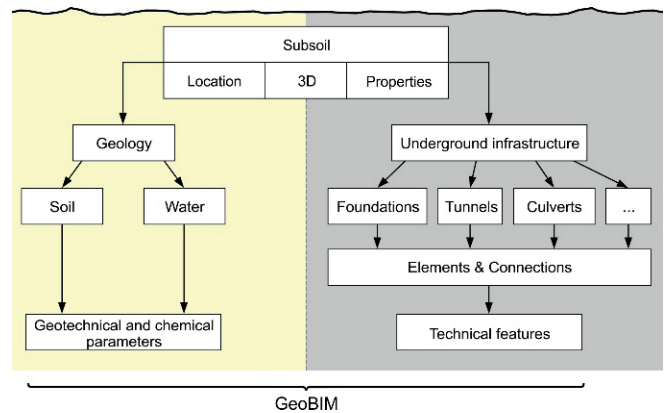


Fig. 2. GeoBIM model chart [18]

DESIGN METHODS

The Eurocode determines design methods for pile foundations and recommends the design should be based on one of the following approaches:

- a) empirical or analytical **calculation methods** whose validity has been demonstrated by static load tests in comparable situations;
- b) the results of **static load tests**, which have been demonstrated, by means of calculations or otherwise, to be consistent with other relevant experience;

- c) the results of dynamic load tests whose validity has been demonstrated by static load tests in comparable situations;
- d) the observed performance of a comparable pile foundation, provided that this approach is supported by the results of site investigation and ground testing.

Thus far, as engineering practice has always shown, the most common and traditional approach is a design based on calculations in which the load test is only verifying the final solution. Using empirical or analytical **calculation methods** requires its coherence with variety of static load tests performed in comparable situations and the wide experience of a designer in charge. In general, soil investigation is often insufficient and represents single points (eg. boreholes, soundings, etc.). This may lead to unsafe simplifications. Determining soil deformation and strength parameters may also be questionable. Part of the design risk may come from inaccurate calculation methods or the software used to estimate pile bearing capacity. Therefore, it should be noted that EC7 allows the use of the static load tests approach as a method of design risk mitigation.

There is no better and more reliable direct method of pile bearing capacity assessment than a **load test** performed on full-scale piles. Nonetheless, a tight construction schedule is often the main reason for not conducting the tests. It is generally believed, however, that the utilization of field test results in the design process will minimize risk and lead to safe and optimized foundation solutions. Consequently, well-planned field loading tests should be conducted in advance to production piles to allow early verification of the design performance in terms of pile stiffness and ultimate bearing capacity in soil conditions relevant for the specific site.

The adopted testing procedures, particularly with respect to the number of piles tested, loading steps and the sequence and duration of loading/unloading cycles, shall be such that conclusions can be drawn about the deformation behaviour, creep and rebound of a piled foundation from the measurements recorded. Moreover, the loading shall be such that the ultimate pile bearing capacity should be readily assessed [6]. This is often difficult to achieve for compression piles when the load versus settlement plots show a continuous curvature. In these cases, according to EC7, a limit settlement of pile head equals to 10% of pile base diameter can be adopted as an “ultimate” settlement.

OVERALL CONCEPT OF A CASE STUDY

The presented case is an example of the implementation of a field test programme as a method of design risk mitigation. It represents a design solution that deals with a heavy foundation of a gantry crane beam as one of the elements of the Deepwater Container Terminal (DCT) extension (Fig. 3). A new 656 m quay, with adjacent 25 ha container storage yards, allows for the terminal to meet the growing demand for deep-sea services in Central-Eastern Europe and enables the handling of ultra large container vessels [1]. The

DCT is located in the industrial part of the city of Gdańsk, on the Vistula Spit which forms a natural barrier against sea intrusion. Soil sedimentation transported by the Vistula River was the main phenomenon in creating this geological formation. The region is known for its difficult ground and water conditions, with a significant presence of marine and alluvial deposits represented by sands and soft organic silts with very low strength and deformation parameters [2].



Fig. 3. Bird view of the new quay wall and container storage yards (acc. DCT Gdańsk S.A.)

The geotechnical part of the design concerning the new berth and the adjacent container storage yards was divided into two major parts: the foundation of the Ship-To-Shore (STS) gantry crane beam, and deep ground improvement of the platform area, quay wall area (45 m landwards from the seaside crane rail) and of the transition zone between both areas (Fig. 4). A significant portion of the works comprised a reclaimed area of an existing basin, with a backfill depth of 3 to 14 m. and therefore represented a challenging geotechnical task.

In the **platform area** the aim of the soil improvement was to compact loose fill to even the settlements and ensure sufficient stiffness to the pavement structure. The function of the improved upper layer was to distribute the loads and transmit them uniformly to a deeper layer of silt which governed total settlements. In the **transition zone**, soil improvement elements were adopted in variable grids and lengths to ensure a smooth transition within the range of allowable settlements. In all cases the adopted geotechnical solutions were tailored to local soil profiles, loading conditions and functional requirements. In the most crucial zone, the **quay wall area**, ground improvement aimed not only to reduce the settlements of the pavement under the surcharge load, but also reduced the earth pressure acting on the quay wall structure.

This paper focuses on the detailed design process of the gantry crane beam foundation.

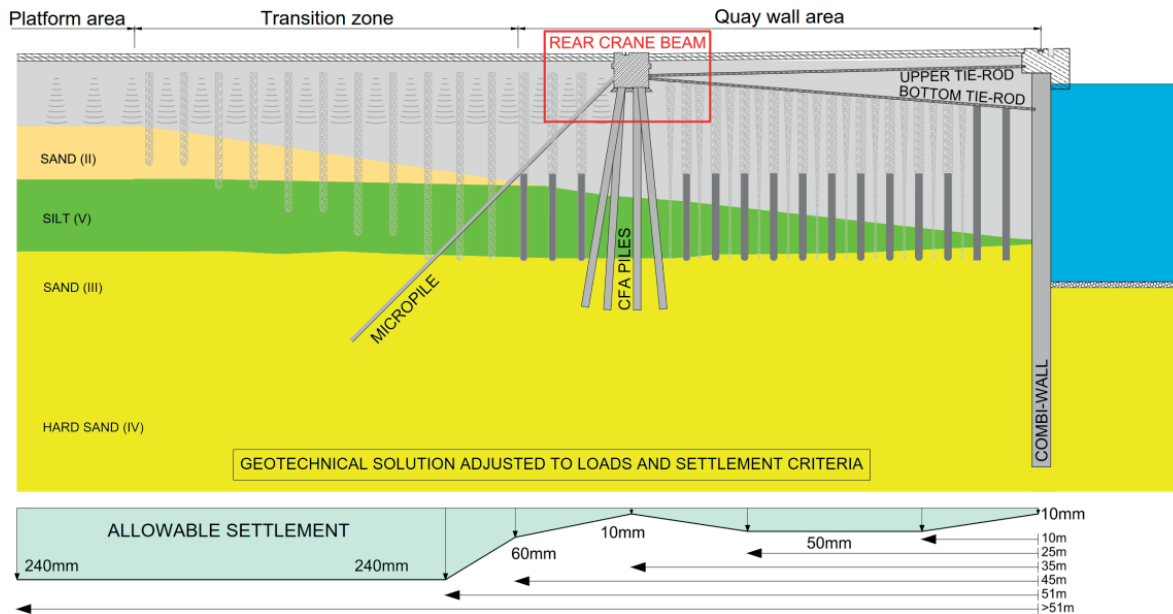


Fig. 4. A typical cross-section of the quay wall in offshore part of the project

DESIGN PROCESS

The design process started with analysing the employer's requirements [7] and soil investigation. The quay wall was designed as a combi-wall steel pile structure, with front capping beam anchored by means of pair of tie-rods in the Rear Crane Beam (RCB), which was founded on a system of raked Continuous Flight Auger (CFA) piles and micropiles (Fig. 4 and 6). The 656 m long beam was divided into 27 sections and loaded with STS cranes with the following characteristics: rail centre-to-centre 35 m, corners 4, wheels per corner 8 (spacing 1000 mm) [7]. In addition, basic crane loads defined in the employer's requirements had to be factored by 1.5 (g_c) to allow for possible future increase in equipment specification. Moreover, this increase did not include partial safety factors which should be used in the design. Consequently, for the final design crane loads had to be increased appropriately, as indicated in Tab. 1.

Tab. 1. Crane loads

load	Vertical load [kN/m]		Horizontal load [kN/m]
	dead	live	live
basic	564	376	141
characteristic ¹	846	564	212
design ^{2, 3}	1396	931	318

Notes: ¹ Incl. employer's factor for future load increase ($g_c=1.5$); ² Incl. partial safety factors for actions: $\gamma_c=1.35$ for permanent unfavorable actions, and $g_d=1.50$ for variable unfavorable actions; ³ Incl. the reliability class factor $g_n=1.1$, applicable for vertical loads according to [14] only.

For geotechnical analyses two most representative soil profiles were selected, and used to design the rear crane beam and its supporting elements. The analysis of the beam was done considering six positions of the crane, identified as the most critical (Fig. 5).

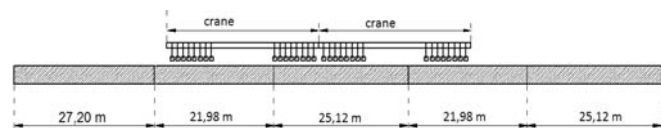


Fig. 5. Example of tandem crane loads acting on the RCB consisting of five sections

The behavior of the structure was analyzed in a linear-elastic as well as a non-linear range using FEM [3], and inspecting the convergence of both analysis. Two independent FEM models were used to investigate the performance of gantry crane beam and foundation elements. The first model, created with Plaxis 3D software, aimed to represent the behavior of a complete quay wall structure taking into account sea actions. The second one, created with Robot Structural Analysis software, focused on a proper modelling of the isolated RCB and its elements (Fig. 6). In this case the forces acting on the front capping beam due to dredging works, waves, mooring forces, surcharge loads, crane operations, temperature fluctuations, tensioning forces, etc. had to be transferred to the rear crane beam through the upper and bottom tie-rods (Fig. 7). In the course of a multi-stage analysis possible failures modes of the anchoring system were also analyzed considering various accidental combinations. Finally, the maximum anchoring forces were determined and used in the analytical RCB model.

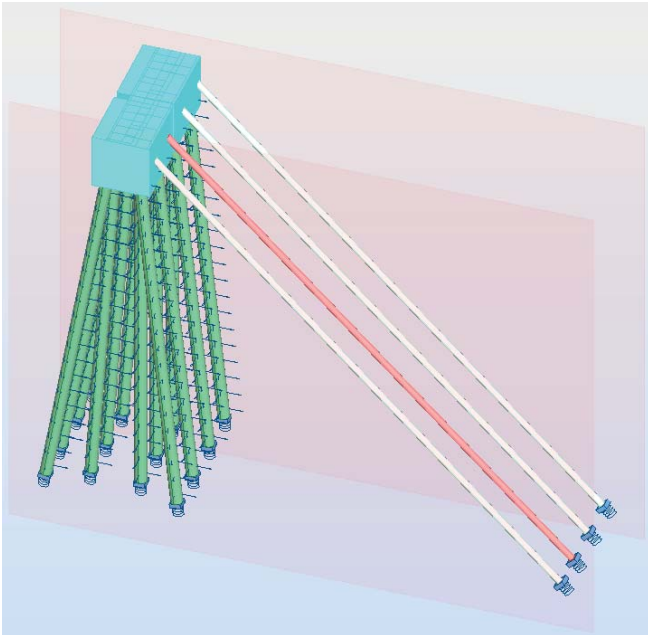


Fig. 6. FEM model of the RCB

For FEM modelling of CFA piles elastic beam elements were used together with interface elements at the pile to soil boundaries. Because of a special hinged connection between micropiles and the RCB, the micropiles were modelled by means of string elements capable of transferring tension forces only (Fig. 7).

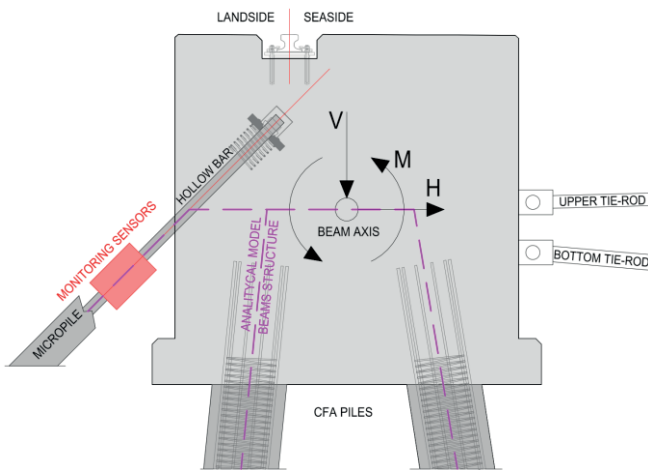


Fig. 7. Cross-section of the RCB showing CFA piles and the tie-rod (V – vertical force, H – horizontal force, M – bending moment). The red section indicates the location of monitoring sensors.

Also sensitivity analyses were conducted to check possible system failure caused by micropile defect, assuming a missing element in most unfavorable locations. The results of the sensitivity analysis for accidental combinations did not govern the design of micropiles as normal forces were 30-35% lower than in the original model. The RCB analytical models were also checked for reduced horizontal stiffness of springs representing soft soil layers (organic silt) or even without soil improvement elements in the quay wall area. All these

results showed insignificant increase of internal forces in the micropiles in comparison to Ultimate Limit State (ULS) results. This led to a conclusion that the resistance of RCB to lateral deflection is governed by the stiffness of the upper sand layers, which was also proved by FEM analysis using Plaxis 3D.

The simulations performed taking into account the most unfavorable sections of the RCB showed uniform reaction of the designed foundation elements. In the ULS condition, the predicted axial forces in CFA piles and micropiles due to the action of design loads were about 2180 to 2275 kN and 1750 to 1950 kN, respectively. For the micropiles this range of forces can be compared with the internal bearing capacity of 2670 kN of the hollow bar element type T103S.

As for the observational method and EC7 recommendations, the geotechnical design should be verified on real-scale elements on site and prior to the construction works to validate the effectiveness of the solution adopted. Consequently, a detailed plan of preliminary field loading tests was elaborated and executed to reduce the design risk to a minimum.

PRELIMINARY FIELD TESTS

The rear crane beam was to be supported on racked CFA piles up to 29 m long, with a diameter of 650 mm and the inclination angle of 9.5°. Field tests were performed with two representative CFA piles 20.5 and 29.0 m long (C1 and C2, Fig. 8). The aim of tests was to verify the preliminary design predictions and to determine acceptance criteria for the production piles. The load test set-up and the loading procedure adopted aimed at reaching the ultimate load corresponding to pile head settlement of 10% of the pile base diameter (i.e. $s_{min} > 65$ mm), in line with EC7 [6].

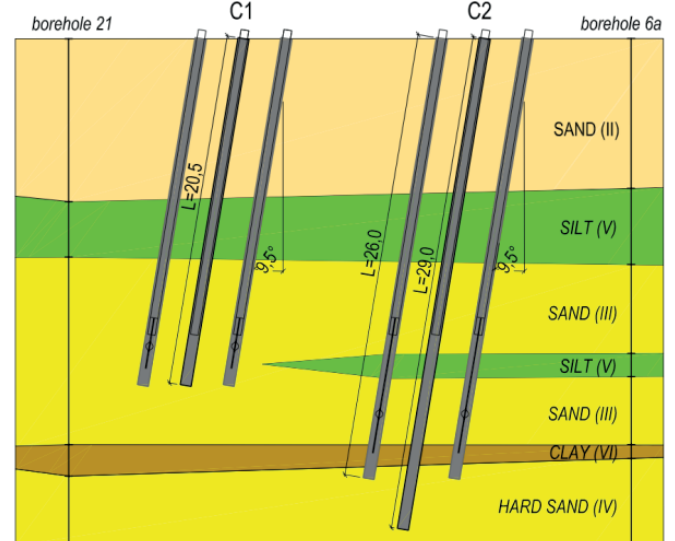


Fig. 8. Scheme of CFA piles used for two loading tests

The load-settlement curves obtained from field tests enabled determination of the bearing capacity by means of the bisector method [8] and evaluation of pile stiffness in the working load range (Fig. 9). The particular shape of these curves made it possible to model the piles precisely in the calculation simulations.

Results of the load tests confirmed the assumed bearing capacity of CFA piles. For the shorter pile C1 the ultimate bearing capacity was 4500 kN, leading to allowable design load of 3000 kN per pile with account for the negative skin friction effect. The longer pile C2 achieved 7000 kN bearing capacity during the test, resulting in analogous design load of 4500 kN per pile. It should be noted that both tested piles remained stable up to the last loading step.

Test piles proved to be safe enough to support the design load of 2275 kN, estimated from the most conservative FEM model. The corresponding pile stiffness under the design load was 238 to 325 MN/m, which was in line with the prediction of the preliminary design. Based on the test results the RCB model was updated, and revised design analyses were conducted. Then, it was decided to commence the production CFA piles. For quality assurance it was planned to execute 9 additional post-production static loading tests on selected piles. In case of unsatisfactory results of control tests a contingency plan to install additional piles was prepared. However, all control tests reached the required axial pile stiffness, being in average 424 MN/m. It has been estimated that the adopted program of preliminary field tests and proper quality control procedures enabled saving of approximately 4000 lm of CFA piles without compromising safety.

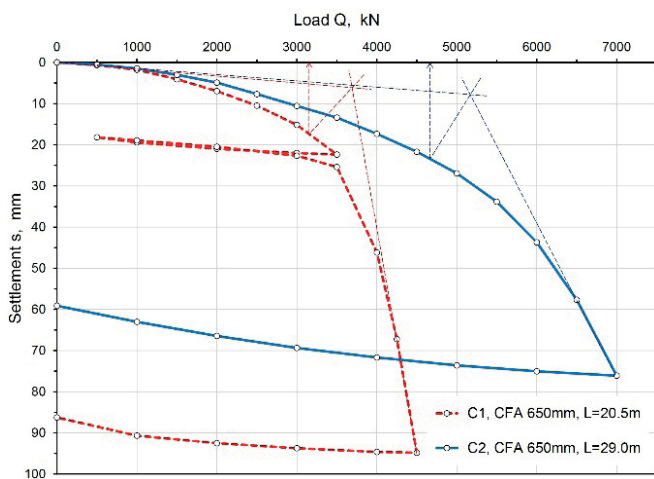


Fig. 9. Static load tests of C1 and C2 testing piles

The rear crane beam was also designed to be anchored by means of self-drilling T103S hollow bar system micropiles with a diameter of 300 mm, inclined at 45° degrees and up to 36 m long. Field tests were performed on five micropiles (M1 to M5). The aim of the tests was to verify the preliminary design assumptions, determine unit skin friction in isolated sand layers and check the ultimate bearing capacity of full-length

micropiles (Fig. 10), limited by tensile strength of the hollow bar system of 3550 kN, according to product specification.

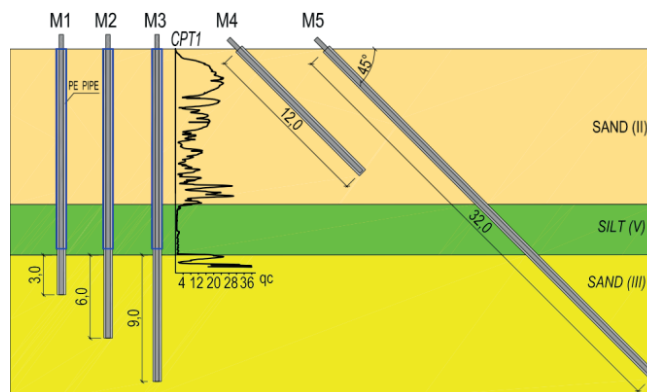


Fig. 10. Schematic diagram of tested micropiles with soil profile

Field tests performed on vertical micropiles (M1-M3) enabled assessment of the ultimate skin friction (τ_{ult}) in the bottom sands (stratum III). The hollow bars were isolated with PE pipes to create a free length, resulting in zero friction in the upper layers.

Load test done on inclined micropile (M4) enabled assessment of the ultimate bearing capacity in the upper sands (stratum II). The full-length micropile (M5) was used to determine the axial stiffness that could be used in the RCB analytical model. This test was carried out above the yield pull-out force of the bar of 2680 kN, and reached the load of about 3400 kN.

Tab. 2. Results of micropile tests

Micropile	R_{tk} [kN]	L_r [m]	Q_{test} [kN]	τ_{ult} [kPa]
M1	890	3,0 ^a	1260	446
M2	1780	6,0 ^a	2340	414
M3	2670	9,0 ^a	2900	342
M4	1800	12,0 ^b	1700	150
M5	>4000	32,0	~3400	-

where: R_{tk} – calculated ultimate load; L_r – length of grouted body (^a in the bottom sands; ^b in the upper sands); Q_{test} – maximum load during test; τ_{ult} – ultimate skin friction.

For micropiles M1-M3 it can be noticed that the ultimate skin friction for 3.0 m of grouted body was significantly higher than for 6.0 m and 9.0 m, in particular (Tab. 2). Most likely, the difference was caused by a high variability of sand compaction within sands. For the final design conservative values of 342 kPa and 150 kPa were used for the bottom and upper sands, respectively.

The load-uplift curves obtained from the field tests for M4 and M5 micropiles are presented in Figure 11. During the

M5 test, yield strength of the bar was reached. Taking into account creep criteria ($k_s < 2,0$ mm) determined in codes [4], [5], next-to-last load step represent the bearing capacity of tested micropiles. The resulting axial stiffness of the full-length micropile was approximately 160 MN/m, and was used in the final design calculations.

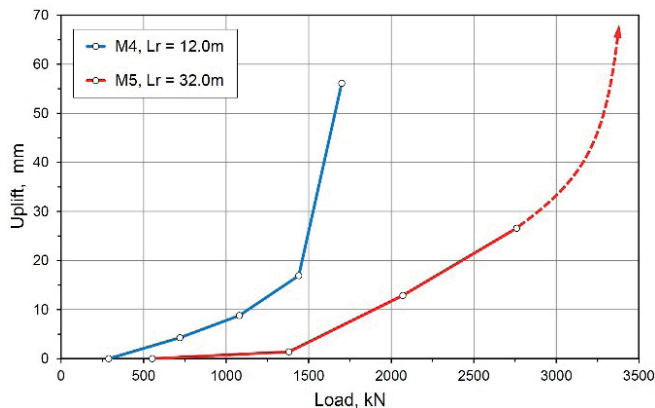


Fig. 11. The results of static load tests of M4 and M5 micropiles, corrected for bar elongation

A computational back analysis of the most unfavourable sections of the RCB revealed a uniform loading of the micropiles. Test micropiles proved to be safe enough to carry on the design load of 1950 kN, estimated from the most conservative FEM model. In addition, the field tests help to specify the QA criteria.

Finally, it was decided to commence production micropiles. For quality assurance it was planned to conduct 6 additional post-production static load tests on micropiles. Similarly to CFA piles, a contingency plan to install additional micropiles was prepared. However, all tests reached the expected axial stiffness of production micropiles of 165 MN/m, in average.

TECHNICAL MONITORING

Because of a complex character of the design and works carried out to construct the quay wall it was decided to verify the implemented design solution of rear crane beam foundations by applying an innovative monitoring system, installed on the hollow bars of 7 micropiles spread along the beam. The location of monitoring sensors installed on a micropile is highlighted in red in Figure 7. The development and set-up of the monitoring system, calibration of the sensors in laboratory and the assembly of the equipment on site has been described in detail by Miśkiewicz et al. [10].

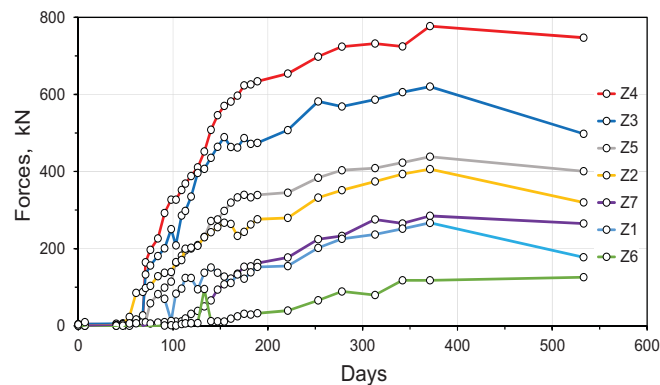


Fig. 12. Tensile forces in the micropiles

The observations on site continued in varying weather conditions for over 500-days (Fig. 12). The results obtained confirmed that the actual tensile forces in the micropiles are on the safe side. In the most loaded bar, Z4, the maximum measured force was $F_{meas} = 777$ kN. For comparison, the calculated unfactored tensile force in a representative cross-section and for the corresponding stage of quay wall construction was $F_{calc,k} = 807$ kN, indicating a ratio of $F_{meas} / F_{calc,k} = 0.96$. Consequently, the monitoring results confirmed high accuracy of design calculations.

The grand opening ceremony of terminal T2 took place on the 24th of October 2016, corresponding to 250 day in Figure 12. Since then a small relaxation of tensile forces has been noticed. At present, the monitoring system is still operational, and the long-term data are collected for control and further analyses.

CONCLUSIONS

The presented case study illustrates the design practice based on Eurocodes, with special emphasis on the observational method. Nonetheless, in the authors' opinion, EC7 is an extensive general document, which is lacking detailed implementation rules. Currently, the next version of more "easy-to-use" Eurocode 7 is in preparation, and should be introduced in 2020.

In the end a designer is responsible for the accuracy of the applied solution and has to account for potential risk. This is why, before choosing any geotechnical solution, a ge-engineer has to consider a variety of components: applicability of certain technology and its limits, type of structure, type of applied loads, structure sensitivity to settlements and ground conditions. It is also highly recommended that field tests should be performed prior to commencement of works, to set appropriate QA/QC procedures and monitor 'real life of structure' in order to verify implemented solutions and maintain a high quality of work and reduce potential risk. The applied solution also needs to fit into the construction schedule, and should be economically attractive. As a result,

geotechnical engineering has to face many challenging demands.

The reported case deals only with a part of comprehensive ground engineering works that were implemented at the DCT site. The focus is on the geotechnical design, testing and monitoring of the rear crane beam foundation system and its vital elements. It has been shown that well-planned full-scale preliminary tests and observations allow not only to optimise construction costs, but also significantly help to mitigate design and execution risks. Furthermore, the demonstrated case is another perfect example of a successful co-operation [9], [11] between academia and practitioners to deliver a high quality engineering product that produces savings in costs and programme without compromising safety.

BIBLIOGRAPHY

1. Buca R., Mitrosz O.: *Complex Geotechnical Engineering for Port of Gdansk Development – Gateway to Central-Eastern Europe*. Proceedings of 13th Baltic Sea Geotechnical Conference, Vilnius 2016, pp. 290-296.
2. Buca R., Mitrosz O.: *Inżynieria geotechniczna a rozbudowa Portu Gdańsk* (in Polish). Journal GDMT, October – December /4/2016/57, pp. 60-63.
3. Chróścielewski J., Sabik A., Sobczyk B., Witkowski W.: *Nonlinear FEM 2D failure onset prediction of composite shells based on 6-parameter shell theory*. Journal Thin-Walled Structures 105, 2016, pp. 207-219.
4. Code DIN 4125:1990. *Ground anchorages. Design, construction and testing*.
5. Code PN-EN 1537:1999. *Execution of special geotechnical work – Ground anchors*.
6. Code PN-EN 1997-1:2008. *Eurocode 7: Geotechnical design – Part 1: General rules*.
7. DCT Gdańsk S.A.: *Employer's requirements*. Gdańsk July 2014.
8. Krasiński A.: *Analiza jednostkowego oporu gruntu niespoistego wzdłuż pobocznic i pod podstawą pala w zależności od średnicy pala oraz uziarnienia i stanu naprężenia w gruncie* (in Polish). Doctoral Thesis, Gdańsk University of Technology, 1998.
9. Miśkiewicz M., Meronk B., Brzozowski T., Wilde K.: *Monitoring system of the road embankment*. Baltic Journal of Road and Bridge Engineering (in press).
10. Miśkiewicz M., Pyrzowski Ł., Wilde K., Mitrosz O.: *Technical monitoring system for a new part of Gdańsk Deepwater Container Terminal*. Polish Maritime Research 2017, 24(S1), pp. 149-155. DOI: 10.1515/pomr-2017-0033.
11. Miśkiewicz M., Okraszewska R., Pyrzowski Ł.: *Composite footbridge – synergy effect in cooperation between universities and industry*. ICERI2014: 7th International Conference of Education, Research and Innovation, ICERI Proceedings, 2014, pp. 2897-2903.
12. Nicholson D., Tse C., Penny C.: *The Observational Method in ground engineering – principles and applications*. Construction Industry Research and Information Association (CIRIA) Report 185, London 1999.
13. Ordinance of the Polish Ministry of Transport, Construction and Maritime Economy. *Document no 2012.0.463* (in Polish), dated 25th of April 2012.
14. Ordinance of the Polish Ministry of Transport and Maritime Economy. *Document no 1998.101.645* (in Polish), dated 1st of June 1998.
15. Patel D., Nicholson D., Huybrechts N., Maertens J.: *The observational method in geotechnics*. Proceedings of XIV European Conference on Soil Mechanics and Geotechnical Engineering, Madrid 2007, pp. 24-27.
16. Peck R.B.: *Advantages and limitations of the observational method in applied soil mechanics*. Journal Geotechnique 1969, 19(2), pp. 171-181.
17. Pyrzowski, Ł., Miśkiewicz, M., Chróścielewski, J.: *The effect of fishing basin construction on the behaviour of a footbridge over the port channel*. Polish Maritime Research 2017, 24(S1), pp. 182-187. DOI: 10.1515/pomr-2017-0037
18. Topolnicki M., Buca R.: *Możliwości zastosowania modelowania BIM w geotechnice* (in Polish). Proceedings of seminar IBDiM i PZWFS „Głębokie Wykopy”, Warsaw 2016.
19. Topolnicki M.: *Ryzyko związane ze wzmocnianiem gruntu za pomocą kolumn o różnej sztywności* (in Polish). Proceedings of XXVIII Ogólnopolskie Warsztaty Pracy Projektanta Konstrukcji, Wisła 2013.

CONTACT WITH THE AUTHORS

Mikołaj Miśkiewicz

e-mail: mmisk@pg.edu.pl

Gdansk University of Technology,
Faculty of Civil and Environmental Engineering
Narutowicza 11/12, 80-233 Gdansk

POLAND

Oskar Mitrosz

e-mail: omitrosz@keller.com.pl

Keller Polska Sp. z o.o.
ul. Rdestowa 51A, 81-577 Gdynia

POLAND

Tadeusz Brzozowski

e-mail: tbrzozowski@keller.com.pl

Keller Polska Sp. z o.o.
ul. Rdestowa 51A, 81-577 Gdynia

POLAND

MODELLING OIL SPILL AROUND BAY OF SAMSUN, TURKEY, WITH THE USE OF OILMAP AND ADIOS SOFTWARE SYSTEMS

Ali Cemal Toz

Dokuz Eylul University, Turkey

ABSTRACT

Bay of Samsun is one of the most important oil transport gateways in Black Sea. The region is surrounded with the coasts which have various levels of environmental sensitivity. The purpose of this study is to investigate the oil spill and predict the future accidents likely to be encountered around the Bay of Samsun. To be well informed about fate, this study makes the best possible use of two trajectory models. One of them, ADIOS (Automated Data Inquiry for Oil Spills), has been applied to natural degradation calculations, and the other one, OILMAP (oil spill model and response system), has been used for surface spread simulation. Hence in order to identify the risky areas three scenarios have been developed. Their results reveal that in case of oil spills, with average environmental conditions, there is a risk of contamination for the city of Samsun. Although the area under the risk is the same, contamination density is totally different depending upon the quantity and the type of spilt oil. The results gained through these efforts are hoped to be useful for many organizations dealing with oil spill response operations and contribute to an effective coordination among the relevant institutions.

Keywords: trajectory; oil spill; Bay of Samsun ,Turkey; ADIOS; OILMAP; Black Sea; modelling

INTRODUCTION

When various types of oil get in contact with the water, numerous processes of physical and biological changes initiate suddenly. The processes have great effects on forms and behaviour of oil. The trajectory of oil in marine environment is directly related to several factors such as sea currents, winds, salinity, and oil type. [15,12,30].

The main purpose of this study is to predict oil spill trajectory in spill incidents and thereby help in selecting priorities of oil spill response activities in Bay of Samsun. This study also aims to perform risk assessment for important resources in the affected region and to assist in developing coastal planning and management. Besides, modelling results of the study could be useful for guidance of decisions makers.

MATHEMATICAL MODEL

In this part a mathematical analysis defining weathering processes of oil is described. Short term processes are defined individually making use of available physical and environmental data (e.g. wind speed, temperature, oil composition etc.). Short term weathering processes are surface spread, evaporation and dispersion.

SURFACE SPREAD

This motion can be described as the movement of oil on the surface of water. The most commonly used spreading model has been developed by Fay [7]. In this process three phases involving dominant spreading and retarding forces are

determined. The gravity-inertial spreading phase which lasts only few minutes is the first phase. Tension-viscous, the third phase, occurs when the slick may be dispersed. The second phase which is considered mainly by models, is known as the gravity-viscous spreading forces and formulated as follows [1]:

$$D_{Fay} = \Delta_{p-w} \left(\frac{\Delta_w g \cdot V^2}{\sqrt{V_w}} \right)^{1/3} \cdot t^{-1/2} \quad (1)$$

Here, Δ_{p-w} is the relative oil water density, g – gravitational acceleration, V – initial spill volume, v_w – the kinematic viscosity of water, and t – the time after release. The second diffusion factor is defined to explain eddy diffusion of the surface water in addition to the first factor. Elliot and Hurford [6] conclude that such process is “non-Fickian” and a time dependent diffusion parameter better represents empirical results [19].

Shifting of oil due to the surface spread is mainly under the effects of winds and currents. The wind-based current speed is calculated equal to 3% (1%-6%) of wind velocity [24]. When both wind-based currents and tidal currents are present, the resultant movement can be calculated with the sum of two vector quantities [10]. Roughly two thirds of this movement represents Stokes drift of the surface waves. The remaining one third represents the movement of the slick along the water surface [19].

EVAPORATION

Evaporation is typically one of the most important weathering processes which start in short period just after spill. Evaporation is the main reason of the shifting of oil molecules from liquid phase to vapour phase. More volatile substances tend to evaporate more quickly than less volatile ones [16]. Evaporation rate of oil is dependent on various factors [25] explained as follows:

- *Oil Type*
Light oil evaporates more rapidly than heavy oil.
- *Temperature*
Higher temperatures increase the rate of evaporation.
- *Wind Force*
Oil evaporates more rapidly with increasing wind speed.
- *Surface Area*
The greater the area the more rapid the evaporation.

Molecules of spilt oil dissipate at different rates and are transported and weakened by environmental impacts. Since the rate of spreading relies on the consistency of the oil, light oils dissipate more quickly due to both an expansion in exposed zone and their higher rate of lighter molecules.

Estimations of evaporation rates is basically necessary to determine the consistency level of oil and changes in oil properties with time. Such calculations are carried out with simple methods, mainly based on an analytical model proposed by Stiver and Mackay [29].

If a liquid of the vapour pressure P (P_a) is spilled over an area of a (m^2), the rate of evaporation is given as follows [29]:

$$N = k_a P / (RT) \quad (2)$$

where N is the molar flux (mol/s), k_a – the mass transfer coefficient under the prevailing wind conditions (m/s), R – the gas constant [8.314 Pa.m³/(mol.K)], and T – the environmental temperature (K). Eq.1 can be arranged to give [10]:

$$dF_v / dt = k_a P_v / (V_o RT) \quad (3)$$

where F_v is the volume fraction evaporated, t – time (s), v – the liquid’s molar volume (m³/mol), and V_o – the initial volume of spilt liquid (m³). Its rearranging gives [16]:

$$dF_v = [P_v / (RT)] (k_a dt / V_o) \quad (4)$$

or

$$dF_v = H d\theta \quad (5)$$

The right side of Eq. 4 has been split into two dimensionless groups. The group “ $k_a t / V_o$ ” is termed the “evaporative exposure” and is denoted “ θ ”. The evaporative exposure is a function of time, the spill area and volume (or thickness), and the mass transfer coefficient (dependent on the wind speed). The evaporative exposure can be viewed as the ratio of exposed vapour volume and initial liquid volume [10].

The group $P_v / (RT)$ or H is a dimensionless Henry’s law constant or the ratio of the equilibrium concentration of the substance in the vapor phase, $P / (RT)$, and that in the liquid (l/v). It is a function of temperature but not of other environmental conditions [10].

The product $H\theta$ is thus the ratio of the amount which has evaporated and the amount originally present. If the liquid is pure, H is independent of F_v and Eq. 6 can be integrated directly to give [29] :

$$H\theta \quad (6)$$

If k_a and temperature are constant, the evaporation rate is constant and evaporation is complete (F_v is unity) when θ achieves the value of $1/H$. If the liquid is a mixture, H depends on F_v and Eq. 5 can be integrated only if H is expressed in function of F_v , i.e. the principal variable of vapour pressure is expressed in function of composition.

The evaporation rate decreases in the course of time. If the liquid is pure, the resistance to mass transfer must lie entirely in the air phase because there is no necessity for the substance to diffuse in the liquid phase to the interface. The mass transfer coefficient k is then entirely an air-phase resistance term. If the liquid is a mixture it is possible that there is a contributing liquid-phase resistance, especially if

the substance has a high air-liquid partition coefficient or if the liquid is viscous. The second approach is to use a gas stripping technique with an exit gas rate G (m^3/s). If the exit gas is saturated, the evaporation rate will be $GP/(RT)$ (mol) as follows [11] :

$$dF_v/dt = [GP/(RT)](v/V_o) \quad (7)$$

or

$$dF_v = H d\theta \quad (8)$$

The evaporative exposure θ is defined as Gt/V_o and is the actual ratio of vapour volume and liquid volume. The identical nature of Eq.4 and Eq.7 suggests that if surface (tray) and stripping experimental data are plotted in the form of F_v versus θ , the points should lie on a common line, θ being defined either as $k_a t/V_o$ or Gt/V_o [29].

NATURAL DISPERSION

Natural dispersion is the breaking of oil into small pieces due to motion of waves. This process has direct effect on the expansion of surface area which causes acceleration of biodegradation process [2]. The scattering rate is directly related to thickness of oil layer, surface tension, persistency, and environmental factors such as temperature, wavelength, wind speed etc [23].

The majority of oil spill modelling software used in industry utilize empirical expression proposed by Delvigne and Sweeney [4] to calculate dispersion rates. The relationship is mainly characterized by its dependence on the oil type, the energy of breaking waves lost in turbulence, and the fraction of sea surface covered by whitecaps, per unit time; the latter quantities are estimated empirically [23].

$$F_{WC} = C_b (U_w - U_{wi})/T_w \quad (9)$$

Where the local wind speed U_w is measured at the height of 10 m above MWL, U_{wi} represents a wind speed necessary for the "initiation" of breaking ($\approx 5m/s$), T_w is a characteristic wave period, and C_b ($\approx 0.032 sm^{-1}$) is a constant; A semi-empirical relation for the energy dissipation per unit surface area in a breaking event is given by:

$$D_{ba} \approx 0.0034 p_w g H_{rms}^2 \quad (10)$$

Where H_{rms} represents root mean square (rms) value of the wave height in the wave field, (m), p_w is water density (kg/m^3) and g represents gravity acceleration (m/s^2) [5].

MATERIALS AND METHOD

In this study, two numerical modelling software systems were utilized to calculate and predict fate and trajectory of spilt oil in marine environment. For the calculation and simulation of weathering processes of oil the OILMAP and ADIOS software systems were selected for simulation.

OILMAP consisting a number of modules which can assist in planning, emergency decision making and case prosecution, is a PC - based spill model and response system created by Applied Sciences Associates (ASA). This software is being utilized globally since the mid-1990s by oil companies, academic institutions and research centres [28]. The simulation results obtained from OILMAP have been validated and approved at international level [18, 26]. The reliability and performance level of OILMAP was found quite satisfactory based on field observations and hind-casting past hydrocarbon spills such as Persian Gulf War spill and Braer spills [27]. This oil spill software is considered the industry standard for use and complies with the ASTM Standard F2067-07 "Standard Practice for Development and Use of Oil Spill Models" [26, 17]. It was also used to calculate and simulate oil spill weathering processes of some global disasters such as Amoco Cadiz, Ixtoc and Persian Gulf War spills [18].

The system consists of single trajectory model for weathering process and stochastic model for contingency planning [11]. The model uses the specific properties of each oil type, including density, viscosity and surface tension to predict weathering processes such as spreading, evaporation, entrainment, and shoreline interactions [13]. The codes of software are available for different water areas such as open sea, near shore waters, semi-confined coastal waters, estuaries, rivers, lakes, and reservoirs [19].

The other model, ADIOS, is commonly used as an extensive oil products library containing more than a thousand crude oils and refined products [22]. It is also used as a reference weathering model, being compared with other new models, when ground-truth weathering data is not available. This software is developed by Lehr et al. [19] using the evaporative algorithm developed by Stiver and Mackay [29]. However, ADIOS does not simulate oil spill trajectory [8] and initiates the formation of a water-in-oil emulsion in their computer models until a specified percent evaporation for the crude oil has occurred. ADIOS can simulate oil transport and fate for water surface only. In this study the model was used for calculations of natural dispersion and evaporation. The

simulation capabilities of each software system are shown in Tab. 1.

Tab.1. Simulation capabilities of selected models

	ADIOS	OILMAP
Advection	-	+
Diffusion	-	+
Wind Drift	-	+
Stokes Drift	-	-
Floating Objects	-	+
Backtracking	-	+
Stranding	+	+
Spreading	+	+
Evaporation	+	+
Emulsification	+	+
Natural Dispersion	+	+
Vertical Movement	-	+
Dissolution	-	+
Sedimentation	-	-

Source: [8]

STUDY SITE AND EXPERIMENTAL DESIGN

Bay of Samsun located in southern part of Black Sea, with a diverse ecosystem, is selected to be model area in the study. The environmental sensitivity map with indicated spill point is shown in Fig.1.

It is clearly seen from the figure that the coasts have different levels of environmental sensitivity. For example Nature Parks are the habitat for over 320 species of birds. The shorelines of the Bay of Samsun concentrate migratory shorebirds and migrant land birds. Also some animals in danger of extinction such as ruddy ducks and sturgeon fish live in this area [20].

The Nature Parks contain different types of natural areas such as delta marshes, cultivated areas and fish stocks. The areas have the second priority of wildlife protection areas. There are two fishing ports located near the spill point. The anchovy fish is the mainstay of fisher folk. The fish stocks and fishing activities are expected to be badly affected in case of oil spill. These areas have the second priority of protection. There are some recreational areas including parks, cafeterias and living spaces considered risky areas. Summer resorts and beaches are located along the northwest coast of the Bay of Samsun [20].

Heavy industry has an accelerating development to satisfy the needs of population of the region in the last decade, and many industry branches have increased their capacities which

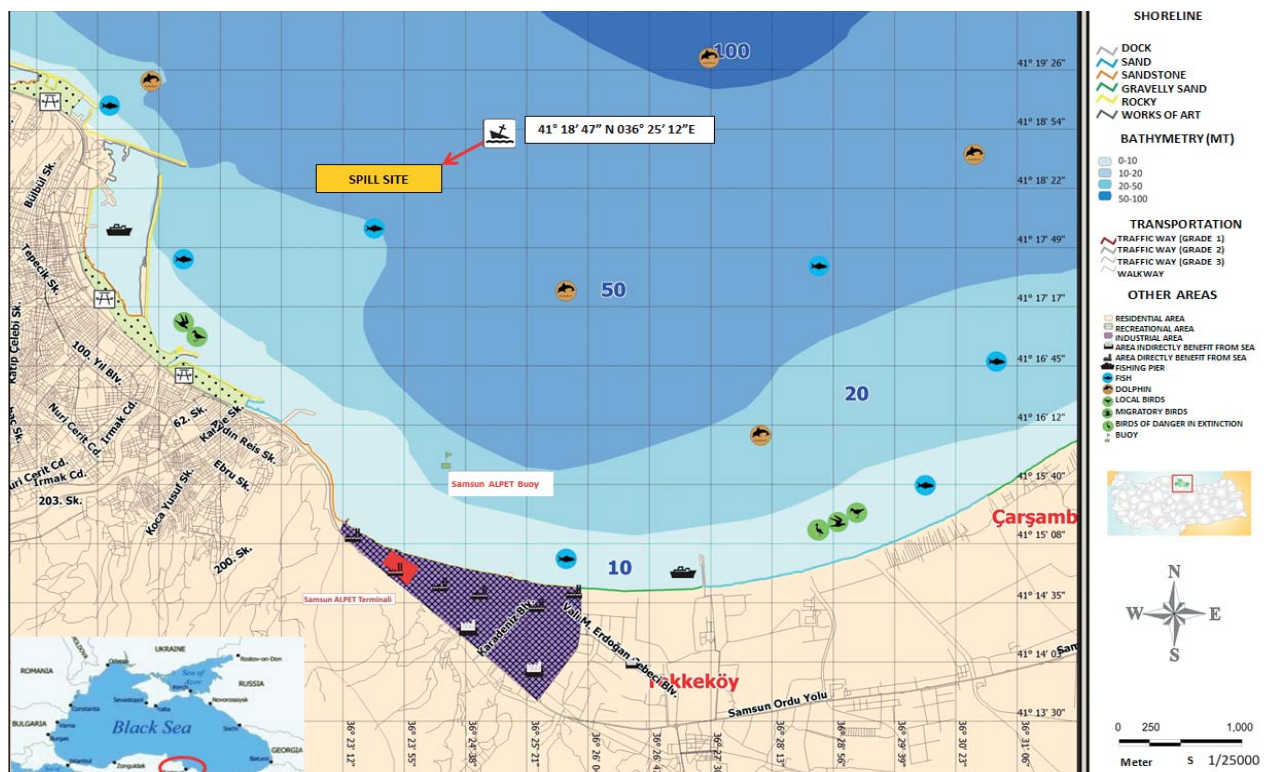


Fig. 1. Study area map: Environmental sensitivity map of Bay of Samsun, Turkey. Source: Adopted from [20].

have led to an increase in marine transportation. Density of Black Sea shipping traffic is shown in Fig 2.

Note. The color coding represents traffic density in each area. The numbers refer to quantity of distinct vessels on a daily basis and count their positions per square km. The colours stand for : blue – less than 30; green – 30 to 70; yellow – 71 to 140; red – more than 140.

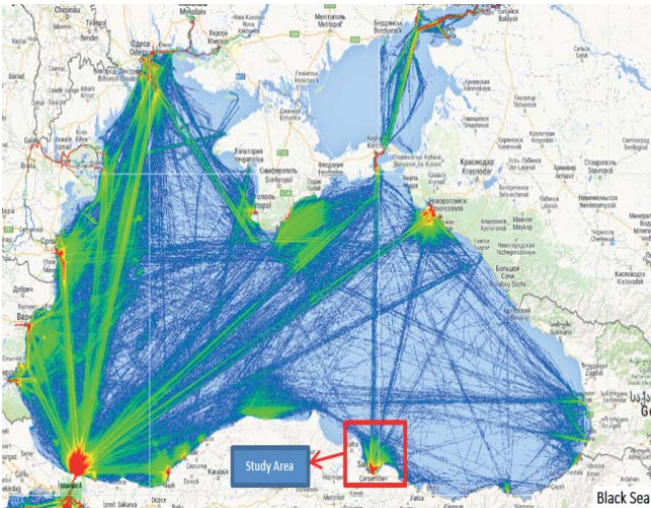


Fig 2. Black Sea shipping traffic density map (2000-2015) Source: [21]

There are 16 commercial ports operating in the region. Port of Samsun in which specific kind of cargo is handled has become the major gateway for the industrial zone. Main import products are coal, scrap, grain, wood and oil [3]. Oil terminals are also located in the region. Petrol Office, Total Oil, Alpet, Aygaz, Akpet and Milangaz are the main terminals in which oil and other harmful substances are handled. The main cargoes handled in the terminals are LPG, petrol, fuel oil and diesel oil.

The area is considered risky for some reasons. Black Sea trade is characterized by “the use of aged, smaller vessels, working well beyond their economic life and moving low value goods” [14]. The vessel accident reports indicate that losses of ships and other accidents mostly occur in certain regions such as Black Sea, which has the second greatest proportion (13%) in terms of loss concentration just after Far East (17%), The cited report has shown that vessels of age over 20 years often start a geographical move east when they are no longer able to be registered by better known classification institutions. In Fig. 3 oil spill density in Black Sea is shown.

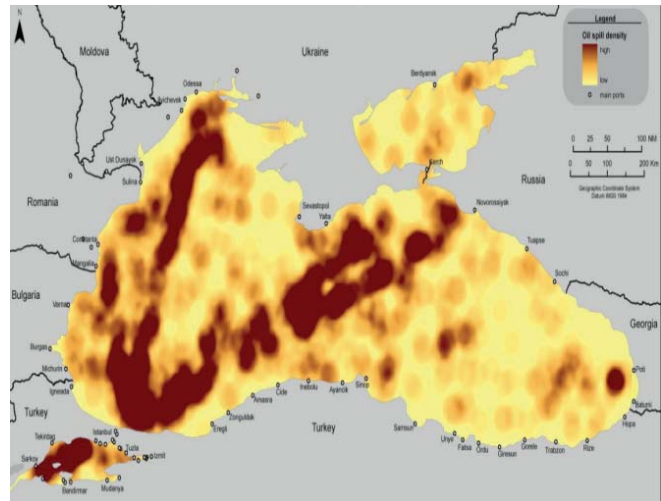


Fig. 3. Oil spill normalized density (2000-2004) Source: [9]

Note. The oil spill density has been spatially normalized to the spill widths [= extent , size ?]. The darker areas signify the high anomaly regions.

The oil spill risks for the area were identified by applying Monte Carlo simulation, which allows to identify probability of spillage. The simulation results indicate that there are three main risks which may cause oil pollution in the area. The details of the simulation are shown in Tab. 2.

Tab. 2. Risk analysis results

Accident Type	Spill Quantity (avg./ m ³)	Number of Ships (A)	Spill Area/ Area of Samsun Bay (B)	Spill Probability (C)	Accident Probability (AxBxC)
Collision	500	54	1/9	0.101	6.06x10 ⁻³
Grounding	370	54	1/9	0.07	4.2x10 ⁻³
Sinking	200	54	1/9	0.193	1.16x10 ⁻²

Source: Adopted from [21]

From Tab. 2 it can be clearly concluded that there are three main accident risks which may cause oil spill in the area. This reveals that value of probability of vessel sinking is higher than for other accidents. The average spill quantities show that the greater value of cargo is spilt in case of collision.

POLLUTANTS

In this study three types of pollutants of different physical characteristics were selected. The pollutants have various weathering characteristics while spilled onto water. So the risks may vary as a result of different physical and chemical properties. The main weathering process determinants are of a wide range and strong relationship to each other. The table for comparing specifications of pollutants is shown below.

Tab. 4. Comparison of specifications of pollutants

	Units	Crude Oil	Diesel Oil	Fuel Oil
Density at 15 °C	kg/m ³	889.0	852.0	975.0
Pour point	°C	-18	-15	30
Flash Point	°C	20	52	60
Viscosity at 50 °C	mm ² /s	10.2	2.9	80
H ₂ S Content	%	1.1	2.0	0.5

ENVIRONMENTAL DATA

The regional environmental data are obtained from long-term observation statistics which has been prepared by State Meteorological Institution. The main environmental determinants (temperature, winds and sea currents) of great effects on weathering processes, have been considered in the study. The speed and direction of the regional winds are identified in accordance with the frequencies of SSW (towards) direction with 2.9 m/s average yearly speed. Local sea currents which have been generated by the coastal wave motion and wind force are also calculated as acting from north with 0.05 m/s speed for the spill area. Water temperature has been considered to be 15°C which is the average yearly temperature.



Fig.4(a). Scenario 1a (F/O – fuel oil spill of 125m³)

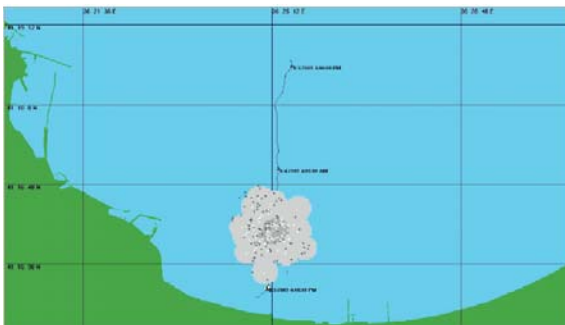


Fig. 4(b). Scenario 1b (F/O 250m³)

SCENARIOS AND MODEL

Three scenarios have been identified and used in the model as shown in Tab. 5.

Tab. 5. Summary of scenarios with spill information

Scenario	Oil Type	Amount (m ³)	Model Run Period (h)
1a	FUEL OIL (F/O)	125	24
1b		250	24
1c		500	24
2a	DIESEL OIL (D/O)	40	24
2b		80	24
2c		160	24
3a	CRUDE OIL (C/O)	125	24
3b		500	24

As indicated in Tab. 5, each scenario is divided into three sub-scenarios regarding the spill amount. The scenarios run with hourly period using particular environmental data and spill amount. Every spill scenario starts from the geographical position of 36° 26' 41''E/41° 15'26'' N. The model has run basing on the actual hourly weather data.

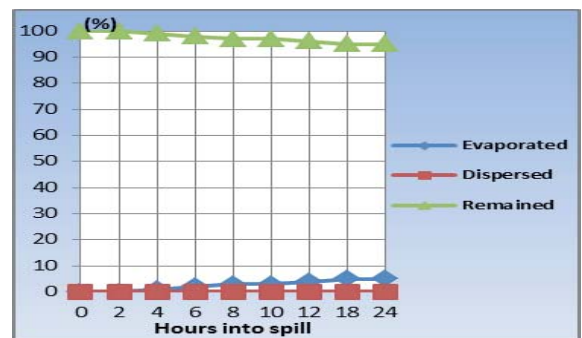


Fig. 5(a). F/O degradation chart (s/1a)

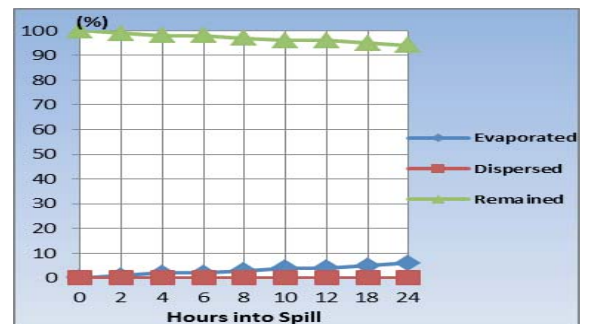


Fig. 5(b). F/O degradation chart (s/1b)



Fig.4(c). Scenario 1c (F/O 500m³)

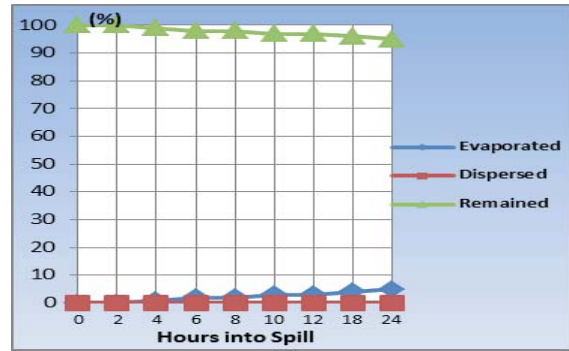


Fig. 5(c). F/O degradation chart (s/1c)

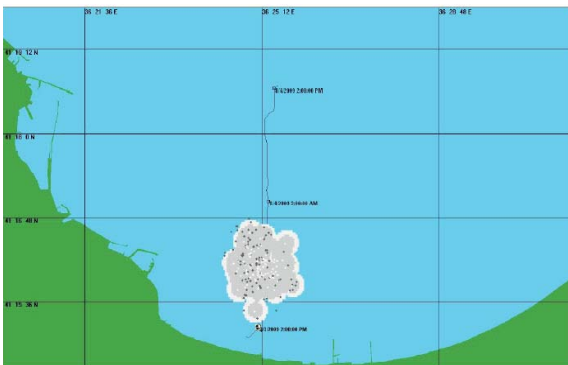


Fig.4(d). Scenario 2a (D/O - diesel oil spill of 40m³)

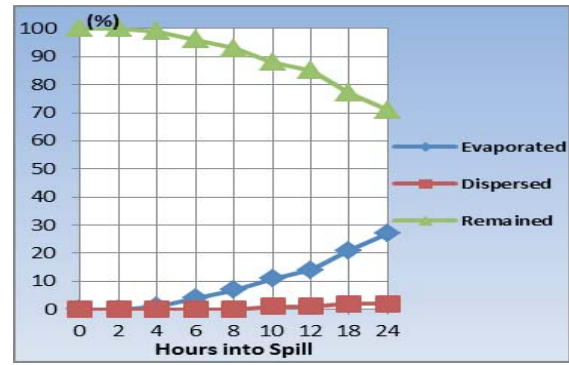


Fig. 5(d). D/O degradation chart (s/2a)



Fig.4(e). Scenario 2b (D/O 80m³)



Fig. 5(e). D/O degradation chart (s/2b)



Fig.4(f). Scenario 2c (D/O 160m³)

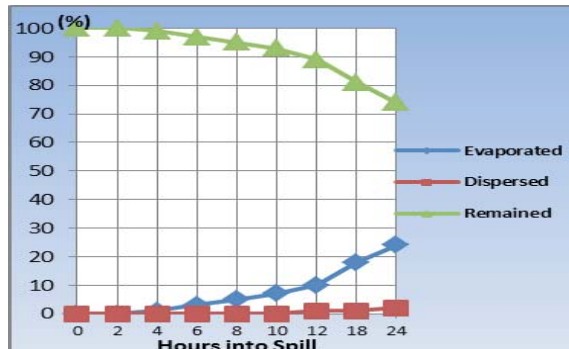


Fig. 5(f). D/O degradation chart (s/2c)

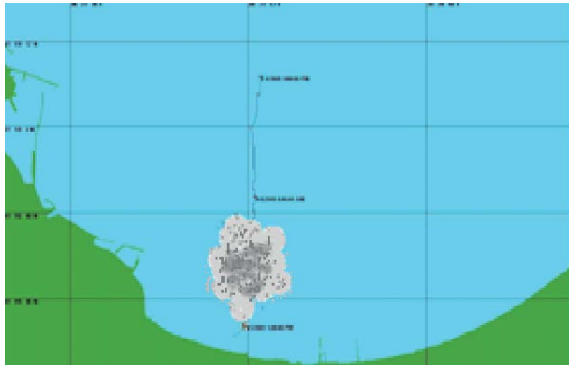


Fig.4(g). Scenario 3a (C/O 500m³)



Fig. 4(h). Scenario 3c (C/O 125m³)



Fig.5(g). C/O degradation chart (s/3a)



Fig.5(h). C/O degradation chart (s/3b)

RESULTS

The printouts of each scenario show that the movement of spill was mostly affected by sea currents and surface wind forces. The main weathering processes (evaporation, spreading, dispersion) are directly affected by environmental factors. Degradation of oil starts instantly when spilled onto water. The tracking of spill shows that the affected area is the same for all scenarios. As fuel oil is more viscous its floating part is greater than evaporation and dispersion. Diesel oil is more likely to disperse than float which constitutes more risks for benthic organisms. The evaporation process of crude oil starts earlier than that of diesel oil. Finally evaporation rates are quite close to each other. The spread velocity of fuel oil is lower than that of the other pollutants, owing to that response teams gain time to mobilize.

The study shows that the affected area and density of contamination have a strong relationship with the amount of pollutants. Spill area reaches 4 km² for fuel oil spill, 4.5 km² for diesel oil spill and 5.3 km² for crude oil spill after 6 h period. The results indicate that refined substances are more resistant to spreading than crude ones. The different types of coast structure reveal that vulnerability to oil spill and finally generated wastage is changing.

According to the simulation, it is clear that fishing ports and Nature Park are under the risk of contamination for all scenarios. For this reason response operations team has to be

mobilized at this area. In the below given Fig. 4 presenting weathering process fuel oil spill is shown with grey colour; diesel oil spill - with light grey and crude oil - with dark grey. This colouring represents contamination density. Estimated beaching time is calculated for 9 h after spill.

The figures present time dependent weathering process of each pollutant with different amount.

According to the illustrations concerning the first scenarios, only 6% of fuel oil (Fig.5a), 30% of diesel oil (Fig.5d) and 32% of crude oil (Fig.5h) are evaporated after 24 h. Diesel oil needs approximately 18 h to evaporate one quarter of total amount. Crude oil evaporation rates reach such values in shorter period. However fuel oil survives for longer period due to strong cohesive force and high viscosity. After 6 h period, only 2% of fuel oil is evaporated and 98% remains on water but diesel oil is degraded faster with 8% evaporation and 1% natural dispersion rates. Crude oil evaporates only with the rate of 22% within this period. Finally, 91% of diesel oil, 78% of crude oil and 98% of fuel oil remained on water after 6 h period. After 9 h period, beaching amounts are calculated equal to 120 m³ (96%) for fuel oil, 34 m³ (85%) for diesel oil and 90 m³ (75%) for crude oil.

According to the degradation processes concerning the second scenarios, only 5% of fuel oil (Fig.5b) and 27% of diesel oil (Fig.5e) are evaporated after 24 h. After 6 h period, only 2% of fuel oil evaporated and 98% remains on water. Although 4% of diesel oil is evaporated in this period but no

dispersion was observed. After 9 h period, beaching amounts are calculated equal to 242.5 m³ (97%) for fuel oil, 70.4 m³ (88%) for diesel oil and 90 m³ (75%) for crude oil.

The figures regarding to the third scenarios indicate that after 6 h period, only 2% of fuel oil (Fig.5c), 3% of diesel oil (Fig.5f) and 19% of crude oil (Fig.5h) evaporated. After 24 h period, 5% of fuel oil, 24% of diesel oil and 29% of crude oil evaporated. In this period, only 2% of diesel oil has been naturally dispersed and no dispersion was observed for the other substances. After 9 h beaching quantities are calculated equal to 485 m³ (97%) for fuel oil, 355 (71%) and 108 m³ (93%) for diesel oil.

CONCLUSION AND DISCUSSION

In this study an oil spill trajectory released around Bay of Samsun was investigated and the trajectory of future accidents was predicted. Although many studies on oil spilling models were reported in literature, only a few of them dealt with Black Sea region which has closed sea conditions. The spilled oil badly affects the closed sea area due to the fact that there is no way for the spilled oil to escape so as to stop damaging effects to environment.

Two trajectory models were applied in this study. OILMAP, which was used to simulate trajectory of oil spill, is considered as a valid and reliable model by oil spill science and related industry circles. The simulation results can be considered highly satisfactory because this simulation model applied also in the past to simulate oil spill weathering process of global disasters meets the requirements of international standards (ASTM Standard F2067-07).

Another one, ADIOS, is also used as a reference weathering model. The software was also applied to simulate weathering processes of real spills. However, ADIOS does not simulate oil spill trajectory and initiate the formation of a water-in-oil emulsion until after a specified percent evaporation of crude oil has occurred. ADIOS can simulate oil transport and fate only for water surface. Codes of the software system are available for different water areas such as open sea, near shore waters, semi-confined coastal waters, estuaries, rivers, lakes, and reservoirs.

Although the models in question are supported by oil spill science and industry circles, the results can be used only to assist in making better decisions.

Within this scope it was clearly identified that environmental factors (winds, currents, temperature etc.) and pollutant characteristics (viscosity, boiling point, specific gravity etc) are the main determinants of weathering process. The results revealed that in case of oil spills, with average environmental conditions, there is a risk of contamination for the city of Samsun. Although the area under the risk is the same, contamination density is totally different depending upon the quantity and the type of spilled oil.

Beaching amount of fuel oil is higher than that for other substances; so, their negative impact on environment is quite different. Not only beached quantity but also oil type is the

main factor of contamination density which determines response strategy and cleaning operations. Basing on this study it was also concluded that the degradation life time is dependent on the oil type and viscosity.

One of the most important conclusions of the study is that increase in spilled oil quantity results in decrease of degradation rates. Besides, refined products such as fuel oil and diesel oil cannot degrade as easy as crude products. This study indicates that although specifications of crude oil are similar to diesel oil, their calculated weathering processes run differently.

The simulation results can be utilized for guidance purposes only. The characteristics and behaviour of oil spilled in an uncertain marine environment may differ slightly from those simulated. The results may be useful for many organizations related to oil spill response operations. The information can be also used to improve the emergency management systems in order to protect the human health, coastal management, and marine environment.

LIMITATIONS OF THE STUDY

- Oil spill science needs accurate and reliable data. Although the models used in this study are based on the available real data, their results present only predictions of an oil trajectory.
- In real environment, the oil spill trajectory is extremely complicated due to uncertainties of data such as spill location, oil type, environmental factors and oil spill response.
- The models are very sensitive to uncertainties of data, such as quantity of spilled oil and environmental conditions. Besides, results are dependent on the quality of the environmental parameters. Therefore the reliability of data providing services is so important for getting better solutions.
- The specifications of the oil contained in the models' library may not match those of the spilled product; however, additional oil trajectory analysis can be carried out.

RECOMMENDATIONS FOR FURTHER RESEARCH

- In the future similar studies should be conducted with different spill models in order to determine validation level of the research.
- This study is based on the scenarios derived from risk assessment studies concerning oil spill in Bay of Samsun. Other risk assessment methods can be used for better results. Besides, for real oil spill conditions dynamic data should be included to find instant and reliable solutions.

ACKNOWLEDGEMENTS

The author would like to thank Turkish State Meteorological Service and Seagull Oil Spill Response Ltd for their help in providing data and Dokuz Eylul University Maritime Faculty for their support to this project.

BIBLIOGRAPHY

1. Ahlstrom S.W.: A mathematical model for predicting the transport of oil slicks in marine waters. Battelle Pacific Northwest Laboratories Richland, Wash, USA 1975.
2. Blaikley D.R., Dietzel G.F.L., Glass A.W., Van Kleef P.J.: Sliktrak-A computer simulation of offshore oil spills, cleanup, effects and associated costs. EPA/API Oil Spill Conference Proceedings, New Orleans, USA 1977, pp. 45-52.
3. Bloem, M.A., Putten M.A, Deveci A.,Tuna O.: Maritime Turkey: market research. Maritime By Holland, Netherland 2013.
4. Delvigne G.A.L., Sweeney C.E.: Natural dispersion of oil. Oil & Chemical Pollution 1988, Vol. 4, pp. 281-310.
5. Delvigne G.A.L.: Natural dispersion of oil by different sources of turbulence. International Oil Spill Conference Proceedings, California, USA 1993, pp.415-419.
6. Elliot A.J., Hurford N.: The influence of wind and wave shear on the spreading of a plume at sea. Oil and Chemical Pollution 1989, Vol.5, pp.347-363.
7. Fay J.A.: The spread of oil slicks on a calm sea. Fluid Mechanics Laboratory, Dept. of Mech. Eng., MIT, Cambridge, Mass. 1969.
8. Fernandes R., Neves R., Viegas C., Leitão P., Hidromod L.: Integration of an oil and inert spill model in a framework for risk management of spills at sea: a case study for the Atlantic area. In 36th AMOP Technical Seminar on Environmental Contamination and Response, Portugal 2013, pp. 4-6.
9. Ferraro G.: Monitoring sea-based oil pollution in the black sea: jrc activities ?
10. Fingas M.: Modeling oil and petroleum evaporation. Journal of Petroleum Science Research 2013, Vol. 2, No: 3.
11. Fingas M.: Oil spill science and technology – prevention, response, and cleanup. Gulf Professional Publishing (Elsevier), Burlington, MA, USA 2011.
12. Fingas M.: Oil spill science and technology. Gulf Professional Publishing (Elsevier), Burlington, MA, USA 2016.
13. IMO (International Maritime Organization): Catalogue of computer programs and internet information related to responding to oil spills, London, UK 2000.
14. International Transport Workers' Federation (ITF): Unions slam 'sea of shame', [online]. Available: www.itfglobal.org/pressarea/index.cfm/pressdetail/7543/region/1/section/0/order/1[accessed 20th November 2012]
15. ITOPF (International Tanker Owners Federation): Fate of oil spills, London, UK 2002.
16. Jordan R.E., Payne J.R.: Fate and weathering of petroleum spills in the marine environment. Ann Arbor Science, Ann Arbor, MI, USA 1980.
17. King B., McAllister F., Hubbert G.: Data requirements for calibration and validation of the spill model OILMAP. In, Marine Meteorology and Related Oceanographic Activities. WMO Report No. 44. MARPOLSER 98 Proceedings 1999 Vol.1 Research Papers, WMO/TD – No. 959, pp. 35-52.
18. Kolluru V., Spaulding M.L., Anderson E.: A three dimensional subsurface oil dispersion model using a particle based technique. 17th Arctic and Marine Oil Spill Program, Technical Seminar, June 8-10, Vancouver, British Columbia, Canada 1994, pp. 767-784.
19. Lehr W., Jones R., Evans M., Simecek-Beatty D., Overstreet R.: Revisions of the ADIOS oil spill mode. Environmental Modeling & Software 2002, Vol. 17 No. 2, pp.189-197.
20. MARSER (Seagull Oil Spill response Limited): Black Sea Oil spill response plan, Turkey 2015.
21. Mityagina M., Lavrova O.: Satellite survey of inner seas: oil pollution in the Black and Caspian seas. Remote Sens. 2016, Vol. 8, pp.875.
22. NOAA (National Oceanic and Atmospheric Administration): Automated data inquiry for oil spills, USA 2012.
23. Papadimitrakis I., Psaltaki M., Markatos N.: 3-D oil spill modeling: natural dispersion and the spreading of oil-water emulsions in the water column'. Global Nest Journal 2011, Vol.13 No. 4, pp. 325-338.
24. Soltanpour M., Wijayaratna N., Hajisalimi Z.: Numerical modeling of oil slick spread in the Persian Gulf. International Journal of Maritime Technology 2013, Vol.1 No.1, pp.57-66.
25. Speight J.G., Arjoon K.K.: Bioremediation of petroleum and petroleum products. Hoboken, Salem, Mass: John Wiley&Sons, N.J, USA 2012.
26. Spaulding M.L., Howlett E., Anderson E., Jayko K.: OILMAP- A global approach to spill modeling. 15th Annual Arctic and marine Oilspill Program, Technical Seminar, Edmonton, Canada 1992.

27. Spaulding M. L., Kolluru V. S., Anderson E., Howlett E.: Application of three dimensional oil spill model (WOSM/OILMAP) to hindcast the Braer spill. Spill Science and Technology Bulletin 1994, Vol. 1, No: 1, pp. 23-35.
28. Spaulding M.L., Opishinski T., Anderson E., Howlett E., Mendelsohn D.: Application of OILMAP and SIMAP to predict the transport and fate of the North Cape spill. Narragansett, RI. 19th Arctic and Marine Oil Spill Program, Technical Seminar, June 12-14, Calgary, Alberta, Canada 1996, pp. 745-776.
29. Stiver W., Mackay D.: Evaporation rate of spills of hydrocarbons and petroleum mixtures. Environment Science and Technology 1984, Vol. 18, 834–840.
30. Zalewski P., Gucma L.: Damage probability of offshore pipelines due to anchoring ships. Polish Maritime Research 2003, Vol. 4, pp. 6-12.

CONTACT WITH THE AUTHOR

Ali Cemal Toz
e-mail: ali.toz@deu.edu.tr

Dokuz Eylül Üniversitesi
Denizcilik Fakültesi
Tınaztepe Yerleşkesi
35160-Buca-İzmir
TURKEY